Universidad de Oviedo
University of Oviedo

PROGRAMA DE DOCTORADO EN BIOGEOCIENCIAS

Detection, modeling and monitoring of terrain movements by means of A-DInSAR techniques

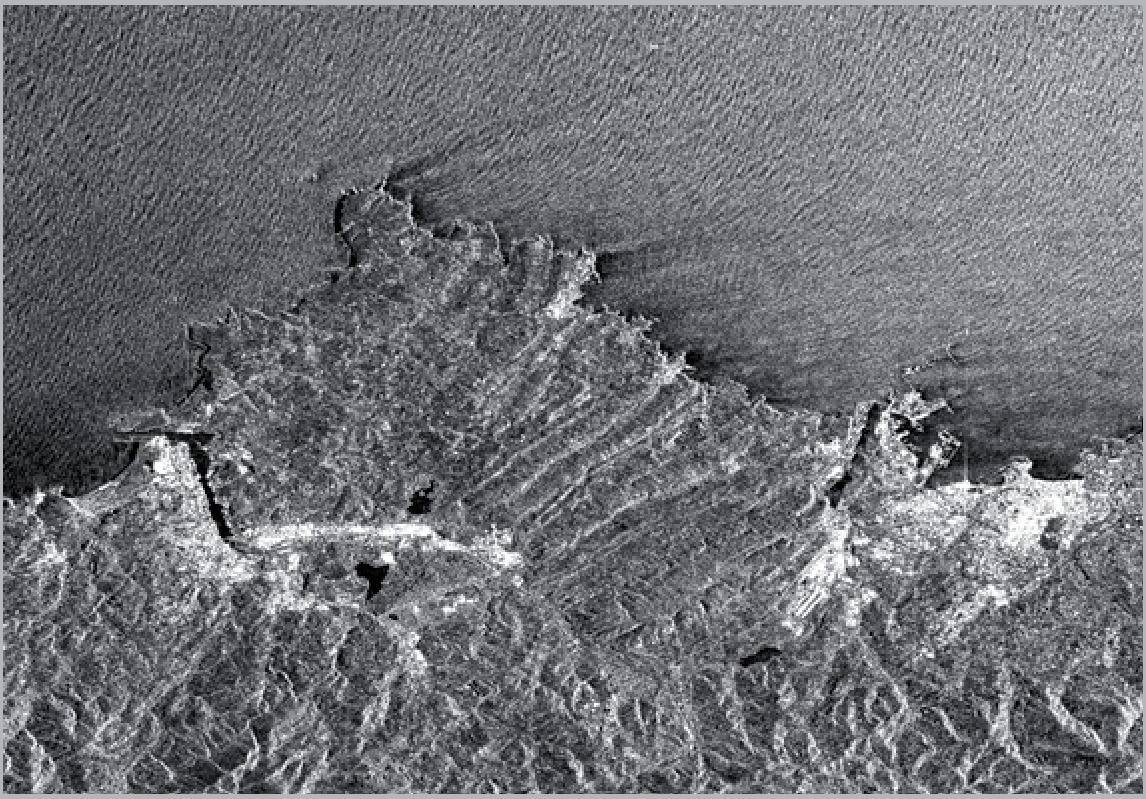

Detección, modelización y monitorización de movimientos del terreno mediante técnicas A-DInSAR

José Cuervas-Mons González de Sela

Tesis Doctoral

2023

Universidad de Oviedo
University of Oviedo

PROGRAMA DE DOCTORADO EN BIOGEOCIENCIAS

Detection, modeling and monitoring of terrain movements by means of A-DInSAR techniques

Detección, modelización y monitorización de movimientos del terreno mediante técnicas A-DInSAR

José Cuervas-Mons González de Sela

Directores: María José Domínguez Cuesta
Félix Mateos Redondo

Tesis Doctoral

2023

Universidad de Oviedo

RESUMEN DEL CONTENIDO DE TESIS DOCTORAL

1.- Título de la Tesis	
Español/Otro Idioma: Detección, modelización y monitorización de movimientos del terreno mediante técnicas A-DInSAR	Inglés: Detection, modeling and monitoring of terrain movements by means of A-DInSAR techniques

2.- Autor	
Nombre: JOSÉ CUERVAS-MONS GONZÁLEZ DE SELA	
Programa de Doctorado: BIOGEOCIENCIAS	
Órgano responsable: CENTRO INTERNACIONAL DE POSTGRADO	

RESUMEN (en español)

En esta tesis doctoral se han aplicado varias técnicas A-DInSAR (Interferometría SAR Diferencial Avanzada) con el objetivo principal de detectar, modelizar y monitorear movimientos del terreno desde enero de 2018 a febrero de 2020, en tres áreas de la zona central de Asturias (N de España) y en el Área Metropolitana de Lisboa (SO de Portugal). Concretamente, en Asturias las zonas de estudio corresponden al entorno del Cabo Peñas (incluyendo la Península de Podes), el deslizamiento del Faro de Tazones y a un área montañosa situada en la Cuenca Carbonífera Central.

La investigación ha supuesto las siguientes etapas metodológicas: 1) procesamientos A-DInSAR a partir de los software PSIG y P-SBAS utilizando tres grupos de imágenes SAR diferentes: i) 113 imágenes SAR de los satélites Sentinel-1A/B en órbita descendente, desde enero de 2018 a febrero de 2020; ii) 109 imágenes SAR del satélite Sentinel-1A desde enero de 2018 a abril de 2020, 48 de ellas en órbita ascendente y 61 en órbita descendende; 2) obtención de mapas de velocidades medias de deformación en la dirección suelo-satélite (LOS) (mm/año) y de las series temporales de deformación (mm); 3) aplicación de las metodologías de post-procesado A-DInSAR de Active Deformation Areas (ADA tools) y estimación de las componentes Vertical y Horizontal de la deformación; 4) integración en un Sistema de Información Geográfica de toda la información con datos geoespaciales y medidas topográficas tomadas mediante estación total y validación de las deformaciones obtenidas mediante salidas de campo y 5) interpretación desde el punto de vista geológico de los resultados obtenidos.

En el entorno del Cabo Peñas se han detectado velocidades máximas LOS de −17,1 a 37,4 y −23,0 a 38,3 mm/año, relacionadas con asentamientos del terreno e inestabilidades de ladera. En el deslizamiento del faro de Tazones, las medidas topográficas han mostrado desplazamientos mensuales máximos de algunos puntos desde 1 m, hasta más de 14 m. Sin embargo, las características del movimiento y la

FOR-MAT-VOA-010 (Reg.2018)

naturaleza del terreno no han permitido obtener buenos resultados con las técnicas A-DInSAR.

En el sector de la Cuenca Carbonífera Central, las deformaciones medidas presentaron velocidades máximas LOS de −18,4 y 9,5 mm/año. Estas velocidades son compatibles con subsidencia y recuperación del nivel freático en un entorno de minería subterránea de carbón. Sin embargo, debido a la confidencialidad de los datos geológico-mineros, estas hipótesis no pudieron ser corroboradas. También se detectaron deformaciones relacionadas con inestabilidades de ladera superficiales.

En el Área Metropolitana de Lisboa se han obtenido 4 ADAs en órbita ascendente y 3 ADAs en órbita descendente, relacionadas con subsidencia industrial y urbana con una velocidad máxima LOS estimada de −25,5 mm/año. La máxima velocidad Vertical medida fue −32,4 mm/año. Los datos geológicos e hidrológicos, permitieron relacionar esta subsidencia con la compactación continua de depósitos aluviales y antrópicos.

Esta investigación supone una importante contribución al conocimiento de movimientos en masa, en ámbitos mineros y costeros, en el caso de Asturias y, en ámbitos urbanos, en el Area Metropolitana de Lisboa. Además, se ha demostrado la fiabilidad del procesado P-SBAS para la detección y monitorización de movimientos del terreno a escalas regional y local, así como la utilidad del uso conjunto de datos A-DInSAR y medidas topográficas *in situ*.

RESUMEN (en Inglés)

In this doctoral thesis, several A-DInSAR (Advanced Differential SAR Interferometry) techniques have been applied in three areas of Central Asturias (N Spain) and in the Lisbon Metropolitan Area (SW Portugal), to the main aim of detecting, modeling and monitoring of ground motion from January 2018 to February 2020. Specifically, the study areas in Asturias correspond to the Peñas Cape surrounding (including the Podes Peninsula), the Tazones Lighthouse landslide and a mountainous area located in the Central Coal Basin.

The research has involved the following methodological steps: 1) A-DInSAR processing from PSIG and P-SBAS software using three different sets of SAR images: i) 113 SAR images from the Sentinel-1A/B satellites in descending orbit from January 2018 to February 2020; ii) 109 SAR images of Sentinel-1A satellite from January 2018 to April 2020, 48 of them in ascending orbit and 61 SAR images in descending orbit; 2) Obtaining of mean deformation velocity maps in the Line-of-Sight (LOS) direction (mm year^{-1}) and deformation time series (mm); 3) Application of A-DInSAR post-processing methodologies of Active Deformation Areas (ADA tools) to estimate the deformation Vertical - Horizontal components; 4) Integration of all the-information, with geospatial data and topographic measurements taken by total station and validation of the

deformations by field campaigns in a Geographic Information System and 5) Interpretation of the results obtained from a geological point of view.

The Peñas Cape environment has shown maximum LOS velocities from −17.1 to 37.4 and −23.0 to 38.3 mm year^{-1}, linked to ground settlements and slope instabilities. In the Tazones Lighthouse landslide, topographic measurements have shown maximum monthly displacements of some points from 1 m to more than 14 m. However, the characteristics of the movement and the nature of the terrain have not allowed to obtain good results through A-DInSAR techniques.

In the sector of the Central Coal Basin, the measured deformations presented maximum LOS velocities of −18.4 and 9.5 mm year^{-1}. These velocities are compatible with subsidence and phreatic level recuperation in an underground coal mining environment. However, these hypotheses could not be corroborated due to the confidentiality of geological-mining data. Deformations related to surficial slope instabilities were also detected.

In the Lisbon Metropolitan Area, 4 ADAs in ascending orbit and 3 ADAs in descending orbit have been related to industrial and urban subsidence, with maximum LOS velocities of −25.5 mm year^{-1}. The maximum measured Vertical velocity was −32.4 mm year^{-1}. The geological and hydrological data allowed to relate this subsidence to continuos compation of alluvial and anthropic deposits.

This research is an important contribution to the knowledge of mass movements at mining and coastal areas in the case of Asturias and at urban environment in the Lisbon Metropolitan Area. Furthermore, the reliability of the P-SBAS processing for ground motion detection and monitoring at regional and local scales has been demonstrated, as well as the usefulness of using A-DInSAR data together with topographic measurements taken *in situ*.

SR. PRESIDENTE DE LA COMISIÓN ACADÉMICA DEL PROGRAMA DE DOCTORADO EN BIOGEOCIENCIAS

AGRADECIMIENTOS - ACKNOWLEDGEMENTS

Solo aquellas personas que han realizado una tesis doctoral saben lo complicado, y a la vez reconfortante, que puede llegar a ser alcanzar el final de un proyecto de esta envergadura. En algún momento de su vida, el estratega cartaginés Aníbal Barca dijo *“Hallaré un camino o me lo abriré”*. Al igual que él, para llegar al final de esta tesis doctoral, tuve que ir abriendo numerosos caminos para salvar todas las dificultades encontradas, contando con la inestimable ayuda de numerosas personas sin las cuales, este trabajo no hubiera visto nunca la luz.

Agradezco, en primer lugar, a mis directores María José Domínguez Cuesta y Félix Mateos Redondo, por el continuo interés en sacar adelante esta investigación, por su infatigable búsqueda de financiación y por ser siempre pilares fundamentales de este trabajo.

A Anna Barra, Oriol Monserrat y al resto de investigadores de la división de Geomática del Centro Tecnológico de Telecomunicaciones de Cataluña por su inconmensurable interés en introducirme y enseñarme todos los aspectos teóricos y prácticos de las técnicas A-DInSAR y por permitirme utilizar, sin ningún tipo de restricción, el software PSIG y la herramienta ADA tools.

A Cristina Reyes Carmona, por enseñarme algunos de los procedimientos A-DInSAR expuestos en esta tesis doctoral.

A Montserrat Jiménez Sánchez, por sus valiosas observaciones sobre los resultados e interpretaciones obtenidas durante esta investigación, especialmente en el área del Cabo Peñas y en la ciudad de Langreo. A Pelayo González Pumariega, por sus comentarios sobre el análisis e interpretación de los datos topográficos. A Juan José Álvarez Fernández, por facilitar algunos de los documentos y planos mineros utilizados.

A José Luis Zêzere, Sergio Oliveira, Raquel Melo y Susana Pereira, por sus valiosos datos, comentarios y correcciones aportados para el análisis e interpretación del Área Metropolitana de Lisboa, y por hacer inolvidable mi estancia realizada en el IGOT.

A Edgar Berrezueta, por ser mi mentor en el precioso mundo de la investigación y de las publicaciones científicas. A Laura Rodríguez, Daniel Ballesteros y Pablo Valenzuela, por sus especiales comentarios sobre como abordar con ímpetu el doctorado y la futura vida de investigador.

Al Departamento de Geología de la Universidad de Oviedo, donde se realizó la mayor parte de la investigación aquí descrita. Reconocimiento especial a Amalia Jiménez Bautista por su papel como tutora y a María Aida González Díaz, coordinadora del Doctorado en Biogeociencias, quienes me ayudaron a superar todos los entresijos burocráticos que implica el doctorado. A Chano Antuña, por su continuo soporte para resolver las incidencias informáticas que fueron surgiendo.

A mi familia por todo su apoyo incondicional. A mis amigos, a las precari@s de Lisboa, a l@s Ulesin@s y a Bárbara, por su importante apoyo emocional a lo largo de estos años.

Esta tesis está dedicada a mi abuelo Pepe, geólogo autodidacta.

Esta tesis doctoral fue parcialmente financiada por el proyecto COSINES, cofinanciado por el Ministerio de Economía, Industria y Competitividad (MINECO), por la Agencial Estatal de Investigación (AEI) y por el Fondo Europeo de Desarrollo Regional (FEDER) [Ref. CGL2017-83909-R]; por el proyecto SEDTRIGE [Ref. FUO-128-19]; por el proyecto SLIDE-A&PCR [Ref. FUO-21-069] y por el Programa de Apoyo y Promoción de la Investigación 2021 de la Universidad de Oviedo [Ref. PAPI-21-PF-22].

This doctoral thesis was partially funded by the COSINES project, co-funded by the Ministry of Economy, Industry and Competitiveness (MINECO), by the State Research Agency (AEI) and by the European Regional Development Fund (ERDF) [Ref. CGL2017-83909-R]; by the SEDTRIGE project [Ref. FUO-128-19]; by the SLIDE-A&PCR project [Ref. FUO-21-069] and by the Research Support and Promotion Programme 2021 of the University of Oviedo [Ref. PAPI-21-PF-22].

INDEX

FIGURES INDEX

TABLES INDEX

RESUMEN

En esta tesis doctoral se han aplicado varias técnicas A-DInSAR (Interferometría SAR Diferencial Avanzada) con el objetivo principal de detectar, modelizar y monitorear movimientos del terreno desde enero de 2018 a febrero de 2020, en tres áreas de la zona central de Asturias (N de España) y en el Área Metropolitana de Lisboa (SO de Portugal). Concretamente, en Asturias las zonas de estudio corresponden al entorno del Cabo Peñas (incluyendo la Península de Podes), el deslizamiento del Faro de Tazones y a un área montañosa situada en la Cuenca Carbonífera Central.

La investigación ha supuesto las siguientes etapas metodológicas: 1) procesamientos A-DInSAR a partir de los software PSIG y P-SBAS utilizando tres grupos de imágenes SAR diferentes: i) 113 imágenes SAR de los satélites Sentinel-1A/B en órbita descendente, desde enero de 2018 a febrero de 2020; ii) 109 imágenes SAR del satélite Sentinel-1A desde enero de 2018 a abril de 2020, 48 de ellas en órbita ascendente y 61 en órbita descendende; 2) obtención de mapas de velocidades medias de deformación en la dirección suelo-satélite (LOS) (mm/año) y de las series temporales de deformación (mm); 3) aplicación de las metodologías de post-procesado A-DInSAR de Active Deformation Areas (ADA tools) y estimación de las componentes Vertical y Horizontal de la deformación; 4) integración en un Sistema de Información Geográfica de toda la información con datos geoespaciales y medidas topográficas tomadas mediante estación total y validación de las deformaciones obtenidas mediante salidas de campo y 5) interpretación desde el punto de vista geológico de los resultados obtenidos.

En el entorno del Cabo Peñas se han detectado velocidades máximas LOS de −17,1 a 37,4 y −23,0 a 38,3 mm/año, relacionadas con asentamientos del terreno e inestabilidades de ladera. En el deslizamiento del faro de Tazones, las medidas topográficas han mostrado desplazamientos mensuales máximos de algunos puntos desde 1 m, hasta más de 14 m. Sin embargo, las características del movimiento y la naturaleza del terreno no han permitido obtener buenos resultados con las técnicas A-DInSAR.

En el sector de la Cuenca Carbonífera Central, las deformaciones medidas presentaron velocidades máximas LOS de −18,4 y 9,5 mm/año. Estas velocidades son compatibles con subsidencia y recuperación del nivel freático en un entorno de minería subterránea de carbón. Sin embargo, debido a la confidencialidad de los datos geológico-mineros, estas hipótesis no pudieron ser corroboradas. También se detectaron deformaciones relacionadas con inestabilidades de ladera superficiales.

En el Área Metropolitana de Lisboa se han obtenido 4 ADAs en órbita ascendente y 3 ADAs en órbita descendente, relacionadas con subsidencia industrial y urbana con una velocidad máxima LOS estimada de −25,5 mm/año. La máxima velocidad Vertical medida fue −32,4 mm/año. Los datos geológicos e hidrológicos, permitieron relacionar esta subsidencia con la compactación continua de depósitos aluviales y antrópicos.

Esta investigación supone una importante contribución al conocimiento de movimientos en masa, en ámbitos mineros y costeros, en el caso de Asturias y, en ámbitos urbanos, en el Area Metropolitana de Lisboa. Además, se ha demostrado la fiabilidad del procesado P-SBAS para la detección y monitorización de movimientos del terreno a escalas regional y local, así como la utilidad del uso conjunto de datos A-DInSAR y medidas topográficas *in situ*.

ABSTRACT

In this doctoral thesis, several A-DInSAR (Advanced Differential SAR Interferometry) techniques have been applied in three areas of Central Asturias (N Spain) and in the Lisbon Metropolitan Area (SW Portugal), to the main aim of detecting, modeling and monitoring of ground motion from January 2018 to February 2020. Specifically, the study areas in Asturias correspond to the Peñas Cape surrounding (including the Podes Peninsula), the Tazones Lighthouse landslide and a mountainous area located in the Central Coal Basin.

The research has involved the following methodological steps: 1) A-DInSAR processing from PSIG and P-SBAS software using three different sets of SAR images: i) 113 SAR images from the Sentinel-1A/B satellites in descending orbit from January 2018 to February 2020; ii) 109 SAR images of Sentinel-1A satellite from January 2018 to April 2020, 48 of them in ascending orbit and 61 SAR images in descending orbit; 2) Obtaining of mean deformation velocity maps in the Line-of-Sight (LOS) direction (mm year^{-1}) and deformation time series (mm); 3) Application of A-DInSAR post-processing methodologies of Active Deformation Areas (ADA tools) to estimate the deformation Vertical - Horizontal components; 4) Integration of all the-information, with geospatial data and topographic measurements taken by total station and validation of the deformations by field campaigns in a Geographic Information System and 5) Interpretation of the results obtained from a geological point of view.

The Peñas Cape environment has shown maximum LOS velocities from −17.1 to 37.4 and −23.0 to 38.3 mm year^{-1}, linked to ground settlements and slope instabilities. In the Tazones Lighthouse landslide, topographic measurements have shown maximum monthly displacements of some points from 1 m to more than 14 m. However, the characteristics of the movement and the nature of the terrain have not allowed to obtain good results through A-DInSAR techniques.

In the sector of the Central Coal Basin, the measured deformations presented maximum LOS velocities of −18.4 and 9.5 mm year^{-1}. These velocities are compatible with subsidence and phreatic level recuperation in an underground coal mining environment. However, these hypotheses could not be corroborated due to the confidentiality of geological-mining data. Deformations related to surficial slope instabilities were also detected.

In the Lisbon Metropolitan Area, 4 ADAs in ascending orbit and 3 ADAs in descending orbit have been related to industrial and urban subsidence, with maximum LOS velocities of −25.5 mm year^{-1}. The maximum measured Vertical velocity was −32.4 mm year^{-1}. The geological and hydrological data allowed to relate this subsidence to continuos compation of alluvial and anthropic deposits.

This research is an important contribution to the knowledge of mass movements at mining and coastal areas in the case of Asturias and at urban environment in the Lisbon Metropolitan Area. Furthermore, the reliability of the P-SBAS processing for ground motion detection and monitoring at regional and local scales has been demonstrated, as well as the usefulness of using A-DInSAR data together with topographic measurements taken *in situ*.

ABBREVIATIONS

A-DInSAR	Advanced Differential SAR Interferometry
ADA	Active Deformation Area
ALS	Airborne laser scanning
AoI	Area of Interest
APS	Atmospheric phase screen
AR	Active corner reflector
ASF	Alaska Search Facility
BAPA	Base de datos de Argayos del Principado de Asturias
CPT	Coherent Pixels Technique
CTTC	Telecommunications Technological Center of Catalonia
DA	Dispersion of amplitude
DEM	Digital elevation model
DFOS	Distributed fibre-optic sensing
DS	Distributed scatterer
DInSAR	Differential SAR Interferometry
ESA	European Space Agency
GB-SAR	Ground-Based SAR
GEP	Geohazards Exploitation Platform
GIS	Geographical Information System
GNSS	Global navigation satellite system
GPR	Ground penetration radar
GPS	Global positioning system
HRDEM	High resolution DEM
HUNOSA	Hulleras del Norte S.A.
InSAR	SAR Interferometry
IPTA	Interferometric Point Target Analysis
IW	Interferometric Wide swath
LIDAR	Ligh detection and ranging

LMA	Lisbon Metropolitan Area
LOS	Line-of-Sight
LP	Low Pass filter
MA	Mean amplitude
MASW	Multichannel analysis of surface waves
PCR	Passive corner reflector
PS	Persistent - Permanent Scatterer / Points
P-SBAS	Parallel Small BAseline Subset
PSIG	Persistent Scatterer Interferometry of Geomatics Division
QI	Quality index
RSET	Rod surface-elevation table
S1TBX	Sentinel-1 Toolbox
SAR	Synthetic Aperture Radar
SLC	Single Look Complex
SPINUA	Stable Point Interferometry over Unurbanised Areas
SPN	Stable Point Network
SRTM	Shuttle Radar Topography Mission
StaMPS	Standfor Method of Persistent Scatterer
Thr	Threshold
TLS	Terrestrial laser scanning
TS	Time series
UAV	Unmanned aerial vehicle
VLOS	LOS velocity

1. INTRODUCTION

1.1 Motivation and justification

In Asturias (N Spain) and in the Lisbon Metropolitan Area (LMA, SW Portugal), as in other parts of the World, there is a significant problem related to slope instabilities and subsidence phenomena. These processes generate huge economic losses every year and even cause human losses.

Due to the high incidence of these phenomena, since 1995, the Department of Geology of the University of Oviedo has been collecting data on terrain instabilities, subsequently creating the BAPA (*Base de datos de Argayos del Principado de Asturias*) database with the purpose of recording and classifying all the ground movements that occur throughout the Asturian territory (Domínguez-Cuesta *et al.*, 1999; Valenzuela, 2017). In this way, 62 slope instabilities and subsidence events are approximately recorded per year, with a maximum number of events recorded of 262 (in 2013). One report estimated the total direct cost of landslides in Asturias at 66 million euros per year (González Moradas and Lima de Montes, 2001). On the other hand, Asturias has been an important region of underground and opencast coal mining, from the 19th century to the 21st century. This coal mining activity comes associated to multiple problems linked to slope instabilities and subsidence phenomena (López-Fernández *et al.*, 2002; Riesgo-Fernández *et al.*, 2020). Consequently, mining operations are characterized by a high confidentiality of the geological-mining data collected. This means that the data are very restricted in its use or not available for analysis. This information corresponds to: 1) Geology at depth; 2) Location of underground mine works; 3) Borehole, pumping and water level data and 4) Geotechnical monitoring data of mined areas. In this line, the Central Coal Basin is characterized by a high confidentiality of the geological-mining and hydrogeological data collected around the mining works and pits. Currently, it is only possible to access some technical documents of HUNOSA open to the public and mining plans prior to 1967, the year in which HUNOSA was created and acquired the private mining companies working in the region.

On the other hand, the LMA is characterized by a high and fast urban and industrial development in the last 40 years. This fact has led to an increase in geological hazards and a need for adequate urban planning. In this line, several authors as Campos Costa *et al.* (2010) and Carvalho *et al.* (2018) addressed their studies in the LMA from a seismic or soils liquefaction hazards point of view. Other researchers have focused on the flood risk and damage in buildings produced by extreme rainfalls episodes (Leal *et al.*, 2019; Leal *et al.*, 2020). Regarding landslide topic, Melo *et al.* (2018) and Vaz *et al.* (2018) studied the landslide occurrence in Lisbon region according to regional and local rainfall thresholds. On the other hand, Pereira *et al.* (2020) performed a landslide risk index in

Portugal, recognising the LMA as an important landslide hazard area. In this line, it has been estimated an extension of 18,000 ha with landslide incidence (Comissão Exècutiva Metropolitana de Lisboa, 2019), which corresponds to 5.9% of LMA territory. In addition, other studies focused on the urban planning and policies (Medeiros *et al.*, 2021), hydrodynamic and geochemistry of Tagus River (Vaz *et al*, 2019), among others.

During the last two decades, techniques based on Synthetic Aperture Radar (SAR) have been successfully used in the detection, modeling and monitoring of ground deformations (Ferreti *et al.*, 2001; Berardino *et al.*, 2002). These techniques calculate with millimeter precision the ground surface displacement that occurs between two different radar images, collected by sensors aboard a satellite. A progressive comparison of the images during a certain period of time (usually years) allows a multi-temporal analysis of the displacement, by which time series of surface displacement and annual mean velocities can be obtained (Massonet and Feigl, 1998). Moreover, these techniques allow the monitoring of large areas of land (of about 10,000 km^2). Therefore, the application of A-DInSAR techniques is suitable for detecting, modeling and monitoring ground movements associated to slope instabilities and subsidence in Asturias and in the LMA.

Considering that A-DInSAR techniques are only capable of detecting very slow movements (< 1.6 m $year^{-1}$) (Canuti *et al.*, 2004), this research has been adressed to assess the potential and limitations of the A-DInSAR techniques for mapping and monitoring of ground movements. For this purpose, Sentinel-1 data has been used by means of different approaches: a robust and supervised approach (PSI technique from PSIG software), an unsupervised-automatic approach (P-SBAS technique from GEP service) and A-DInSAR post-processing methods, topographical monitoring and field campaigns.

The content of this thesis report is summarzed below to facilitate the understanding of the text and the structure of this work.

In **Chapter 1 - Introduction**, the background on landslide and subsidence phenomena and problem statement are presented. **Chapter 2 - Study areas** describes in detail the different criteria considered for selecting and analyzing the study areas. **Chapter 3 - Methodology** is assigned to explaining the methodological procedure followed. In **Chapter 4 - Results**, A-DInSAR results and topographic measurements are presented and described in depth. The **Chapter 5 - Discussion** is specially focused on the geological interpretation of slope instabilities and subsidence phenomena detected and monitored. Furthermore, main found limitations, possible improvements and future lines of research are exposed and discussed. **Chapter 6 - Conclusions** lists the conclusions drawn from this research.

1.2 Landslides and subsidence phenomena

1.2.1 Landslide processes

The term landslide was defined by Cruden (1991) as a movement of a mass of rock, debris or earth down a slope (Figure 1). Phenomena as ground subsidence and collapses, snow avalanches and ice falls are excluded (Cruden and Varnes, 1996). According to Varnes (1978) and Cruden and Varnes (1996), the landslide kinematics is one of the principal criteria to classify mass movements. In this line, these authors classified five kinematically types of landslide movement: fall, topple, slide, spread and flow (Figure 2 and Table 1). Another criterion is the type of material involved (Table 1) in a landslide that can be rock and/or a soil (Varnes, 1978). Soil could be divided into earth and debris. According to Varnes (1978), first term describes material in which 80 percent or more of the particles are smaller than 2 mm. Debris contains a large proportion of coarse material: 20 to 80 percent of the particles are larger than 2 mm (Varnes, 1978).

Figure 1. Example of landslide that occurred in the village of La Cortina (Asturias), on June 28, 2018.

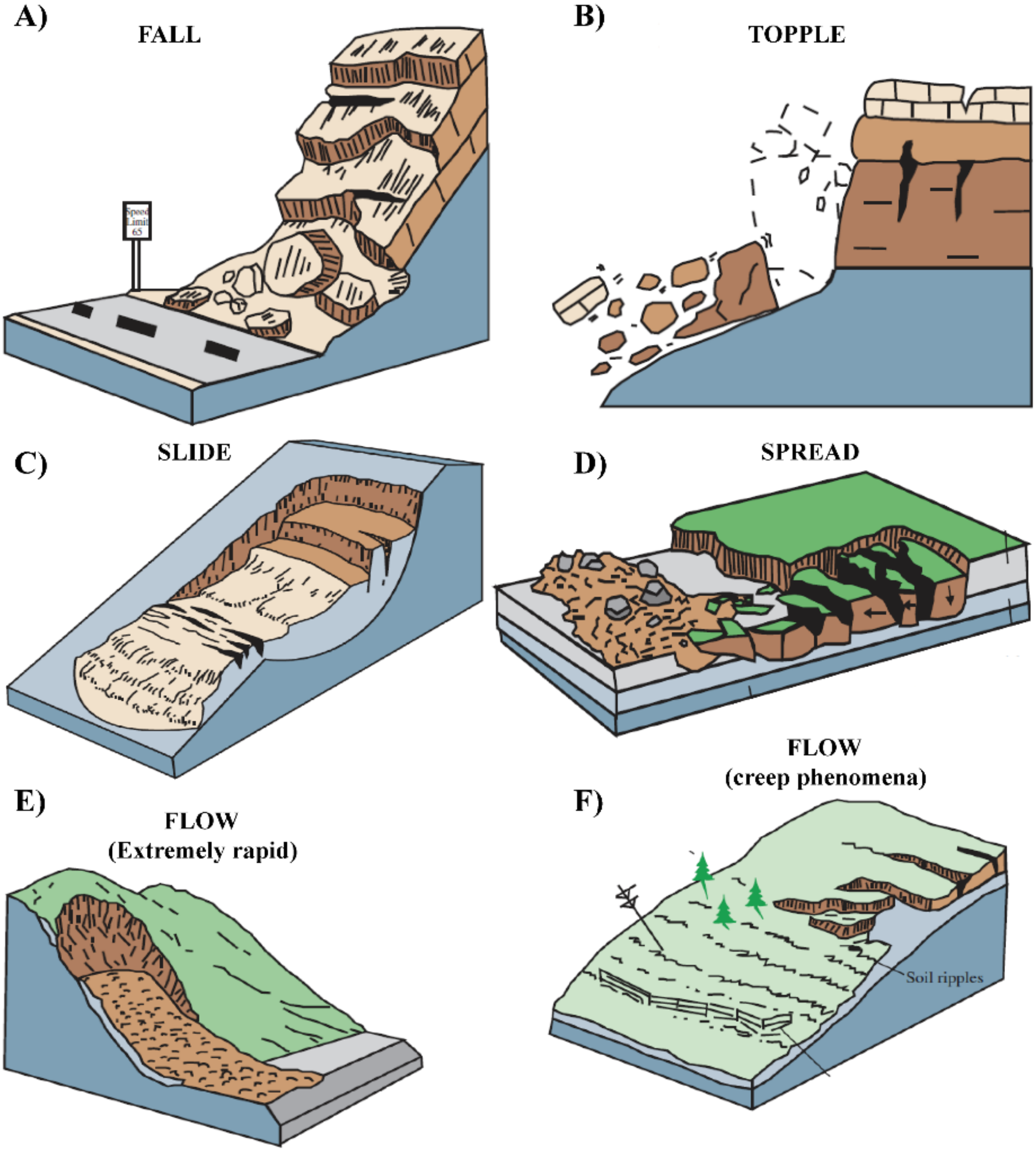

Figure 2. Classification of landslides by Varnes (1978) according to the type of movement. Taken and modified from USGS (2016).

Varnes' classification according to the type of movement is described below (Table 1) (Varnes, 1978; Cruden and Varnes, 1996). **Fall** (Figure 2 A): is the detachment of soil or rock from a steep slope along a surface and subsequent descend through the air by falling, bouncing or rolling. These kinds of movements are very rapid to extremely rapid (Table 2). **Topple** (Figure 2 B): is the forward rotation out of the slope of a mass of rock or soil about a point or axis below the center of gravity. The occurrence of these movements depend on the geometry of the moving mass and the surface of separation, the orientation and extent of the discontinuities. Topples velocity ranges from extremely slow to extremely rapid (Table 2). **Slide** (Figure 2 C): is a downslope movement of a rock or soil developing on surfaces of ruputure or on relatively thin zones of intense shear strain. First signs of movement are cracks in the original ground surface. These movements can be distinguished in rotational or translational slides (Table 1). Rotational slides move along a curved and concave surface of rupture. They occur most frequently in homogeneous materials. However, translational slides are characterized by the mass displacements along a planar surface of rupture. The velocity of these types of instability can be from extremely slow to slow movements (Mansour *et al.*, 2011) (Table 2). **Spread** (Figure 2 D): is an extension of a cohesive soil or rock mass combined with subsidence of the fractured and cohesive material into softer underlying material. This movement may result from liquefaction or flow of the softer material. Also, failure is usually triggered by rapid ground motion produced, for example, by an earthquake or by anthropic factors. **Flow** (Figure 2 E): is a spatially continuous movement in which surfaces of shear are short-lived, closely spaced and not preserved. Also, these movements are often associated with the presence of water. There are different types of flows and their velocity of movement ranges from extremely slow to extremely rapid (Table 2). A particular type of flow is **creep** phenomena (Figure 2 F), which is the continuous extremely slow (Table 2) and downward movement of slope, produced by shear stress. Finally, a **complex movement** is a slope instability produced by combination of two or more types of the previous movement.

Table 1. Varnes'classification of slope movements. Taken and modified from Varnes (1978).

Type of movement		**Type of material**		
		Bedrock	**Engineering soils**	
			Predominantly coarse	**Predominantly fine**
Fall		Rock fall	Debris fall	Earth fall
Topple		Rock topple	Debris topple	Earth topple
Slide	Rotational	Rock slide	Debris Slide	Earth slide
	Translational			
Lateral spread		Rock spread	Debris spread	Earth spread
Flow		Rock flow	Debris flow	Earth Flow
Complex		Combination of two or more principal types of movement		

Another way to classify landslides is the velocity of mass movement. Cruden and Varnes (1996) designed a scale of 7 levels according to mass movement velocity (Table 2). These levels range from extremely slow (< 16 mm year^{-1}) to extremely rapid (> 5 m seg^{-1}). In addition, each velocity rate implies different effects and consequences. Table 2 defines the probable destructive significance of the seven velocity classes (Cruden and Varnes, 1996). For example, in the case of an extremely slow slope instability, the expected damage will be imperceptible without instrumentation, while an extremely rapid movement will produce human losses and destruction of buildings (Table 2).

Table 2. Abbreviated version table of velocity scale and expected damage of slope instabilities. Taken and modified from Varnes (1978) and Cruden and Varnes (1996).

Description	Velocity	Class	Expected damage
Extremely rapid	> 5 m seg^{-1}	7	Catastrophe; human losses; buildings destroyed by impact of displaced material
Very rapid	< 5 m seg^{-1}	6	Possible human losses
Rapid	< 3 m min^{-1}	5	Scape evacuation possible; structures, possessions, and equipment destroyed
Moderate	< 1.8 m hour^{-1}	4	Some temporary and insensitive structures can be temporarily maintained
Slow	< 13 m month^{-1}	3	Remedial construction can be undertaken during movement; insensitive structures can be maintained with frequent maintenance work if total movement is not large during a particular acceleration phase
Very slow	< 1.6 m year^{-1}	2	Some permanent structures undamaged by movement
Extremely slow	< 16 mm year^{-1}	1	Imperceptible without instruments; construction possible with precautions

Landslides are one of the most widespread geohazards in the World, producing a significant social and economic impacts. During period comprehended between 1998 and 2017, > 4.8 million people, with 18,414 fatalities, were affected by landslide incidence in the World (Wallemacq *et al.*, 2018). In Europe, about 312 fatalities were caused by landslides between 1998 and 2009 (Spizzichino *et al.*, 2010), whose direct costs were estimated to reach up to €48 billion. These costs included damage of infrastructures such as roads, railways, pipelines, structures, embakments, and buildings. The study of Hache *et al.* (2016) revealed that in 27 European countries, including Turkey, 1,370 deaths and 784 injuries were recorded from 476 landslide events between 1995-2014. In Portugal, along 151 years (1865 - 2015), a total of 292 landslides caused 237 fatalities, 434 injured, 823 evacuated and 1,620 displaced people (Pereira *et al.*, 2020). In Spain, the General Directorate of Civil Protection and Emergencies reported 32 deaths due to landslides between 2000 and 2019 (DGPCE, 2020). Ferrer (1995) indicated that economic losses due to landslides could reach €180 million euros per year between 1986 and 2001, while Ayala *et al.* (2004) estimated economic damage during the period 1990-2000 at €42 million per year.

According to Margottini *et al.* (2013), incidence and recurrence of landslides are conditioned by topographical and geo-environmental aspects related to: 1) Soil properties; 2) Geological structure; 3) Lithology; 4) Weather conditions; 5) Slope morphology; 6) Land cover; 7) Water flow and 8) Human activities (Figure 3). These factors reduce the stability of the slope and may even reactivate old landslides (e. g. Azañón *et al.*, 2016). On the other hand, triggering factors cause the slope to move from stable to actively unstable. The most common natural triggers include volcanic eruption, earthquake shaking, slope saturation and anthropic activities (Wieczorek, 1996). Rainfall and heavy rains are the most important physical process for landslide incidence in the World, including Portugal and Asturias (Domínguez-Cuesta *et al.*, 1999; Menéndez-Duarte *et al.*, 2003; Crosta and Frattini, 2008; Valenzuela, 2017; Vaz *et al.*, 2018).

Figure 3. Complex movement developed in the A-66 highway works in Cornellada town (Asturias) on April 16, 2021. Its triggering was linked to rainfall and anthropic activities. Photo taken by the La Nueva España newspaper.

1.2.2 Subsidence phenomena

Subsidence phenomena are natural or anthropic processes which consist of sudden or gradual downward sinking of the ground surface with little or no horizontal motion (Jackson and Bates, 1997). Ground subsidence can be produced by internal geological processes, such as isostatic adjustments, volcanism, folding, faulting or by natural or anthropic exogenous processes (Prokopovich, 1979) (Table 3). Main causes of exogenous subsidence can be dissolution, ice thaw, piping, consolidation related to sediment loading, piezometric falls related to reduced aquifer recharge, fluid withdrawal related to oil and gas exploitation, underground mining and tunneling (Table 3) (González de Vallejo, 2002; Galloway *et al.*, 2016; Shirzaei *et al.*, 2021).

Table 3. Subsidence phenomena classification according to tectonic or surficial causes. Taken and modified from Prokopovich (1979).

Subsidence phenomena	
Endogenic (tectonic) processes	**Exogenic (surficial) processes**
Isostatic adjustements	Dissolution
Volcanism - Seismic activity	Ice thaw
Folding	Underground erosion (piping)
Faulting	Land compaction - consolidation
	Groundwater and other fluids over-exploitation
	Underground mining
	Tunneling

Tectonic subsidence is usually defined as the sinking of the Earth`s crust on a large scale. Isostatic adjustements are linked to response of the lithosphere to sedimentary, ice and water loads. These cases are well-known in the Mississippi Delta (U.S.A) and the Ganges - Brahmaputra Delta (Bangladesh and India), with subsidence rates of a few millimeters per year (Wolstencroft *et al.*, 2014; Karpytchev *et al.*, 2018). Large earthquakes are followed by a postseismic deformation phase, during which afterslip occurs within the fault zone causing vertical motions of the land surface (Shirzaei *et al.*, 2021). For instance, after the 2004 Sumatra - Andaman earthquake produced 20 - 30 mm of subsidence in Bangkok (Thailand) in the first 5 years after the earthquake, worsening flooding hazards (Satirapod *et al.*, 2013; Shirzaei *et al.*, 2021). Normal faulting and folding can also contribute to subsidence. According to Shirzaei *et al.* (2021), normal faults or growth faults, form when higher density sediments overlie weak and deformable strata. These faults initiate near the surface and propagate downward as the overburden loading continues, exhibiting displacements that can produce deep subsidence (Crans *et al.*, 1980). Lithospheric folding is an important mode of basin formation in compressional intraplate regions with associated subsidence (Cloething and Burov, 2011).

Subsidence linked to dissolution is usually related to salt, gypsum and carbonate rocks dissolution (e. g. Anderson *et al.*, 1998; Gutiérrez-Santolalla *et al.*, 2005; Pando *et al.*, 2013). This phenomenon is produced in presence of water and it can generate interconnected system of voids with subsequent collapses. Subsidence linked to ice thaw consists on vertical movements that occur after the disappearance of ice sheets or permafrost (e. g. Shiklomanov *et al.*, 2013). Subsurface erosion subsidence is caused by flows of water or other fluids that produce a mechanical process of particle entrainment of a soil or rock below the surface (e. g. Sato and Kuwano, 2015). This can lead to the formation and growth of underground cavities, sinkholes and collapses of the surface (Figure 4).

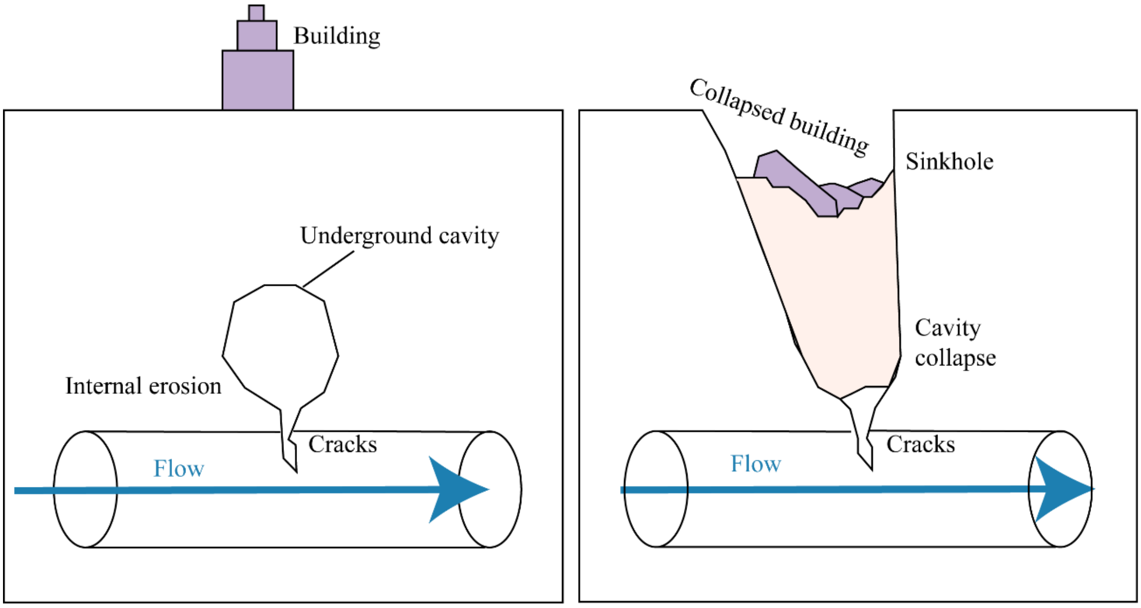

Figure 4. Simplified scheme of subsidence caused by underground erosion (piping). Taken and modified from Sato and Kuwano (2015).

Subsidence due to land compaction (e. g. Kooi and de Vries, 1998) is produced as consequence of: 1) The weight made by sediment acumulation; 2) By vertical loal related to buildings; 3) The hydro-compaction (e. g. Rogers *et al.*, 1994), which is the settling that occurs in some types of soils with a low moisture content and located above the phreatic level, when they are saturated and 4) By groundwater and other fluid over-exploitation (Gambolati and Teatini, 2021), which is produced as a result of the gradual closure of the vois filled by the extracted fluid.

Underground mining (e. g. Parmar *et al.*, 2019; Cando Jácome *et al.*, 2020) and tunneling (e. g. López-Fernández *et al.*, 2013; Valenzuela *et al.*, 2015) can produce settlements and voids of the terrain due to drawdown of the water table, consolidation of soil or rock layers or collapse of mining galleries and tunnels (Figure 5). The subsidence can lead to the total collapse of the terrain, resulting in the destruction of buildings and infrastructures (Figure 5).

Figure 5. A 40 m deep hole produced in 2021 by underground mining activity in the town of Zaruma (Ecuador). Photo taken by the El Universo newspaper.

Active subsidence is one of the key factors damaging metropolitan areas and road networks, specially in coastal cities, because land subsidence increases the flooding risk (Herrera *et al.*, 2021; Wu *et al.*, 2022) (Figure 6). According to Bucx *et al.* (2015), direct damage are the loss of functionality or integrity of structures like buildings, roads and underground utility networks. The most common indirect effects of damage are related to changes in relative water levels, both groundwater levels and surface water levels (Bucx *et al.*, 2015). In 1991, the National Research Council estimated that annual costs in the United States from flooding and structural damage caused by land subsidence exceeded $125 million (Galloway *et al.*, 1999). Some reports about annual subsidence costs were published by China between 2001 - 2010, where were estimated US$1.5 billion. In 2006, in the Netherlands were estimated annual costs of US$3.5 billion (Bucx *et al.*, 2015). Bonachea *et al.* (2014) carried out a review of economic losses related to different cases of subsidence in Spain. For instance, subsidence produced in Murcia city (between 1992 - 1995 and 2004 - 2008) linked to groundwater withdrawal generated damages to more than 150 buildings with an estimated cost of about €50 million (Mulas *et al.*, 2003; Tessitore *et al.*, 2015).

There are many studies about active subsidence in large urban areas and transportation facilities. The most remarkable examples are Beijing, with velocities of 52 mm year^{-1}

(e.g. Zhu *et al.*, 2015), Rome, where velocity detected was 23.3 mm year^{-1} (e.g. Orellana *et al.*, 2020), Mexico City, with velocities that can reach from 0.4 to 1.5 m year^{-1} (e.g. Ortiz-Zamora and Ortega-Guerrero, 2010), New Delhi, with rates of subsidence near 11 cm per year (e.g. Garg *et al.*, 2022), Houston, with velocities of 37 mm year^{-1} (e.g. Kearns *et al.*, 2015), Guayaquil, with velocities of 19.2 mm year^{-1} (e.g. Cuervas-Mons *et al.*, 2021a) or Manila, whose maximum velocity detected is on the order of 15 cm year^{-1} (e.g. Raucoules *et al.*, 2013) (Figure 6).

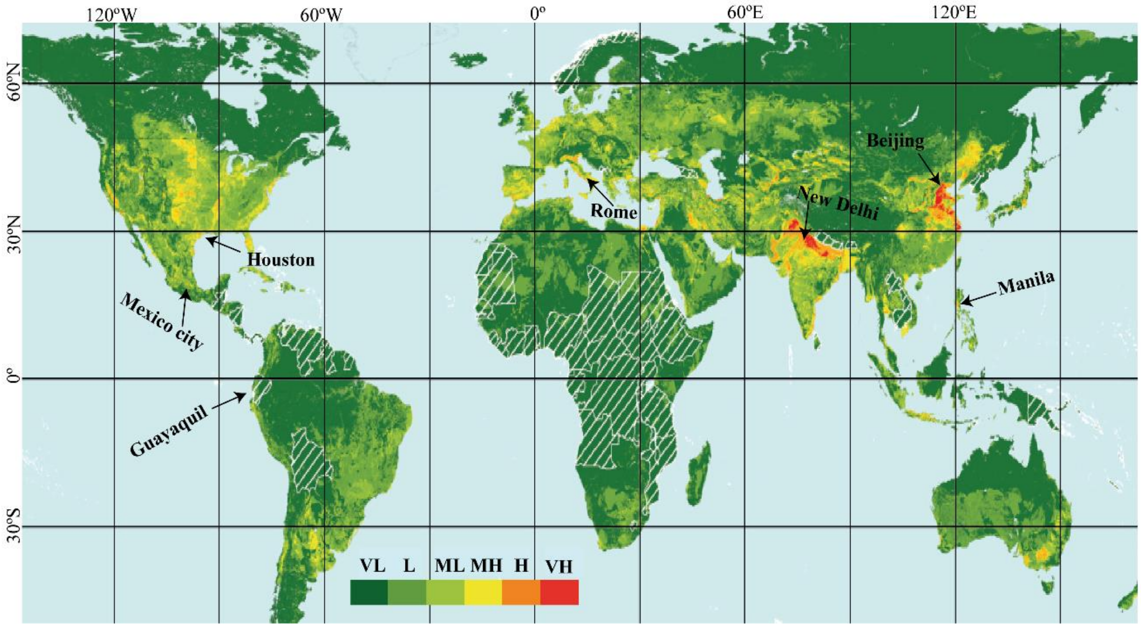

Figure 6. Potential global subsidence in the World. Intervals range from very low - VL to very high - VH. White polygons indicate countries where groundwater data are not available.Taken and modified from Herrera *et al.* (2021).

1.2.3 Landslide and subsidence detection and monitoring

Landslide control and monitoring

Landslide monitoring is the key for the recognition of its ocurrence as well as for taking early warning measures. This control helps to understand the mechanism and type of movement and to suggest reliable thresholds for landslide activity and early warning (Chae *et al.*, 2017). Some essential works and reviews about landslide detection and monitoring are provided by Gili (1989), Mikkelsen (1996) and Chae *et al.* (2017). With respect to landslide monitoring, it can be considered four major categories. The first one is geomorphological mapping by means of field works and photointerpretation (Domínguez-Cuesta *et al.*, 2007; Bruschi *et al.*, 2012; Guzzetti *et al.*, 2012; Rodríguez-Rodríguez *et al.*, 2018). During this procedure, different natural and anthropic surficial deposits are identified and mapped (Figure 7). According to Keaton and DeGraff (1996), features such as bedrock exposures, vigorous vegetation marking shallow groundwater, breaks in slope angle, terraces, ground cracks, tilted trees, and areas of eroded bare slopes should be noted for subsequent examination on the ground.

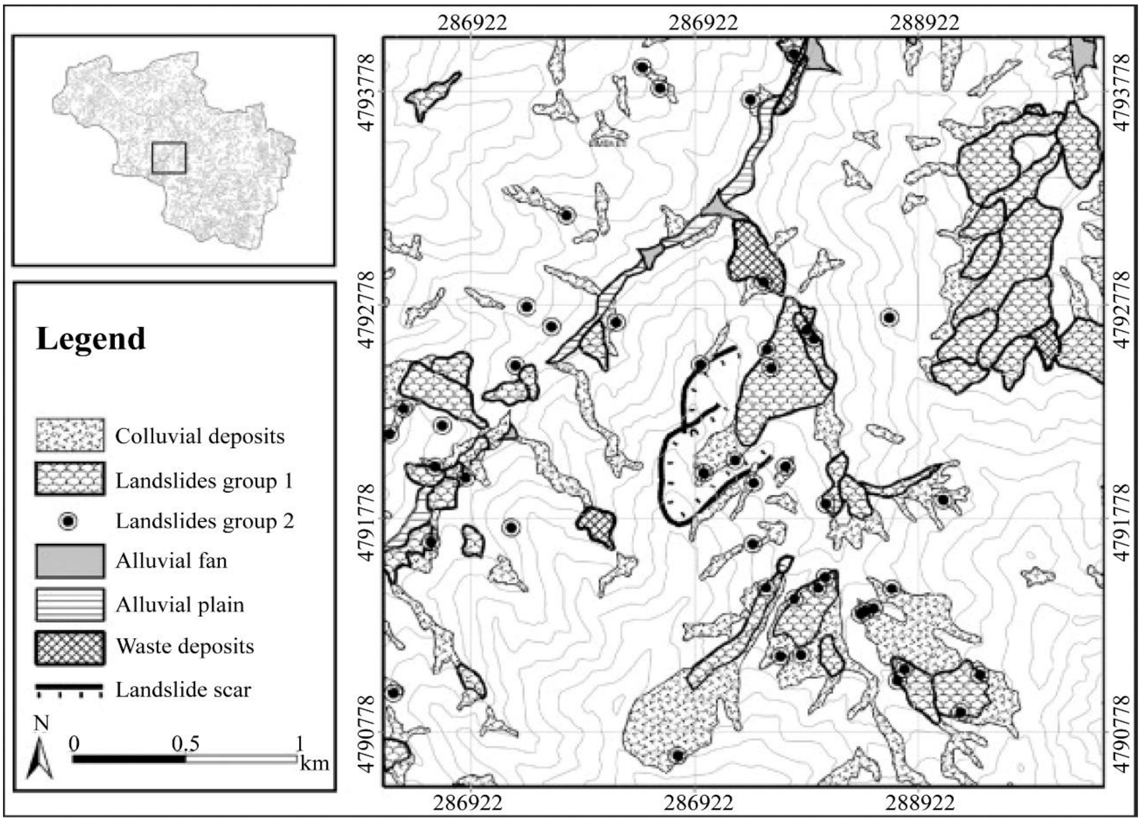

Figure 7. Geomorphological mapping and identification of landslides in Santa Barbara basin (Central Coal Basin, Asturias).Taken and modified from Domínguez-Cuesta *et al.* (2007).

The second category is related to the use of conventional *in situ* instruments (Chae *et al.*, 2017) (Figure 8). According to Mikkelsen (1996) these *in situ* ground methods are usefully used to: 1) Determine the depth and shape of the sliding mass; 2) Determine absolute lateral and vertical movements whitin the sliding mass; 3) Determine the rate of movement - velocity; 4) Monitor groundwater levels and pore pressure and 5) Monitor and assess of the effectiveness of various control measures. Conventional *in situ* instruments can be installed on the surface or inside boreholes. These methods include inclinometers, extensometers, tilmeters and topographical monitoring with total station (Bruckl *et al.*, 2013; Chae *et al.*, 2017; Peternel *et al.*, 2022). However, main limitations of conventional monitoring techniques can be the large extension of the area to be monitored and high costs, inaccessibility of the study area and problems linked to installation and maintenance (Tofani *et al.*, 2013). In addition, rainfall and soil moisture can be measured by means of gauges to comprehend the role of water as triggering and conditioning factor of the mass movements ocurrence (Guzzetti *et al.*, 2007; Valenzuela *et al.*, 2019b; Domínguez-Cuesta *et al.*, 2021) (Figure 8).

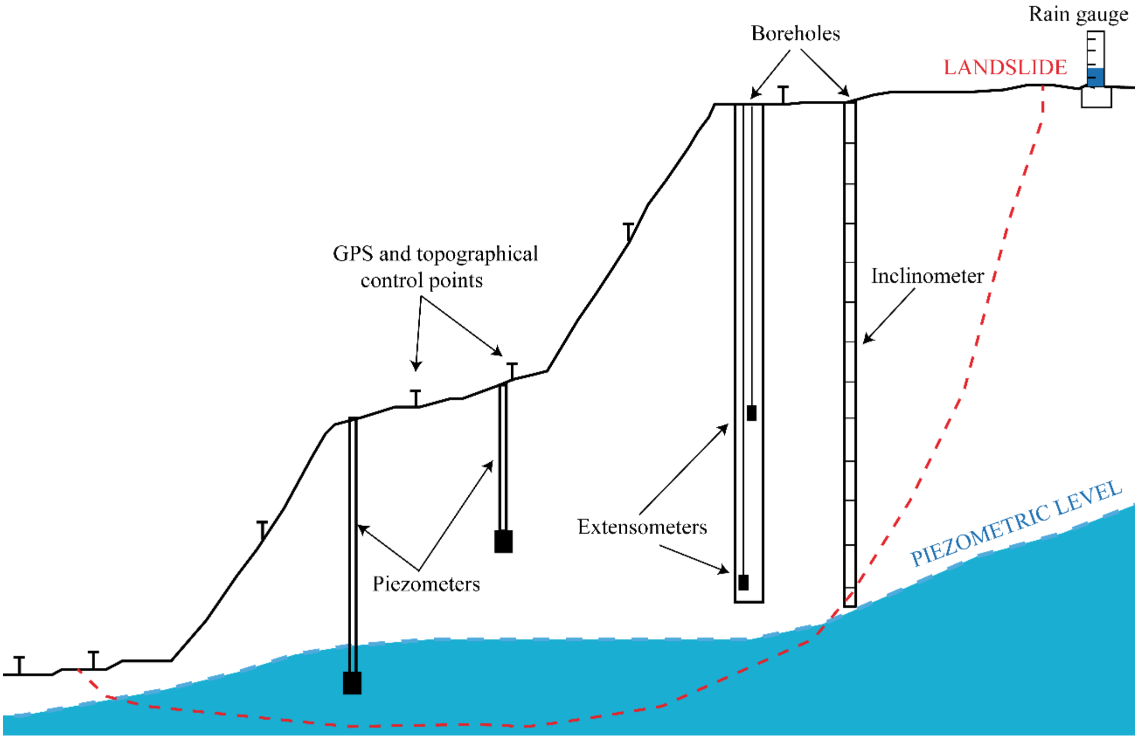

Figure 8. Some conventional auscultation instruments for controlling and modeling the stability of a landslide. Taken and modified from Oteo (1978).

The development of inclinometers has been the most important contribution to the analysis and detection of landslide movements in the past century. Typical inclinometer consists of a 25-mm diameter semirigid plastic tube which is inserted into a borehole (Mikkelsen, 1996). There are two main classes of inclinometers: probe inclinometer and in-place inclinometers. First type consists of a probe containing a pendulum transducer that is fitted with wheels and lowered by and electrical cable down grooved to control alignment (Mikkelsen, 1996). Probe inclinometers can measure changes in inclination on the order of 1.3 to 2.5 mm over a 33-m length of casing. On the contrary, in-place inclinometer employs a series of servo-accelerometer or electrolytic sensors and two-axis measurement. The results is the relative and total displacement of each sensor (Mikkelsen, 1996) and they can be used to measure velocities in the hourly time (Figure 9). Its precision is ± 0.01 mm in 1 m.

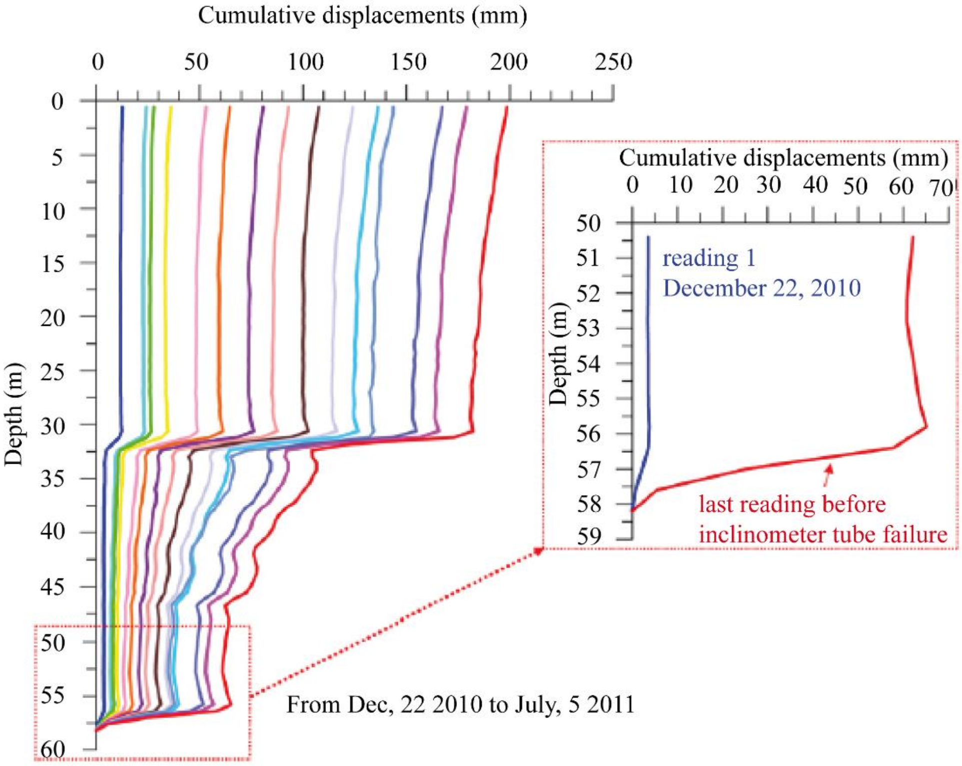

Figure 9. Example of inclinometer measurements in a landslide showing cumulative displacements versus depth and two different slinding surfaces at 32 m and 56-58 m depth. Taken and modified from Bandini *et al.* (2015).

Extensometers consists of a sheathed steel cable, which is anchored inside a borehole, below the sliding surface. The cable is kept taut by a counterweight and a pulley. Its rotation is registered by means of the rotation or by means of a potentiometer. This system allows continuous recording of horizontal movements (Gili, 2003). Precision of extensometers is around 0.1-2 mm. On the other hand, tilmeters are a group of tools that allow to detect tilt of a surface point. They are useful to monitor slope movements with important rotational component and are widely used in open-pit mines and civil infrastructures control. Main advantages of these instruments are light weight, simple operation, compactness and relative low costs (Mikkelsen, 1996).

Total station is a portable instrument which consists of an electronic tachnometer, capable of measuring vertical and horizontal positions within a three-dimensional coordinate framework (East - X, North - Y and elevation - Z) (Keaton and DeGraff, 1996). The coordinates and levels of the all control points can be measured easily and with an accuracy of 1 mm in vertical and 0.1 mm in horizontal or inclined. However, the accuracy of total station surveys can be influenced by weather and atmospheric conditions (Keaton and DeGraff, 1996). Topographical monitoring by means of a total station consists of measuring set of prims distributed over the area to be auscultated (Navarro-Freixas, 2013). It allows to monitor the ground motion of a landslide or the instability of a slope over time (on the order of months or years) and to identify movement and stable zones (Figure 10).

Figure 10. Topographic control of a cliff in the Luarca town (Asturias, Spain) during a field campaign of COSINES project (Ref. CGL2017-83909-R).

The last groups are the remote sensing techniques that include: 1) Terrestrial and unmanned aerial vehicle (UAV) photogrametry; 2) Ligh detection and ranging (LIDAR); 3) DInSAR and A-DInSAR methods and 4) Global navigation satellite system (GNSS) (Gili *et al.*, 2000; Jaboyedoff *et al.*, 2012; Colomina and Molina, 2014; Mondini *et al.*, 2021; Peternel *et al.*, 2022) and the geophysical techniques: Seismic, electric, electromagnetic, ground penetration radar (GPR) and gravimetric methods.

The remote sensing techniques allow to obtain 2D or 3D information of the terrain with high accuracy and high spatial and temporal resolutions. This information includes: 1) Detection and quantification of ground motion; 2) High resolution point clouds of the topography; 3) Control and monitor of inaccessible areas and locations and 4) Real-time data monitoring. However, and according to Tofani *et al.* (2013), the main limitations of the remote sensing methods are related to the mass movement characteristics, that is, landslide velocity and dimension of mass movement. Other factors that limit these techniques are the limited underground penetration capability and the atmospheric disturbance effects (Chae *et al.*, 2017).

According to Hussain *et al.* (2022), photogrammetry is based on orthomosaic photos taken at different angles, which can be used for the construction of a high-resolution digital elevation models (HRDEM). Then, DEMs calculated at different time steps are compared to detect time-lapse changes. In this line, terrestrial photogrametry is carried out by using a camera located in a stationary position and on an elevated level or on traditional tripods (e. g. Jordá-Bordehore *et al.*, 2017). On the other hand, aerial photogrammetry is based on the UAV platforms, which has been widespread recently as a complementery technique used to increase the realibility of other remote sensing and conventional instrumentation results (Hussain *et al.*, 2022). These systems have grown in the last decade due to the low cost of aircraft and the advances in digital image analysis (Klemas, 2015). UAV systems have been succesfully applied to estimate geometry, to show depletion or accumulation of material and to identify geomorphological features of landslides (Rossi *et al.*, 2018; Domínguez-Cuesta *et al.*, 2022b) (Figure 11).

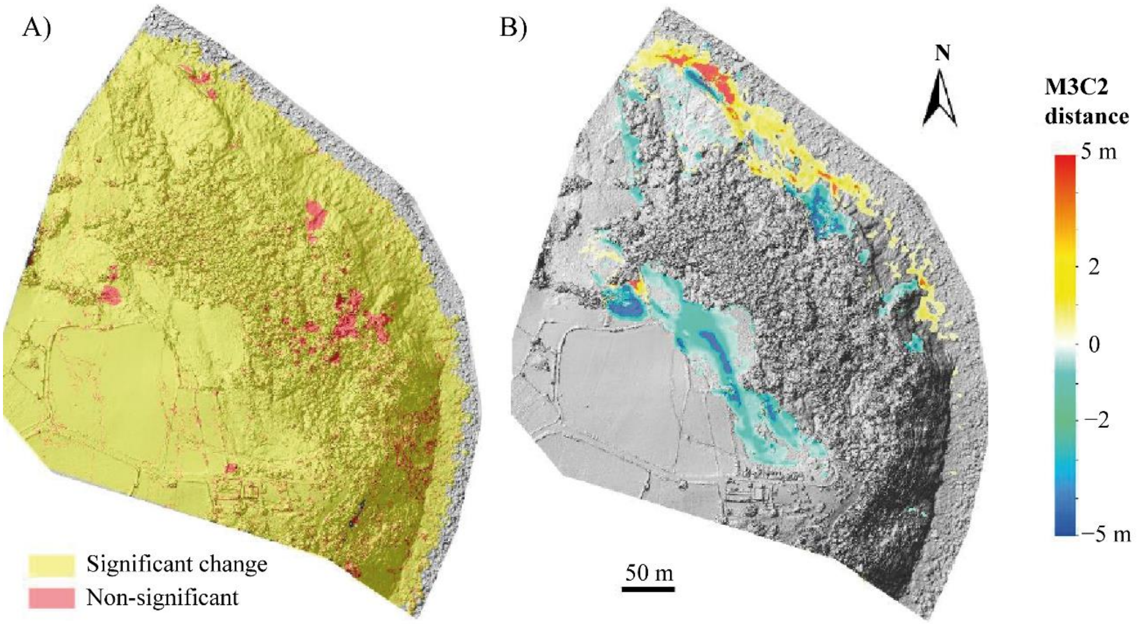

Figure 11. UAV photogrammetry obtained at the Tazones Lighhouse landslide (Asturias, Spain) between November 17, 2018 and November 29, 2019. Ground resolution close to 2.2 cm px^{-1}. **A)** Changes observed between acquisition dates. **B)** Distance measured by using M3C2 algorithm. Taken and modified from Domínguez-Cuesta *et al.* (2022b).

Spatial resolution of UAV systems ranges from 1-50 cm and field of view is comprehended between 50 m and 1 km. However, main limitations are related to the instruments and the field conditions. Firtsly, the precise detection and characterization of geomorphic characteristics will always remain a challenge in landslide mapping due to the dynamic nature of the phenomena (Karantanellis *et al.*, 2021). Isolated trees and sparse vegetation are cleared away by applying automatic filters and manual refinement which may lead to unrealible volume calculations (Hussain *et al.*, 2022) (Figure 11). Eventually, vegetation effect does not allow the detection of fissures and other features of the ground, which are useful for precise landslide delimitation (Rossi *et al.*, 2018).

LIDAR techniques provide high resolution point clouds of the topography and its main applitations are detection, characterization and mapping of landslides, measuring displacements and monitoring of deformation (Van Den Eeckhaut *et al.*, 2007; Rodríguez-Rodríguez *et al.*, 2018; Wang *et al.*, 2013; Jiang *et al.*, 2022) (Figure 12).

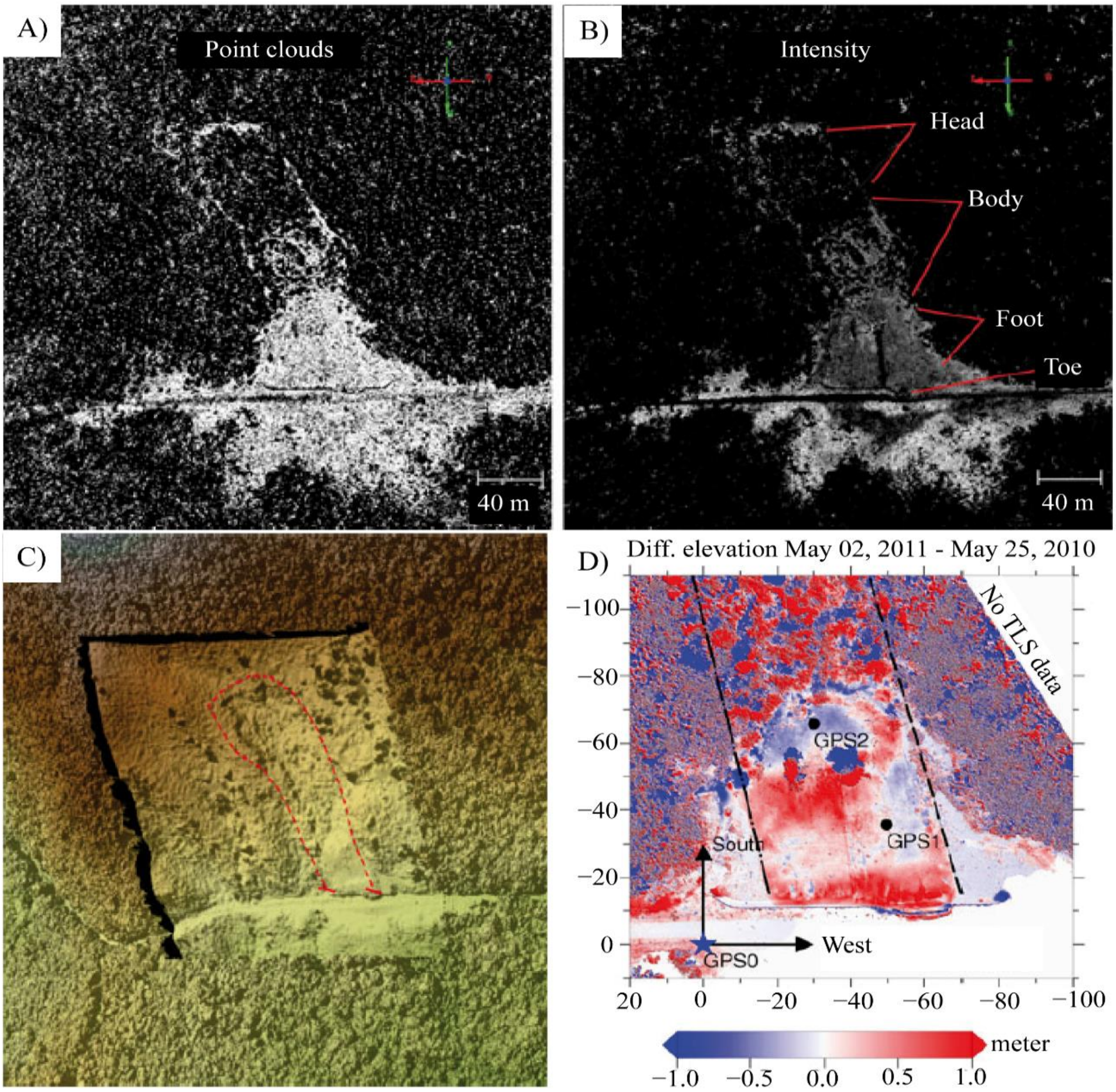

Figure 12. Example of LIDAR application for mapping and monitoring of a landslide**. A)** Image showing 2D distribution of ground returns (point clouds) collected by ALS (1,500 points m^{-2}). **B)** Intensity of point clouds. **C)** DEM with 5 cm resolution derived from ALS data. **D)** Changes of elevations derived from two TLS DSMs on February 5, 2011 and May 25, 2010. Red and blue color patterns indicate increasing and decreasing of elevations of ground surface, respectively. Taken and modifed from Wang *et al.* (2013).

In this line, LIDAR is used to create accurate and precise high resolution digital elevation models (HRDEM), which are 3D point clouds with a high density of points (Jaboyedoff *et al.*, 2012). According to these authors, this density depends on the sensor: metric to decimetric resolution for airborne laser scanning (ALS) and centimetric to millimetric resolution for terrestrial laser scanning (TLS) (Figure 12 A-C). In the case of the ALS, point density ranges from 0.5 to 100 ps m^{-2} while TLS density ranges from 50 to 10,000 ps m^{-2}. Between main advantages of these techniques are the acquistion of real 3D information, the fast data acquisition and easy set up and portability. Also, both methods can be jointly used to solve acquisition problems like the shadow areas produced by surfaces which are parallel to the LOS of one of the sensor (Jaboyedoff *et al.*, 2012). Nevertheless, instrumentral accuracy is lower under unfavourable conditions as poorly reflecting or very rough surfaces and bad weather conditions. Other limitation is the necessity of post-processing for filtering and alignment of the acquired data.

DInSAR and A-DInSAR methods are widely applied to detect, model and monitor of landslides (e. g. Cascini *et al.*, 2010; Barra *et al.*, 2016; Mateos et al., 2018; Reyes-Carmona *et al.*, 2021) due to high spatial and temporal resolution. The analysis and study of landslides is carried out by using differential interferograms (in the case of conventional DInSAR) and displacement maps and deformation time series (in the case of the A-DInSAR techniques) (Figure 13). These methods are described in detail in the chapters 1.3.2 and 1.3.3.

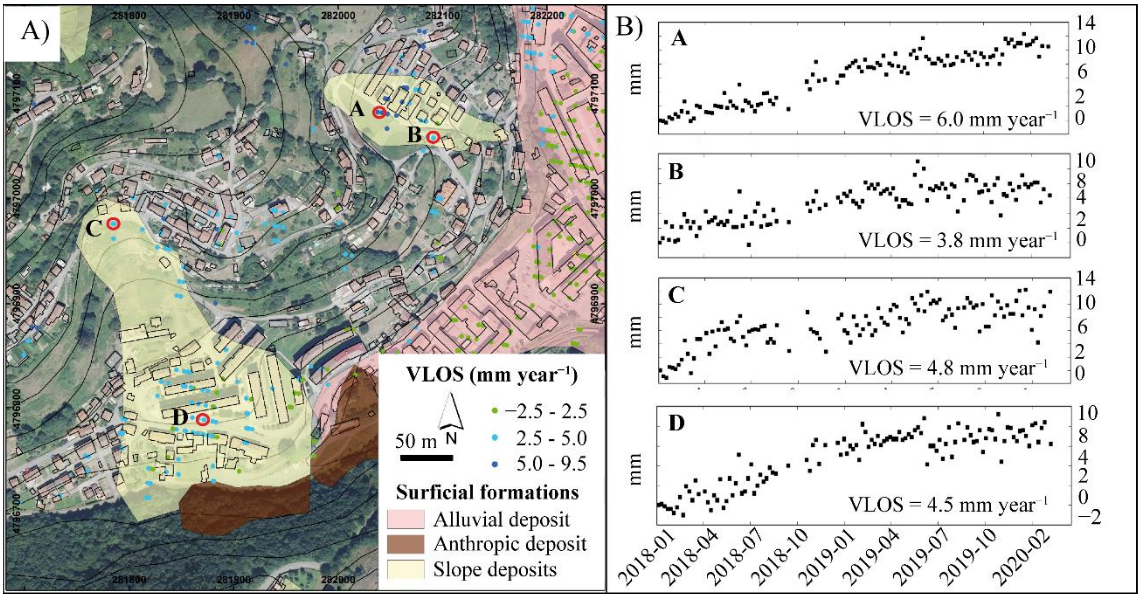

Figure 13. Landslide detection in the Central Coal Basin (Asturias, Spain) using A-DInSAR techniques. **A)** LOS mean deformation velocity map (mm year^{-1}). **B)** Deformation time series observed in the landslides. Taken and modified from Cuervas-Mons *et al.* (2021c, 2022a).

GNSS is a radionavigation, timing and positioning system that can obtain longitude, latitude and height (X, Y, Z coordinates) (U.S. government, 2021). In this way, a GNSS system calculates the position using a set of values called observables. They consist of logged data derived from the electromagnetic waves received from each satellite (Gili *et al.*, 2000). The computation can be made using the code or/and phase of the carrier. Code measurements are used to determine X, Y, Z and the receiver clock delay, while carried phase measures the changes in phase (phase angle) between the satellite and the receiver with time (Gili *et al.*, 2000). GNSS techniques are widely used to determine point displacements in the surrounding and into the landslide area (Figure 14). Between main GNSS constellations in the World are GPS, GLONASS (Russia), Beidou (China), IRNSS/NavIC (India), QZSS (Japan) and Galileo (Europe) (U.S. government, 2021). In the case of GPS, this system has been operational since 1995 with a constellation of 24 satellites at an average orbit altitude of about 20,000 km, arranged in six orbital planes inclined 55° relative to Earth's equator (Gili, 2003). As of October 2017, there were a total of 31 operational satellites in the GPS constellation (Gili, 2003). Some advantages of these systems are large areas to cover during surveys, high precision, low costs, ease of operating the equipment and the procedure, data capture and computation are always the same (Gili *et al.*, 2000). For instance, precision of GPS systems ranges from 5 to 10 mm + 1 to 2 ppm (Gili, 2003). However, GNSS techniques present the following limitations (Gili *et al.*, 2000): 1) Errors due to the process of station point identification, antenna installation and antenna height measurements; 2) Operations are restricted in forested and mountain areas, treecanopy and buildings could restrict the reception of the satellite signal and antenna must have good sky visibility; 3) Special atmospheric conditions and adequate illumination are required for accurate measurements.

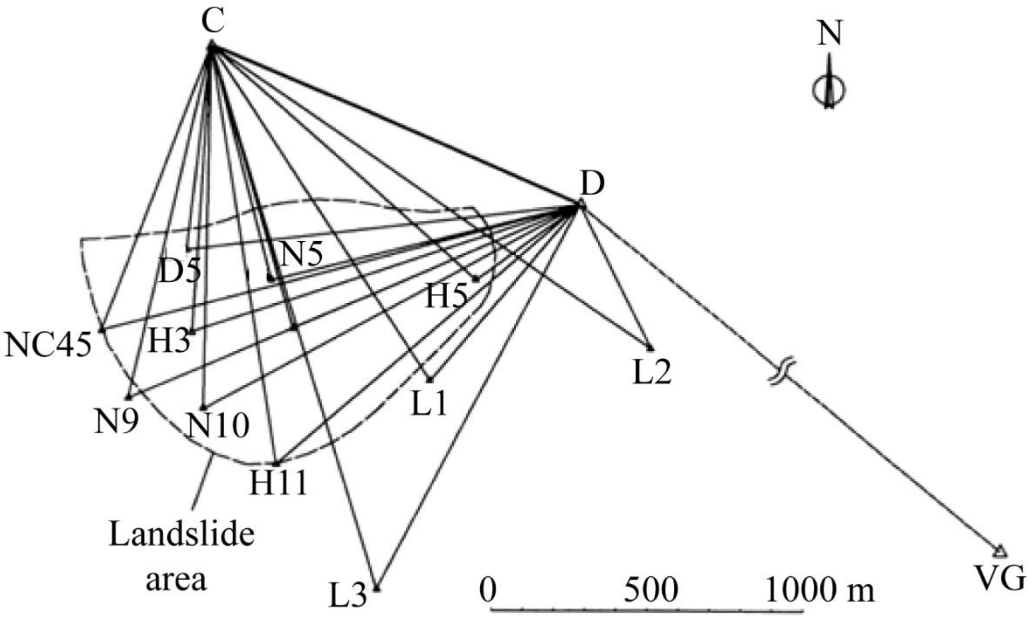

Figure 14. Example of GPS network applied to monitor a landslide and its surroundings. C and D are the bases and the rest of the points are control targets. Taken and modified from Gili *et al.* (2000).

Geophysical methods are based on the acquisition of physical measurements from which physical parameters can be deduced. Remarkable reviews about geophysical methods applied in landslide investigation are from M^c Cann and Forster (1990) and Jongmans and Garambois (2007). According to these authors, main advantages of these methods are: 1) High flexibility, quick and deployment on slopes; 2) Non-invasive information about the internal structure of the soil and/or rock mass and 3) Large volume of data to be investigated. However, main drawbacks are a lower resolution in depth and obtaining of indirect information related to physical parameters instead geological or geotechnical properties. This produces the necessity to have always to calibrate the instruments to carry out a relaible interpretation (Jongmans and Garambois, 2007).

First geophysical methods in landslide investigation are seismic techniques: Seismic refraction, seismic reflection, seismic tomography, seismic noise measurements or H/V method, inversion of surface waves (Jongmans and Garambois, 2007; Grit and Kanli, 2016) and multichannel analysis of surface waves (MASW) (Yalcinkaya *et al.*, 2016). They provide geometry of the landslide structure, internal bedding and the rupture sufaces of slope instabilities by means of carrying out P-wave and S-wave profiles and analyzing the variation in depth of P- and S-wave velocities (Figure 15) (Grit and Kanli, 2016).

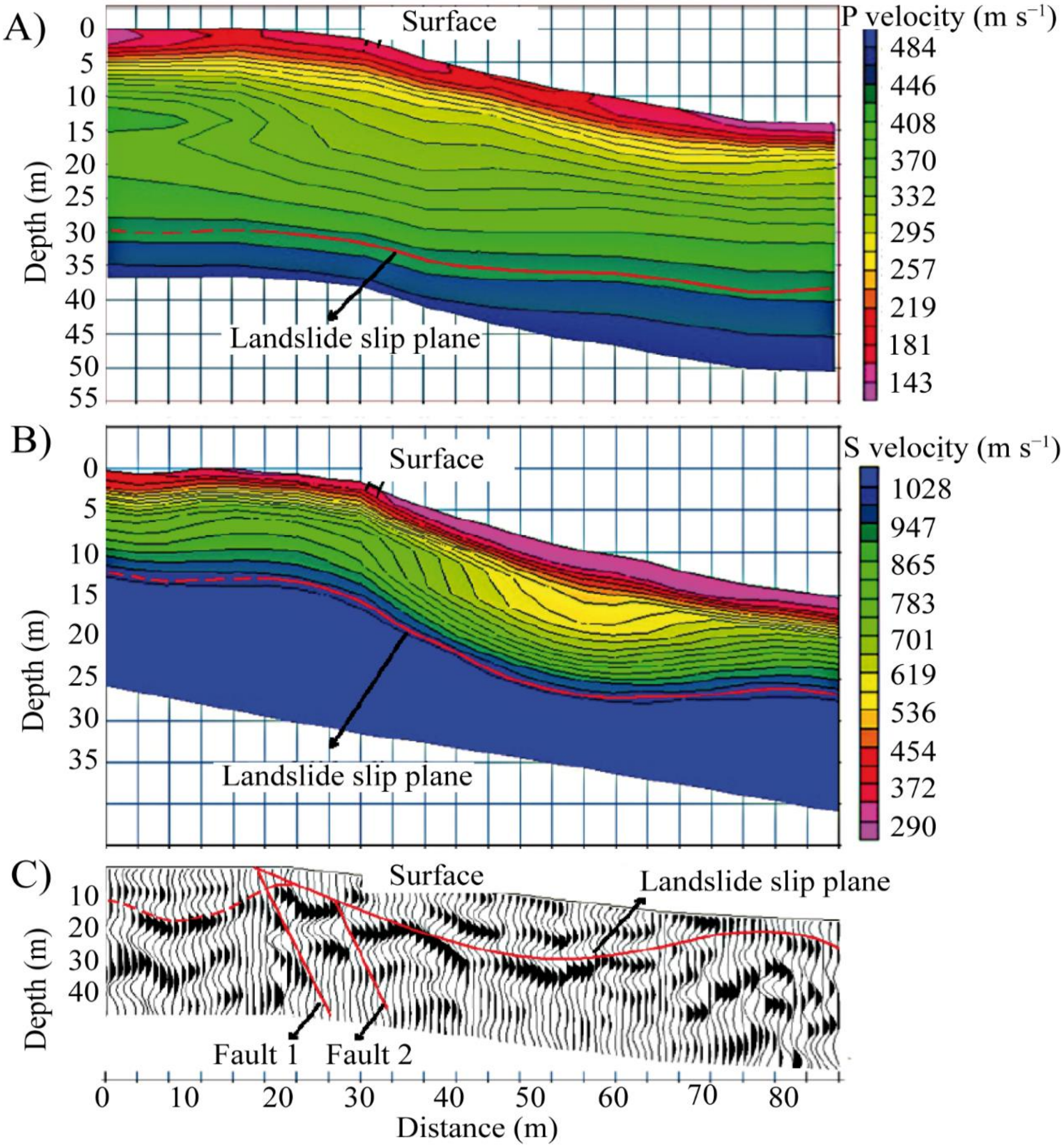

Figure 15. Seismic methods applied in the study of a landslide: **A)** MASW, **B)** Seismic refraction tomography and **C)** Seismic reflection depth cross-section. Taken and modifed from Grit and Kanli (2016).

Main electrical methods are electrical resistivity, induced polarization and spontaneous potential. They are based on measuring the electrical potentials between electrode pairs connected to another electrode pair or to a high impedance voltmeter. They can be used in three differents ways: 1) Vertical electrical sounding; 2) Profiles and 3) Electrical tomography (Jongmans and Garambois, 2007). They provide the electrical resistivity and spontaneous-potential, which allow to distinghish the clayey materials versus water-saturated zones or water level inside the landslide body (Figure 16). Moreover, they allow to identify the boundary between the stable ground and the landslide material (Figure 16).

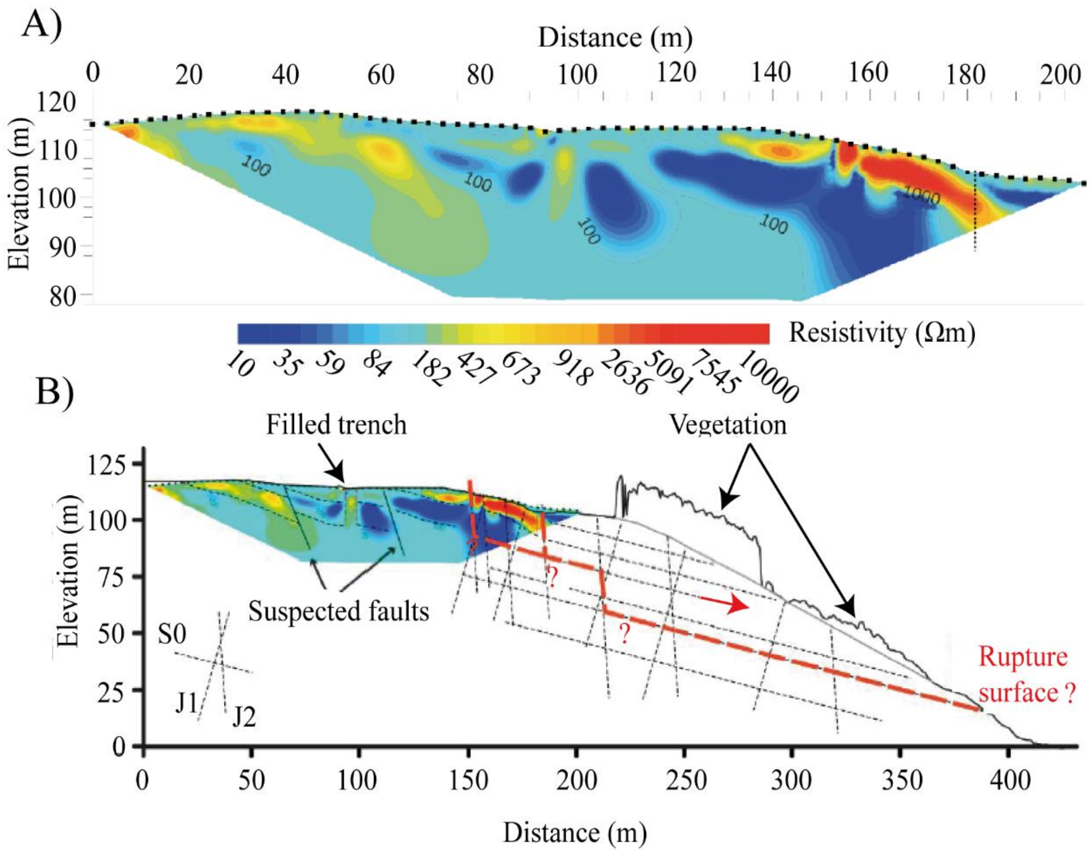

Figure 16. A) Example of an electrical resistivity tomography profile and **B)** his geomorphological interpretation carried out in the Tazones Lighthouse landslide (Asturias, Spain). Taken and modified from Domínguez-Cuesta *et al.* (2022b).

Electromagnetic methods (Jongmans and Garambois, 2007) are mainly used to determine the geometrical limits of the unstable mass. These methods, which yields a single apparent electrical resistivity value, allows quick profiling and mapping. Penetration ranges from a few meters to a few tens of meters and depends on the coil separation (from 10 to 40 m). These methods have to be combined with other geophysical techniques for landslide investigation.

Other geophysical method is the Ground Penetration Radar (GPR). According to Jongmans and Garambois (2007), this technique is widely applied to landslide research because: 1) It has high resolution, from a few cm to a few m; 2) It presents wide range of penetration depth in resistive materials and 3) It is sensitive to dielectric, electric and magnetic contrast and to water content (Figure 17 A). For this reason, GPR investigation has been focused on 2D and/or 3D evaluation and interpretation of discontinuities inside the rock mass (Jeannin *et al.*, 2006), rock fall stability assessment (e. g. Deparis *et al.*, 2007) and characterization the stratigraphy at potential landslide sites and search of the potential failures (e. g. Borecka and Herzig, 2015) (Figure 17 B).

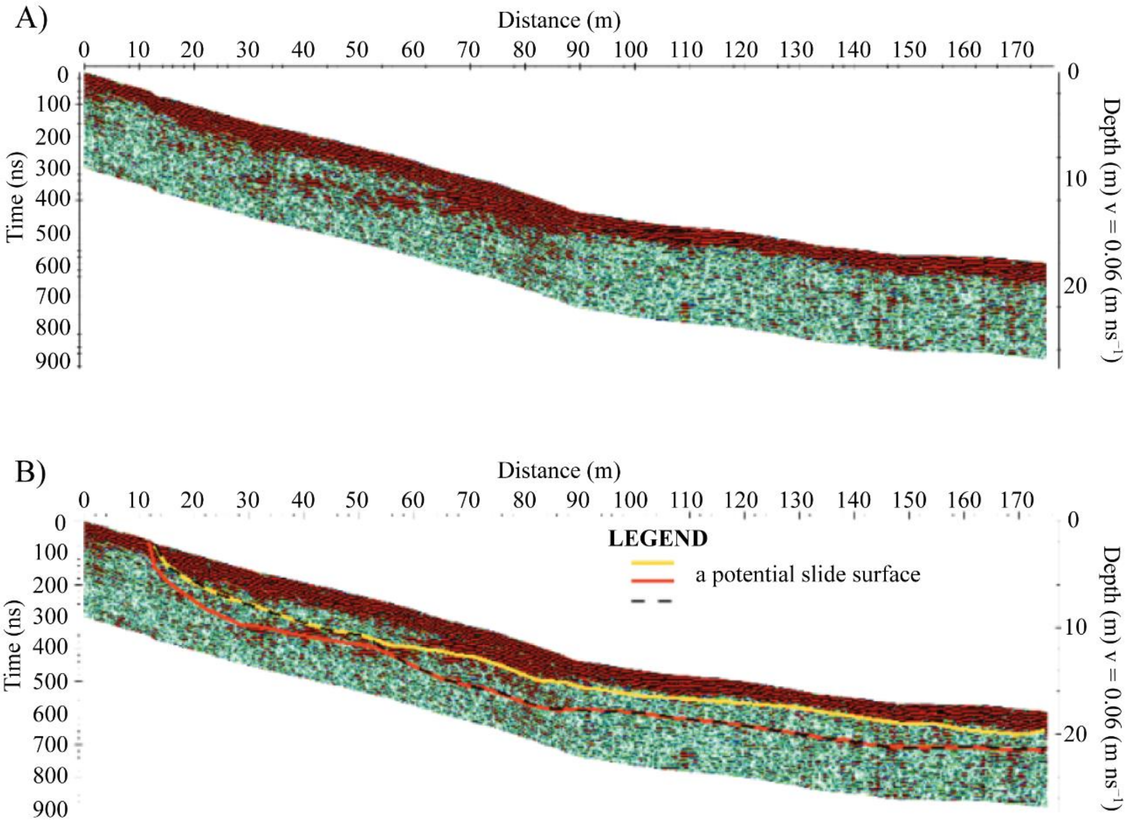

Figure 17. A) 2D GPR profile and B) geological interpration identifiying potential slide surfaces. Taken and modified from Borecka and Herzig (2015).

Last geophysical techniques are the gravimetric studies (Jongmans and Garambois, 2007). They detect gravimetric anomalies generated by density contrasts. Gravimetric surveys in slope instability issue are addressed to estimation of landslide body thickness and identification of the moving and stable mass. Another result can be the location and geometry of heterogeneities within the moving mass (Jongmans and Garambois, 2007). Nevetheless, the use of gravimetric surveys is uncommon because they need a long and difficult data processing. The main problem is separating anomalies of interest from the overlapping effects of other features (Jongmans and Garambois, 2007).

Subsidence control and monitoring

According to Fernández-Oliveras (2009), the study of subsidence phenomena has been commonly carried out on the basis of monitoring networks and *in situ* measurements through different auscultation instruments. The group of terrestrial instrumental methods are the following (Shirzaei *et al.*, 2021): levelling, borehole extensometers, inclinometers, piezometers, rod surface-elevation table (RSET; in conjunction with marker horizon device) and distributed fibre-optic sensing (DFOS). The review of Shirzaei *et al.* (2021) presents a detailed evaluation about these *in situ* and remote sensing techniques applied in active coastal subsidence. Tomás *et al.* (2014) provide a review about the main advantages and limitations of A-DInSAR techniques and a cost comparative study with respect to conventional techniques in active subsidence in Spain.

Levelling is the oldest geodetic method used for measuring subsidence. This technique was developed in the 19th century and continues to be applied. The method allows surveyors to carry out an elevation from a known reference point to other geodetic marks using a precisely leveled telescope and a pair of graduated vertical rods (Gambolati and Teatini, 2021) (Figure 18). For each survey, the elevation difference between two benchmarks is recorded twice by accumulating the elevation differences between a series of temporary turning points (Figure 18). The method assumes the stability of the reference benchmark, thus special care must be taken in tectonically active zones (Gambolati and Teatini, 2021). In general, benchmarks are spaced 1 km apart and turning points are 20 to 100 m apart. The accuracy of this instrument depends on the equipment, field procedure, atmospheric conditions and corrections applied to field observations (Dzurisin, 2007). Nowadays, there are digital levels that help fulfill the selected accuracy, eliminating the human errors and increasing the measurement speed.

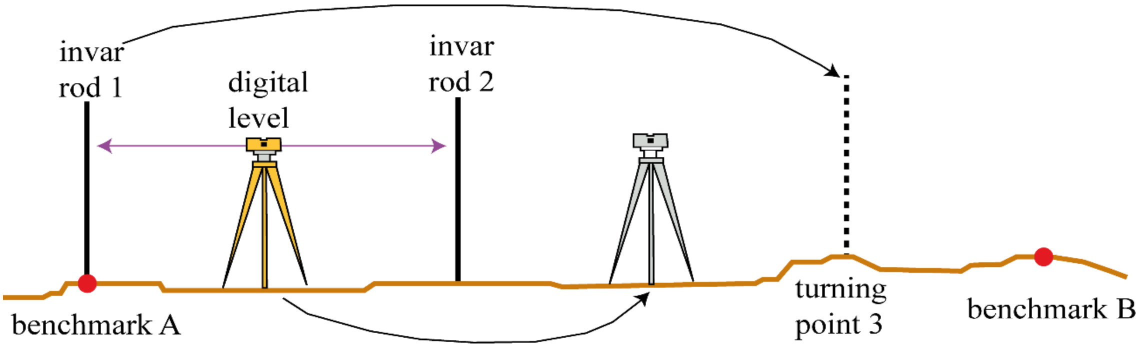

Figure 18. Sketch of a leveling survey to measure land subsidence. Taken and modified from Gambolati and Teatini (2021).

In a similar way to montoring landslides, conventional instruments can be used. Borehole extensometers provide continuous measurements of the 1D changes in the thickness of layers at hourly sampling rates and millimeter-level precision and allows to estimate the consolidation rates (Vanizek *et al.*, 1980; Fernández-Oliveras, 2009; Shirzaei *et al.*, 2021). The instrumental precision heavily depends on the actual extensometer implementation, but a nominal deformation resolution of 0.01 - 0.1 mm can be achieved over a 200-1000 m depth (Gambolati and Teatini, 2021). Inclinometers can be used to monitor changes in elevation of horizontal motions at the edges of the subsidence zone (Mikkelsen, 1996; Fernández-Oliveras, 2009). On the other hand, piezometers are used to monitor the groundwater level and pore pressure, as groundwater withdrawals can produce or facilitate land subsidence (Galloway *et al.*, 1999). However, the opposite effect can occur: recovery of the aquifer by recharge (Ezquerro *et al.*, 2014). This phenomenon results in positive deformations that can be observed by conventional instruments and remote sensing techniques (Figure 19).

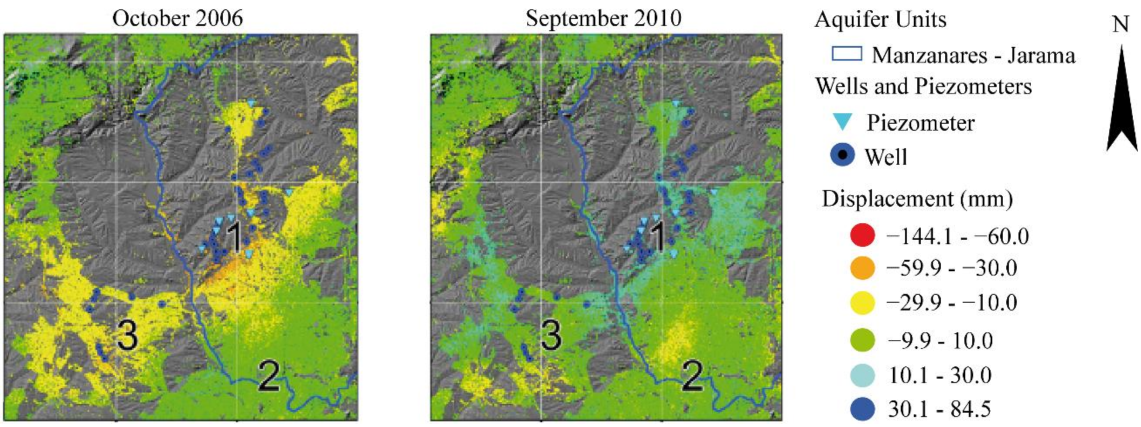

Figure 19. Application of A-DInSAR techniques to the detection of land subsidence in October 2006 due to over-exploitation of aquifers in Madrid (Spain) and subsequent recuperation by recharge in September 2010. Taken and modified from Ezquerro *et al.* (2014).

RSET is a high-precision tool that measures small-scale surface-elevation change owing to shallow coastal subsidence developed in wetland sediments (Boumans and Day, 1993; Shirzaei *et al.*, 2021) (Figure 20). This tool consists of a portable device that is attached to a permanent benchmark. It has got nine pins mounted on a horizontal arm with a length between 1 - 25 m (Webb *et al.*, 2013). The pins can be lowered to the sediment surface and measure the surface elevation and, therefore, repeated surveys enable surface-elevation change can be determined (Callaway *et al.*, 2013) (Figure 20). This can be done monthly, seasonally or annually. In addition, RSET is installed adjacent to the feldspar marker horizons (Figure 20). These horizons are usually established in 50- by 50- cm plots and they allow to register the cumulative change in sediment accretion since the time of marker deployment. According to Callaway *et al.* (2013), the procedure to obtain the shallow subsidence is estimating the difference between vertical accretion and elevation change. In this way, subsidence data is calculated across multiple years to provide an annual rate of subsidence.

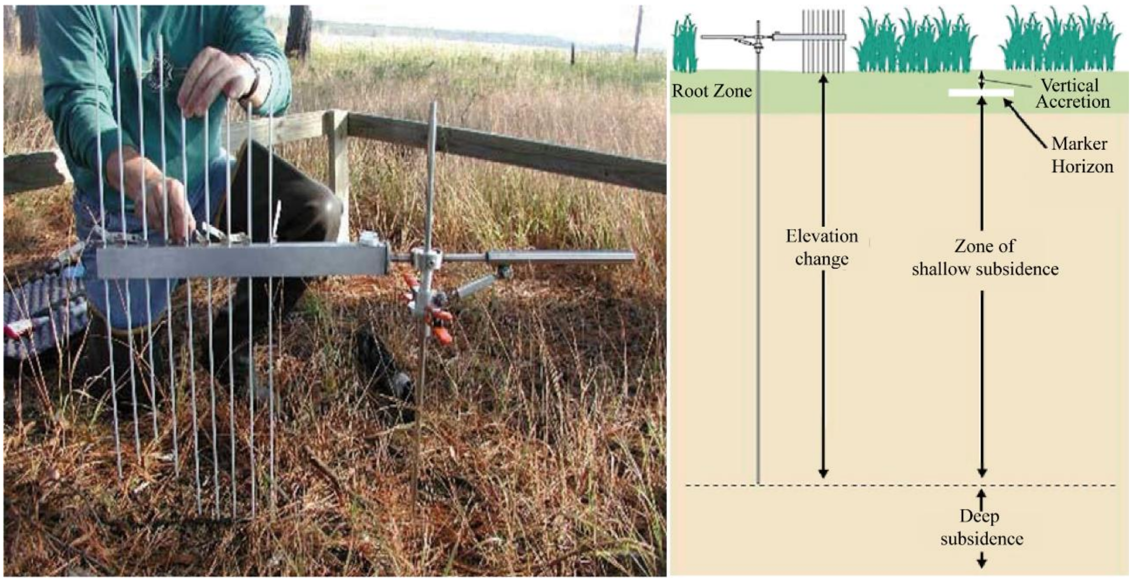

Figure 20. RSET tool used to measure subsidence in wetland sediments. Taken and modified from the USGS website (USGS, 2022).

DFOS is a low-cost tool that provide pointwise observations in geotechnical structures and in aquifer systems (Gu *et al.*, 2018; Zhang *et al.*, 2018). The common assumption that enables the sensing features in optical fibres is that the surrounding environment affects the local properties of the fibre itself (Schenato, 2017) (Figure 21 A - B). There are three different scattering processes: Rayligeh, Raman and Brillouin scatterings, although the sensing mechanism is the same for all of them (Schenato, 2017). According to this author, the back propagating light generated when an optical signal is fed into the fibre is used to probe the local properties of the fibre and, therefore, to figure out the changes in the surrounding environment. In the studies of subsidence, most remarkable DFOS technique is Brillouin Optical Time Domain Reflectormeter which is based on the Brillouin scattering (Schenato, 2017). This tool is applied to: 1) Measure vertical displacements to establish compaction rates (Shirzaei *et al.*, 2021); 2) Detect the strain effect in soils during the drainage-recharge cycle in simulated models of aquifers that are pumped and recharged (Wu *et al.*, 2017) and 3) Monitor ground fissures (Suo *et al.*, 2016) (Figure 21).

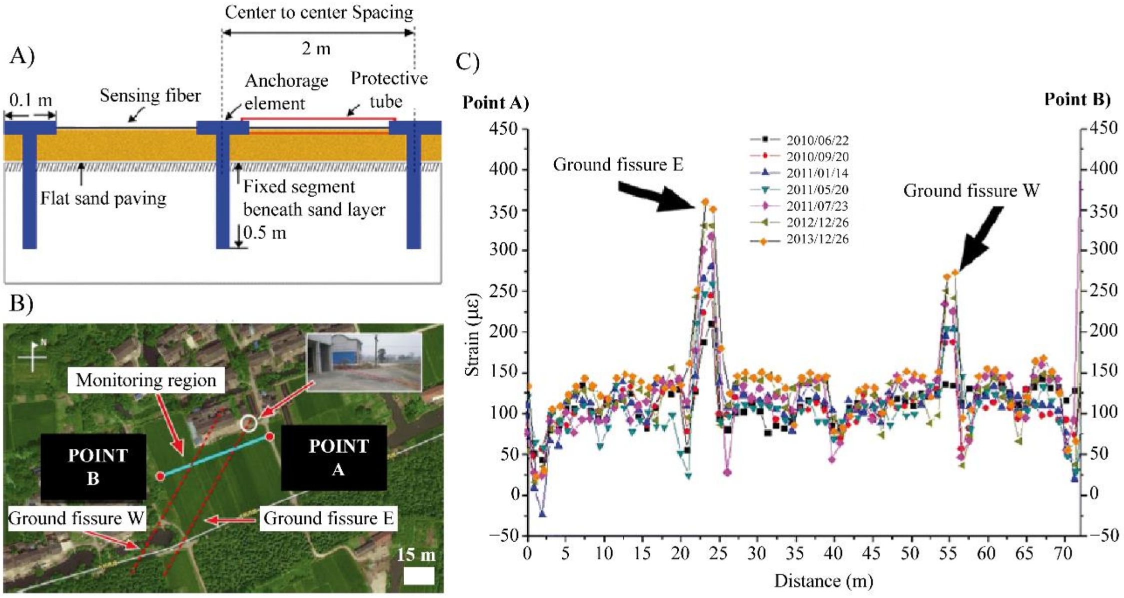

Figure 21. DFOS tool used to measure land subsidence in China. **A)** Deployment setup of a cable for ground fissure monitoring. **B)** Monitoring site and distribution of fissures. **C)** Strain distribution along the cable and detection of deformation located in the both ground fissures. Taken and modified from Suo *et al.* (2016) and Schenato (2017).

As in the case of landslides, remote sensing techniques and geophysical methods can be used to detect and monitor subsidence.

Remote sensing techniques can provide a complete estimate of the total subsidence rate, corroborate ground motion observed by conventional methods and better identify and draw areas of ground subsidence (Shirzaei *et al.*, 2021). For instance, DInSAR and A-DInSAR techniques have been mainly applied to analyze subsidence due to underground mining activities (e. g. Graniczny *et al.*, 2015) and groundwater withdrawal and compaction of the sediments (e. g. Heleno *et al.*, 2011). Regarding LIDAR, the most recent works have been addressed to measure vertical velocities, to compare with respect to GNSS and A-DInSAR dataset (e. g. Hu *et al.*, 2022) and to support coastal subsidence monitoring in conjuntion with land cover data (e. g. Zhong *et al.*, 2022). GNSS techniques are sufficiently accurate to estimate vertical and horizontal movements for subsidence assessment at regional and local scales (Chrzanowski and Chen, 1991; Baldi *et al.*, 2009) (Figure 22). However, they are usually used with UAV methods, A-DInSAR techniques (e. g. Zhang *et al.*, 2022) and conventional instruments. Eventually, UAV photogrammetry is firstly addressed to obtain HRDEMs. Afterward, the measured difference elevations are linked to subsidence rates (Figure 23).

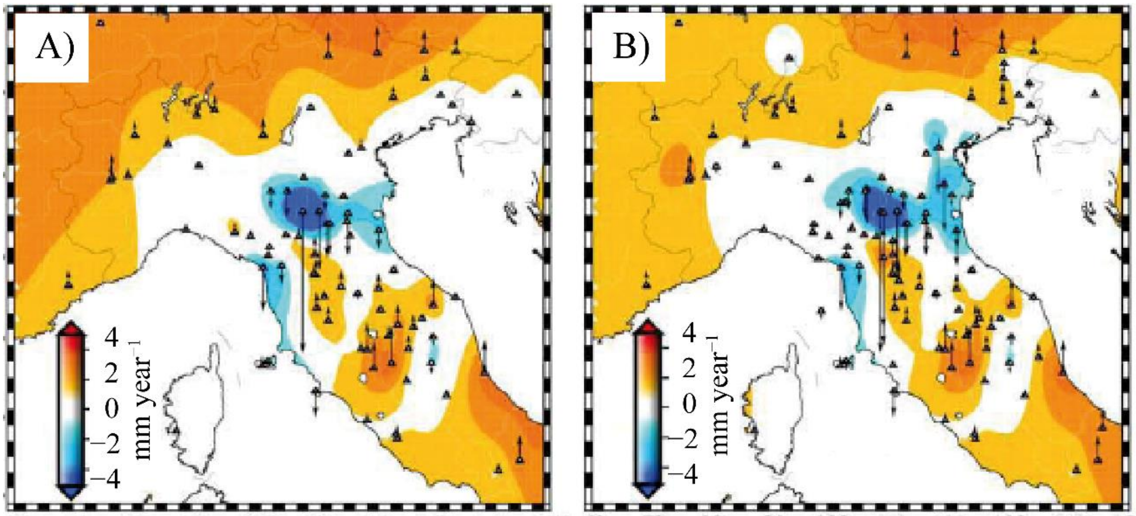

Figure 22. Vertical velocities and contour map in North Italy considering GPS station network with time span longer than **A)** 2.5 years and **B)** one year. Taken and modified from Baldi *et al.* (2009).

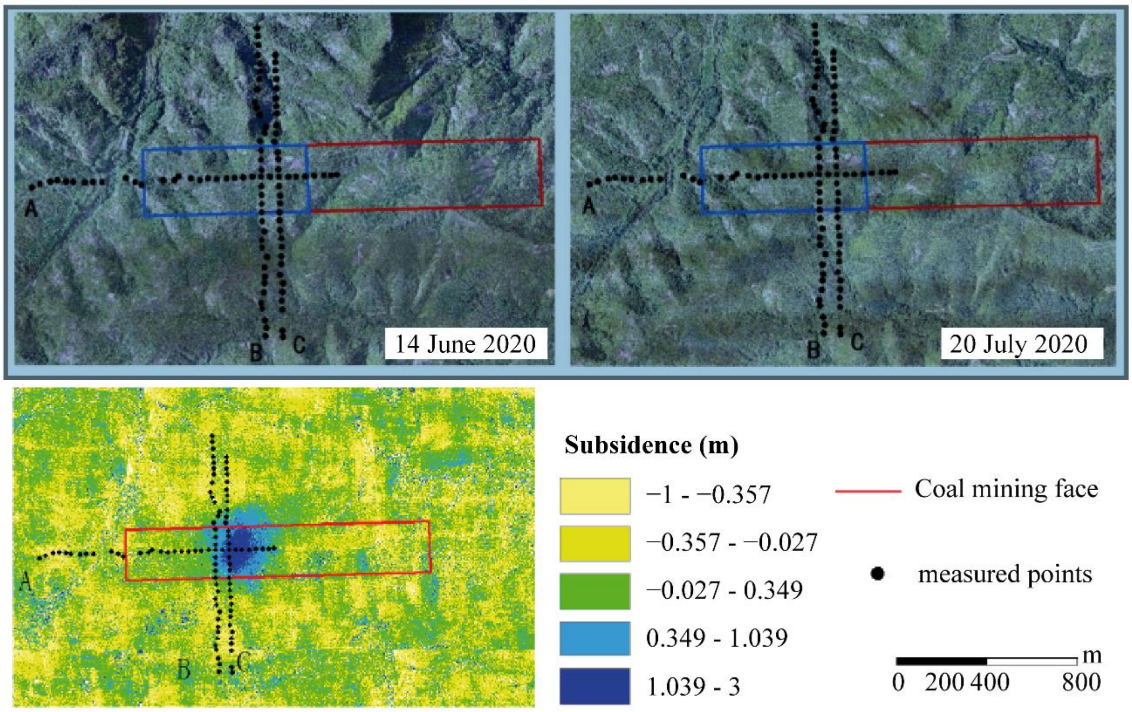

Figure 23. UAV monitoring of surface subsidence induced by underground coal mining. Taken and modified from Zhang *et al.* (2022).

Geophysical methods are widely applied to the detection and monitoring of land subsidence due to underground mining activity, active fault movements and groundwater over-exploitation (Kim *et al.*, 2003; Dindi, 2015; Porzucek and Loj, 2021). According to Kim *et al.* (2003), geophysical techniques are used to: 1) Image the underground structure; 2) Estimate the ground condition; 3) Delineate possible fractures, faults, cavities (Figure 24) and boundaries of subsidence area and 4) Examine the cause of movement.

Figure 24. Gravity method applied to subsidence related to underground mining activities: Distribution of anomalies of gravity (Bouguer anomalies) and distribution of buildings, mining facilities and sinkholes. Taken and modified from Porzucek and Loj (2021).

1.3 InSAR, DInSAR and A-DInSAR theory and fundamentals

1.3.1 SAR principles

The SAR (Synthetic Aperture Radar) is an active remote sensing sensor that operates at microwave frequencies (between 1 and 100 GHz, whose wavelengths are from 0.3 to 100 cm) and is independent of sunlight and weather conditions (Figure 25). These systems send pulses of microwave to the ground surface, receiving them afterward.

Currently, operational satellite SAR systems have been working in the following microwave bands (Ferretti *et al.*, 2007): 1) X-Band, with a frequency of 10 GHz and a wavelength of 3.1 cm; 2) C-Band, with a frequency of 5.3 GHz and a wavelength of 5.5 cm and 3) L-Band, with a frequency of 1.2 GHz and a wavelength of 23.6 cm (Figure 25).

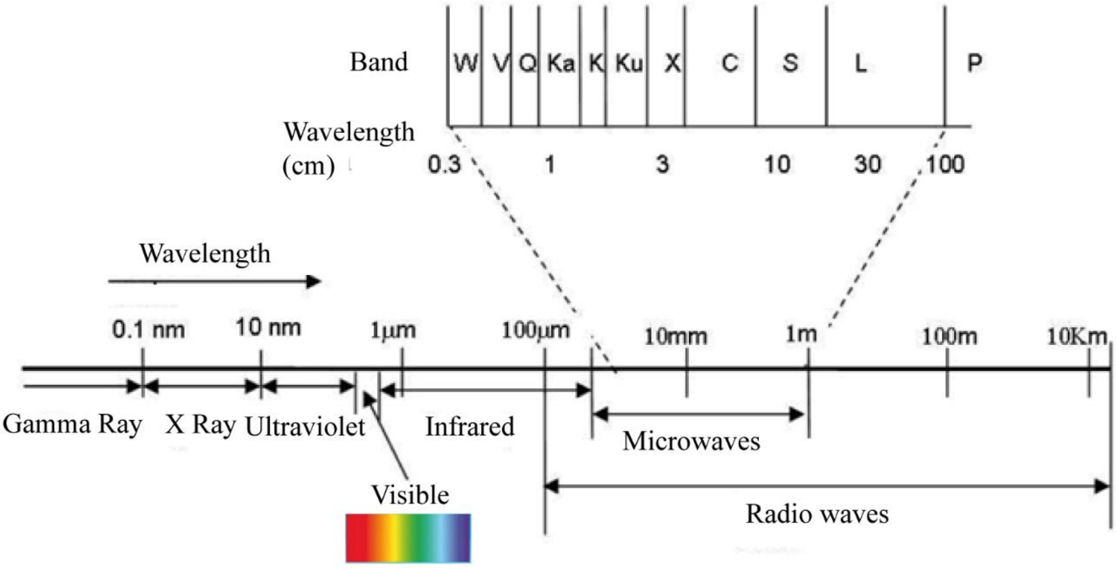

Figure 25. Wavelenght of electromagnetic spectrum, highlighting the microwave lengths. Taken and modified from Fernández-Oliveras (2009).

The SAR images (Figure 26) are composed on two different components: Amplitude of signal and phase. The amplitude component corresponds to the interaction and response of the SAR signal with the terrain. The amplitude value depends on the roughness of the terrain. For example, outcrops or urban areas show strong amplitudes, while smooth flat surfaces show low amplitudes (Ferretti *et al.*, 2007). Therefore, brigh pixels (urban areas or rock outcrops) correspond to areas with high amplitude (strong backscattered radiation). Dark pixels correspond to areas with low amplitude (low backscattered radiation) (Figure 26).

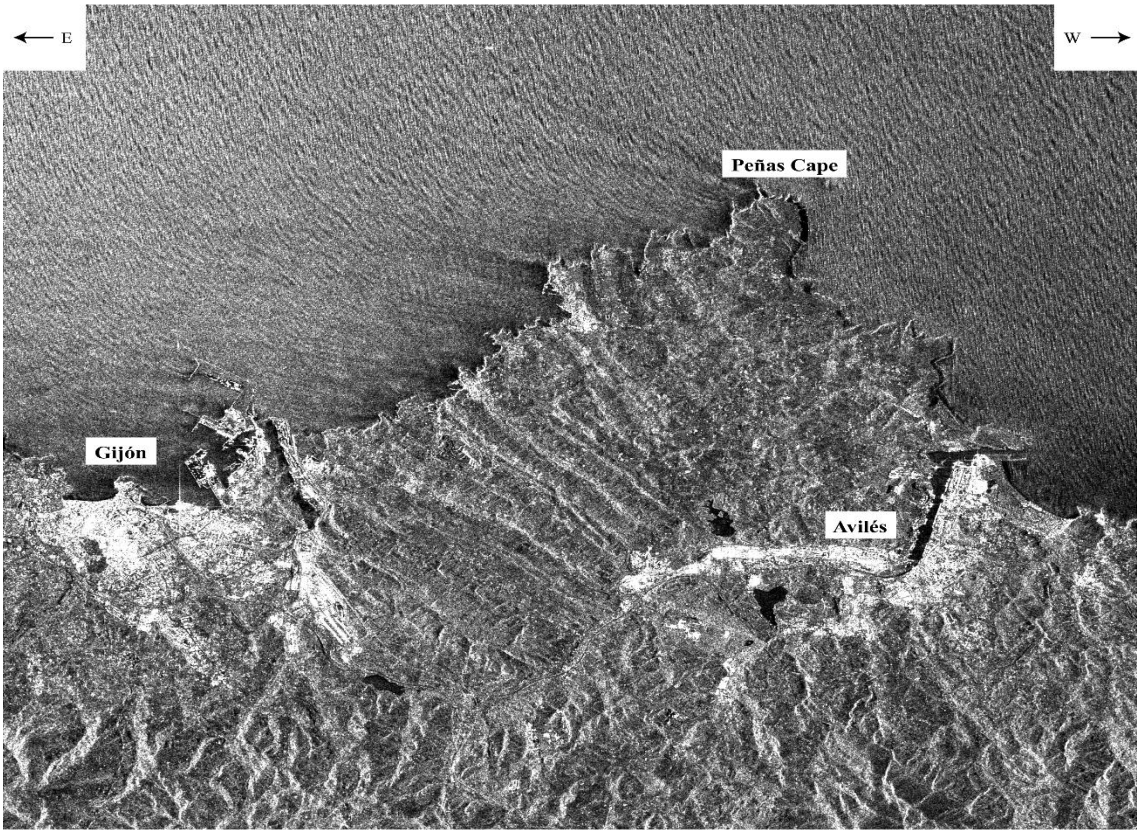

Figure 26. Example of amplitude image provided by Sentinel-1B SAR image on March 5, 2020 including the Peñas Cape, and the cities of Gijón and Avilés. Descending orbit and track 52. The image size is 29.4 km in azimuth (horizontal) and 26.7 km in ground range (vertical). Downloaded from Alaska Satellite Facility website (ASF, 2022) and visualized by means of SNAP Sentinel-1 Toolbox (ESA, 2022). Image displayed in ENVI ®.

The phase component is the most important part of InSAR principles because provides the essential information about terrestrial surface and relief differences. According to Raucoules *et al.* (2007), the phase (ϕ) or difference of phase between transmitted and received signal, is an ambiguous measure (2π) of the distance (R) between the SAR sensor and each area on the ground corresponding to an image pixel. Therefore, the phase change is thus proportional to the two-way travel distance (2R) of the radiation divided by the transmitted wavelength (λ) (Ferreti *et al.*, 2007). This concept is expressed by Equation (1) and shown in Figure 27:

$$\phi = \frac{2\pi}{\lambda} 2R = \frac{4\pi}{\lambda} R \tag{1}$$

Where ϕ is the phase change, λ is the wavelength and R the distance between Radar and the area observed.

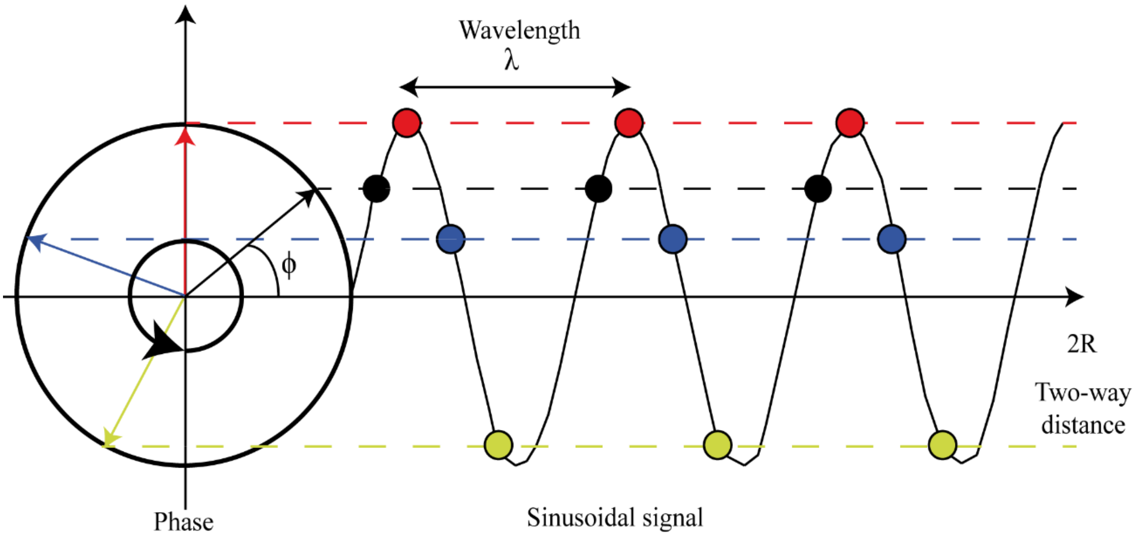

Figure 27. Illustration of phase component of SAR images. Taken and modified from Ferreti *et al.* (2007).

SAR geometry and distortions

An important aspect to SAR images is that vision of SAR sensor is lateral and the terrain motion is obtained along the line-of-sight (LOS) satellite. The LOS direction is usually called slant-range direction (Ferreti *et al.*, 2007). In the case of the Sentinel-1 satellites the LOS inclination is ranging from 32.9º to 43.1º respect to the vertical and in function to each swath (IW1 - 32.9º to IW3 - 43.1º) (ESA, 2019). According to Colesanti and Wasowski (2006), the radar mechanism produces a slope dependent resolution and pixel size along ground range. This introduces different geometric distortion effects that should be taken into account for the adequate and correct interpretation of SAR data. The geometric distortion effects are (Figure 28):

Foreshortening. It consists of a compression or reduction of spatial resolution along the LOS direction. It is produced in areas with oriented slopes facing LOS satellite (Monserrat and Barra, 2020). This effect makes that one large surface is sampled with few pixels and has a strong impact on the amplitude of the detected SAR image. Foreshortened areas are brighter on the image because the resolution cell is larger and the incidence angle is steeper (Ferreti *et al.*, 2007).

Layover. This effect is produced when there is a vertical or sub-vertical element and the top part is the first to respond to the SAR signal (Monserrat and Barra, 2020). This results in a reversal of relief.

Shadow. This effect occurs when the radar does not receive signal of an area. This produces zones with shadows and no data (Monserrat and Barra, 2020).

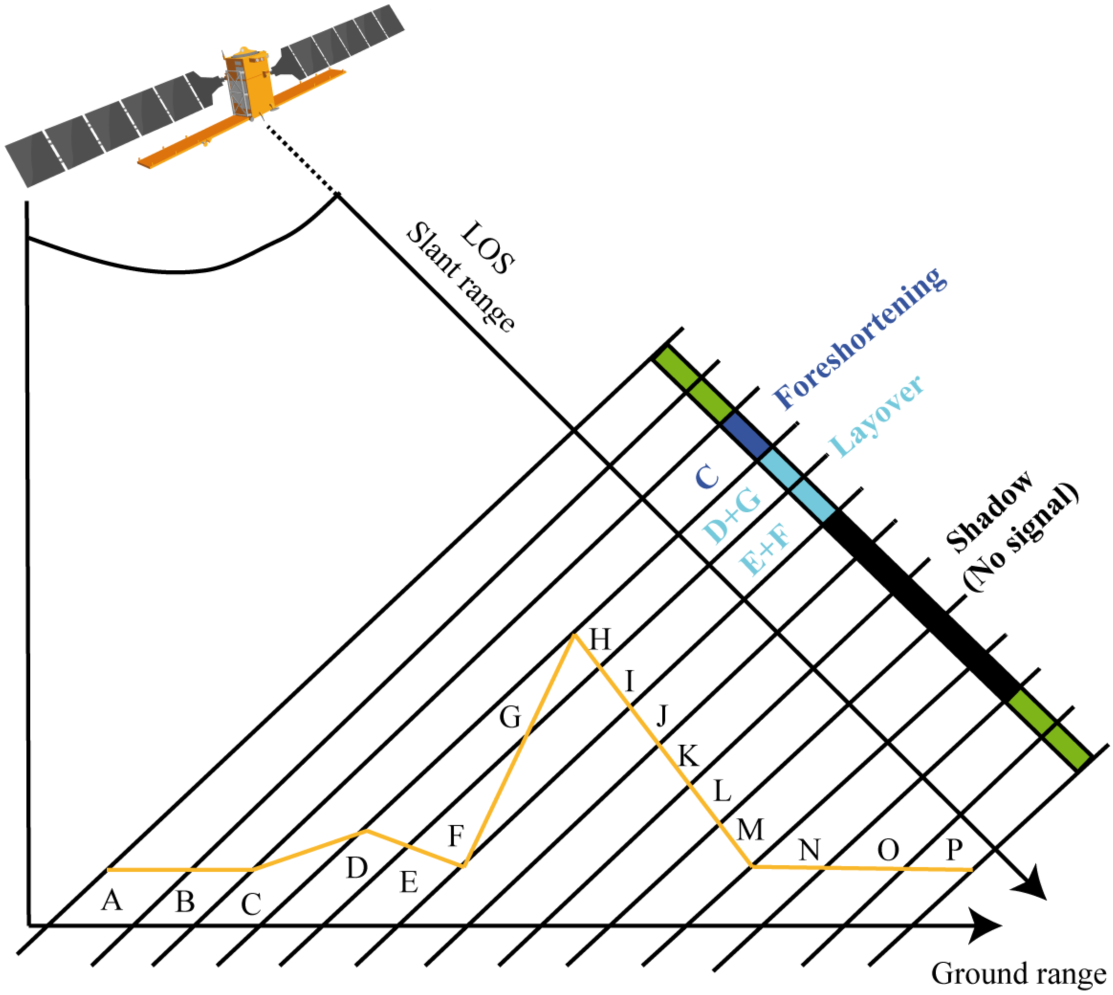

Figure 28. Geometric distortion effects. Foreshortening - (C), Layover - (D, G, E and F) and Shadow - (H - N). Taken and modified from Colesanti and Wasowski (2006).

According to Ferreti *et al.* (2007), another SAR effect is speckle phenomenon, which is directly related to superposition of the signals reflected by many small elementary scatterers within the resolution cell. Their visualization is a sort of granular points screen superimposed on the amplitude image (Figure 29). This effect is usually produced in homogeneous terrains with different amplitudes and different resolution cells. The speckle effect affects the quality and usefulness of SAR images (Figure 29), although it can be reduced and filtered during InSAR processing.

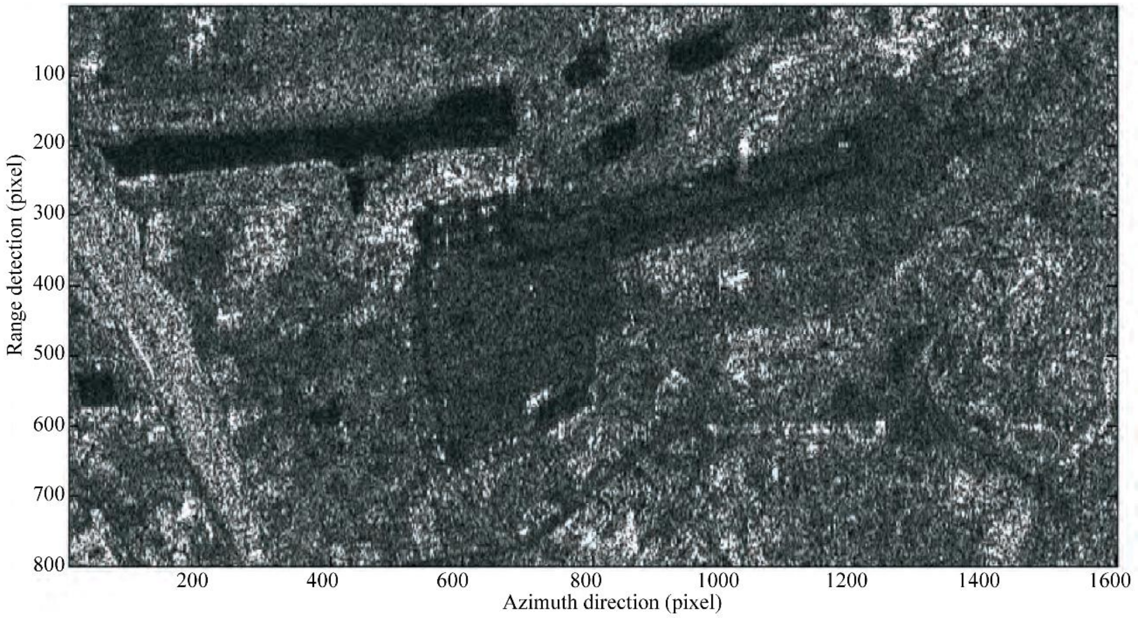

Figure 29. Speckle effect observed in an ERS-2 SAR image of the Linate Airport in Milan (Italy). Taken and modified from Ferreti *et al.* (2007).

SAR satellites dataset

Regarding available SAR dataset, Table 4 lists satellite-borne SAR systems. The SAR sensors on some satellites as ERS-1, ERS-2, Radarsat-1, Envisat-ASAR or Sentinel-1 have operated at C-Band, with repeat cycles between 35 and 6 days. ALOS-1 and 2 and JERS-1 satellites have operated at L-Band with revisit periods from 46 to 3 days. Satellites with X-Band, such as, TerraSAR-X, Cosmo-SkyMed or Kompsat-5, operate with revisit periods between 11 and 28 days. A particular case is Capella constellation, with 36 satellites in orbit and hourly repeat cycles (Table 4).

In order to access and download SAR data generated by these constellations, there are servers and websites where a registered user can access. One remarkable server is ASF Data Search Vertex, funded and supported by Alaska Search Facility (ASF) and NASA (National Aeronautics and Space Administration) (ASF, 2022), where SAR images provided by Sentinel-1, ALOS PALSAR, Radarsat-1, ERS-1 and 2, JERS-1 and Seasat can be downloaded (Figure 30 A). Another server is Copernicus Open Access Hub, which is funded and maintained by the European Space Agency (ESA) and where users can download Sentinel-1 SAR images (ESA, 2022a) (Figure 30 B). Search criteria and filters that can be used on these servers are: 1) Satellite constellation; 2) Area of Interest (AoI) polygon or reference point; 3) Start and end date of monitoring period and 4) Additional search parameters as file type, beam mode, polarization, sensor mode, track, frame or orbit direction (Figure 30 B).

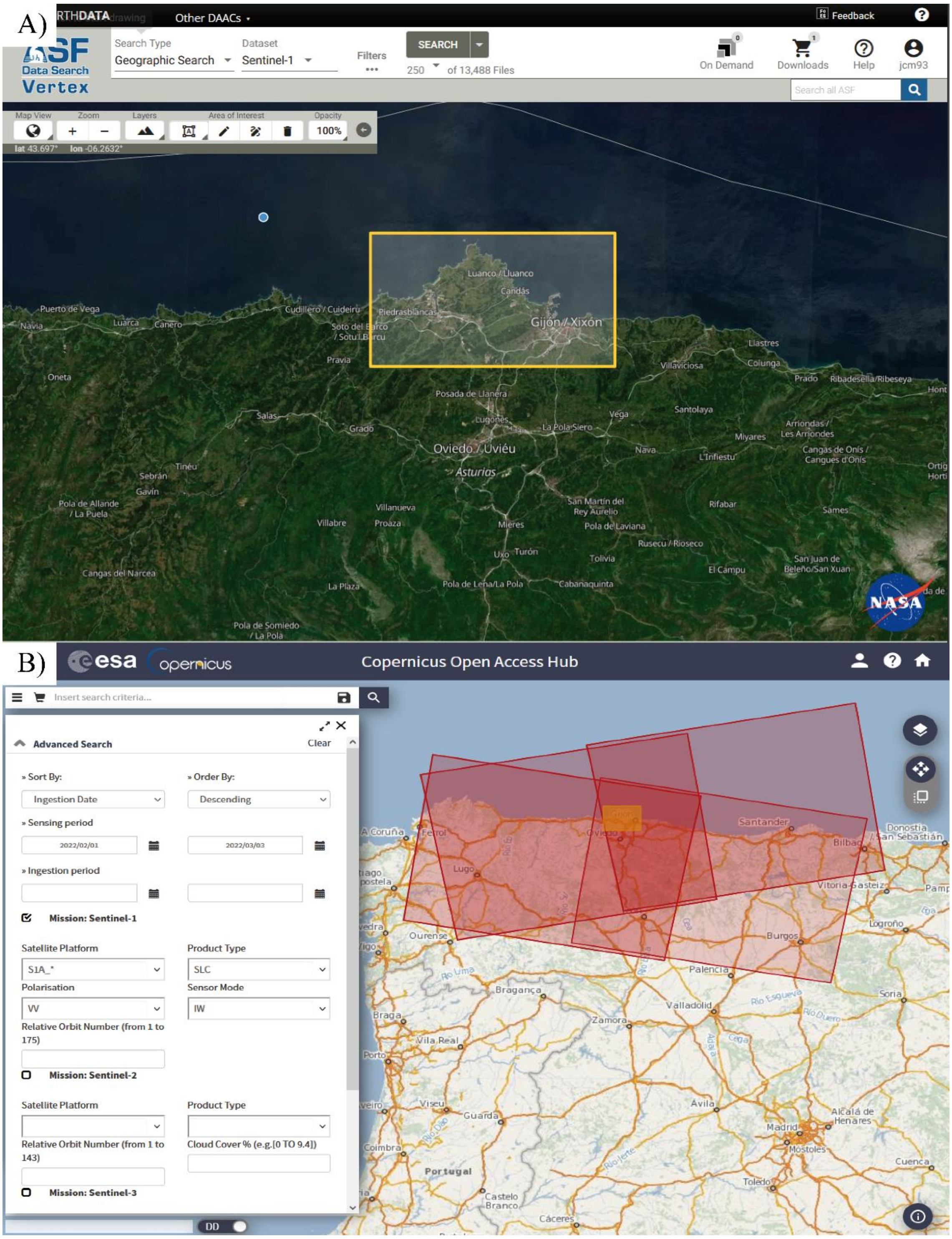

Advanced Search

Clear

» Sort By: Ingestion Date

» Order By: Descending

» Sensing period: 2022/02/01 – 2022/03/03

» Ingestion period:

☑ Mission: Sentinel-1

Satellite Platform: S1A_*

Product Type: SLC

Polarisation: VV

Sensor Mode: IW

Relative Orbit Number (from 1 to 175):

☐ Mission: Sentinel-2

Satellite Platform:

Product Type:

Relative Orbit Number (from 1 to 143):

Cloud Cover % (e.g.[0 TO 9.4]):

☐ Mission: Sentinel-3

Figure 30. Interfaces of **A)** Alaska Search Facility and **B)** Copernicus Open Access Hub with the following search criteria: 1) AoI: Peñas Cape (North Spain); 2) SAR images of Sentinel-1A IW SLC images and polarization VV; 3) The sensing period between February, 1 and March, 3 2022; 4) Descending and ascending trajectories.

In this work, only the Sentinel-1A/B satellites dataset has been used (Table 4). The main characteristics of these satellites are summarized and described below.

Sentinel-1 satellite constellations

According to the ESA (2019), Sentinel-1 is an imaging radar mission providing continuous all-weather, day-and-night imagery at C-band. The Sentinel-1 constellation provides high reliability, improved revisit time, geographical coverage and rapid data dissemination to support operational applications in the priority areas of marine monitoring, land monitoring and emergency services (Figure 31). Also, one main advantage of Sentinel-1 dataset is the open and free access versus other satellite dataset, which can present expensive acquisition and access of SAR data (Table 4). Sentinel-1 constellation was launched on April 3, 2014 from European Spaceport in French Guyana, allowing to obtain SAR data each 12 (Sentinel-1A) and 6 days (Sentinel-1B) (Table 4).

Figure 31. Artist`s impression of the Sentinel-1A satellite during radar scan of the Earth`s surface. Taken from ESA (2022b).

Sentinel-1 data products distributed by ESA include (ESA, 2019): 1) Raw Level-0 data; 2) Processed Level-1 Single Look Complex (SLC) data comprising complex imagery with amplitude and phase; 3) Ground Range Detected Level-1 data with multi-looked intensity only and 4) Level-2 Ocean data for retrieved geophysical parameters of the ocean. On the other hand, the Sentinel-1 C-band SAR instruments support operation in single polarization (HH or VV) and dual polarization (HH+HV or VV+VH), implemented through one transmit chain (switchable to H or V) and two parallel receive chains for H and V polarization. Sentinel-1 satellites operate in four acquisition modes (ESA, 2019): 1) Stripmap (SM); 2) Interferometric Wide swath (IW); 3) Extra-Wide swath (EW) and 4) Wave mode (Figure 32). In this research, SAR data used is SLC product acquired in VV polarization and IW mode. This mode is characterized by a 250 km swath at 5 m by 20 m spatial resolution (single look). Also, IW mode captures three swaths (Figure 32).

Currently, multiple tools are available to visualize and process Sentinel-1 data. The most remarkable software is the Sentinel-1 Toolbox (S1TBX), which was developed by the ESA (Veci *et al.*, 2014; ESA, 2022c). S1TBX consists of a collection of processing tools, data product readers and writers and a display and analysis application to support the large archive of data from ESA SAR missions including Sentinel-1, ERS-1 and 2 and ENVISAT (ESA, 2022c). Also, it can support SAR missions of Radarsat-2, ALOS 1-2, CosmoSkymed and TerraSAR-X. The S1TBX includes tools for calibration, speckle filtering, coregistration, orthorectification, mosaicking, data conversion, polarimetry and interferometry (Veci *et al.*, 2014; ESA, 2022c).

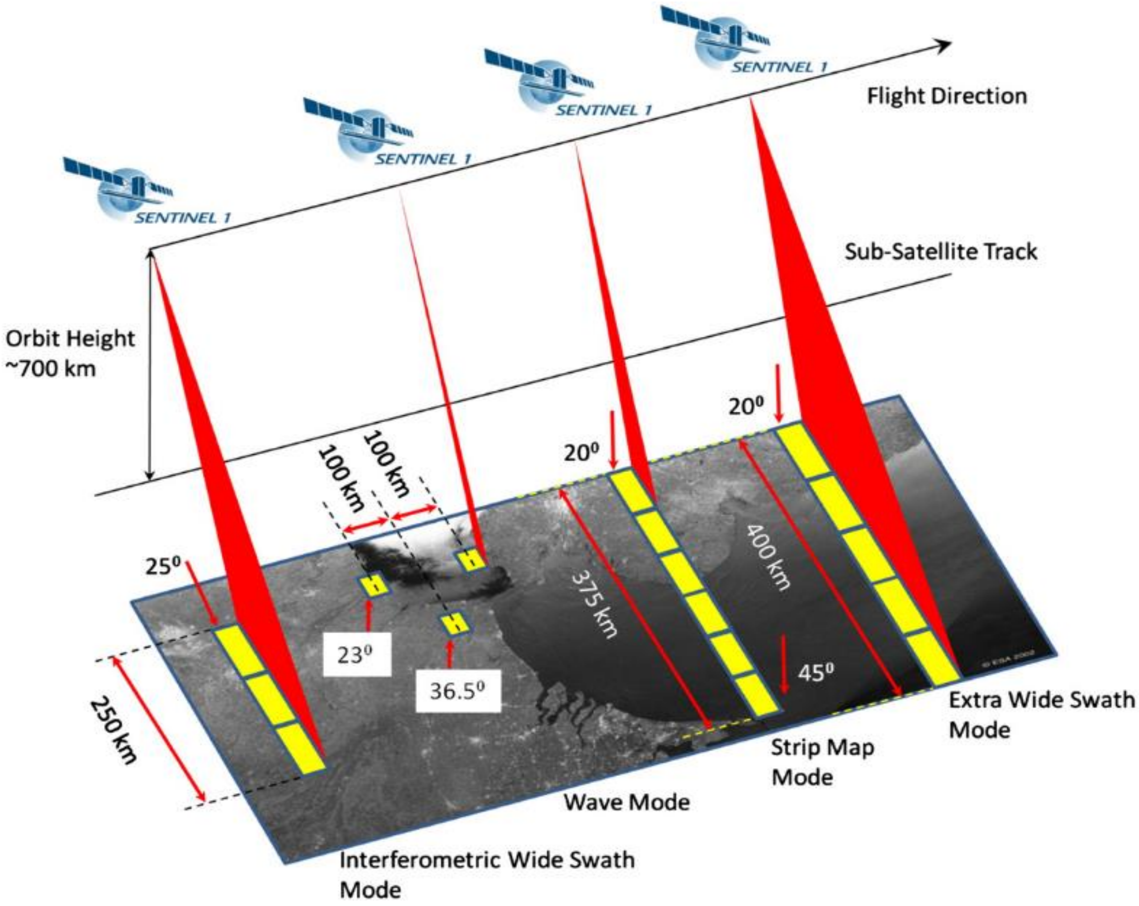

Figure 32. Different acquisition modes of Sentinel-1 satellites. In this research, the Wide Swath Interferometric Mode was used. Taken from ESA (2022).

Table 4. Main SAR satellite constellations and principal characteristics. Taken and modified from Massonet and Feigl (1998), Meyer (2019), Mondini *et al.* (2021) and ESA (2022b).

Satellite	Number	Band	Wavelenght	Resolution	Revisit	Period	Agency	Access
SEASAT	1	L,1.2 GHz	23.5 cm	25 x 25 m	3 d	6/1978 - 10/1978	NASA	Free
ERS-1	1	C, 5.3 GHz	5.6 cm	30 x 26 m	35 d	7/1991 - 4/2001	ESA	Restrained
JERS-1	1	L, 1.2 GHz	23.5 cm	18 x 18 m	44 d	11/1992 - 11/1998	NASDA, MITI , STA	Restrained
ERS-2	1	C, 5.3 GHz	5.6 cm	30 x 26 m	35 d	4/1995 - 9/2011	ESA	Restrained
Radarsat-1	1	C, 5.3 GHz	5.6 cm	28 x 25 m	24 d	11/1995 - 3/2013	CSA	Commercial
Envisat ASAR	1	C, 5.3 GHz	5.6 cm	30 x 30 m	35 d	3/2002 - 4/2012	ESA	Restrained
ALOS-1	1	L, 1.2 GHz	23.6 cm	10 m	46 d	1/2006 - 5/2012	JAXA	Open and free
COSMO-SkyMed	4	X, 9.6 GHz	3.1 cm	5m	16 d	6/2007 -	ASI	Commercial, Limited
TerraSAR-X	2	X, 9.6 GHz	3.1 cm	3.3 x 1.7 m	11 d	6/2007 -	DLR	Commercial, Limited
Radarsat-2	1	C, 5.4 GHz	5.5 cm	28 x 25 m	24 d	12/2007 -	MDA	Commercial
Risat-1	1	C, 5.3 GHz	5.6 cm	3 x 4 m	25 d	4/2013 -	ISRO	Commercial
Kompsat-5	1	X, 9.6 GHz	3.2 cm	3 x 3m	28 d	3/2014 -	KARI	Commercial
Sentinel-1	2	C, 5.4 GHz	5.5 cm	14 x 4 m	6 - 12 d	4/2014 -	ESA	Open and free
ALOS-2	1	L, 1.2 GHz	22.9 cm	3 x 3 m	14 d	5/2014 -	JAXA	Commercial, Limited
PAZ	1	X, 9.6 GHz	3.1 cm	3 x 3 m	11 d	4/2018 -	Hisdesat	Commercial
Saocom-1	2	L, 1.2 GHz	23.5 cm	3 x 3 m	6 d	10/2018 -	CONAE	Open and free
Radarsat Cons.	3	C, 5.4 GHz	5.5 cm	16 x 16 m	12 d	4/2019 -	CSA	Commercial
Capella X-SAR	36	X, 9.6 GHz	3.1 cm	0.5 x 0.5 m	Hourly	9/2020 -	Capella	Commerical

1.3.2 InSAR and DInSAR techniques

SAR Interferometry (InSAR) and Differential SAR Interferometry (DInSAR) techniques are based on processing and comparison of two SAR images (called respectively, master and slave) covering same scene and taken on different dates. These techniques evaluate, on a pixel-by-pixel basis, the phase difference between the master and slave SAR images (Raucoules *et al.*, 2007). The information provided refers to topography and displacement of terrain surface (Fernández-Oliveras, 2009). The temporal difference between master and slave images is called temporal baseline, while interferometer baseline is the spatial separation between the satellite orbits (Figure 33). Its perpendicular projection to the slant range is called the perpendicular baseline (Ferreti *et al.*, 2007) (Figure 33).

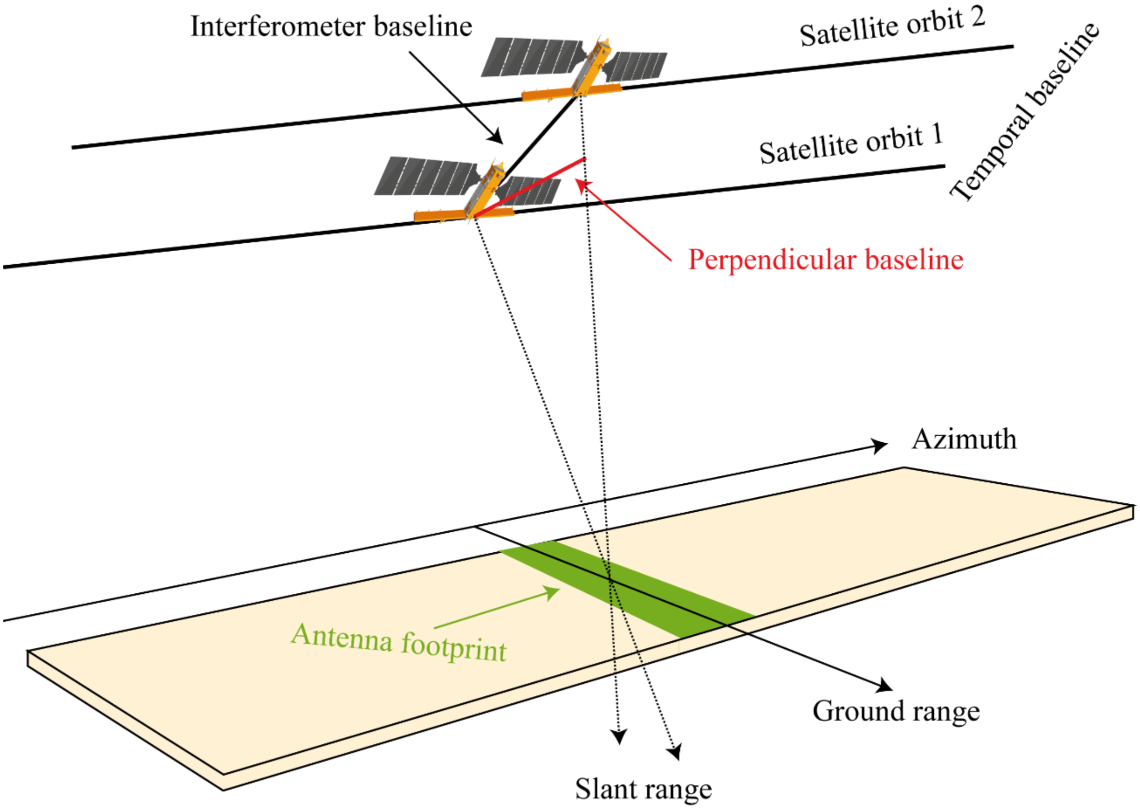

Figure 33. Geometry of a satellite interferometric SAR system. The antenna footprint is the area illuminated on the ground by the sensor. Taken and modified from Ferreti *et al.* (2007).

According to Rott (2009), the phase difference between the slave and master SAR images or interferometric phase ($\Delta\phi$), is related to the difference in the propagation path of the two radar beams (Figure 34). According to Crosetto *et al.* (2005), if it is assumed that the terrain is stable between acquisitions, the phase is related to the distance difference SP - MP (Figure 34). When a point has been displaced from $P_{(T0)}$ to $P^1_{(T1)}$

between master ($M_{(T0)}$) and slave ($S_{(T1)}$) acquisitions, the phase change includes topographic phase component and deformation of terrain (Sousa and Bastos, 2013) (Figure 34).

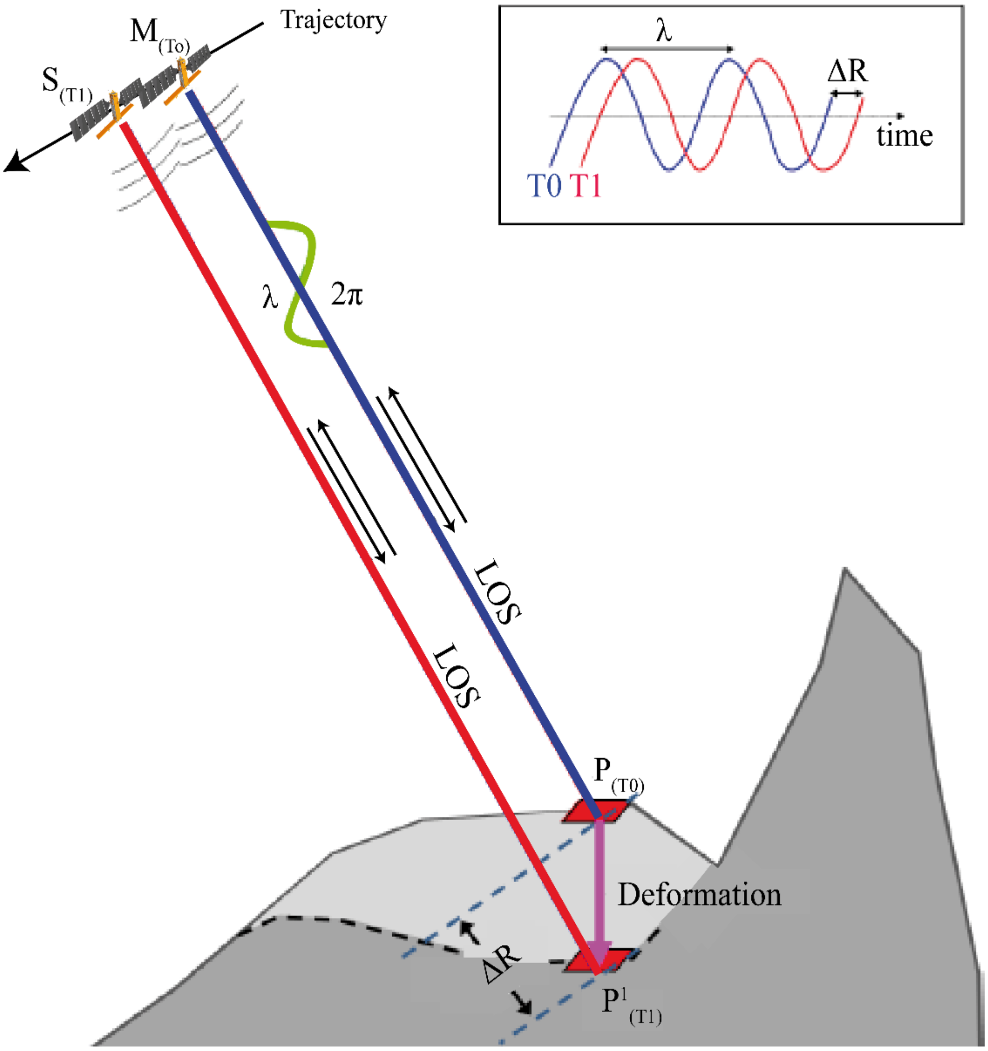

Figure 34. Schematic diagram of deformation measurement procedure using DInSAR. Taken and modified from Crosetto *et al.* (2005) and Sousa and Bastos (2013).

According to Crosetto *et al.*(2005), this concept can be described by the following expression (Equation (2)):

$$\Delta\phi = \phi_S - \phi_M = \frac{SP - MP}{\frac{\lambda}{4\pi}} + \frac{SP^1 - SP}{\frac{\lambda}{4\pi}} + \phi_{noise} + \phi_{atm} = \\ = \Delta\phi_{topo} + \Delta\phi_{Defo} + \Delta\phi_{noise} + \Delta\phi_{atm} \tag{2}$$

Where $\Delta\phi_{topo}$ is the phase difference due to changes in the terrain topography, $\Delta\phi_{Defo}$ is the phase difference associated to displacement of the ground in LOS direction, $\Delta\phi_{noise}$ is the noise component (for example, orbital artifacts and processing errors), $\Delta\phi_{atm}$ is the phase difference due to atmospheric component and λ is the wavelength of radar wave.

In this way, an interferogram is formed by very precise co-registration of these two SAR images, multiplying one image with the complex conjugate of the other (Rosen *et al.*, 2000; Rott, 2009). The interferogram generated (Figure 35) contains information of phase components, which is relative to topography, deformation of terrain and errors related to atmospheric contribution and orbital artifacts (Equation (2)). This information is comprehended between -π and π, which is called wrapped phase (Fernández-Oliveras, 2009). The phase difference is shown by a color pallet whose full path correspond to full rotation 2π or 360º (Figure 27 and Figure 35) (Klees and Massonet, 1998; Fernández-Oliveras, 2009).

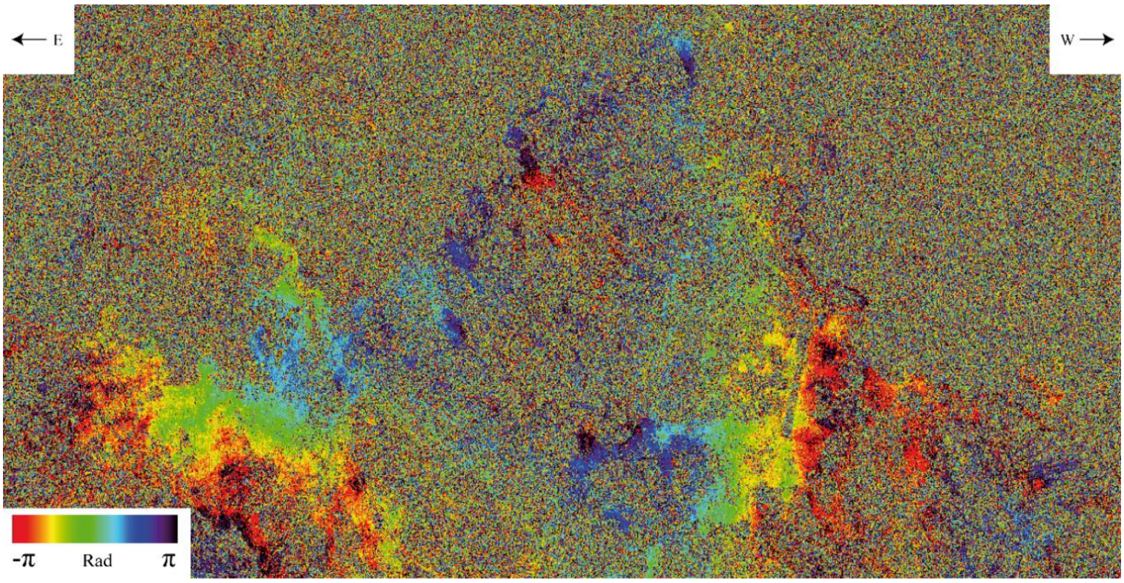

Figure 35. Wrapped interferogram of Peñas Cape generated by two Sentinel-1 IW SLC SAR images (June 4, 2019 - June 28, 2019) with 24-day time baseline. The interferogram was processed using the PSIG approach. Image displayed in ENVI ®.

Applications

The first work published of SAR images application was carried out by Gabriel *et al.* (1989). In this work DInSAR techniques were applied to study ground deformation associated to expansion of clays due to water absorption in California, U.S.A.

Studies on deformation of the Earth`s crust due to seismic events and volcanic activity were among the first promising applications of SAR images and DInSAR techniques

(Massonet and Feigl, 1998). A significant example is the work of Lundgren *et al.* (2003), who analyzed the spatial and temporal patterns of ground deformation of the Mount Etna volcano since 1993. On the other hand, Fialko *et al.* (2005) estimated the pre-, co- and postseismic deformation using ERS-1, ERS-2 and Envisat ASAR dataset in the earthquake of Bam, Iran (Mw = 6.5). In this line, Wang *et al.* (2007) studied the coseismic deformation and slip distribution of the 1997 Manyi earthquake in Tibet (Mw = 7.5) using ERS-2 SAR (Figure 36). In addition, interferometric deformation maps have been used to estimate the measurements of surface deformation before, during and after the eruption (Lu *et al.*, 2005) and to study the uplift and magma intrusion of large calderas (Wicks *et al.*, 2006). Other application was to model the shape of magma chambers (Yun *et al.*, 2006).

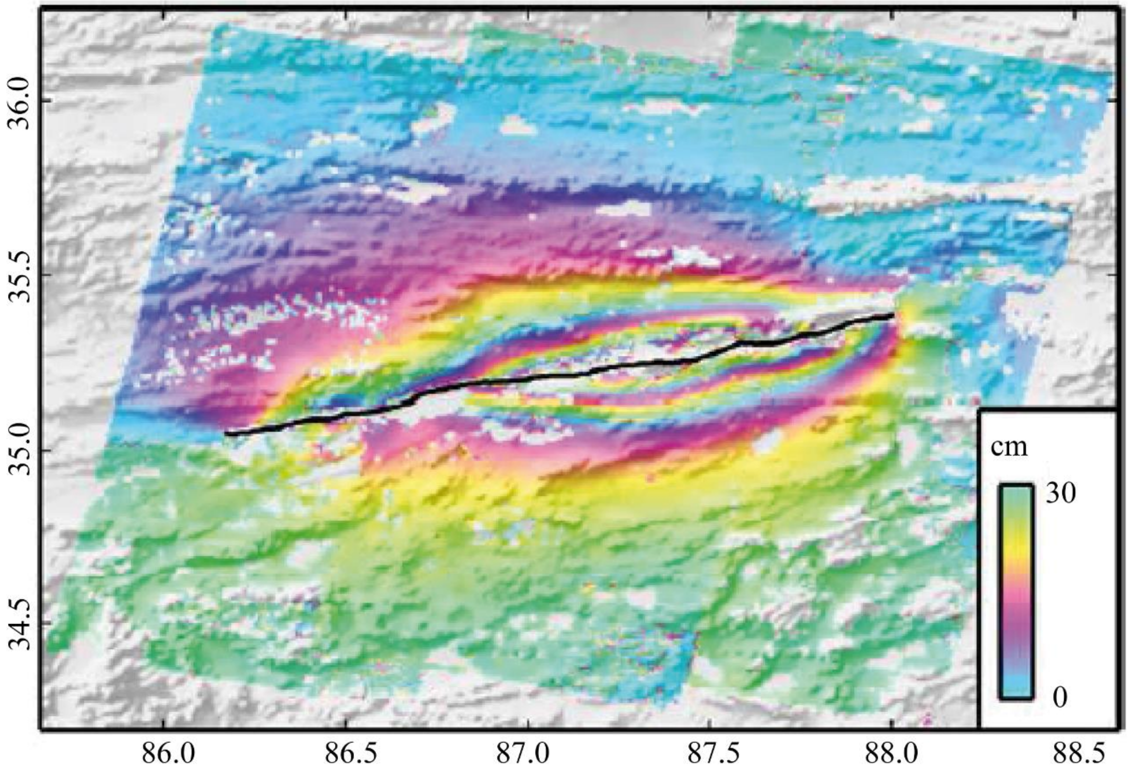

Figure 36. Wrapped interferogram showing coseismic deformation due to the Manyi earthquake. Each color cycle represents 30 cm of displacement in the LOS direction. Taken and modified from Wang *et al.* (2007).

Another important application of InSAR and DInSAR techniques can be found in the glaciology (Joughin *et al.*, 2010). An InSAR product is surface topography of ice sheets using differential interferograms and DEM (Joughin *et al.*, 1996). Moreover, there are some studies about surface velocity and deformation of glaciers and ice sheets by using InSAR and DInSAR techniques as support of studies on ice dynamics and thinning and mass balance (Kwok *et al.*, 2000; Rignot *et al.*, 2002; Gray *et al.*, 2005).

Landslides and subsidence hazards are other important applications of InSAR and DInSAR techniques. In the slope movement investigations, the works of Carnec *et al.* (1996), Berardino *et al.* (2003), Catani *et al.* (2005), Strozzi *et al.* (2005) and Corsini *et al.* (2006) are the most remarkable examples. As to land subsidence topic, the studies were focused on the sinking produced by mining activity (Carnec and Delacour, 2000; Strozzi *et al.*, 2003; Raucoules *et al.*, 2003; 2007) and by water withdrawal and aquifers over-exploitation (Sneed *et al.*, 2001; Strozzi *et al.*, 2003) (Figure 37).

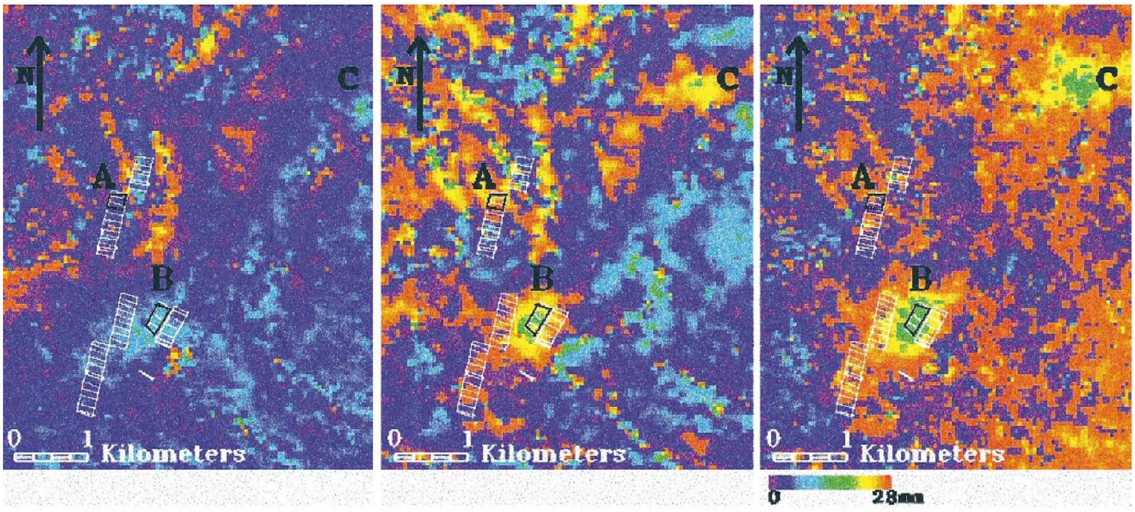

1994

Mar-07 / Mar-10 Mar-10 / Mar-22 Mar-07 / Mar-22

Figure 37. Monitoring of a mining area by different interferograms during 3 days in 1994. The white blocks are underground mining areas developed since 1991 and the black blocks are sectors mined between January and March 1994. Taken from Carnec and Delancourt (2000).

Limitations

Some significant limitations in the detection, monitoring and modeling of ground motion by means of InSAR and DInSAR techniques should be taken account. According to Raucoules *et al.* (2007), these can be summarized in: 1) Loss of coherence with time; 2) Presence of atmospheric components or artifacts; 3) Topographic errors and 4) Instrumental limitations.

Coherence concept refers to the amount of reflectivity variation and it is used as a diagnostic criterion for the quality of the interferograms (Ferreti *et al.*, 2007). It is a normalized index with values from 0 - very low quality to 1 - very high quality (Figure 38). Coherence maps can be used to identify changes in the environment and to obtain information on ground characteristics (Raucoules *et al.*, 2007) (Figure 38). The loss of coherence is the main limitation of DInSAR techniques and corresponds to the term of phase related to noise ($\Delta\phi_{noise}$) (Equation (2)). This loss is due to two different types of decorrelation between the two acquisitions. Firstly, a geometrical decorrelation, which is produced by slighly different imaging geometries between the master and the slave images (Raucoules *et al.*, 2007). Secondly, a temporal decorrelation due to changes of the terrain in the time. These changes can be related to vegetation, water, or wind.

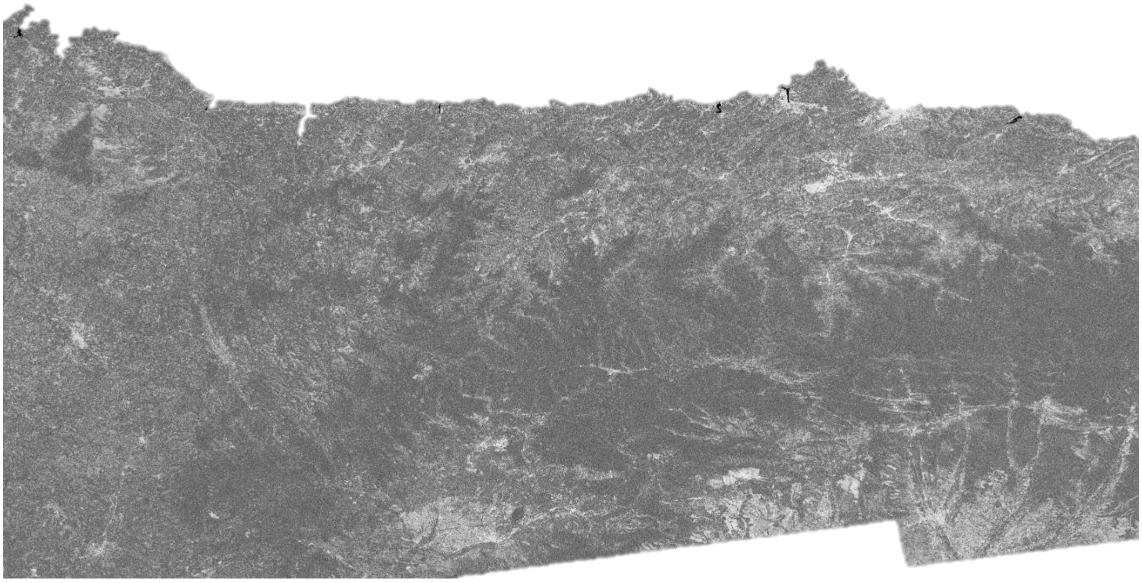

Figure 38. Coherence map of NW Spain using a Sentinel-1A interferometric pair between February 14 and 26, 2016. Dark areas are very low coherence values (~0) while white areas are very high coherence values (~1).

Atmospheric component consists of spatial and temporal variations of phase between the acquisitions due to fluctuations within the tropospheric and ionospheric layers ($\Delta\phi_{atm}$) (Equation (2)) (Raucoules *et al.*, 2007). Noise produced by uncorrected atmospheric component is difficult to distinguish from the ground motion. Also, the phase measurements can be affected by a residual contribution produced by an insufficient accuracy of the orbital information (Raucoules *et al.*, 2007).

The magnitude of the phase errors related to topography ($\Delta\phi_{topo}$) (Equation (2)) is a function of the (Raucoules *et al.*, 2007): 1) Quality and resolution of DEM; 2) Quality and precision of co-registration of interferograms and 3) Separation between the satellite orbits (perpendicular baselines).

Finally, the instrumental limitations refer to those directly related to the of each satellite. These limitations are: 1) Period of revisit of each satellite (Table 4); 2) The pixel size of the SAR image (Table 4); 3) Availability of SAR image dataset according to the AoI and the period of analysis (Table 4) and 4) Ambiguity of displacement data according to the wavelength of the SAR sensor.

These limitations have been partially resolved by the development of advanced techniques (A-DInSAR), which represented a significant advance in the study of ground deformations. In the following chapter (1.3.3), A-DInSAR techniques are presented and described in detail.

1.3.3 A-DInSAR techniques

The A-DInSAR (Advanced Differential Synthetic Aperture Radar Interferometry) techniques (Ferretti *et al.*, 2001; Berardino *et al.*, 2002; Mora *et al.*, 2003) were developed the beginning of XXI century. They are based on the generation of displacement maps (Figure 39) from a large set of SAR images obtained over the same area and acquisition orbits temporarily separated. They allow to study the deformation produced by the displacements of the terrain of any area of the planet in a long period of time. Also, these techniques allow to detect and measure millimetric precision deformations with a minimum topographic error and reduced atmospheric component (Fernández-Oliveras *et al.*, 2009) (Figure 39).

In a similar way to the conventional DInSAR techniques, A-DInSAR techniques have widely been applied in seismic deformation and earthquakes (Lanari *et al.*, 2010; Solaro *et al.*, 2016; Béjar-Pizarro *et al.*, 2018; Kuang *et al.*, 2018; Carboni *et al.*, 2022), volcanic activity (Hooper *et al.*, 2007; De Novellis *et al.*, 2017; Pepe *et al.*, 2018; Di Traglia *et al.*, 2021; Corsa *et al.*, 2022), glacial, ice and permafrost environments (Euillades *et al.*, 2016; Chen *et al.*, 2021; Zhang *et al.*, 2021), landslides (Herrera *et al.*, 2011; Notti et al., 2015; Barra *et al.*, 2016; Solari *et al.*, 2019; Reyes-Carmona *et al.*, 2020) and land subsidence (Heleno *et al.*, 2011; Sanabria *et al.*, 2014; Delgado-Blasco *et al.*, 2019; Haghighi and Motagh, 2019; Cigna and Tapete, 2021a). Moreover, A-DInSAR techniques have extensively been focused on the monitoring and control of essential infrastructures, such as bridges, tunnels, roads, railways, dams and oil/gas fields (Perissin *et al.*, 2012; Bandini *et al.*, 2015; Chang *et al.*, 2016; Del Soldato *et al.*, 2016; Wasowski *et al.*, 2018).

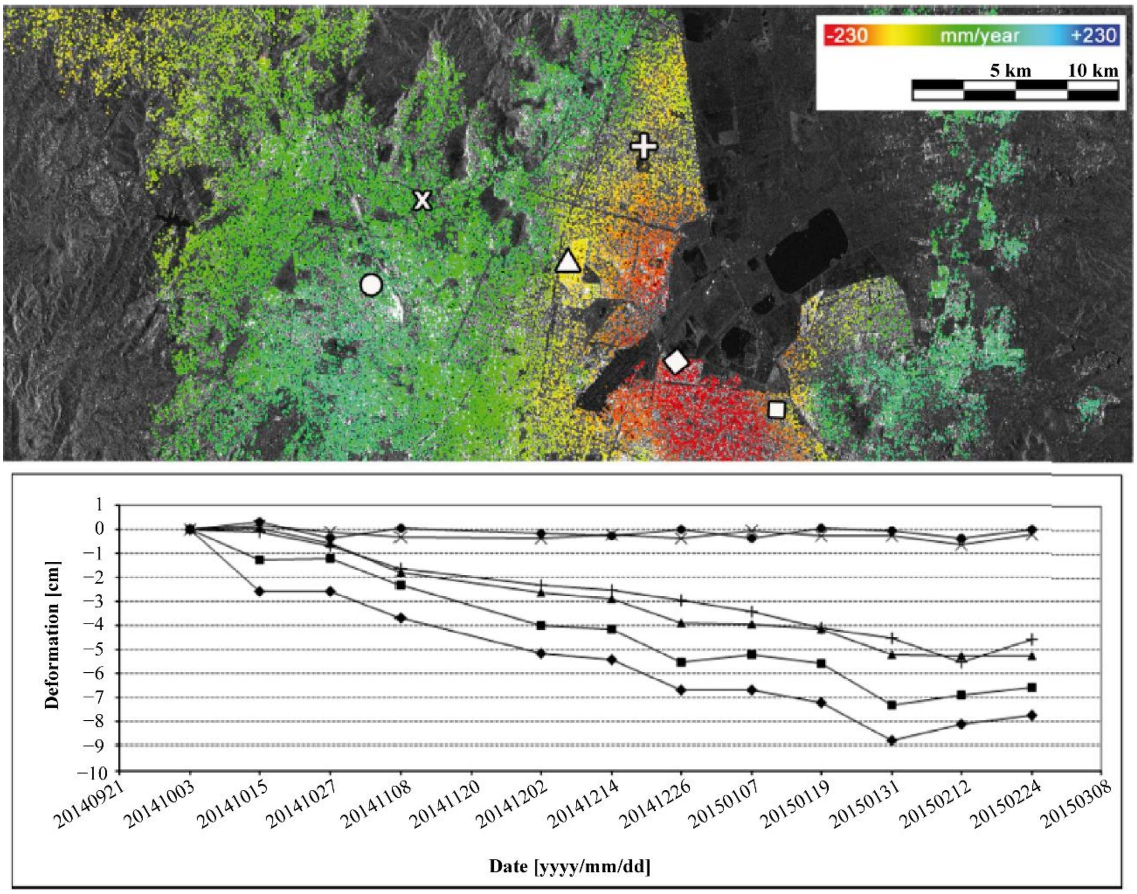

Figure 39. Example of ground motion and deformation time series detected by Sentinel-1A-DInSAR in México city. Taken from Crosetto *et al.* (2016).

Nowadays, there are multiple A-DInSAR techniques and algorithms that allow to process the large amount SAR data. In this line, Crosetto *et al.* (2016) provide a comprehensive review of such methods into the Permanent Scatterer (PS) techniques group, while Lanari *et al.* (2007) published an overview of Small Baseline Subset (SBAS) algorithm. On the other hand, Osmanoglu *et al.* (2016) carried out a review about different algorithms developed for time series analysis into the A-DInSAR processing.

The main A-DInSAR methods and algorithms (Table 5) are described below.

PS (Permanent Scatterer) (Ferreti *et al.*, 2000, 2001). This technique is based on the assessment of the deformation by means of single pixels, called Permanent Scatterers (PS), which are coherent over long time invervals (Ferreti *et al.* 2007). According to Osmanoglu *et al.* (2016), the chain of this algorithm consists of the followed procedure: 1) Generation of single master stack interferograms and removal of topographic component; 2) Selection of PS candidates according to the Dispersion Amplitude (DA) criterion; 3) Assessment of linear and non linear deformation velocities for each pixel selected; 4) Estimation and removal of atmospheric phase screen (APS) by means of a low pass (LP) filter. According to Crosetto *et al.* (2016), the principal disadvantage of this method is that is limited to the scatterers that exhibit sufficiently high coherence or amplitude, and therefore it cannot be adequately used in non-urban environments. In addition, this method requires a great number of SAR images (more than 30) and an adequate density of PS per km^2 (more than 25 PS km^{-2}) (Fernández-Oliveras *et al.*, 2009). The flow chart of PS algorithm is shown in Figure 40. Some works which have applied PS technique to landslide and subsidence investigation are from Raucoules *et al.* (2007), Meisina *et al.* (2008) and Solari *et al.* (2016).

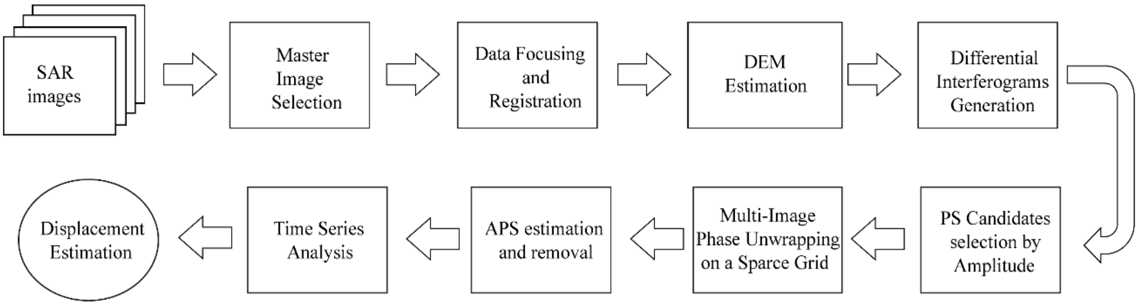

Figure 40. Permanent Scatterer technique flow chart (Ferreti *et al.*, 2000, 2001).

SBAS (Small Baseline Subset DInSAR) (Berardino *et al.*, 2002). This algorithm uses Distributed Scatterers (DS) and singular value decomposition (SVD) to connect independent unwrapped interferograms in time (Osmanoglu *et al.*, 2016). The DS are targets located on debris and non-urban areas or land with short vegetation that present a low average temporal coherence. However, if a group of pixels share same statistical behaviour can exceed the coherence threshold and become PS (Ferreti *et al.*, 2011). In this way, authors like Mora *et al.* (2003) recommend coherence values larger than 0.7. Also, this technique is based on the combination of the interferograms with short baselines to minimize the spatial and temporal decorrelation (Berardino *et al.*, 2002). Unwrapped interferograms include topography, atmosphere and deformation information. After defining and removing topographic phase contribution, the resulting interferograms are converted to deformation mean velocities by means of SVD approach (Berardino *et al.*, 2002). The deformation time series are obtained by means of multiple unwrapped interferograms by using a specific spatial and temporal baseline. Finally, an atmospheric filtering is applied at the end of the processing using a spatio-temporal filter (LP Filter). The block diagram of SBAS algorithm is shown in Figure 41. Some works which has succesfully applied SBAS technique in landslides and subsidences are from Polcari *et al.* (2014), Cigna *et al.* (2017) and Yu *et al.* (2017).

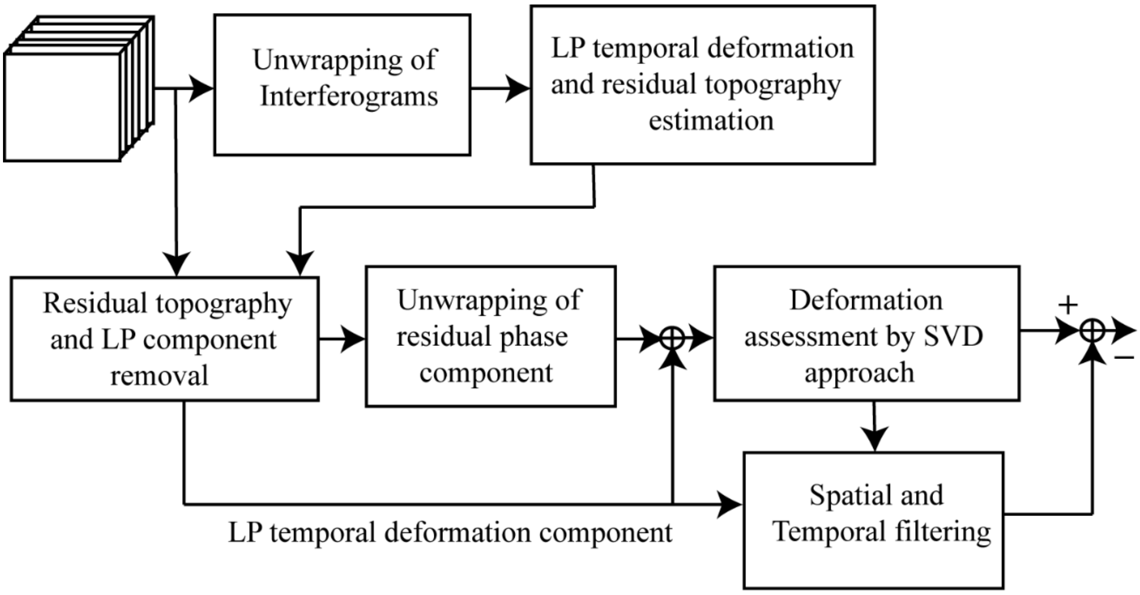

Figure 41. SBAS algorithm flow chart. Taken and modified from Berardino *et al.* (2002).

Based on these major techniques, different algorithms have been designed during the 21st century, among which the following are worth mentioning (Table 5):

PSI (Permanent Scatterer Interferometry) (Biescas *et al.*, 2007 and Devanthéry *et al.*, 2014; 2019). This approach is based on the PS technique and the method of Coherent Pixels Technique (CPT), being developed by the Geomatics Division of Centre Tecnològic de Telecomunicacions de Catalunya (CTTC). This method has been applied in this research, so it will be described in detail in section 3.1.1. PSIG Approach. Some works which have applied PSI approach to landslide and subsidence processes are Notti *et al.* (2015); Reyes-Carmona *et al.* (2020) and Cuervas-Mons *et al.* (2021d) (Figure 42).

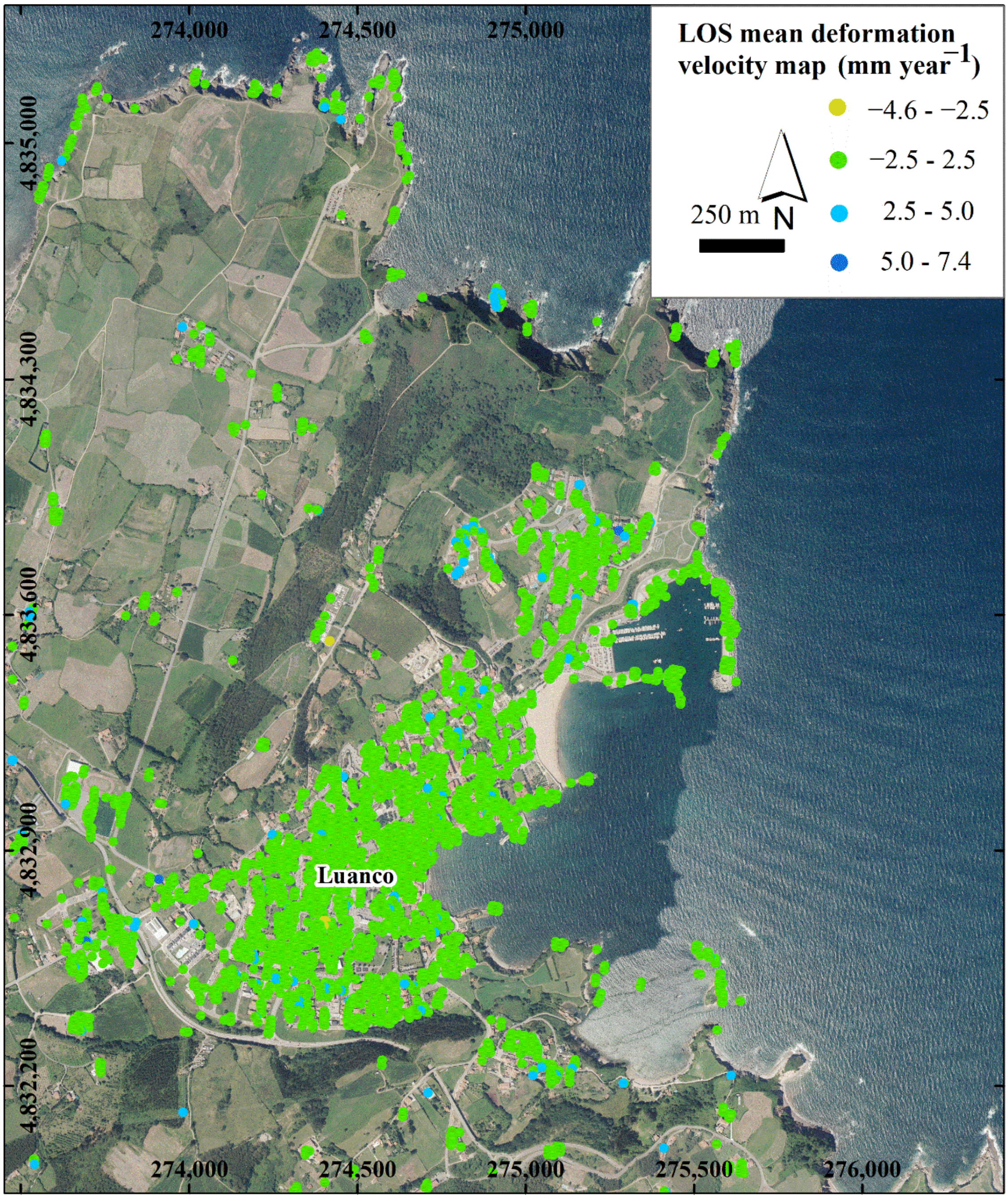

Figure 42. Monitoring of the coastal town of Luanco, Asturias, using the PSI technique. Taken and modified from Cuervas-Mons *et al.* (2021d).

P-SBAS (Parallel-Small BAseline Subset) (Casu *et al.*, 2014). This approach is a parallel version of the SBAS algorithm developed by Berardino *et al.* (2002). This algorithm was specially designed for the exploitation of Envisat ASAR and ERS-1 and ERS-2 satellite datasets (Cuervas-Mons *et al.*, 2021d). Afterward, this technique was adapted for Sentinel-1 IW multitemporal SAR data (Manunta *et al.* 2019). The chain of P-SBAS includes the general steps of A-DInSAR processing: SAR image co-registration, wrapped interferogram generation, unwrapping of phases and estimation of deformation and displacement time series (Casu *et al.*, 2014) (Figure 43). This technique has been applied in this research using Geohazard Exploitation Platform (GEP), which is shown in the sub-section 3.1.2 of methodology. Examples of works that have applied this technique to landslide and subsidence assessment are Cignetti *et al.* (2016), Cigna and Tapete (2021b) and Cuervas-Mons *et al.* (2022b).

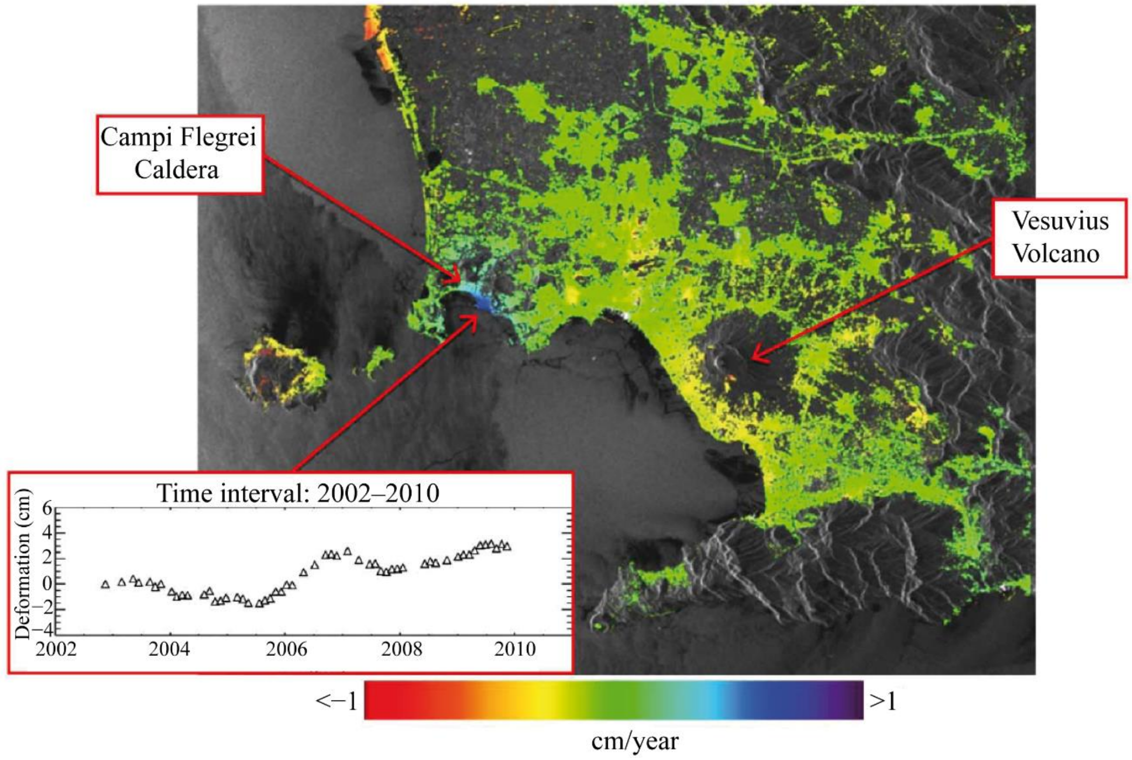

Figure 43. Example of a mean LOS deformation velocity map (cm year^{-1}) of the Napoli Bay, Italy and a deformation time serie obtained using the P-SBAS technique. Taken and modified from Casu *et al.* (2014).

CPT (Coherent Pixels Technique) (Mora *et al.*, 2003). This technique is based on the assessment of the linear and nonlinear displacement components, topographic error and atmospheric component by means of a reduced set of interferograms. In addition, this algorithm does not use a master image, but rather processes jointly all interferograms. The selection of candidate pixels is done according to a coherence threshold. Some works that have applied CPT to landslide and subsidence processes are Tomás *et al.* (2005); Duque *et al.* (2007); Béjar-Pizarro *et al.* (2017) and Bru *et al.* (2018) (Figure 44).

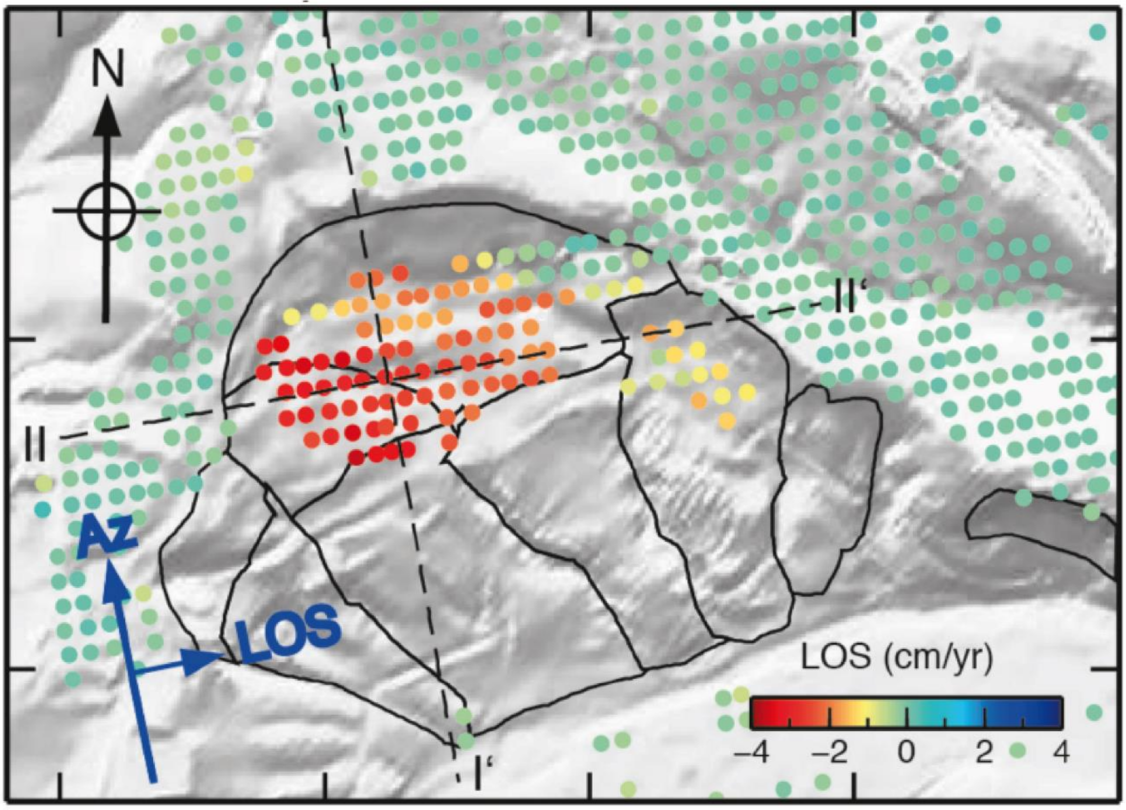

Figure 44. Ground motion detected on the Arcos de la Frontera complex landslide (Andalusia, Spain) using the CPT technique. Taken from Béjar-Pizarro *et al.* (2017).

SPN (Stable Point Network) (Arnaud *et al.*, 2003; Duro *et al.*, 2003). This technique was developed to combine ERS and Envisat ASAR dataset with the main aim of generating long term terrain movements and precise DEM maps with the same resolution of SAR images. The algorithm can use all available phase information in large baseline conditions. The large baseline is used to improve the altitude resolution (Arnaud *et al.*, 2003). The pixel selection is carried out according to an amplitude or coherence threshold. The outputs are (Fernández-Oliveras, 2009): 1) A mean deformation map defined by LOS linear velocity in mm year^{-1}; 2) A residual topographic errors map as an approximation of a Digital Surface Model (Duro *et al.*, 2003) and 3) Deformation Time Series. Some works that have applied SPN to landslide and subsidence processes are from Herrera *et al.* (2009), Bianchini *et al.* (2013), and Herrera *et al.* (2013) (Figure 45).

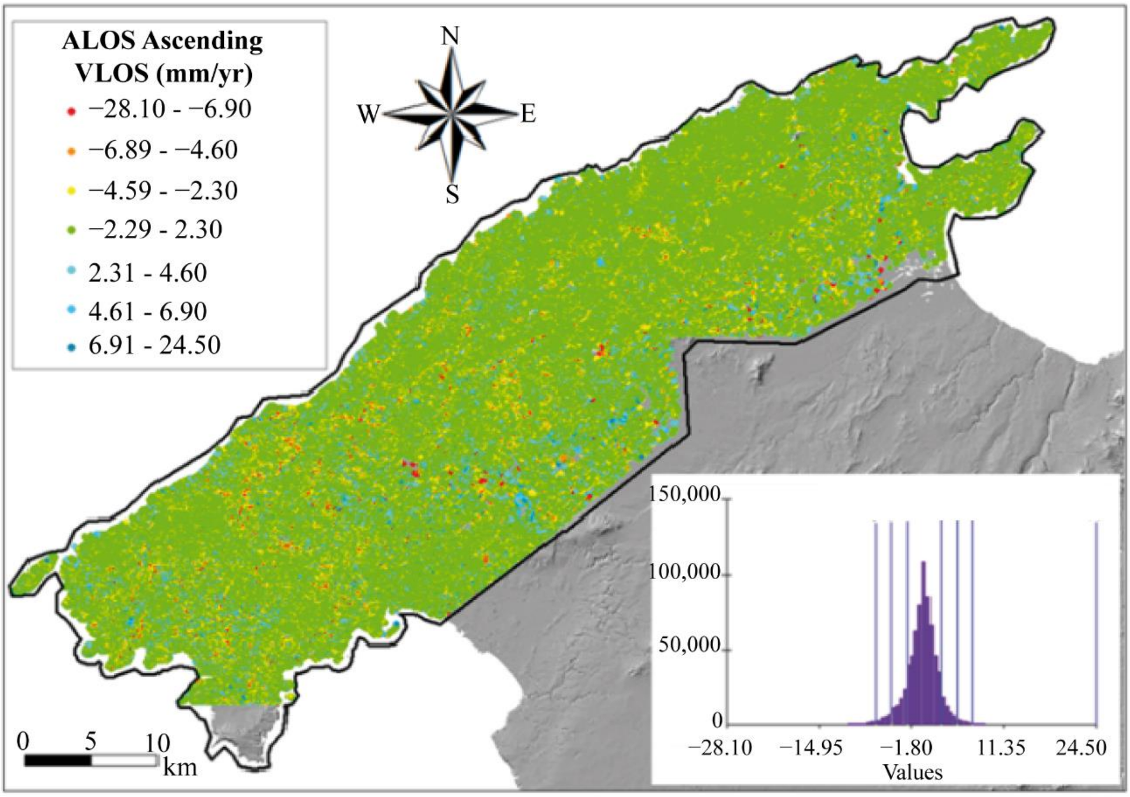

Figure 45. Mean LOS deformation velocity map (mm year^{-1}) of northern sector of Mallorca Island, Spain obtained by using SPN technique. Taken and modified from Bianchini *et al.* (2013).

IPTA (Interferometric Point Target Analysis) (Werner *et al.*, 2003; Wegmüller *et al.*, 2004). This technique uses interferograms, unwrapped phases, deformation rates and residual phases associated to atmospheric component in vector format, allowing a significant reduction of the required disk space. Regarding pixel selection, the Point Targets candidates are selected in two steps. Firstly, an initial selection of points is done according to the low temporal variability of the backscatterer. Afterward, a second selection is carried out using the standard deviation of the phase with respect to the interferometric phase model. Outputs of IPTA approach are linear deformation rates, terrain heights, atmospheric phase terms, precision baseline estimation, deformation phase and quality information (Wegmüller *et al.*, 2004). Authors as Guéguen *et al.* (2009), Polcari *et al.* (2014) and Sarychikhina *et al.* (2021) have applied IPTA algorithm to landslides and subsidence study (Figure 46).

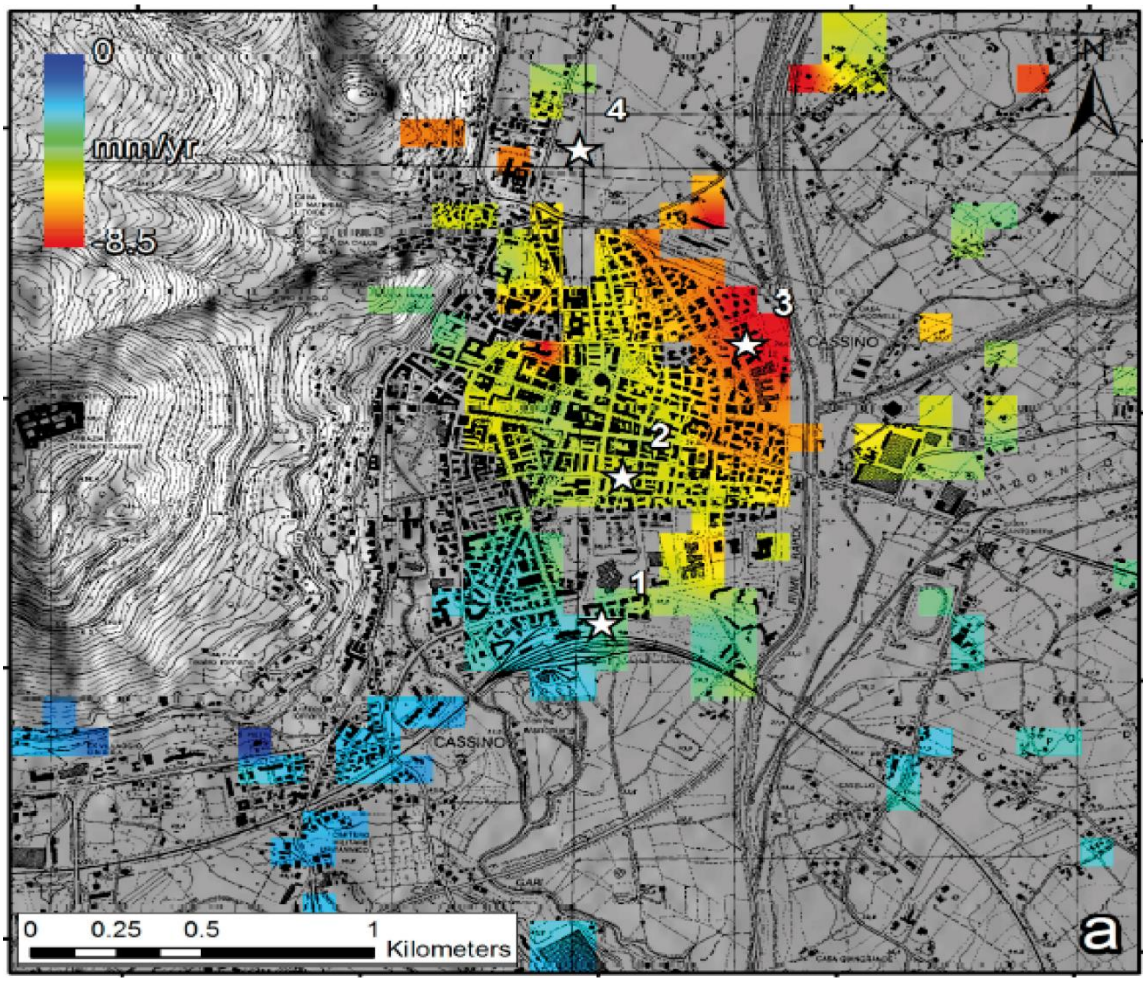

Figure 46. Subsidence detected in Cassino, Italy, using the IPTA algorithm (1992-2000). Taken from Polcari *et al.* (2014).

StaMPS (Standford Method for Persistent Scatterer) (Hooper *et al.*, 2004; Hooper, 2008). This method combines the PS (Ferreti *et al.*, 2000, 2001) and SBAS (Berardino *et al.*, 2002) approaches with the main aim to maximize the spatial sampling of useable signal and to extract the deformation at more points. According to Hooper (2008), this procedure consists of combining the phase of selected pixels from filtered interferograms obtained by SBAS method (Berardino *et al.*, 2002) with the phase of selected pixels from non-filtered interferograms generated by PS method (Ferreti *et al.* 2000, 2001). The selection of PS is done according to the phase stability. This phase stability is defined by amplitude difference dispersion, which is similar to the amplitude dispersion index (DA) of Ferreti *et al.* (2000, 2001). This technique was specially designed to analyze the deformation linked to the activity of the Earth´s crust and volcanic events in non-urban areas (Figure 47). However, STaMPS method has been commonly applied to investigate landslides and subsidence phenomena by Oliveira *et al.* (2015), Bayer *et al.* (2017), and Cian *et al.* (2019).

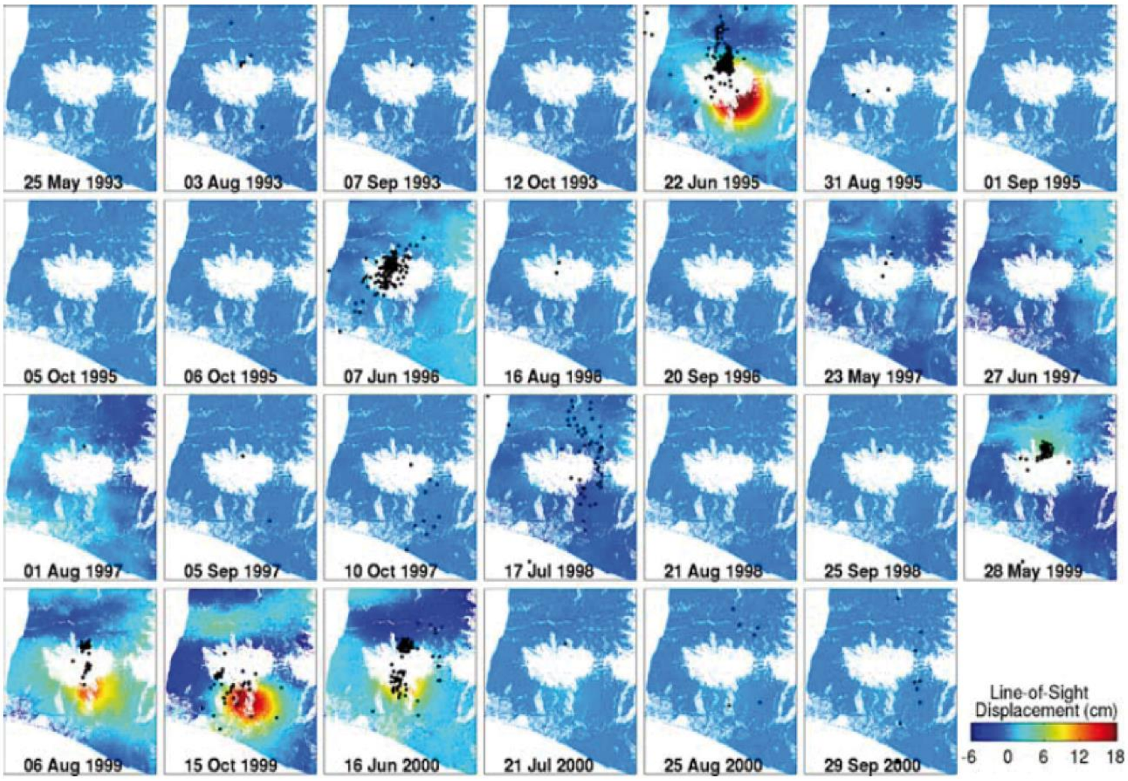

Figure 47. Activity evolution of Eyjafjallajökull volcano (Iceland) measured by the StaMPS algorithm. Taken from Hooper (2008).

SPINUA (Stable Point Interferometry over Unurbanised Areas) (Bovenga *et al.*, 2004; Gulati *et al.*, 2021). This approach is based on the PS technique (Ferreti *et al.*, 2000, 2001) and was developed to process ERS and Envisat ASAR satellite dataset in non-urbanized areas. The chain allows to select different paths: 1) Using a one master image for all the subsequent processing and 2) Connecting all the images by means of a minimum spanning tree (Bovenga *et al.*, 2004). The processing chain includes, in order: Co-registration SAR images and resampling, differential inferferograms generation and selection of PS according to amplitude criterion. This selection is based on the Inverse Coefficient of Variation value and threshold. Afterward, phase unwrapping, atmospheric phase filtering, DEM error and movement estimation are carried out. The SPINUA allows obtain different outputs (Bovenga *et al.*, 2004; Gulati *et al.*, 2021): 1) A full-resolution SAR amplitude map; 2) An APS map for each processed SAR acquisition; 3) PS maps in both SAR and geographical coordinates (WGS84) systems; 4) LOS time series for each PS and 5) A DEM corrected with PS locations. Examples of SPINUA algorithm applications in landslides and subsidence can be seen in Nutricato *et al.* (2009), Bovenga *et al.* (2017) and Wasowski et al. (2018) (Figure 48).

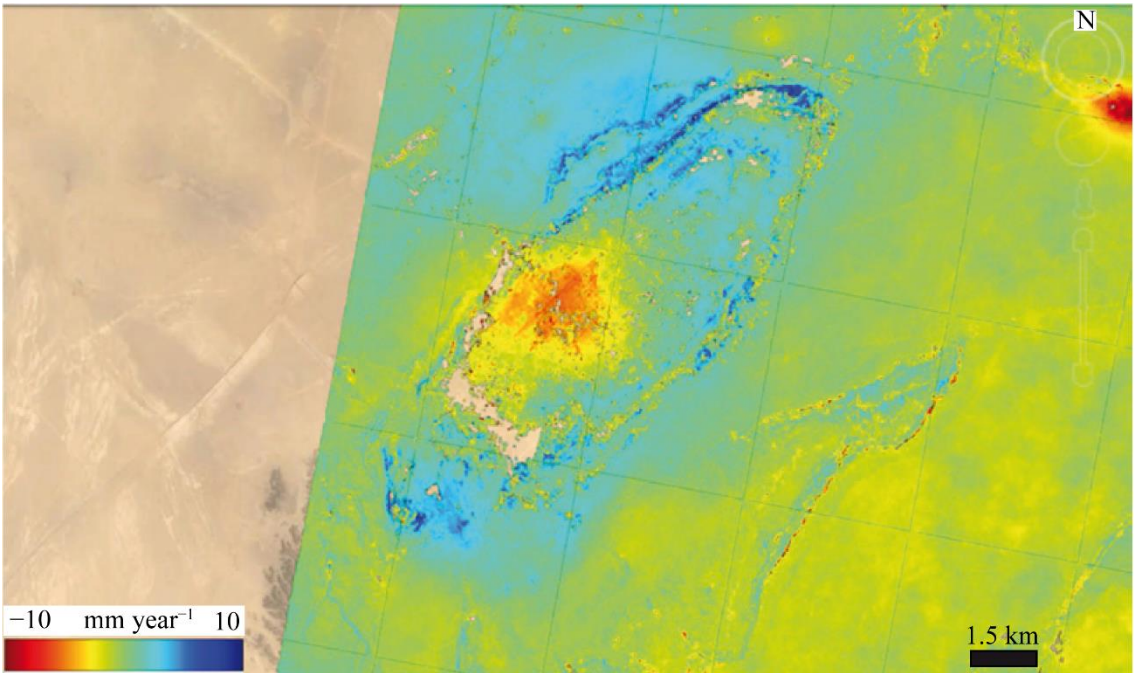

Figure 48. Subsidence produced by hydrocarbon production in the Middle East and detected by means of SPINUA technique. The LOS mean deformation velocity map (mm year^{-1}) is shown in Google Earth. Taken and modified from Wasowski *et al.* (2018).

SqueeSAR (Ferreti *et al.*, 2011). This algorithm was developed with the main aim to increase the density and quality of InSAR measurement points in non-urban areas (Figure 49). This is due to PS technique (Ferreti *et al.*, 2000, 2001) was designed for monitoring urban areas, where the density of points can be higher than 100 PS km^{-2}, while this technique is not useful in non-urban areas because the PS density is very low (< 10 PS km^{-2}) (Figure 49 A). Then, SqueeSAR was developed and based on the processing of both PS and DS, according to their different statistical behavior, to obtain a higher number of points (Figure 49 B) than PS technique (Figure 49 A). SqueeSAR approach has been satisfactory applied in the study of landslide and subsidence processes by Graniczny *et al.* (2015), Bandini *et al.* (2015), Solari *et al.* (2019) and Crippa and Agliardi (2021).

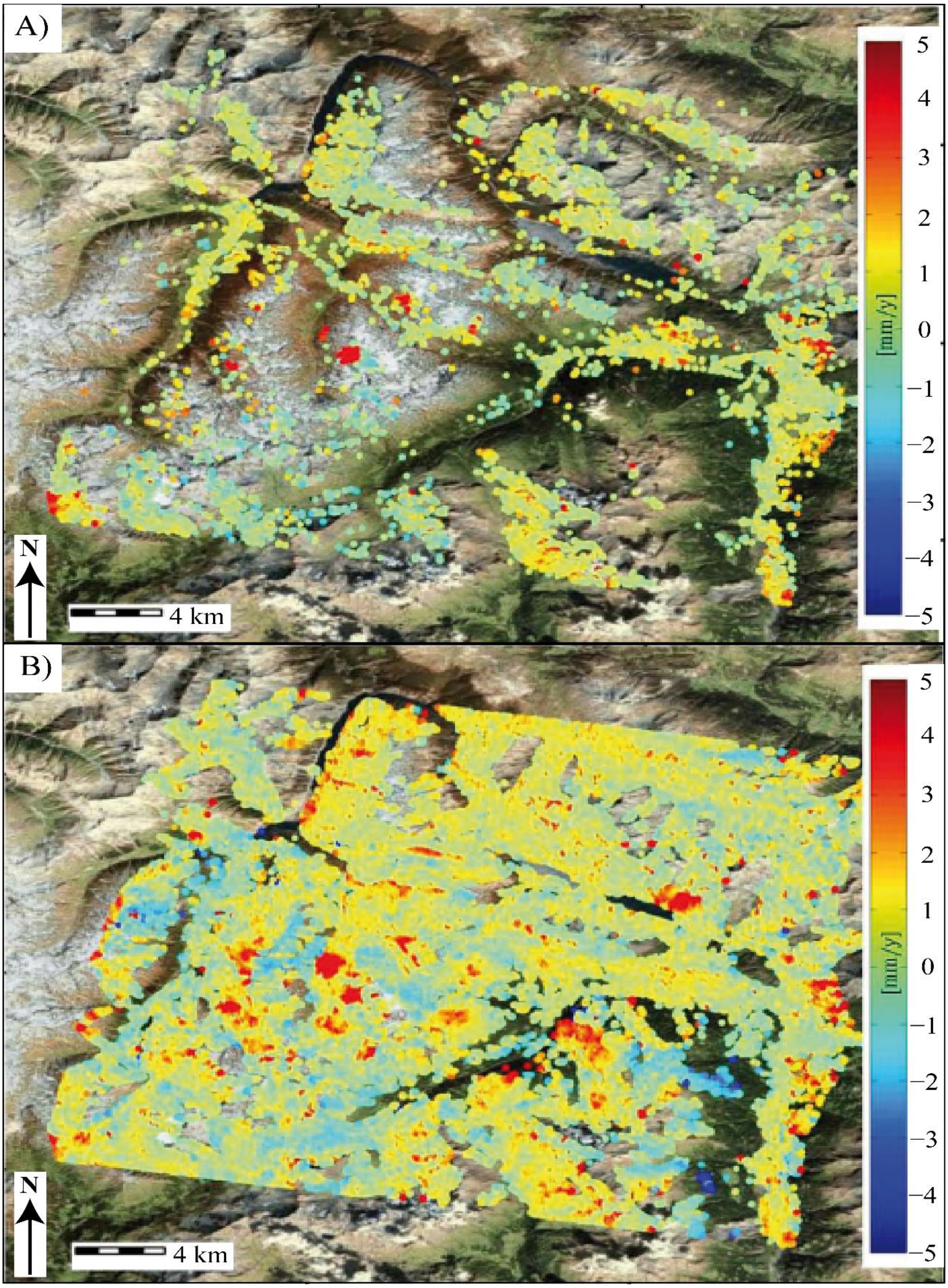

Figure 49. Comparison between the LOS mean deformation velocity maps (mm year^{-1}) in a non-urban area applying **A)** PS technique and **B)** SqueeSAR algorithm. Taken and modified from Ferreti *et al.* (2011).

A particular case of the A-DInSAR technique widely used nowadays is the **GB-SAR (Ground-Based SAR)** (Tarchi *et al.*, 1997). A GB-SAR operates on the same principles as a satellite sensor, but in this case the antenna travels on a rail of few meters, being able to acquire complex SAR images at a rate of one per 2 or 3 minutes (Mateos-Redondo *et al.*, 2016) (Figure 50).

Figure 50. Ground-Based SAR used to detect slope instabilities in Mamorana (Aller, Asturias). SEDTRIGE Project (Ref. FUO-19-128) carried out by GEA Asesoría Geológica S. COOP. ASTUR and co-funded by IDEPA (Ref. IDE/2018/00385).

A detailed and theoretical description of GB-SAR instrument and steps can be found in the works of Monserrat et al. (2014) and Pieraccini and Miccinesi (2019) (Figure 51). The GB-SAR processing is similar to satellital A-DInSAR techniques, including the following steps: Image co-registration, interferogram and coherence image generation, pixel selection, 2D phase unwrapping, phase integration, atmospheric phase component estimation, displacement computation and geocoding (Monserrat *et al.*, 2014). This technique was specially designed to monitor open pits, landslides, urban areas and infrastructures (e. g. dams) within a distance of few kilometers and reaching resolutions finer than 5 x 5 m (Noferini *et al.*, 2007). According to Monserrat *et al.* (2014), GB-SAR data can be acquired using two types of acquisition modes: the continuous (C-GBSAR) and the discontinuous (D-GBSAR). In the first case, it is appropiate to measure fast deformation phenomena, whose displacement rates range from mm day^{-1} to m day^{-1}. Also, this tool provides a near real-time monitoring of the site of interest. However, D-GBSAR is more adequate to monitor extremely slow to slow deformation phenomena (Monserrat *et al.*, 2014). Examples of application of GB-SAR are Antonello *et al.* (2004), Herrera *et al.* (2009), Bozzano *et al.* (2011) and Kuras *et al.* (2020).

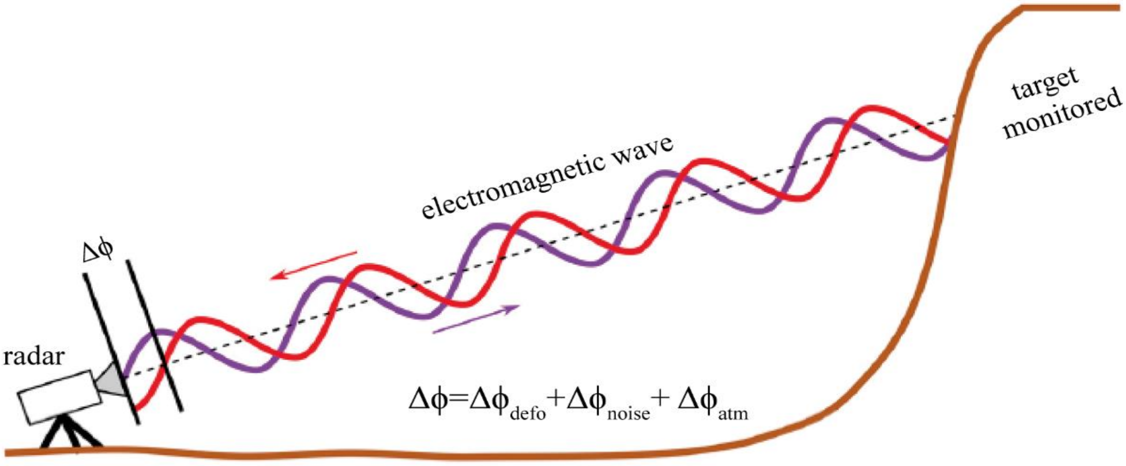

Figure 51. Schematic representation of ground-based SAR principles. Taken and modified from Pieraccini and Miccinesi (2019).

Table 5. Summary of characteristics of the main A-DInSAR techniques. Taken and modified from Tomás *et al.* (2014), Crosetto *et al.* (2016) and Osmanoglu *et al.* (2016).

A-DInSAR technique	Pixel selection criteria	Developer	Remarkable references
PS (Permanent Scatterer)	Amplitude	Dipartimento di Elettronica e Informazione, Politecnico di Milano, Italy	Ferreti *et al.* (2000, 2001) Raucoules *et al.* (2007) Meisina *et al.* (2008) Solari *et al.* (2016)
SBAS (Small BAseline Subset)	Coherence	Institute for Electromagnetic Sensing of the Environment (CNR-IREA), Italy	Berardino *et al.* (2002) Lanari *et al.* (2007) Polcari *et al.* (2014) Cigna *et al.* (2017) Yu *et al.* (2017)
PSI (Permanent Scatterer Interferometry)	Amplitude Coherence	Geomatics Division, Telecommunications Technological Center of Catalonia (CTTC), Spain	Biescas *et al.* (2007) Devanthéry *et al.* (2014) Notti *et al.* (2015) Reyes-Carmona *et al.* (2020) Cuervas-Mons *et al.* (2021d)
P-SBAS (Parallel-Small BAseline Subset)	Coherence	Institute for Electromagnetic Sensing of the Environment (CNR-IREA), Italy	De Luca *et al.* (2015) Cignetti *et al.* (2016) Manunta *et al.* (2019) Cigna and Tapete (2021) Cuervas-Mons *et al.* (2022b)
CPT (Coherent Pixel Technique)	Coherence	Universidad Politécnica de Cataluña, Spain	Mora *et al.* (2003) Tomás *et al.* (2005) Duque *et al.* (2007) Béjar-Pizarro *et al.* (2017) Bru *et al.* (2018)
			Arnaud *et al.* (2003)

SPN (Stable Point Network)	Amplitude Coherence	Altamira Information, Spain	Duro *et al.* (2003) Herrera *et al.* (2009) Bianchini *et al.* (2013) Herrera *et al.* (2013)
IPTA (Interferometric Point Target Analysis)	Backscatterer Phase	GAMMA Remote Sensing, Switzerland	Werner *et al.* (2003) Wegmüller *et al.* (2004) Guéguen *et al.* (2009) Polcari *et al.* (2014) Sarychikhina *et al.* (2021)
StaMPS (Stanford Method for Persistent Scatterer)	Phase stability	Stanford University, USA	Hooper *et al.* (2004) Hooper (2008) Oliveira *et al.* (2015) Bayer *et al.* (2017) Cian *et al.* (2019)
SPINUA (Stable Point INterferometry over Un-urbanised Areas)	Amplitude	Dipartamento Interateneo di Fisica - Politecnico di Bari, Italy	Bovenga *et al.* (2004) Nutricato *et al.* (2009) Bovenga *et al.* (2017) Wasowski *et al.* (2018) Gulati *et al.* (2021)
SqueeSAR	Statistical behaviour	Tre-Rilevamento Europa - T.R.E., Italy	Ferreti *et al.* (2011) Graniczny *et al.* (2015) Bandini *et al.* (2015) Solari *et al.* (2019) Crippa and Agliardi (2021)
GB-SAR (Ground-Based SAR)	Amplitude Coherence	Space Applications Institute, Joint Research Centre of the European Commision, Italy	Tarqui *et al.* (1997) Antonello *et al.* (2004) Herrera *et al.* (2009) Bozzano *et al.* (2011) Kuras *et al.* (2020)

2. STUDY AREAS

2.1 Criteria for selection of study areas

For the purpose of the selection of the study areas in this research, different criteria have been taken into account. The first criterion was the spatial and temporal location of more than 2,800 landslide events registered in the BAPA database (Valenzuela *et al.*, 2017) along the Asturian territory (N Spain) (Figure 52). The BAPA database has allowed to identify and select the principal areas where A-DInSAR techniques were applied. Secondly, the works and projects that have been carried out to date by researchers at the University of Oviedo and by other authors.

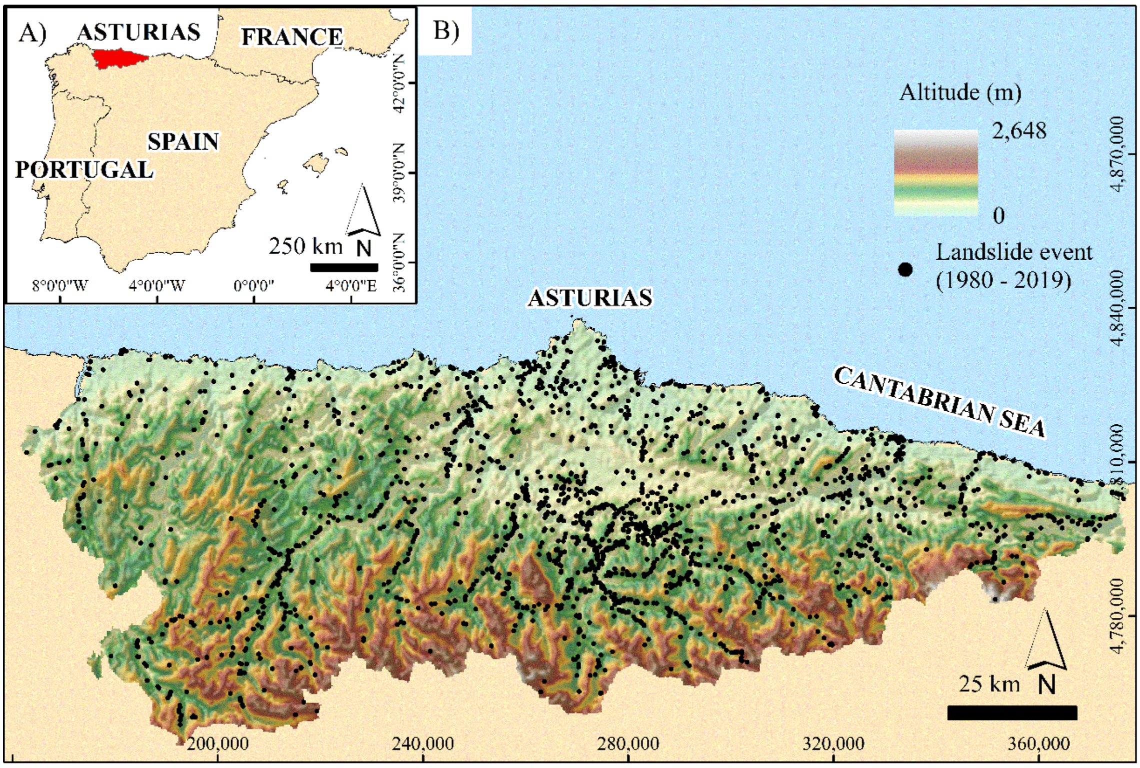

Figure 52. Spatial distribution of the 2,839 landslidse recorded in the BAPA database (1980-2019) (Valenzuela *et al.*, 2017).

Presently, the BAPA landslide and ground movements database, which started to be filled in by scientists of the Department of Geology (University of Oviedo) in 1995, covers the period 1980-2019 and records 2,839 individual landslides (Figure 52). This database is supported on Microsoft Access ® and classifies slope instabilities registered in rockfalls, slides, flows, cracks, subsidences/collapses and undetermined events. Moreover, the database structure includes 105 different data fields (Valenzuela, 2017; Valenzuela *et al.*, 2017) that collect information about: 1) Registration data and source;

2) Spatial and temporal data; 3) landslide information and triggers; 4) Damage, costs and affected infrastructures and 5) Accuracy and fieldwork - validation (Figure 53).

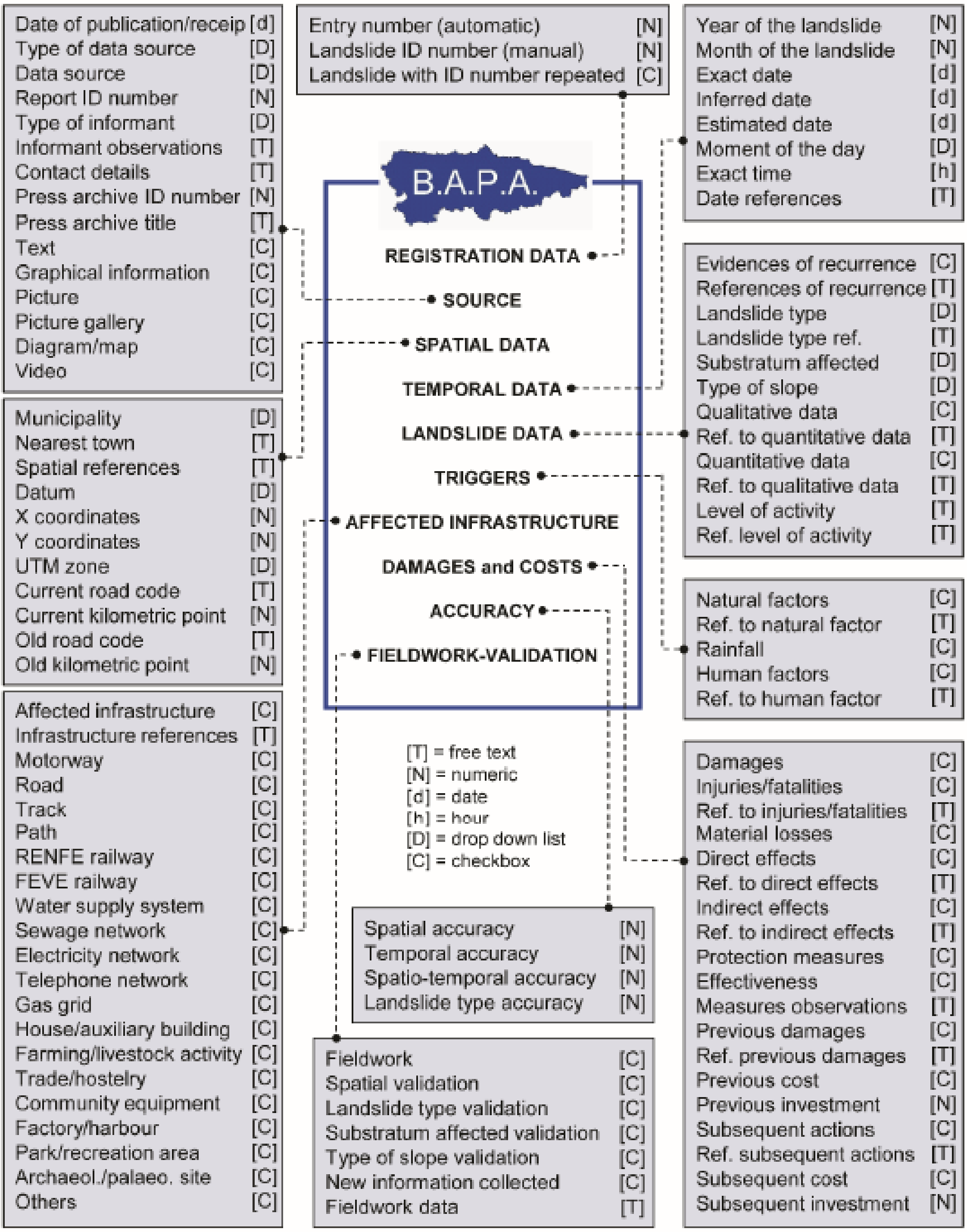

Figure 53. Structure of BAPA database developed by Valenzuela (2017). Taken from Valenzuela (2017).

All landslide events registered between 1980 and 2019 in Asturias were reviewed. This examination was focused on the verification of landslide dataset and the selection of study areas according to the ground instabilities activity. The selected study areas are as follow:

Coastal areas. Two main zones have been chosen: 1) Peñas Cape environment which includes the Podes Peninsula and 2) Tazones Lighthouse landslide (Figure 54 A). In the area of Peñas Cape, 232 mass movements have been registered. 87 of them are classified as rockfalls, 33 as slides, 33 as flows, 4 are cracks and 75 are undetermined instabilities (Figure 54 B). In addition, the Tazones Lighthouse landslide and the Podes Peninsula (into the Peñas Cape environment) have been widely studied in the framework of the COSINES Project (Ref. CGL2017-83909-R). This project, developed between 2017 and 2021, consisted of quantitative and qualitative characterization of the Asturian coastal retreat (Mora *et al.*, 2018). Works as Jiménez-Sánchez *et al.* (2019), Cuervas-Mons *et al.* (2021c) and Domínguez-Cuesta *et al.* (2022a) were developed in the framework of this project. These studies have been focused mainly on the development of slope instabilities that causes coastal retreat, including: 1) Photointerpretation analysis; 2) The use of UAV; 3) Application of A-DInSAR techniques and 4) Field work including geomorphological mapping and topographic campaigns since June 2018. These field campaigns are continuing to date.

Mountain area. 457 mass movements have been registered on the mountain area between 1980 and 2019. 130 of them are classified as rockfalls, 54 as slides, 15 as flows, 10 are cracks, 16 subsidence/collapse and 232 are undetermined instabilities (Figure 55). In this area, SEDTRIGE project (Ref. FUO-19-128) was developed between 2019 and 2020. This project consisted of implementation and utilization of A-DInSAR techniques to develop an expert service for early detection and monitoring of geological risks. Works as Cuervas-Mons *et al.* (2021c, 2022a) were developed in the framework of this project.

Table 6. Landslides recorded in the BAPA database (Valenzuela *et al.*, 2017) in the Peñas Cape and Mountain areas between 1980-2019.

Registered landslides in BAPA (1980 - 2019)	Peñas Cape area	Mountain area
Rockfall	87	130
Slide	33	54
Flow	33	15
Crack	4	10
Subsidence	-	16
Undetermined event	75	232
Total	**232**	**457**

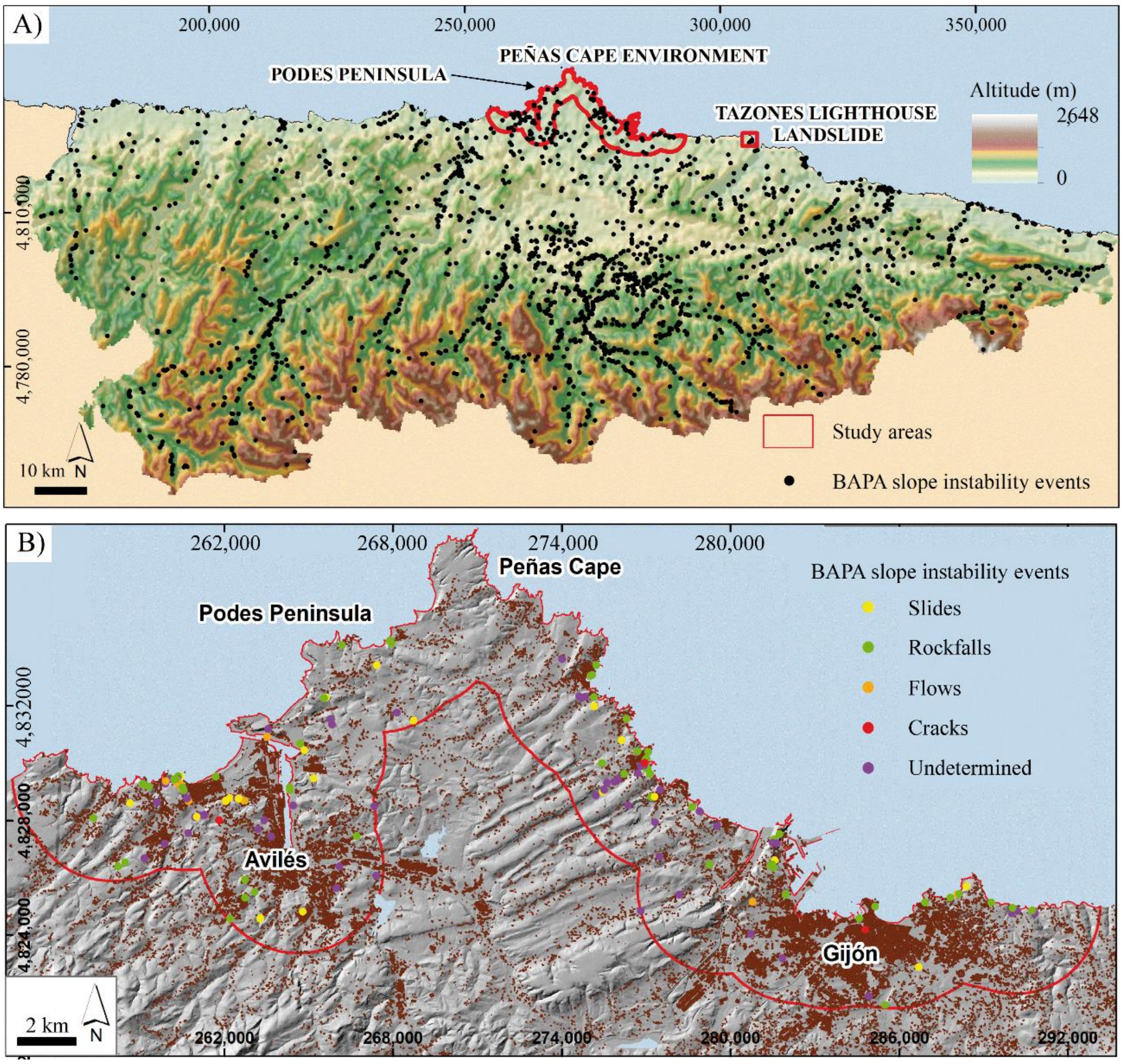

Figure 54. **A)** Location of the coastal study areas in Asturias. **B)** Detail of the Peñas Cape area showing the slope instabilities registered in the BAPA database.

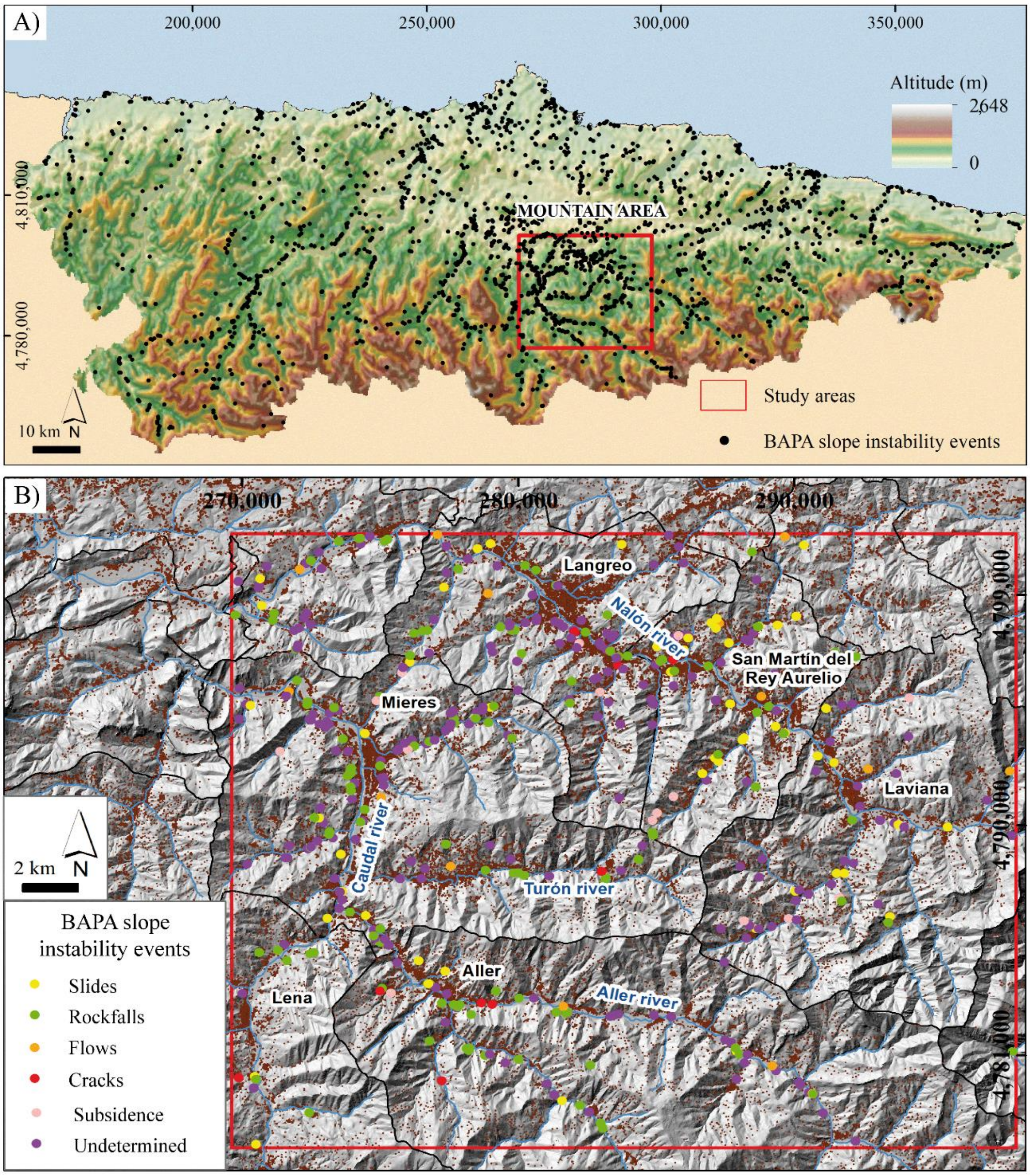

Figure 55. A) Location of the mountain study area in Asturias. **B)** Detail of the mountain area showing the slope instabilities registered in the BAPA database**.**

Finally, the last study area selected was the Lisbon Metropolitan Area (LMA), located in the Central-West of Portugal (Figure 56). The criteria of selection were: 1) An international stay made between September and December 2021 in the Instituto de Geografía y Ordenamento do Territorio (IGOT), in the framework of the partnership between the University of Oviedo and the University of Lisbon and 2) Well-known incidence of landslides and land subsidence in this region (e. g. Heleno *et al.*, 2011; Oliveira *et al.*, 2015; Pereira *et al.*, 2020) and other previous works. As to application of A-DInSAR techniques, Heleno *et al.* (2011) and Catalao *et al.* (2016) used ERS-1/2 and

Envisat ASAR dataset to study subsidence process in the Lisbon city from 1992 to 2006 and between 1995 and 2010, respectively. One the lastest studies is from Cuervas-Mons *et al.* (2022b), who carried out a detailed analysis of urban and industrial subsidence in the LMA using Sentinel-1A dataset between 2018 and 2020.

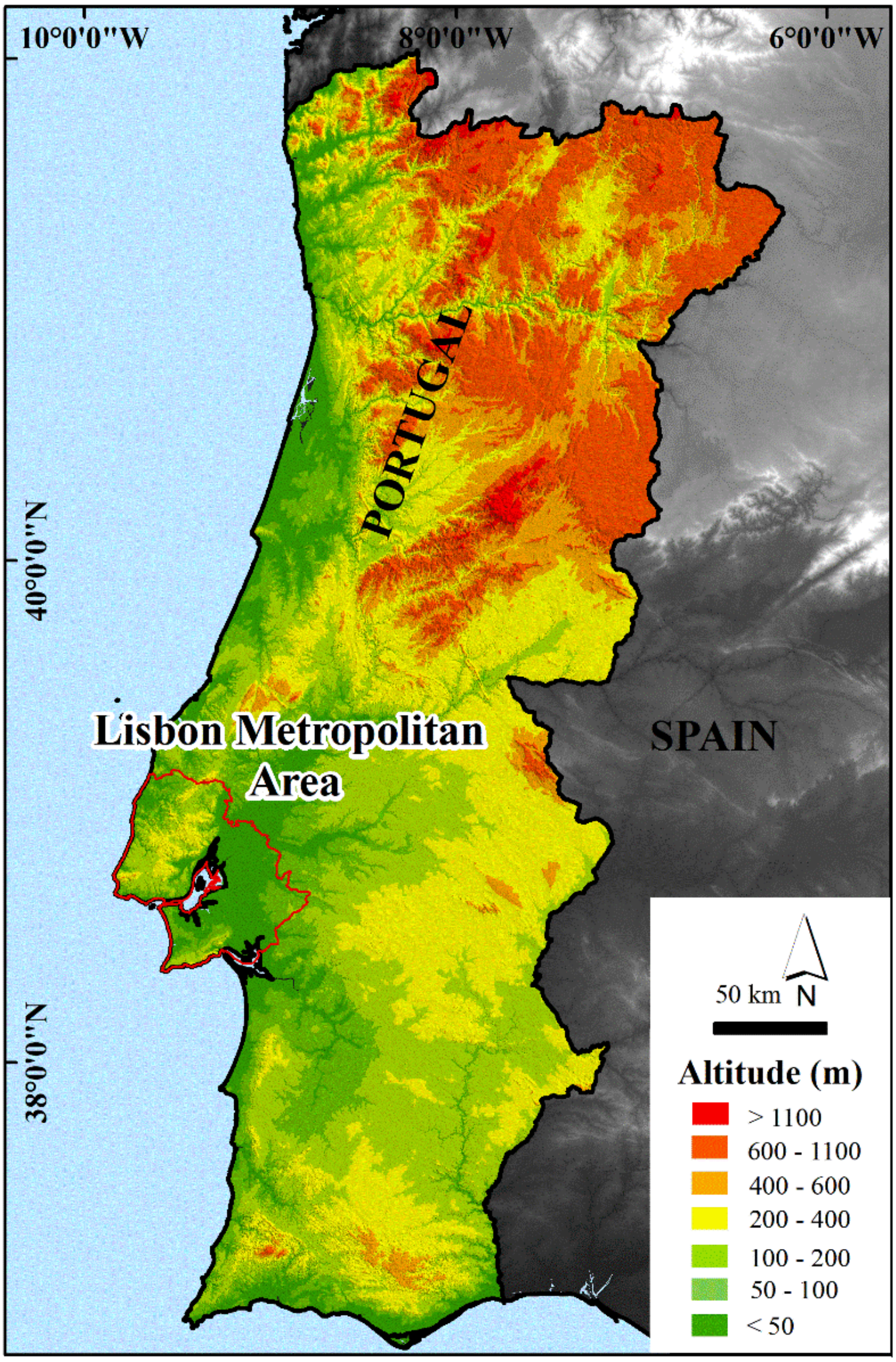

Figure 56. Red line indicates the location of the LMA study area in Portugal.

2.2 Description of the study areas

2.2.1 Peñas Cape environment

Settings

This first study area is located in North centre of Asturias (N Spain), on the coastal region of Peñas Cape environment (Figure 57). The area encompasses 185 km^2 and includes, from West to East, the councils of Castrillón, Avilés, Gozón, Carreño and Gijón. The total population was 393,008 in 2019 (INE, 2021). It is characterized by the presence of the urban areas of Avilés and Gijón (Figure 57), two of the three main cities of Asturias, with significant economic and industry activity and important port infrastructures. In addition, there are other smaller towns as Salinas, Luanco and Candás, whose main economic activities are tourism and fishing. The climate conditions present a characteristic Oceanic climate, with an average annual precipitation and temperature of 1,122 mm year^{-1} and 13.2 ºC, respectively (Avilés-Airport weather station) (AEMET, 2020).

From geomorphological point of view, the study area is characterized by a coastline pattern with inlets and promontories, with beaches that exceed rarely 1.5 km in length, and cliffs with slopes above 65º and high about and greater than 100 m (Domínguez-Cuesta *et al.*, 2019). The predominant relief along the coast is the rasa (Flor, 1983; Flor and Flor-Blanco 2014; López-Fernández *et al.*, 2020), which defines a characteristic flat relief, W-E direction with highs over 60 to 80 meters. It is composed by different deposits such as alluvial, peat, slope and beach deposits, with ages from Pliocene to Holocene (Flor *et al.*, 2006; Flor and Flor-Blanco, 2014). The estuary of Avilés, located at West of the area (Figure 57), is another important geomorphological element. Geomorphological activity is mainly associated to littoral and slope processes, in addition to developing of karst. These slope instabilities, registered on the BAPA database, consist mainly on rockfalls, although there are also some translational and rotational slides, flows and undetermined movements (Valenzuela *et al.* 2017) (Figure 54 B).

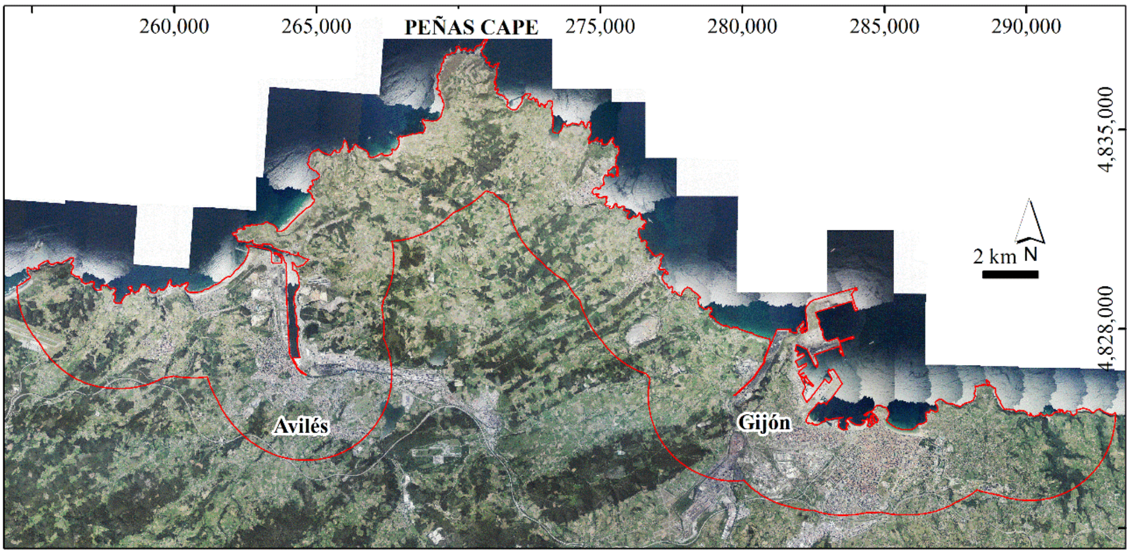

Figure 57. Peñas Cape environment area and main cities. OrtoPNOA 2017 CC-BY 4.0 scne.es.

Geology

The study area is mainly located in the Cantabrian Zone and the Permian-Mesozoic Basin (Julivert, 1976) (Figure 58 A). The bedrock mainly consists of an almost complete Paelozoic succession except Cambric (Figure 58 B). According to Truyols and Julivert (1976) and Arbizu *et al.* (1995), the Lower Paleozoic is predominantly constituted by siliciclastic rocks (quartzsandite, slate, and sandstone), having an Ordovicic volcanic level (volcanodetritic materials, basalt and cinerite) (Figure 58 B). The Upper Paleozoic includes alternations of carbonate and siliciclastics sections (dolostones, limestone, marl, sandstone, slate, shale, and quartzsandite) (Figure 58 B). The Permotriasic and Mesozoic materials are discordantly arranged on this Paleozoic basement (Arbizu *et al.* 1995) and affected by faults with little displacement. These units are constituted by siliciclastic and carbonate materials like slate, sandstone, conglomerate, limestone, dolostone and gypsum. The most recent materials are Quaternary in age and are composed by alluvial, estuary, beach and slope deposits (Figure 58 B).

Regarding to structures (Julivert *et al.*, 1973; Julivert, 1976), the Peñas Cape region is characterized by tectonic structures of deformation during the Variscan orogeny (Arbizu *et al.* 1995). There are major folds that are closed, inclined and vergent to the east. These folds are associated to minor chevron type folds. The folds are cut by reverse faults inclined to the west. The structures affecting the Mesozoic cover are reduced to some faults related to Alpine tectonics, whose maximum displacements can reach tens of metres (Arbizu *et al.* 1995). An oustanding structure in the Peñas Cape area is the Ventaniella Fault which is a quasi-vertical structure oriented NW-SE and 400 km long (López-Fernández *et al.*, 2020). It presents a moderate to low intensity seismicity along some parts of its trace (López-Fernández *et al.*, 2020; Fernández-Viejo *et al.*, 2021). The fault prolongation within the continental platform is represented by the Aviles canyon, one of the deepest submarine valleys in the Atlantic (López-Fernández *et al.*, 2020; Fernández-Viejo *et al.*, 2021).

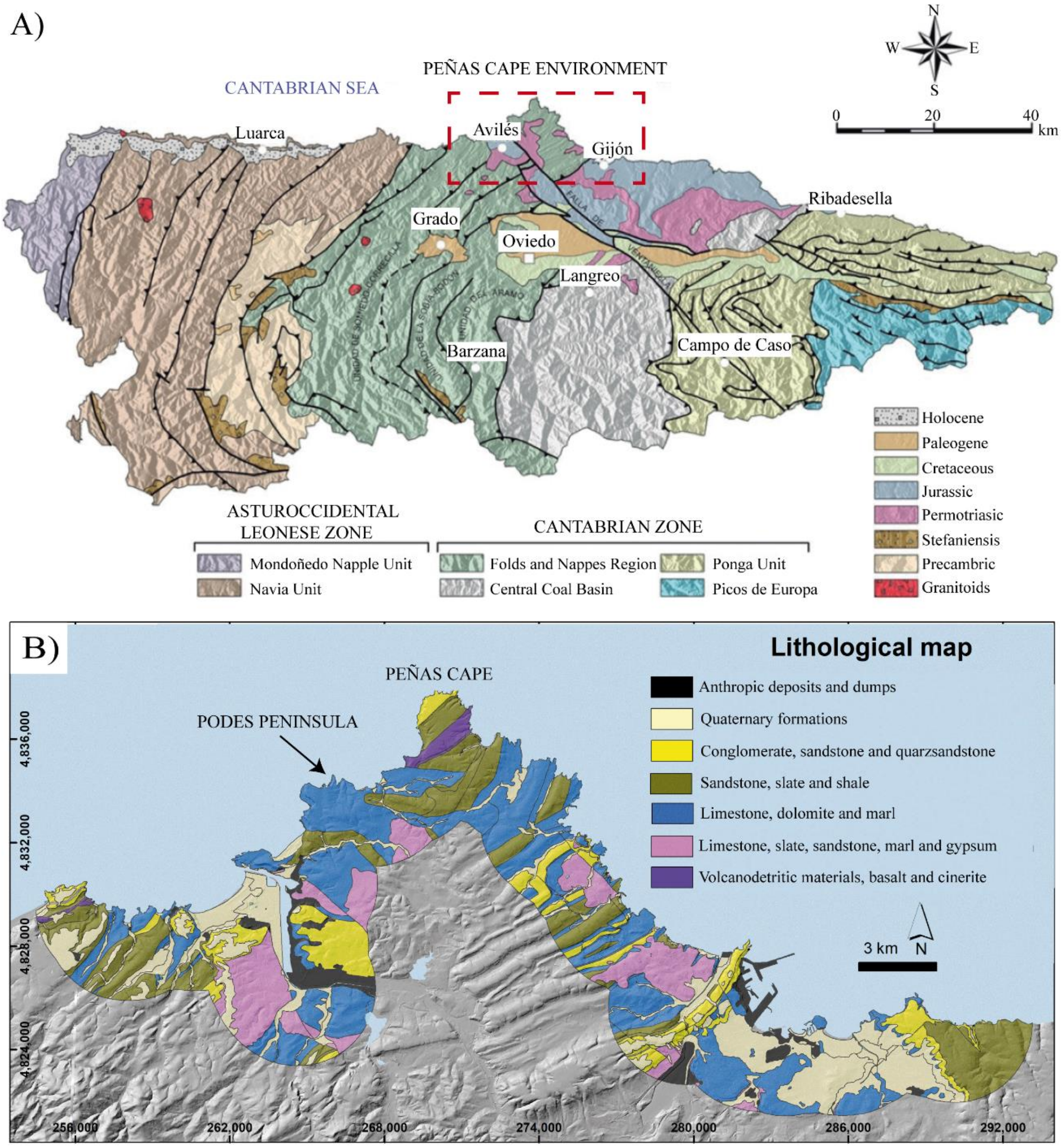

Figure 58. Geological map of Peñas Cape environment. **A)** Regional geological location; Taken and modified from Gutiérrez-Claverol and García-Ramos (2016). **B)** Lithological map of Peñas Cape environment modified from geological maps of Avilés and Gijón (IGME, 1972a, b). DEM with 5 x 5 m spatial resolution (IGN, 2020).

Local area: Podes Peninsula

This sector is located at Southwest of Peñas Cape (Figure 57, Figure 58 and Figure 59). It consists of a rocky peninsula with a N-S orientation called Punta`l Castiellu or Punta Llampero. It is characterized by an extension of 75,622 m^2 and is delimited by sea cliffs 15 - 25 m high, where waves and winds come from west and northwest (Jiménez-Sánchez and Ballesteros, 2017). The predominant relief of the Podes Peninsula is the rasa, whose altitude varies between 25 and 35 m a.s.l (Flor, 1983). This area is known for housing the archaeological site of El Castiellu de Podes or Castro Castiello. It is one of the 29 so-called Castros Marítimos of Asturias (Camino Mayor, 1995).

Figure 59. Panoramic view of the Podes Peninsula with Peñas Cape in the background.

From a geological point of view, Podes Peninsula is located into the Fold and Nappes Region, belonging to the Cantabrian Zone (Figure 58). The bedrock mainly consists of limestone, marl, lutite and sandstone of Devonian Nieva Formation (Figure 60 A) (Jiménez-Sánchez and Ballesteros, 2017). The rocky substrate is fractured by a set of faults and cracks of predominantly NW-SE, N-S and SW-NE orientation (Figure 60 A). From a geomorphological point of view, in the Podes Peninsula there are rock fall and topple deposits, complex movements and translational slides (Figure 60 B) (Jiménez-Sánchez and Ballesteros, 2017). Some of these deposits involve arqueological remains from the Castro Castiello (Jiménez-Sánchez and Ballesteros, 2017). Moreover, some depressions and residual karst can be observed in the rasa (Figure 60 B).

This local area was studied in the framework of the COSINES project between 2017 and 2021 with the main aim to characterize the coastal retreat. In this line, a total station surveying campaign has been conducted from June 2018 to the present day, with six months’ periodicity. The extension of the analyzed area using A-DInSAR techniques is 2.8 km^2.

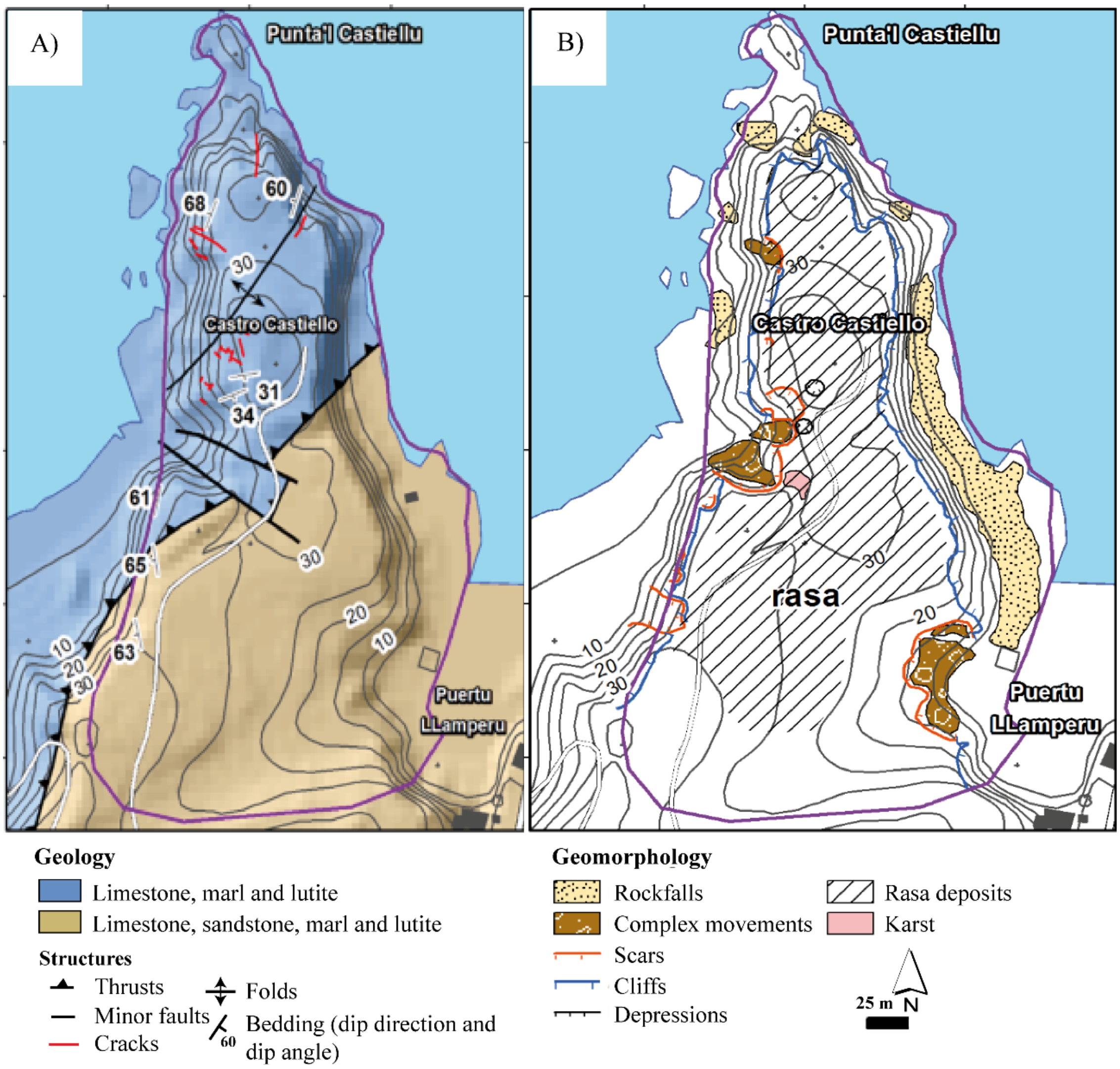

Figure 60. The Podes Peninsula. **A)** Geological map. **B)** Geomorphological map. Taken and modified from Jiménez-Sánchez and Ballesteros (2017) and Jiménez-Sánchez *et al.* (2019).

2.2.2 Tazones Lighthouse landslide

Settings

The study area of the Tazones Lighthouse landslide is located in the Villaviciosa Council, near Villar and Tazones villages (Figure 54 A and Figure 61 A). It includes a sector of 161,103 m^2. Within the studied area there were only two constructions: Tazones Lighthouse and a restaurant (Figure 61 B), currently in ruins as a result of the gravity process (Figure 61 C-E). There is a proliferation of vegetation that covers the entire study area, being able to recognize meadows and eucalyptus plantations, fundamentally, in addition to scrub areas (Domínguez-Cuesta *et al.*, 2022a). The area is highly frequented by tourists who come to see the lighthouse and to walk a section of the Asturian coastal path that runs through the surroundings, known as the Jet Route Trail (Ruta del Azabache). (Domínguez-Cuesta *et al.*, 2022a).

This area is being monthly monitored since June 2018 (in the framework of COSINES project), when irreversible structural damage appeared in a restaurant building in February 2018 (Figure 61 B) located in the surroundings of the lighthouse (Valenzuela *et al.*, 2019).

Geology

The bedrock is composed of Jurassic rocks, predominantly an alternation of marl and sandstone with some limestone layers intercalated. The bedrock is dipping 15-17 ºN. These materials, which constitute the Lastres Formation (Upper Jurassic) (Valuenzuela *et al.*, 1986; García-Ramos and Aramburu, 2010), are mainly composed of sandstone and appear in 1 - 10 m packs, alternating with 5 - 15 m of marl and lutite alternation layers of centimetric to decimetric thickness (Domínguez-Cuesta *et al.*, 2022a). There are some references to the existence of jet mining along the Jurassic rocks of Asturias. These exploitations consisted of the excavation of small galleries through the softest lithologies (Bahamonde *et al.*, 1986; Monte Carreño, 2004). Several jet mining works have been described in the surroundings of the Tazones Lighthouse area (Bahamonde *et al.*, 1986). The Quaternary coverage corresponds to patches of colluvium deposits whose depth does not exceed 2 m and by the presence of the rasa located at 115 m.a.s.l. (Domínguez-Cuesta *et al.*, 2022a).

Nowadays, the Tazones Landslide area is a mass movement that is affecting all slope and it is characterized by the development of ocassional gravity processes and deep cracks that appear at the surface (Figure 61 E). The extension of the mass movement is 70,000 m^2 approximately (Figure 61 A). These open cracks present rhomboid morphological patterns, corresponding to shear and stress fissures (Domínguez-Cuesta *et al.*, 2022a). These open cracks can reach 1,282 m in length and the incipients ones 359 m. Some scarps can present lengths of 266 m (Domínguez-Cuesta *et al.*, 2022a) (Figure 61 E).

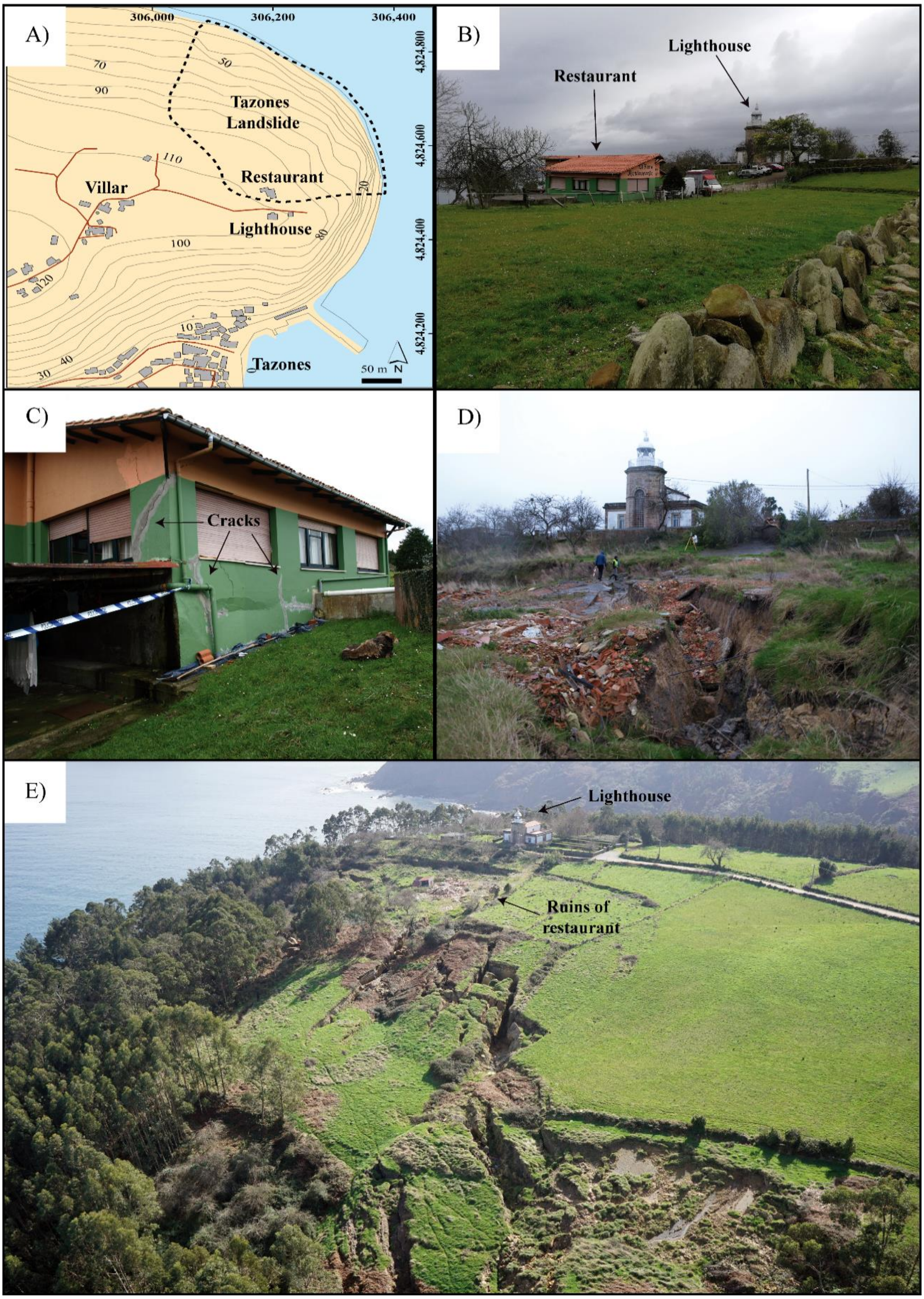

Figure 61. **A)** Location of the Tazones Lighthouse landslide near the villages of Villar and Tazones. **B)** View of the Tazones Lighthouse surroundings on February 20, 2018. **C)** Cracks and damage to the restaurant on the same date. **D)** Ruins of the restaurant on November 18, 2019. **E)** View of the Tazones Lighthouse landslide taken by a UAV on February 17, 2021.

2.2.3 Mountain Area of Asturias

Settings

This study area, located in Central South of Asturias (N Spain), has an extension of 682.57 km^2 (Figure 55). It is characterized by a humid climate, with an annual average precipitation and temperature of 960 mm and 13.3º, respectively (Meteorological Station of Oviedo; AEMET, 2020). The relief presents elevation ranges from 180 to 1,600 m. It presents a high anthropization of the environment, linked to an important mining activity related to the coal underground and open-pit exploitation and the development of significant urban areas as the Langreo and Mieres towns (population of 69,720 inhabitants) (INE, 2021). Other minor populations are Pola de Lena, Aller, San Martín del Rey Aurelio and Pola de Laviana councils (population of 49,813 inhabitants) (INE, 2021), developed along the valleys of Caudal, Aller and Nalón rivers (Figure 62).

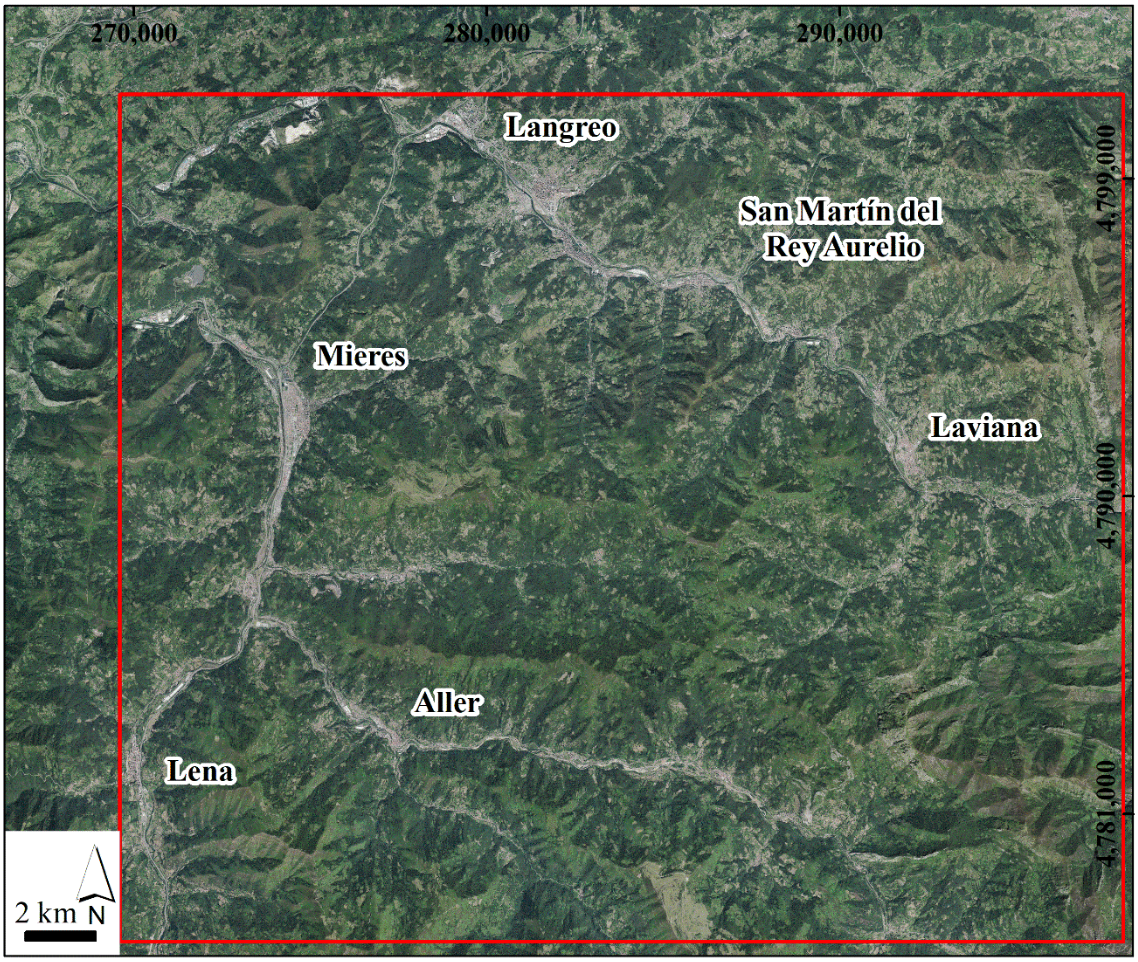

Figure 62. Mountain study area with main towns. OrtoPNOA 2017 4.0 CC-BY scne.es.

Geology

From the geological point of view (Figure 63 A), this region is mainly included in the Cantabrian Zone, specifically in the Central Coal Basin and, some parts, in the Folds and Nappes Region and Ponga Unit (García-Loygorri, 1971; Perez-Estaún *et al.*, 1988) (Figure 63 B). According to Salvador (1993), the bedrock is mainly composed by Devonian and Carboniferous succession of siliciclastic rocks (slate, sandstone, conglomerate and coal layers) and carbonate (limestone, dolostone and marl). The Carboniferous materials present a thinkness of 5,800 m approximately (Álvarez-Álvarez and Fernández-Álvarez, 2021). In the East of area, there are outcrops of Cambrian and Ordovician calcareous and siliciclastic rocks (Figure 63 B). As to quaternary formations, the predominant deposits are those related to gravity processes: colluvium, rock falls, rock avalanches, debris and flows can be found throughout the area (Domínguez-Cuesta, 2003; Valenzuela *et al.*, 2017) (Figure 62). Regarding alluvial deposits, there are alluvial terraces and plains developed by the fluvial activity of the Caudal, Nalón, Turón and Aller rivers (Figure 63 B).

The study area is located over a main structure that represents a large synform within which there is a complex fold and fault structure. This main structure corresponds to the Central Coal Basin. This basin shows an arc morphology with a NE-SW direction in the northern sector, gradually becoming gradually orienting N-S towards the central zone and NW-SE towards the south. There are two fold systems, one parallel to the Hercynian thrusts (longitudinal folds) and the other approximately perpendicular to them (transverse or radial folds) (Fuente Alonso and Sáenz de Santa María Benedet, 1999). On the other hand, there are two major faults following the orientation of the Hercynian thrusts: La Carrera and La Peña Faults (Fuente Alonso and Sáenz de Santa María Benedet, 1999). There are also tectonic structures related to a post-Hercynic extensional stage or to the Alpine event. To the West, forming the boundary of the Central Coal Basin and the Folds and Nappes Region, is the basal thrust of the Aramo Unit. To the East, the carboniferous and underlying materials ride over the Ponga Unit (Escama de Laviana) (Fuente Alonso and Sáenz de Santa María Benedet, 1999).

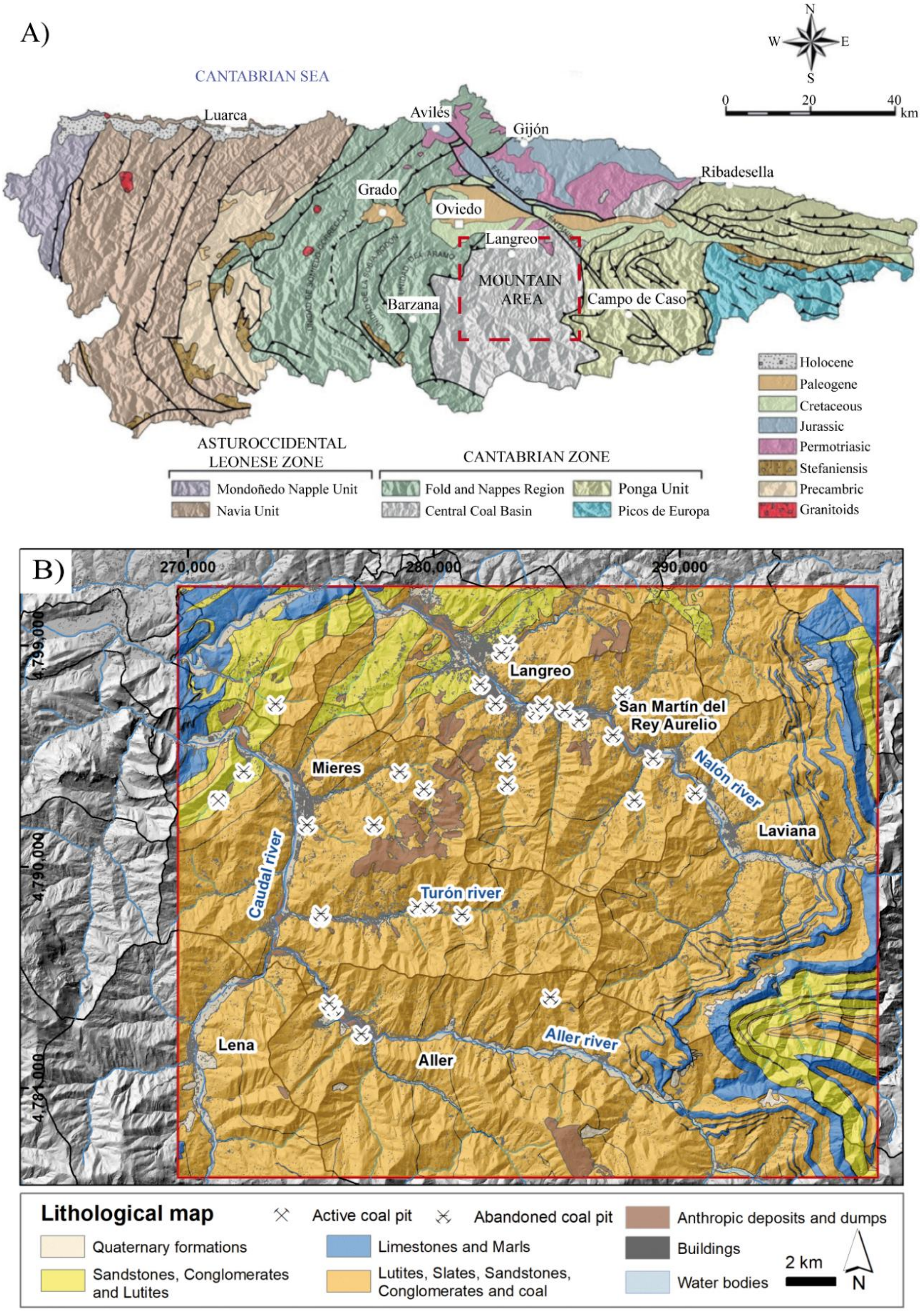

Figure 63. Geology of the mountain study area of Asturias. **A)** Regional geology of Asturias with mountain study area boxed in. **B)** Detail of the lithological map of the Asturian mountain area; taken and modified from Gutiérrez-Claverol and García-Ramos (2016) and Geological Map of Mieres 1:50,000 (IGME, 1973). DEM with spatial resolution of 5 x 5 m (IGN, 2020).

Coal mining activity

The Central Coal Basin (Figure 63 A) was the most important coal extraction area in Spain (Álvarez-Álvarez and Fernández-Álvarez, 2021), with an estimation of exploited coal of more than 420 MT. Nevertheless, nowadays the coal mining activity is ending. According to Martos de la Torre (2014), this coal mining activity was developed in four stages of exploitation: 1) An intense activity of mountain mining was developed (from the 19th century to the early 20th century), which exploited the coal layers accessing from surface outcrops (Figure 64 and Figure 65 A); 2) Vertical pits by private companies (early 20th century), being acquired by HUNOSA S.A in 1967. These pits were developed and exploited until late 20th century although some pits kept active until the first and second decade of the 21st century. These underground exploitations allowed the extraction of coal layers characterized by thickness of 1 - 2 m and slips between 45 - 90º, below valley levels (Table 7 and Figure 63 B, Figure 64 and Figure 65 B). Vertical pits reached average depths of 440 - 500 m and 8 to 13 plants below the phreatic level (Álvarez-Álvarez and Fernández-Álvarez, 2021) (Table 7). As the activity had been brought below the phreatic level, it involved the pumping of groundwater (Figure 64); 3) Development of open-pit mining (Figure 65 C), exploiting the coal located near the surface, involving a massive extraction of waste materials and the creation of dumps. At the same time, it was produced the abandonment of coal underground mining; and 4) Dismantling of these dumps together with the restoration and recovery of the environment and the landscape (Figure 65 D).

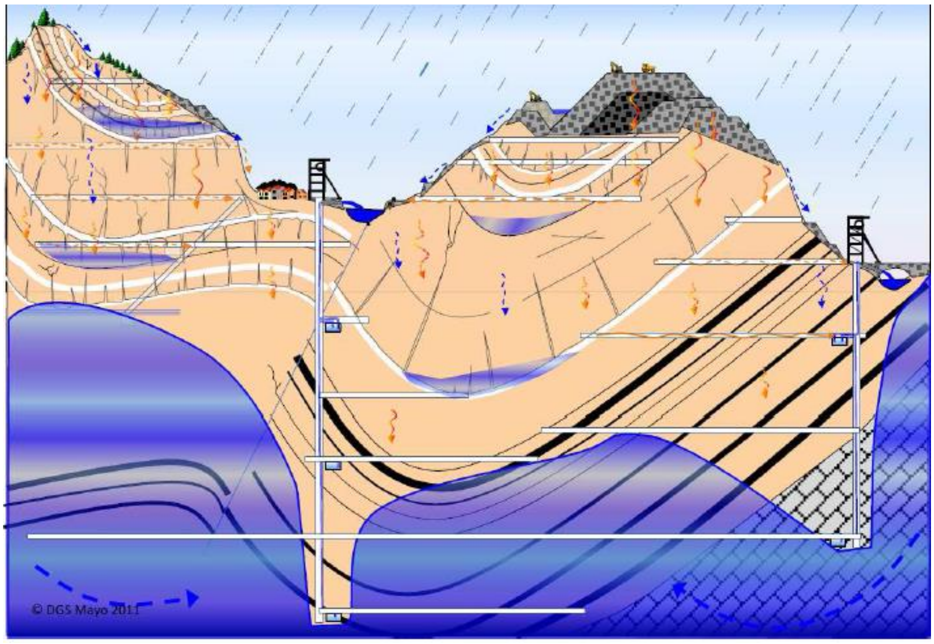

Figure 64. Squeme of mountain and vertical pit mining in the Central Coal Basin. The figure also shows water infiltration, water table and groundwater pumping. Taken from HUNOSA (2018).

Table 7. List of vertical pits of underground coal exploitations in the study area (Gutierrez-Claverol and Luque-Cabal, 1994). Data about geographical location, depth, location, river valley and floors are listed.

Vertical Pit	UTM X (m)	UTM Y (m)	Depth (m)	Location	Valley	N Floors
San José	273568	4796590	650	Olloniego	San Frechoso	10
Llamas	272270	4793856	270	Ablaña	Caudal	6
San Nicolás	271234	4792707	570	Ablaña		7
Barredo	274848	4791676	362	Barredo		5
San Vicente	275364	4787929	628	Figaredo	Turón	11
San Inocencio	275407	4788068	598	Figaredo		11
San José	277571	4791676	398	Turón		8
Santa Bárbara	279334	4788364	545	Turón		11
Espinos	279822	4788387	32	Turón		1
Fortuna (Rincón)	281149	4788044	30	Turón		1
Candín 1	282995	4799045	692	La Felguera	Nalón	13
Candín 2	282750	4798688	678	La Felguera		8
Fondón	281881	4797396	662	Langreo		8
Modesta	282527	4796612	590	Langreo		-
Carrio	290647	4792974	610	Laviana		9
Cerezal	288158	4792681	365	Santa Bárbara		9
Entrego	285916	4795938	573	El Entrego		9
María Luisa	284133	4796265	520	Ciaño		10
Samuño	282916	4794269	583	Puente Humeru		10
San Luis	282996	4793331	422	La Nueva		-
Sorriego	285330	4796338	288	El Entrego		5
Sotón	287283	4795339	558	El Entrego		10
San Vicente	284434	4796581	200	El Entrego		4
Venturo	287664	4796970	232	La Llave		4
Villar	288912	4794393	424	Sotrondio		6
Santiago	275911	4784205	532	Caborana	Aller	11
San Antonio	277051	4783183	547	Moreda		11
San Jorge	275749	4784429	150	Caborana		3
San Fernando	284752	4784670	253	Orillés		4
Polio I	279600	4793139	426	El Carbayón	San Juan	6
Polio II	279597	4793138	396	El Carbayón		5
Tres Amigos	278624	4793832	495	Vegadotos		10

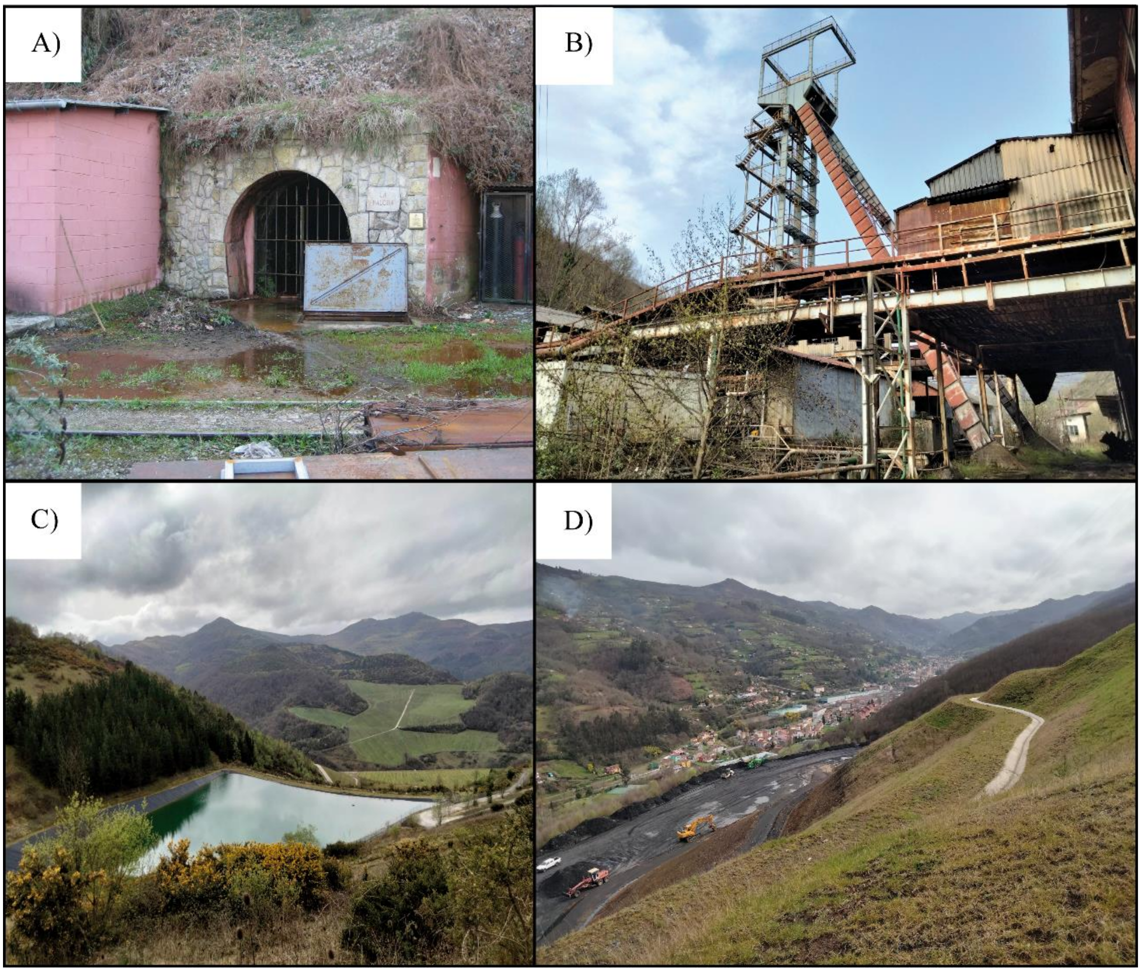

Figure 65. Different types of coal exploitations in the Central Coal Basin. **A)** Mountain mining of La Nalona in Sama de Langreo; Photo taken from Hunosa *et al.* (2011). **B)** Vertical pit of San Inocencio, near Figaredo village. **C)** Mining pool and restored landscape in a former open pit mining site; **D)** Dismantling of the Figaredo coal tip. Photos **B)**, **C)** and **D)** were taken on March 2022.

2.2.4 Lisbon Metropolitan Area

Settings

The Lisbon Metropolitan Area (LMA) is located in the Central West of Portugal and encompasses 4,378 km^2 (Figure 66). The LMA is composed by 18 urban and rural municipalities, with 2.8 million inhabitants. It is the largest urban agglomeration of Portugal, with about 27% of the Portuguese population (Rodrigues *et al.*, 2011). The principal urban cores of the area are the capital, Lisbon, and other cities such as Cascais, Estoril, Setúbal or Sesimbra (Figure 66). It presents a significant economic and industrial activity and relevant port infrastructures. The study area is characterized by an annual mean rainfall of 709 mm, with an annual precipitation average value from 500 mm in Lower Tagus to 1000 mm at the Sintra mountain (Leal *et al.*, 2020). As to elevation, the maximum altitude is over 528 m in the Sintra region and 667 m in Montejunto mountain, at North of study area (Vaz *et al.*, 2018) (Figure 66). The estuary of Tagus River, situated in the centre of the area, is an oustanding geomorphological element of the study area (with an extension of 320 km^2). It is the largest estuarine system in the Iberian Peninsula (Figure 66).

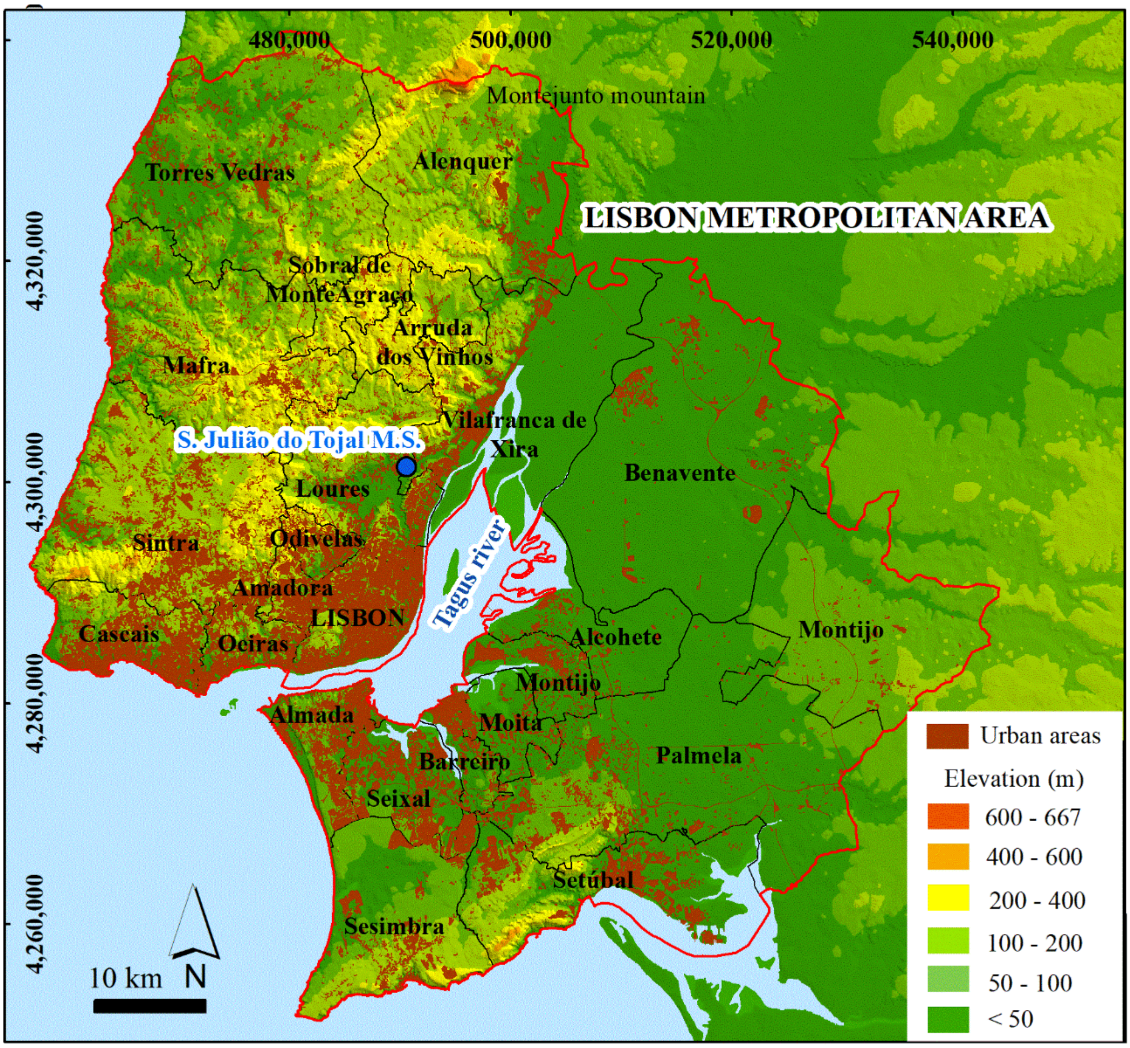

Figure 66. The Lisbon Metropolitan Area and their 18 municipalities. Moreover, location of the meteorological station used for subsidence analysis is shown. Taken and modified from Cuervas-Mons *et al.* (2022b).

The LMA is known due to geological hazards associated to seismic and tectonic activity (Carvalho *et al.* 2018; Oliveira *et al.*, 2020). Additionally, gravity processes and slope instabilities along the coast and the inland are common (Epifânio *et al.*, 2014; García *et al.*, 2016). Moreover, in this region flood episodes linked to intense rainfall periods, and producing damages estimated at millions of euros per year (Leal *et al.*, 2020). Other geohazards, like urban and industrial subsidence (Catalão *et al.*, 2016; Cuervas-

Mons *et al.*, 2022b) and groundwater vulnerability (Lobo Ferreira and Oliveira, 2004), have been demonstrated as important geohazards in the study area.

Geology

From a geological viewpoint (Figure 67), and according to Cabral *et al.* (2003) and Carvalho *et al.* (2005), the LMA is located in the Lower Tagus Cenozoic basin, which is characterized by Paleogene and younger deposits, and in the Lusitanian basin, which is composed by Mesozoic rocks. The bedrock mainly consists of sedimentary rocks, such as sandstone, conglomerate, claystone and carbonate, with ages comprehended between the Jurassic and Pliocene (Figure 67). As to extrusive and intrusive rocks presented in the LMA are Cretaceous age, and are located in the centre and centre west of the study area. In the case of volcanic rocks, these are defined by breccia, basalt and for the volcano-sedimentary complex of Lisbon (Figure 67). The intrusive materials consist of gabbro, granite, sienite, among other. Finally, the most modern materials are Quaternary deposits, composed of fluvial terrace Pleistocene sediments (sands and clays with pebbles) and alluvial Holocene sediments deposited by Tagus River (Carvalho *et al.*, 2018) (Figure 67). The LMA is composed by two main hydrological systems: Tagus - Sado basin and Western Meso - Cenozoic Basin. These systems define detrital and carbonate aquifers (Teixieira *et al.*, 2019).

The Lusitanian basin is affected by several Variscan faults, whose main directions are W-E, SW-NE and N-S (Carvalho *et al.*, 2005). The Lower Tagus Cenozoic Basin and the Lusitanian Basin are separated by some fault systems with N-S, NNE-SSE and SW-NE predominantly directions. These systems are the Setúbal-Pinhal Novo Fault, the Ota Fault, the monoclonal-fault system of Vila Franca de Xira-Lisboa and the Arrábida Fault (Carvalho *et al.*, 2005).

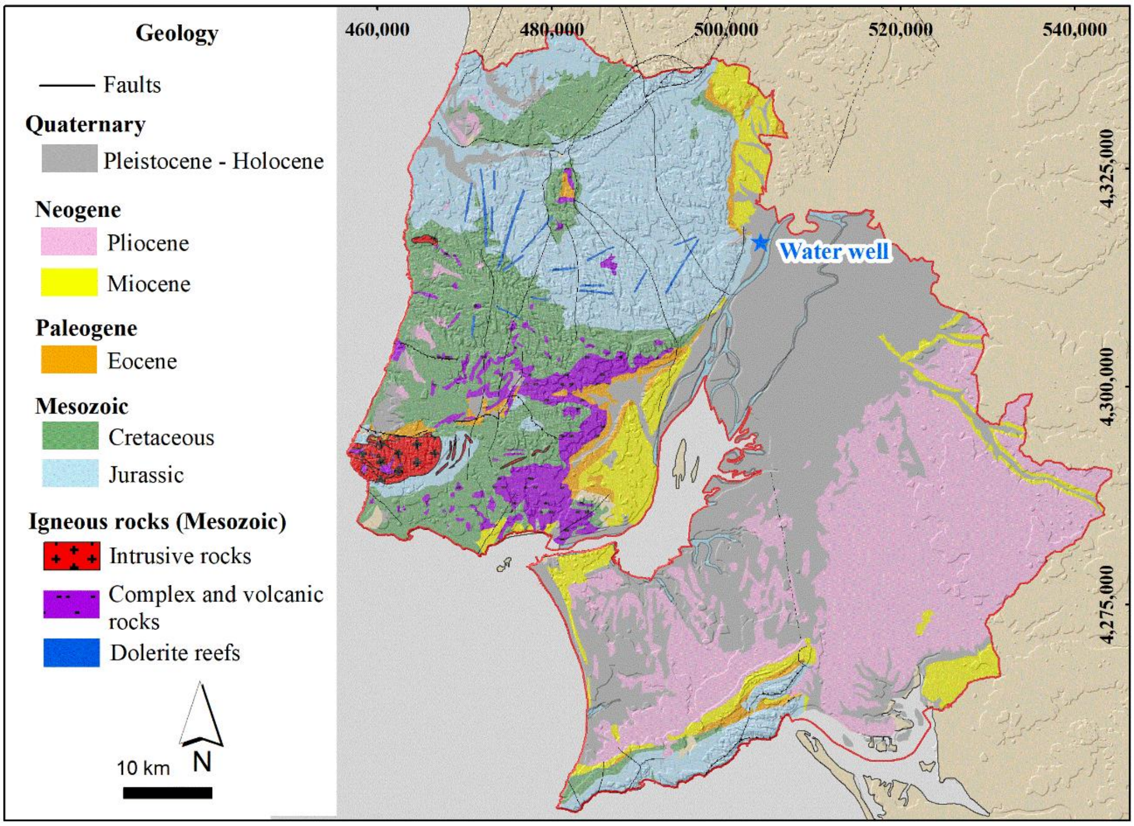

Figure 67. Geology of the Lisbon Metropolitan Area at scale 1:500,000 (LNEG, 1992) and location of the water well used in the analysis of subsidence. Taken and modified from Cuervas-Mons *et al.* (2022b).

2.3 Objectives

The main aim of this work is to apply A-DInSAR techniques to the detection, modeling and monitoring of the terrain movements associated with slope instability and subsidence phenomena in three areas of the Asturias region (Spain) and in the Lisbon Metropolitan Area (Portugal). The specific objectives are the following:

- ✓ To process, present and interpret the LOS mean velocity maps (mm year^{-1}) and deformation time series (mm) linked to slope instabilities and subsidence processes in Asturias and in the Lisbon Metropolitan Area.

- ✓ To compare results of ground movements obtained with the PSIG and P-SBAS techniques with each other and with traditional auscultation techniques.

- ✓ To establish the origin of the detected slope instabilities and subsidence processes in Asturias and in the Lisbon Metropolitan Area.

- ✓ To analyze the potential of A-DInSAR techniques to asses slope instabilities and subsidence in Asturias and in the Lisbon Metropolitan Area.

3. METHODOLOGY

The methodology carried out in this research has involved the following stacks (Figure 68): 1) A-DInSAR processing by means of the PSIG approach and the P-SBAS technique implemented in the ESA´s GEP service: obtaining of the LOS mean deformation velocity maps (mm year^{-1}) and deformation time series (mm); 2) Application of A-DInSAR post-processing by using ADA (Active Deformation Areas) procedure and Vertical-Horizontal components decomposition and 3) Geographical Information System (GIS) integration and interpretation of results.

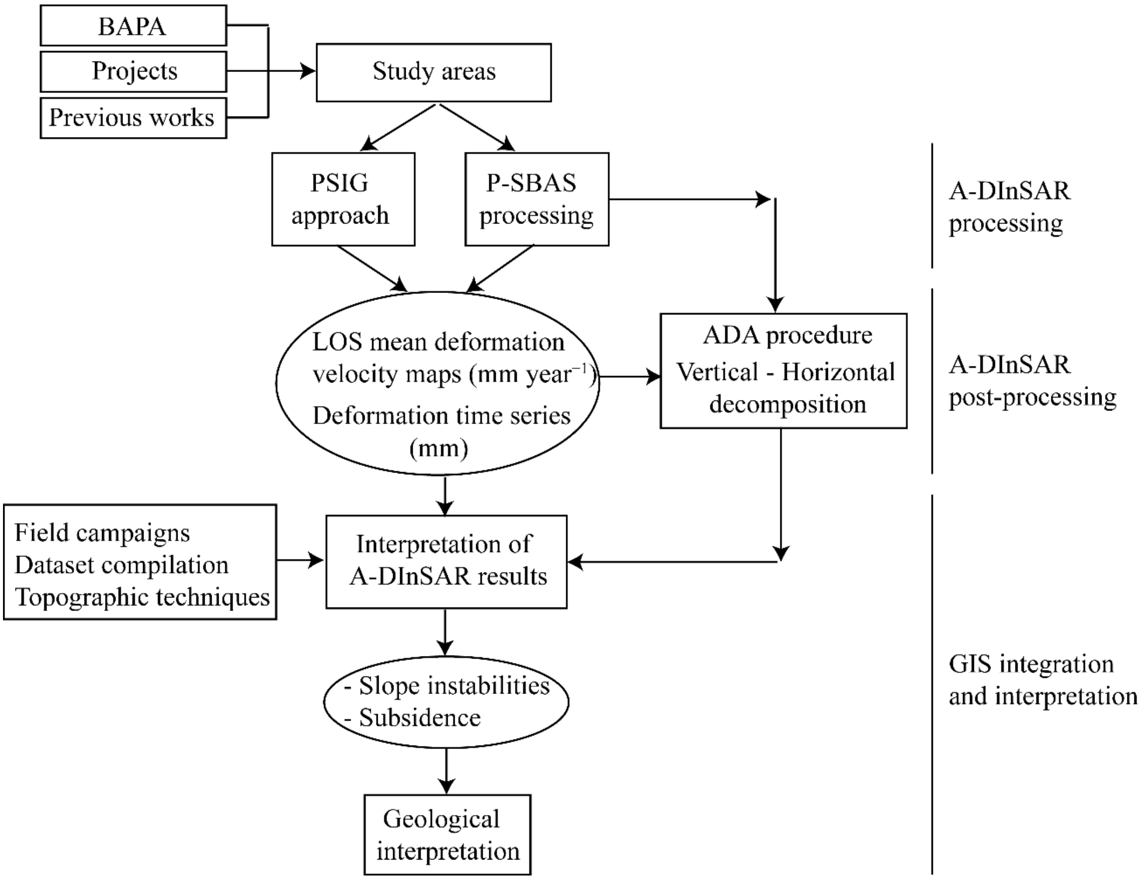

Figure 68. Flow diagram of the methodology applied in this research.

3.1 A-DInSAR processing

3.1.1 PSIG approach

The PSIG is a commercial A-DInSAR software that was developed by Geomatics Division of CTTC. It is based on the method of Persistent Scatterer Interferometry designed by Biescas *et al.* (2007) and Devanthéry *et al.* (2014; 2019). This approach uses a powerful set of Sentinel-1A/B IW SLC SAR images and a large network of interferograms, with the main aim of obtaining LOS Mean Deformation Velocity Maps (mm year^{-1}) and Deformation Time Series (mm) over a regional and local study areas. The motions detected can be related to mass movements, subsidence phenomena among other processes. This A-DInSAR chain is described in detail by Biescas *et al.* (2007), Devanthéry *et al.* (2014, 2019) and the user manual of PSIG software is provided by Barra *et al.* (2019). Other authors who have successfully applied the PSIG approach in landslide and subsidence phenomena are Fernández-Oliveras *et al.* (2009), Notti *et al.* (2015), Barra *et al.* (2016), Barra *et al.* (2017), Reyes-Carmona *et al.* (2020), Cuervas-Mons *et al.* (2021c) and Palamà *et al*. (2022).

The PSIG chain is composed by the following processing steps (Figure 69): 1) Co-registration of SAR downloaded images and generation of wrapped interferograms; 2) Estimation of residual topographic errors and LOS linear velocity by means of Vellin algorithm; 3) Assessment of deformation time series by means of Int2ima algorithm; 4) Estimation and filtering of atmospheric component; 5) Geocoding of A-DInSAR results and exportation them to a GIS. Below, all the steps of this approach are described in detail.

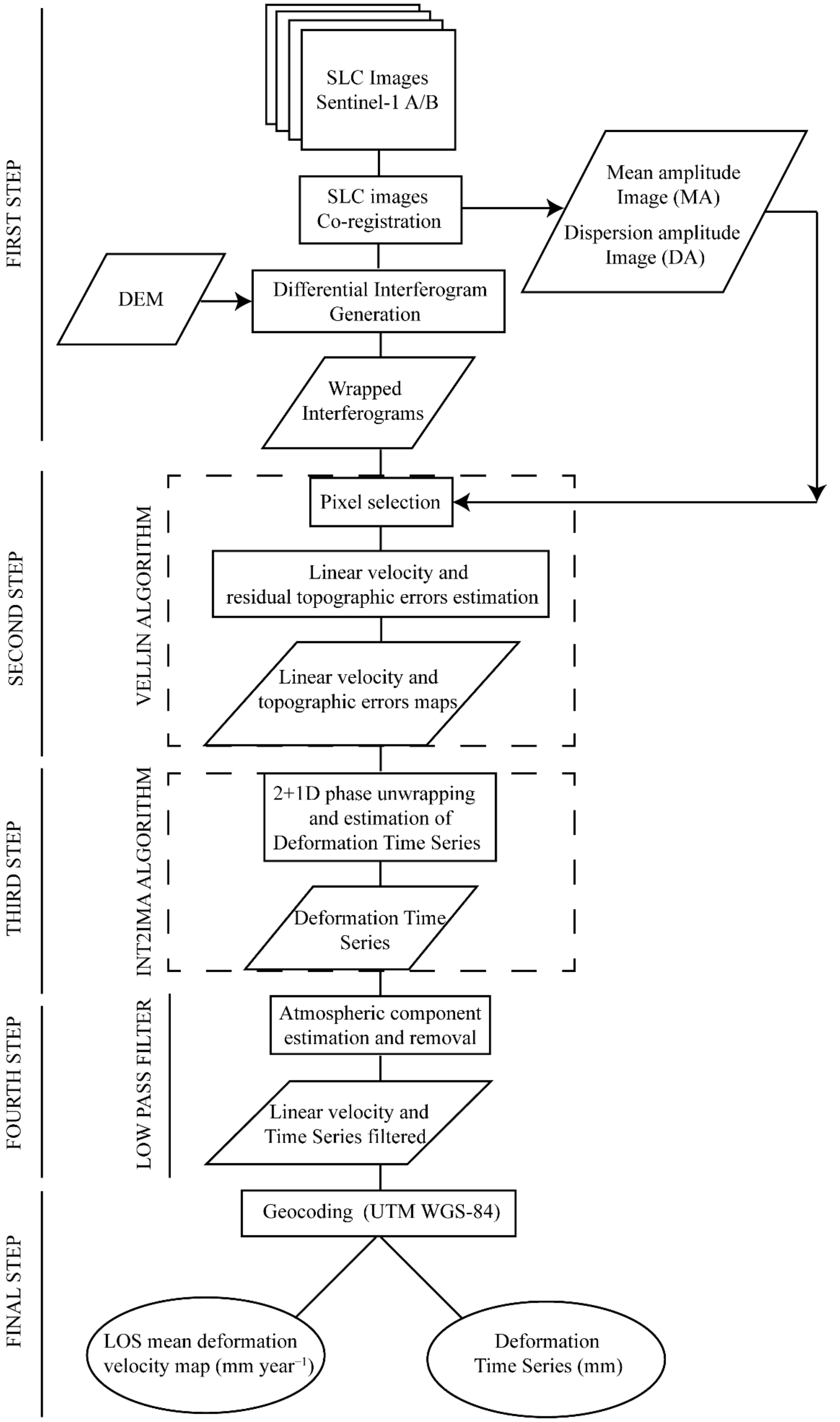

Figure 69. Simplified diagram of the PSIG chain, showing the main followed steps.

Download of Sentinel-1 SAR images

Previously to start the PSIG chain and A-DInSAR processing, a set of SAR images were downloaded by using ASF Data Search Vertex (ASF, 2022) and Copernicus Open Access Hub (ESA, 2022a). The search criteria and filters used in these servers were: 1) Satellite constellation; 2) AoI polygon; 3) Start and end date of monitoring period and 4) Polarization, track and orbit direction (Table 8).

Then, downloaded SAR data for the Sentinel-1A-DInSAR processing consisted of 113 IW SLC SAR images acquired by Sentinel-1A/B satellites in C-Band (5.5 cm wavelength) in the period of January 2018 until February 2020 (Table 8 and Appendix I). The track was 154 in descending orbit (Figure 70).

Table 8. Main acquisition parameters of the Sentinel-1A/B satellites and main characteristics of SAR images downloaded and used in this work.

Satellite	**Sentinel-1**
Sensor	A/B
Band	C
Wavelength	5.55 cm
Acquisition mode	Interferometric Wide
Polarization	VV
SAR product	SLC
Revisit period	6 - 12 days
Resolution	14 x 4 m
Incidence angle range	32.9º - 43.1º
SAR images downloaded	113
Track	154
Trajectory	Descending

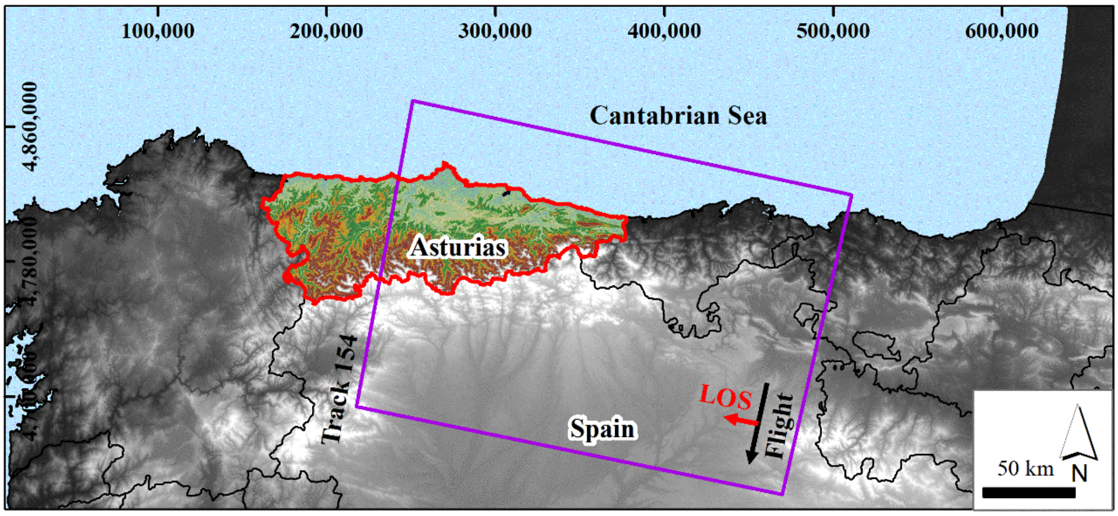

Figure 70. Track 154 in descending trajectory processed by means of PSIG chain.

SAR images co-registration and interferogram generation

In this first stage, the 113 IW SLC SAR images downloaded are used. Firstly, bursts and swaths corresponding to specific study area are designated. In this line, the swath number 03 and burst 02, 03, 04 and 05 were extracted and processed (Table 9). Later, co-registration process is done, consisting of transforming all the images into the same geometry pixel by pixel according to a reference image denominated SuperMaster (SM, Table 9), which usually is the oldest image; the rest of images are called slaves. In this case, the date of the selected SM was: August, 8 2018. Previously to the co-registration of SAR images, it is necessary to make a geometric calibration of SM. This geometric calibration is used for the topographic removal in the wrapped interferograms generated. In this line, a DEM Product SRTM 90m Version 4 (Jarvis *et al.*, 2008) whose data file is srtm_35_04, was downloaded from CGIAR-CSI (2020) and used (Table 9).

The co-registration of images is performed pair by pair: each slave image with the SM. Afterward, wrapped interferograms are produced (Figure 71), including the removal of the topographic component by means of the previous geometrical calibration. During this processing, 934 wrapped interferograms were generated, with temporal baselines between 6 and 756 days (Table 9).

Table 9. Main characteristics and parameters used during SAR images co-registration and interferogram generation.

Parameter	**Value**
SAR images used	113
SuperMaster	23151 (August 8, 2018)
Swath extracted	03
Burst extracted	02 - 03 - 04 - 05
DEM used	SRTM 90m (srtm_35_04)
Interferograms generated	934
Temporal baseline (days)	6 - 756
Maximum Baseline (days)	800

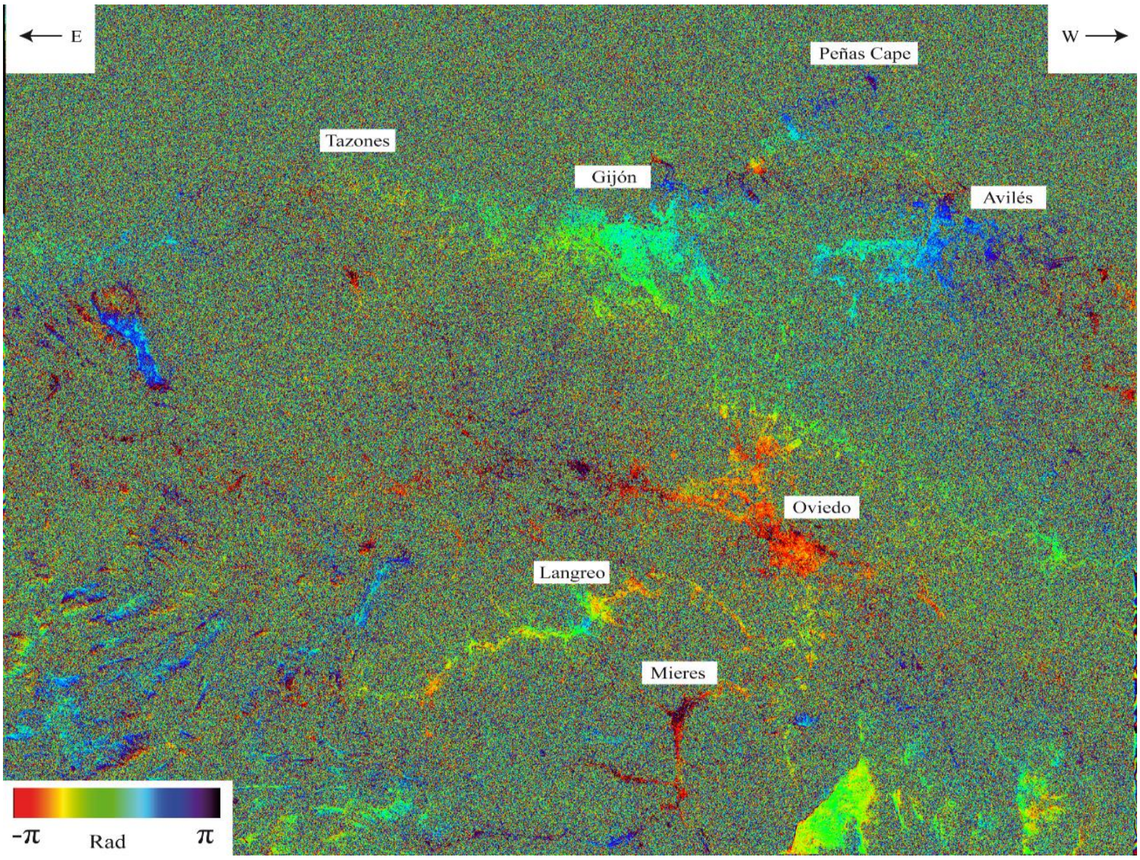

Figure 71. Multilooked 2 x 10 wrapped interferogram of Central Asturias. This interferogram was generated by SAR images of October 25, 2018 and March 30, 2019 (temporal baseline of 156 days).

As mentioned in the Introduction section (subsection 1.3.2), the generated wrapped interferograms contain information of phase components, which includes data of topography, terrain deformation, atmospheric contribution and errors related to orbital artifacts. This information is comprehended between -π and π, which is called wrapped phase and is shown by a color pallet whose full path correspond to full rotation 2π or 360º (Figure 71).

Finally, an image of the mean amplitude (MA) and an image of the dispersion of amplitude (DA) are created by means of all co-registered images. According to Barra *et al.* (2019), each pixel of MA represents the mean value of all amplitude values (Figure 72). In the case of DA, each pixel represents the dispersion of the amplitude values of the same pixel. This step is very important and necessary for point selection (Vellin step), because a low value of DA (and therefore, a high value of amplitude) indicates the presence of PS (Ferreti *et al.*, 2001).

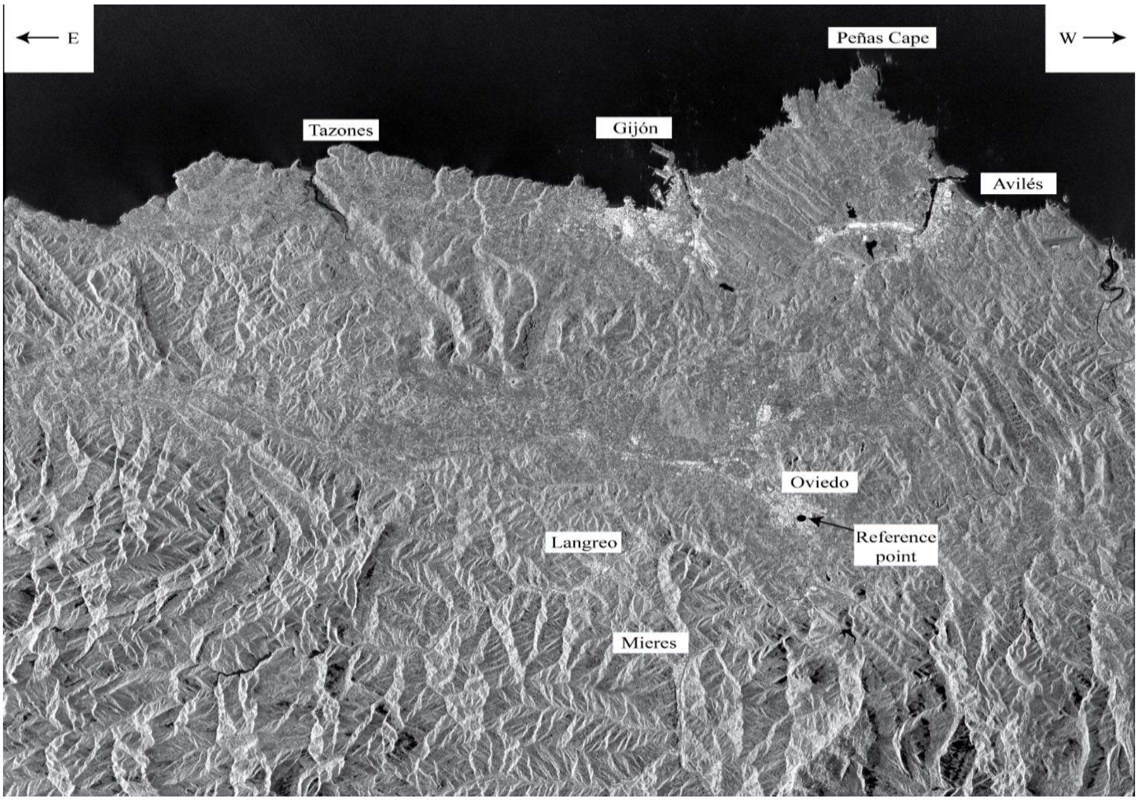

Figure 72. Mean Amplitude image (MA) of Central Asturias generated from all processed SAR images. The image is resized, with a dimension of 2,574 x 2,106 pixels. The dark areas have very low amplitude values, while the bright areas have very high amplitude values.

Estimation of linear velocity and residual topographic errors

This step consists of the application of the Vellin algorithm for calculating the linear mean velocity (velo), residual topographic errors (etopo) and, optionally, the thermal expansion over selected pixels from the stack of wrapped interferograms. This algorithm, which is based on the work of Mora *et al.* (2003), is composed by four different steps: 1) Pixel selection; 2) Etopo-velo calculation; 3) Reordering and 4) Integration.

The **pixel selection** is carried out according to amplitude stability (Ferreti *et al.*, 2000; Ferreti *et al.*, 2001), given by a maximum admissible in the DA (commonly Thr DA is 0.5). High values of MA imply a good quality of pixels (differential phases with low noise), so that bad pixels are discarded. Then, PS candidades are outputted in a vector format file for each interferogram and generating an irregular set of pixels. In addition, the PSIG approach allows another pixel selection criterion to be spatial coherence (Mora *et al.*, 2003).

The **etopo-velo calculation** starts with the connection of the pixels by edges network (Figure 73). According to Barra *et al.* (2019), these edges should be as short as possible in order to minimize the atmospheric effects in the phase component. On the other hand, an edge distance and minimum number of edges must be defined, guaranteeing that the velocity and topographic error values in each pixel are estimated in redundancy and not respond to a single measure (Fernández-Oliveras, 2009). The values of edge distance and minimum number of edges were 200 and 2000, respectively (Table 10). Then, velocity and topographic errors are estimated and computed over each edge by using N differential wrapped phases of each wrapped interferogram and according to these temporal baseline (Figure 73 and Equation (3)) (Barra *et al.*, 2019). To estimate of linear mean velocity, temporal baseline higher than 150 days are used. On the contrary, the topographic errors are estimated with baselines from 6 to 60 days (Table 10). In this way, a total of 533 interferograms were processed.

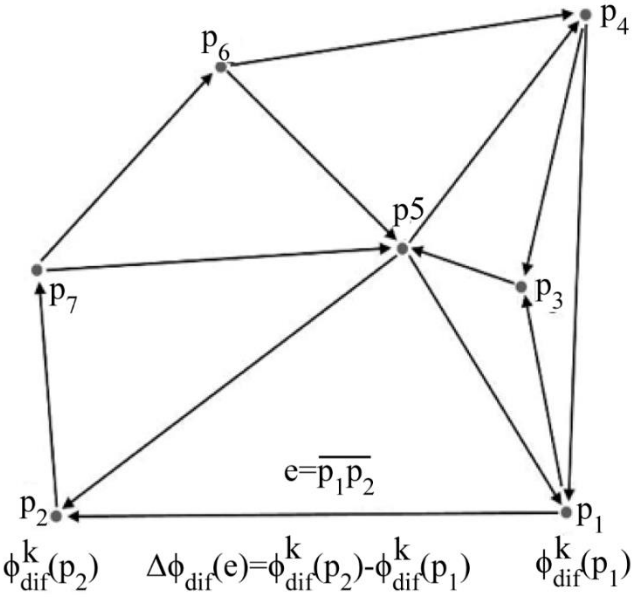

Figure 73. Pixels (p) connection by edges. The differential wrapped phase value ($\Delta\phi^{k}_{dif}$) over each edge (e) is calculated by means of the wrapped phase values ($\phi^{k}_{dif}(p)$). Each edge has one differential phase value for each of the N Interferograms (k). Taken and modified from Biescas *et al.* (2007).

$$\Delta\varepsilon^{k}(e) = \Delta\phi^{k}_{obs}(e) - \Delta\phi^{k}_{m}\big(\Delta v(e), \Delta te(e)\big) \qquad (3)$$

Where $\Delta\phi^{k}_{obs}(e)$ is the differential wrapped phase of edge e_i and interferogram k and $\Delta\phi^{k}_{m}\big(\Delta v(e), \Delta te(e)\big)$ is the modelled differential phase, $\Delta v(e)$ and $\Delta te(e)$ are the unknowns associated to the edge (e) (Barra *et al.*, 2019).

In the **reordening** step, the edges networks are created. Each edge has got a gamma function that denotes its statistical quality refered to differential velocity, topographic errors and thermal expansion. High values of gamma (commonly 0.5 or 0.6) allow to carry out an adequate and reliable reordering. This principal output is the map of groups

(Figure 74), where different connected network of pixels are shown. Each group of pixels have to integrate separately. In this case, two groups of points were obtained. The group 1 was composed by 1,130,159 PS (in red), while group 2 was defined by 84,511 PS (in green) (Figure 74). During this processing only the group 1 was integred (Table 10).

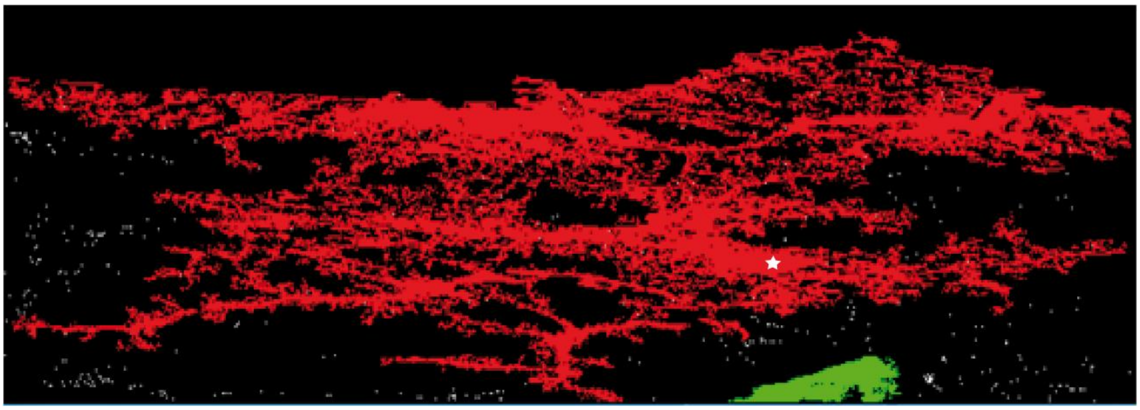

Figure 74. Map of groups in Central Asturias. Group 1 (red): 1,130,159 PS detected. Group 2 (green): 84,511. The white star indicates the location of the selected stable - reference point.

Finally, during the **integration** step**,** the reconstruction of the estimated linear velocity and the topographic error is done from differential velocity and topographic errors, by means of least square adjustment. A significant condition of this step is the establishment of the stable or reference point, which has to a very low DA or very high value of MA (Figure 72) and should be into the group of pixels integrated. This point is usually located by the user in urban areas. In this processing, the selected reference point was located in the city of Oviedo (Figure 72, Figure 74 and Table 10). The main outputs are linear mean velocity (mm year^{-1}) and topographic error (m), whose values are relative to the selected reference point.

Table 10. Main settings and parameters used in the Vellin algorithm.

Step	Parameter	Value
Pixel selection	DA thr	0.5
Etopo-velo calculation	Edge distance	200
	Minimum of edges	2000
	Linear velocity (baseline thr; days)	≥ 150
	Topographic error (baseline thr; days)	≤ 60
	Interferograms processed	533
Reordening	Gamma	0.5
Integration	Group of points integred	1,130,159 PS (Group 1)
	Reference point	−5.862760/43.364576

Deformation Time Series estimation

During this stage, Deformation Time Series are estimated by means of Int2Ima algorithm, which is based on the works of Costantini (1998) and Costantini *et al.* (1999). This processing chain is also called 2+1D phase unwrapping, which has been fully described by Monserrat *et al.* (2009), Devanthéry *et al.* (2014) and Devánthery *et al.* (2019).

The first part of this processing consists of the spatial phase unwrapping of each interferogram of the data stack and over the selected set of PS; It is called 2D because it is performed along azimuth and range space (Monserrat *et al.*, 2009). This step concerns only selected pixels, because these are characterized by low phase noise. However, during this processing it can be developed different critical errors related to phase noise, high deformation rates and/or isolated pixels (big distance between neighbouring pixels) and lonely SAR images (big temporal baseline between processed images). Afterward, the 1D phase unwrapping along time is carried out. This step estimates the phase value of each processed image pixel for pixel, identifying and correcting the errors generated during previous step. According to Monserrat *et al.* (2009), the output of this step is a set of deformation time series (Figure 75), which contain an estimated deformation in correspondence to the date of each processed SAR image (Devánthery *et al.*, 2019). Each phase contains both atmosphere components and orbital errors (Figure 75).

Along the whole 2+1D unwrapping processing there are two main parameters that control the entire procedure (Monserrat *et al.*, 2009). The first one is the residual R associated with the observations (difference between the interferometric phases or observations and the estimated value of these phases); the second one corresponds to redundancy parameter of the interferogram network and of the images processed. This indicator refers to the number of interferograms in which each processed image is found (Monserrat *et al.*, 2009).

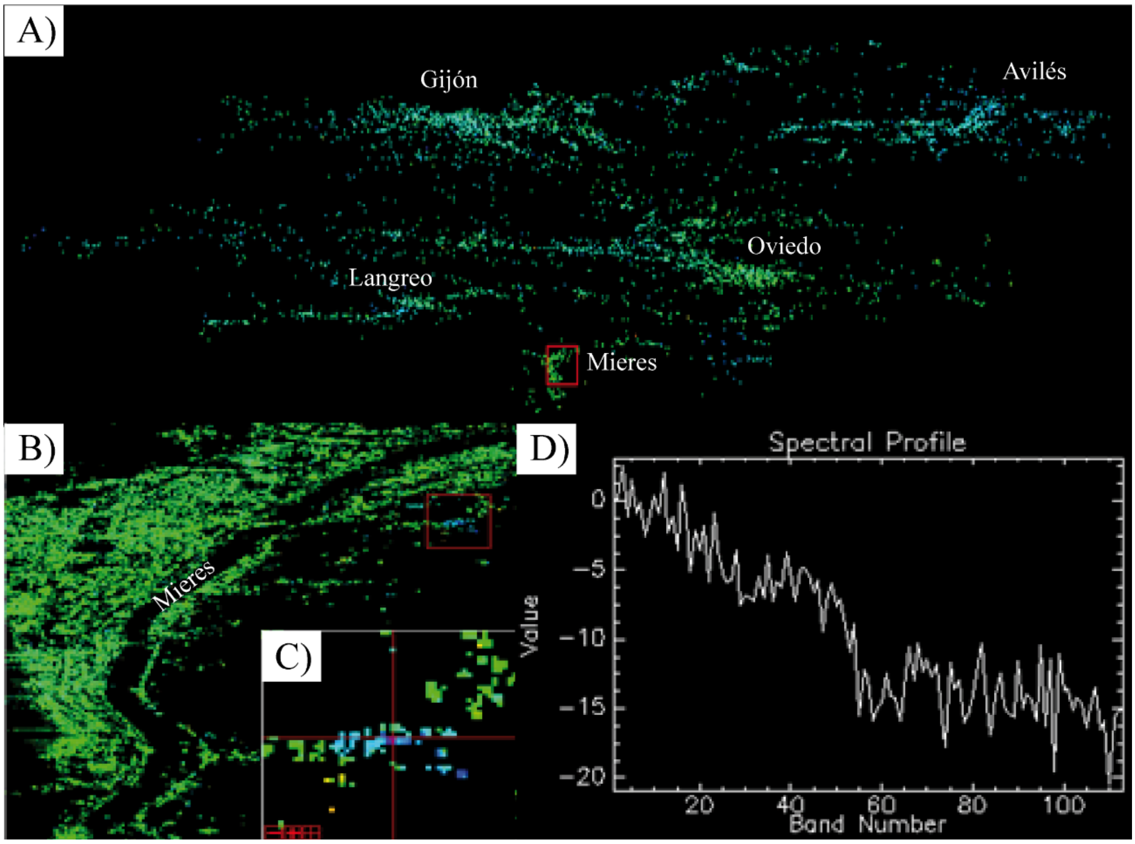

Figure 75. Example of a deformation detected during Int2Ima step. **A)** PS processed from Group 1 of map of group. **B)** and **C)** Deformation measured in a village west of Mieres town and PS selection to show the deformation time series. **D)** Observed time series. X-axis: Number of SAR scenes. Y-axis: Accumulated displacement in mm.

Atmospheric component estimation and filtering

In this step the low frequency component associated to large spatial correlation phenomena is estimated by means of a LP Filter. This filter separates the atmospheric components of the temporally correlated components, which are associated to ground deformation (Barra *et al.,* 2019). The mean value of the estimated atmospheric components is an estimation of the atmospheric phase contribution relative to the master image (Ferreti *et al.,* 2001). Afterward, it is calculated for each slave. The mentioned authors indicate that the obtained accuracy depends on the number of processed images, considered density of PS and the reliability of the difference phases.

Once the deformation time series have been estimated without the atmospheric contribution, the part of the linear movement (LOS mean deformation velocity) is reintroduced in order to obtain the final A-DInSAR results.

Geocoding of A-DInSAR results

This last step consists of georeferencing the A-DInSAR results, assigning to each line and colum position the corresponding WGS 84 geographic coordinates or UTM-WGS84 projected coordinates. The output is a txt file with the following data of each point: ID, X, Y and Z coordinates, LOS mean velocity (mm year^{-1}) and deformation time series (mm). This txt file can be exportable to a GIS. The final output consisted of a LOS mean deformation velocity map (mm year^{-1}) with 410,874 PS detected in an area with an approximated extension of 2,972.6 km^{2}. The LOS mean deformation velocity ranges from −18.4 to 37.4 mm year^{-1} (Figure 76). In order to compare the ground movement rates, active PS were considered as those above ± 2.5 mm year^{-1}. This threshold was selected according to the standard deviation of PSIG results (2σ = ± 2.5).

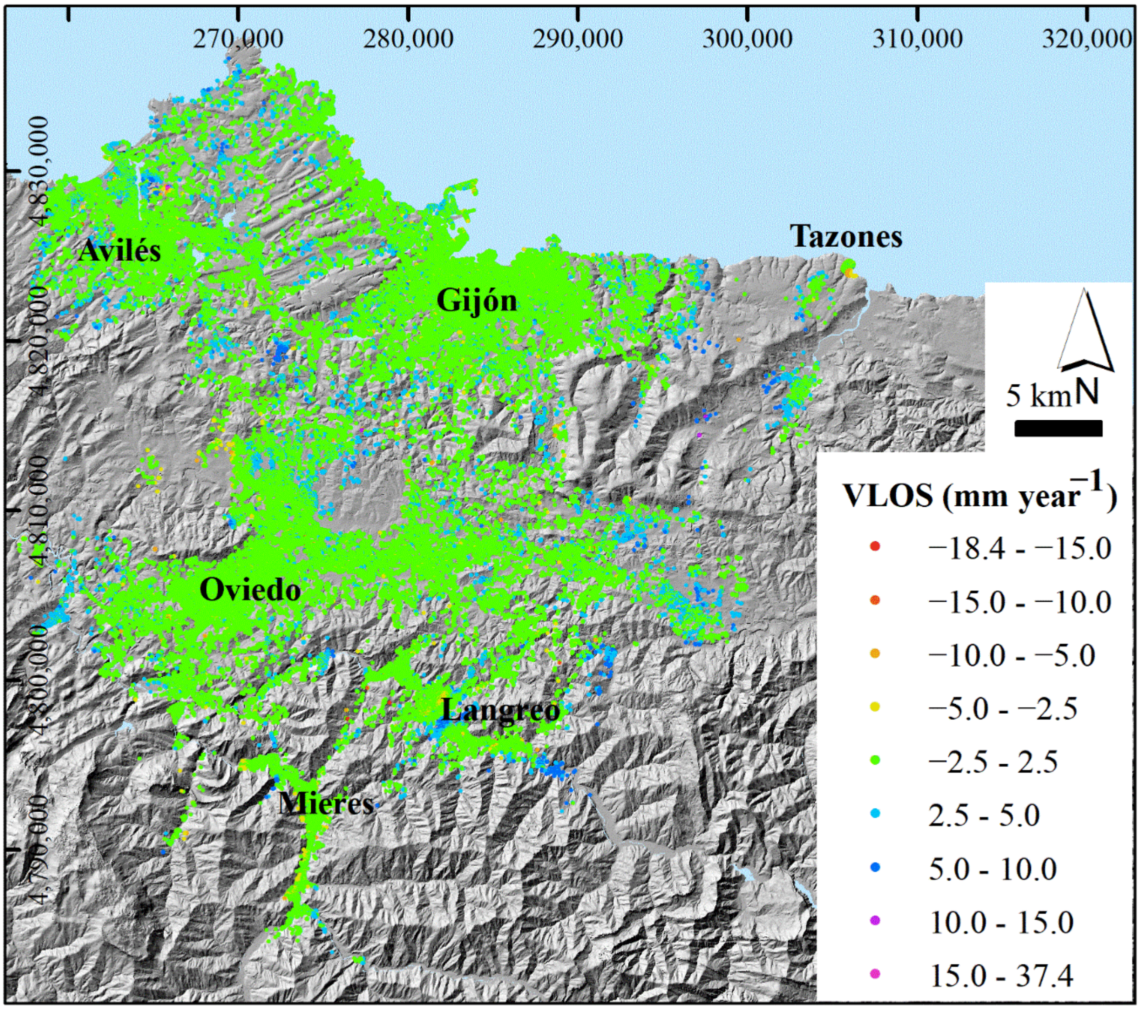

Figure 76. Final output of the PSIG software: mean LOS deformation velocity map (mm year^{-1}) in Central Asturias. DEM 5 x 5 m (IGN, 2020).

The sign of the measured displacement has to be interpreted considering the terrain slope: positive values indicate movement towards the satellite along its LOS direction, while negative values indicate movement away (Figure 76). As Sentinel-1 SAR images were acquired in descending orbit, the adequate sensibility will be got when the terrain presents orientations of 278 degrees with respect to N and a slope of 55º, approximately.

3.1.2 P-SBAS processing

The GEP platform, which was developed and funded by the ESA, allows to apply the service of P-SBAS Sentinel-1 processing on-demand by CNR-IREA (Casu *et al.*, 2014, De Luca *et al.*, 2015 and Manunta *et al.*, 2019). This approach consists of a Multi-temporal DInSAR processing exploiting Sentinel-1A/B data collection. To be able to use this service, it is necessary to become an early user by means of previous submitting.

The automatic P-SBAS chain follows the next steps (Casu *et al.*, 2014 and Manunta *et al.*, 2019) (Figure 77 and Table 11): 1) Selection of Sentinel-1 IW SLC images in function of the AoI, Track and temporal period; 2) DEM conversion in SAR coordinates and geometrical co-registration of SAR images considering a reference point; 3) Generation of differential interferograms by applying a Goldstein filtering (commonly with a value of 0.5); 4) Performing temporal and spatial phase unwrapping over a subset of pixels identified according to coherence value and estimation of deformation and residual topography; 5) Generation of surface displacement time series (cm) and LOS mean deformation velocity maps (cm year^{-1}); 6) Application of APS filter on the resulting time series. The whole processing usually takes about 1 day.

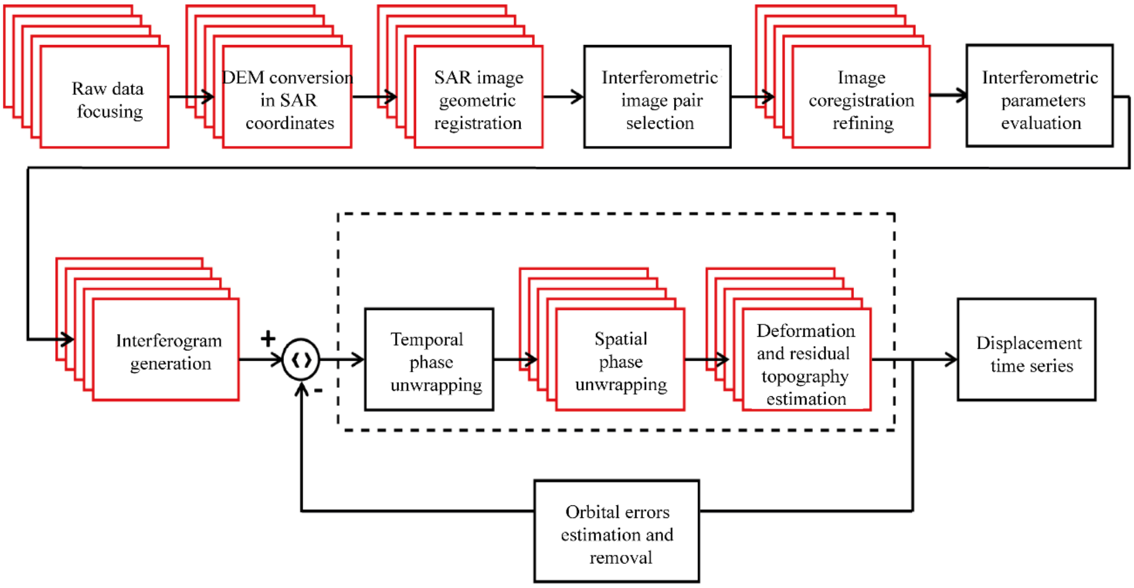

Figure 77. Workflow of the P-SBAS chain. Taken and modified from Casu *et al.* (2014).

In this research, three different processings were carried out by using this P-SBAS technique:

Central Asturias, with 113 Sentinel-1A/B IW SLC images, track 154 and descending trajectory (Figure 70 and Appendix I).

Lisbon Metropolitan Area, with 48 ascending and 69 descending Sentinel-1A IW SLC images (tracks 45 and 125, respectively) (Figure 78, Table 11, Appendix II and Appendix III).

Table 11. Main processing parameters of the P-SBAS chain. The geographical locations of the LMA reference points are shown in Figure 78.

Processing parameters	**P-SBAS processing**
Pixel resolution	90 x 90 m
Used DEM	SRTM_1arcsec (30 m)
Multilooking factor	5 x 20 (azimuth x range)
Goldstein filter	0.5
Applied filter	APS
Reference point in ascending	−9.1902863/38.706933
Reference point in descending	−9.7099499/38.771494

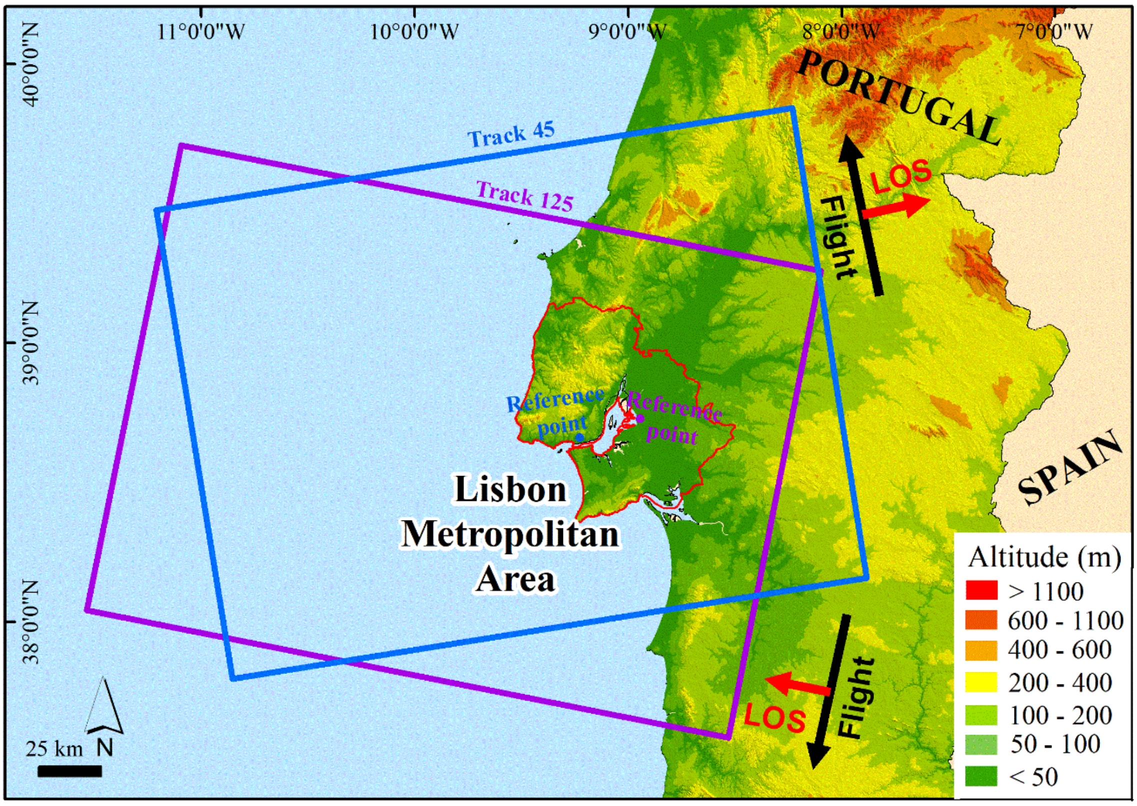

Figure 78. Ascending track 45 and descending track 125 used in P-SBAS processing in the LMA.

A-DInSAR products are obtained in csv format and they contain (Figure 79): LOS mean deformation velocities (cm year^{-1}), deformation Time Series (cm), temporal coherence and topographic level. The LOS mean velocity map can be viewed in kmz format by means of Google Earth. Lastly, geocoding and implementation of LOS mean deformation velocity maps and deformation time series in a GIS are carried out. The final outputs in Central Asturias consisted of a LOS mean deformation velocity map with a total of 726,866 PS and a processed area of 51,883.8 km^2. In the case of the LMA, two LOS mean deformation velocity maps (mm year^{-1}) were obtaining, with ascending 607,024 and descending 975,215 detected PS in areas with extensions of 20,009 and 13,904 km^2, respectively.

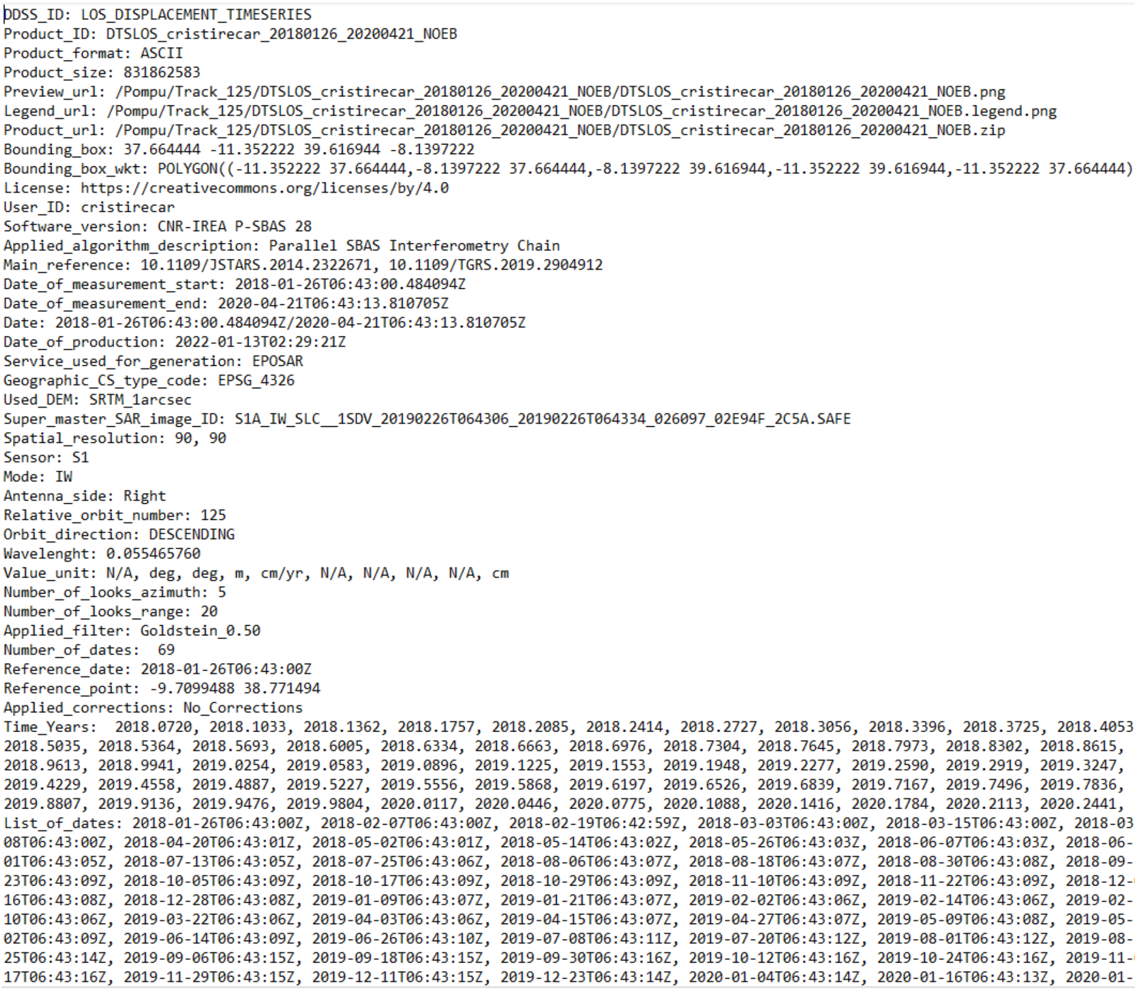

```
DDSS_ID: LOS_DISPLACEMENT_TIMESERIES
Product_ID: DTSLOS_cristirecar_20180126_20200421_NOEB
Product_format: ASCII
Product_size: 831862583
Preview_url: /Pompu/Track_125/DTSLOS_cristirecar_20180126_20200421_NOEB/DTSLOS_cristirecar_20180126_20200421_NOEB.png
Legend_url: /Pompu/Track_125/DTSLOS_cristirecar_20180126_20200421_NOEB/DTSLOS_cristirecar_20180126_20200421_NOEB.legend.png
Product_url: /Pompu/Track_125/DTSLOS_cristirecar_20180126_20200421_NOEB/DTSLOS_cristirecar_20180126_20200421_NOEB.zip
Bounding_box: 37.664444 -11.352222 39.616944 -8.1397222
Bounding_box_wkt: POLYGON((-11.352222 37.664444,-8.1397222 37.664444,-8.1397222 39.616944,-11.352222 39.616944,-11.352222 37.664444)
License: https://creativecommons.org/licenses/by/4.0
User_ID: cristirecar
Software_version: CNR-IREA P-SBAS 28
Applied_algorithm_description: Parallel SBAS Interferometry Chain
Main_reference: 10.1109/JSTARS.2014.2322671, 10.1109/TGRS.2019.2904912
Date_of_measurement_start: 2018-01-26T06:43:00.484094Z
Date_of_measurement_end: 2020-04-21T06:43:13.810705Z
Date: 2018-01-26T06:43:00.484094Z/2020-04-21T06:43:13.810705Z
Date_of_production: 2022-01-13T02:29:21Z
Service_used_for_generation: EPOSAR
Geographic_CS_type_code: EPSG_4326
Used_DEM: SRTM_1arcsec
Super_master_SAR_image_ID: S1A_IW_SLC__1SDV_20190226T064306_20190226T064334_026097_02E94F_2C5A.SAFE
Spatial_resolution: 90, 90
Sensor: S1
Mode: IW
Antenna_side: Right
Relative_orbit_number: 125
Orbit_direction: DESCENDING
Wavelenght: 0.055465760
Value_unit: N/A, deg, deg, m, cm/yr, N/A, N/A, N/A, N/A, cm
Number_of_looks_azimuth: 5
Number_of_looks_range: 20
Applied_filter: Goldstein_0.50
Number_of_dates:  69
Reference_date: 2018-01-26T06:43:00Z
Reference_point: -9.7099488 38.771494
Applied_corrections: No_Corrections
Time_Years:  2018.0720, 2018.1033, 2018.1362, 2018.1757, 2018.2085, 2018.2414, 2018.2727, 2018.3056, 2018.3396, 2018.3725, 2018.4053
2018.5035, 2018.5364, 2018.5693, 2018.6005, 2018.6334, 2018.6663, 2018.6976, 2018.7304, 2018.7645, 2018.7973, 2018.8302, 2018.8615,
2018.9613, 2018.9941, 2019.0254, 2019.0583, 2019.0896, 2019.1225, 2019.1553, 2019.1948, 2019.2277, 2019.2590, 2019.2919, 2019.3247,
2019.4229, 2019.4558, 2019.4887, 2019.5227, 2019.5556, 2019.5868, 2019.6197, 2019.6526, 2019.6839, 2019.7167, 2019.7496, 2019.7836,
2019.8807, 2019.9136, 2019.9476, 2019.9804, 2020.0117, 2020.0446, 2020.0775, 2020.1088, 2020.1416, 2020.1784, 2020.2113, 2020.2441,
List_of_dates: 2018-01-26T06:43:00Z, 2018-02-07T06:43:00Z, 2018-02-19T06:42:59Z, 2018-03-03T06:43:00Z, 2018-03-15T06:43:00Z, 2018-03
08T06:43:00Z, 2018-04-20T06:43:01Z, 2018-05-02T06:43:01Z, 2018-05-14T06:43:02Z, 2018-05-26T06:43:03Z, 2018-06-07T06:43:03Z, 2018-06-
01T06:43:05Z, 2018-07-13T06:43:05Z, 2018-07-25T06:43:06Z, 2018-08-06T06:43:07Z, 2018-08-18T06:43:07Z, 2018-08-30T06:43:08Z, 2018-09-
23T06:43:09Z, 2018-10-05T06:43:09Z, 2018-10-17T06:43:09Z, 2018-10-29T06:43:09Z, 2018-11-10T06:43:09Z, 2018-11-22T06:43:09Z, 2018-12-
16T06:43:08Z, 2018-12-28T06:43:08Z, 2019-01-09T06:43:07Z, 2019-01-21T06:43:07Z, 2019-02-02T06:43:06Z, 2019-02-14T06:43:06Z, 2019-02-
10T06:43:06Z, 2019-03-22T06:43:06Z, 2019-04-03T06:43:06Z, 2019-04-15T06:43:07Z, 2019-04-27T06:43:07Z, 2019-05-09T06:43:08Z, 2019-05-
02T06:43:09Z, 2019-06-14T06:43:09Z, 2019-06-26T06:43:10Z, 2019-07-08T06:43:11Z, 2019-07-20T06:43:12Z, 2019-08-01T06:43:12Z, 2019-08-
25T06:43:14Z, 2019-09-06T06:43:15Z, 2019-09-18T06:43:15Z, 2019-09-30T06:43:16Z, 2019-10-12T06:43:16Z, 2019-10-24T06:43:16Z, 2019-11-
17T06:43:16Z, 2019-11-29T06:43:15Z, 2019-12-11T06:43:15Z, 2019-12-23T06:43:14Z, 2020-01-04T06:43:14Z, 2020-01-16T06:43:13Z, 2020-01-
```

Figure 79. Final csv file output from P-SBAS processing containing information about processing parameters, acquisition date and deformation data. In this case, descending processed track 125 is shown.

3.2 A-DInSAR post-processing

A-DInSAR post-processing was applied in order to enhance the analysis and interpretation of ground motion detected by PSIG and P-SBAS methods. First, LOS decomposition was performed to asses Vertical and Horizontal motion. On the other hand, Active Deformation Areas procedure (ADA tool) was applied. These A-DInSAR post-processing tools were only applied in the LMA, because this study area is the only one where both ascending and descending A-DInSAR processing were available. These procedures are described in detail below.

3.2.1 LOS decomposition to evaluate Vertical and Horizontal motion

This methodology allows to calculate the Vertical (Equation (4)) and Horizontal (Equations (5)) deformations from LOS ground motion detected in both trajectories (Figure 80). This approach can help to mitigate the geometric limitations of SAR and facilitate data interpretation (Barra *et al.*, 2022). However, the Vertical - Horizontal decomposition requires the presence of both ascending and descending data in the same sampling, because there is loss of information where an area is not covered by PS from both trajectories (Barra *et al.*, 2022). There are different approaches and methodologies to obtain Vertical and Horizontal components (e. g. Tofani *et al.*, 2013; Chan *et al.*, 2017; Tomás *et al.*, 2019). In this research, the procedure proposed by Notti *et al.* (2014) and Béjar-Pizarro *et al.* (2017) was applied. This procedure is based on the application of the Inverse Distance Weighted (IDW) method and the raster calculator in a GIS. In this case, ArcGIS 10.3 ® was used.

Firstly, displacement rates along LOS direction from both trajectories were interpolated using the IDW method. The main parameters in this step were: power 1, search radios 100 m, minimum number of points 3 and pixel resolution of 90 m. Secondly, the interpolated ascending ($vLOS_a$) and descending ($vLOS_d$) were used to estimate Vertical and Eastward components (Equations (4) and (5)) using the raster tool.

$$V_{vertical} = \frac{\left(\left(\frac{vLOS_d}{E_d}\right) - \left(\frac{vLOS_a}{E_a}\right)\right)}{\left(\frac{H_d}{E_d} - \frac{H_a}{E_a}\right)} \quad (4)$$

$$V_{eastward} = \frac{\left(\left(\frac{vLOS_d}{H_d}\right) - \left(\frac{vLOS_a}{H_a}\right)\right)}{\left(\frac{E_d}{H_d} - \frac{E_a}{H_a}\right)} \tag{5}$$

Where Ha, Hd, Ea and Ed (Equations (6) - (9)) represent the direction cosines of the ascending (a) and descending (d) LOS vector. They are calculated from the incidence angles (α_a and α_d) and the LOS azimuths ($\gamma_a$and γ_d) in degrees (Béjar-Pizarro *et al.*, 2017):

$$H_a = cos(\alpha_a) \tag{6}$$

$$H_d = \cos(\alpha_d) \tag{7}$$

$$E_a = cos(90 - \alpha_a)\ x\ cos(270 - \gamma_a) \tag{8}$$

$$E_d = cos(90 - \alpha_d)\ x\ cos(270 - \gamma_d) \tag{9}$$

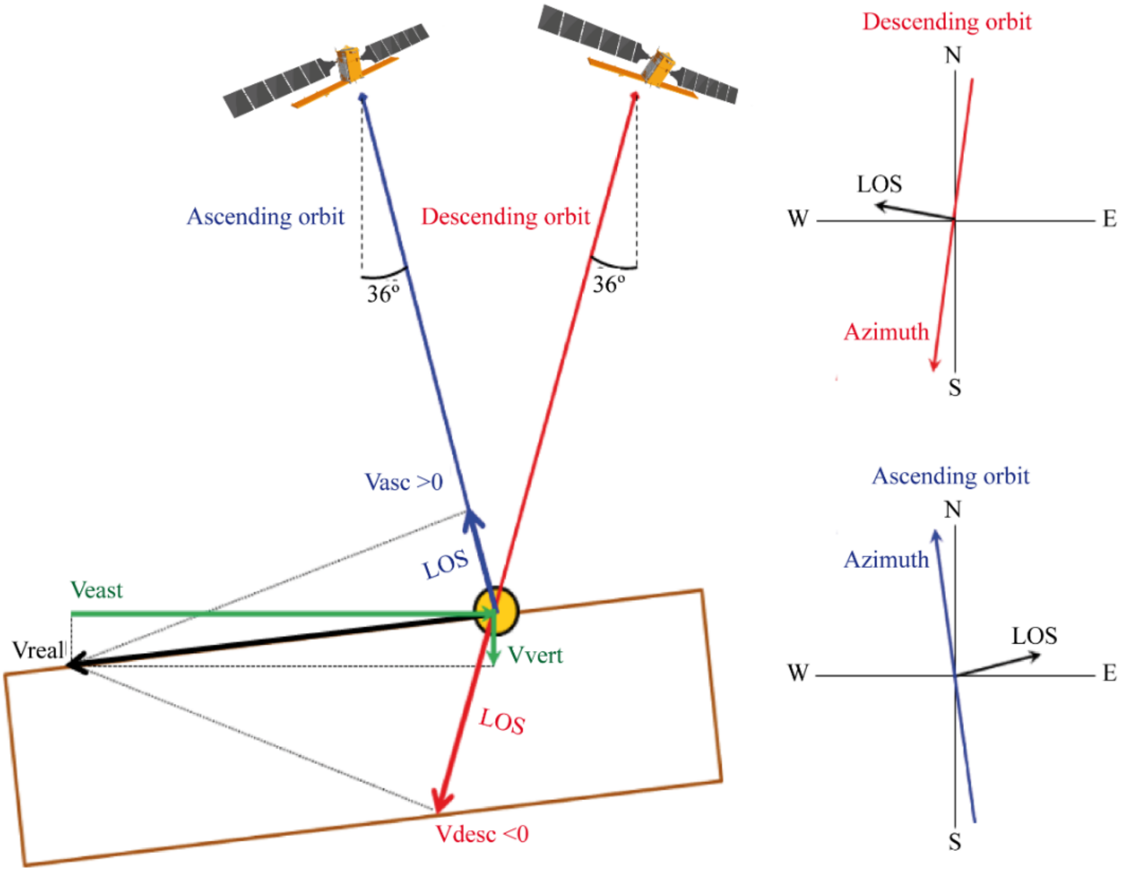

Figure 80. Decomposition of Vertical and Horizontal (E-W) deformation components from ascending and descending trajectories. Taken and modified from Tofani *et al.* (2013).

The considered ascending and descending input data to estimate Vertical and Eastward components (Equations (4) and (5)) are summarized in Table 12.

Table 12. Ascending and descending input data used during LOS decomposition and estimation of Vertical and Horizontal components.

Ascending dataset		**Descending dataset**	
LOS azimuth (γ_a)	80º (1.4 rad)	LOS azimuth (γ_d)	280º (4.9 rad)
LOS Incidence angle (α_a)	36º (0.6 rad)	LOS Incidence angle (α_d)	36º (0.6 rad)
Ha = $\cos(\alpha_a)$	0.81	Hd = $\cos(\alpha_d)$	0.81
Ea = $\cos(90 - \alpha_a) \text{ x } \cos(270 - \gamma_a)$	−0.58	Ed = $\cos(90 - \alpha_d) \text{ x } \cos(270 - \gamma_d)$	0.58

3.2.2 Active Deformation Areas (ADA) methodology

This methodology has been designed by CTTC and described by Barra *et al.* (2017), Tomás *et al.* (2019) and Navarro *et al.* (2020). This software (ADAFinder v 1.1.31 ®) performs the identification and extraction of Active Deformation Areas (ADAs), allowing to focus the analysis and interpretation in those areas with active ground motion (Barra *et al.*, 2022) (Figure 81). These areas are composed by a determined number of active PS, with mean, maximum and minimum values of VLOS detected (mm year^{-1}), mean value of accumulated displacements (mm), velocity classes and a quality index (Barra *et al.*, 2017) (Figure 81). This quality index (QI, from 1-very reliable to 4-not reliable) allows to recognize the temporal and spatial noise level in the deformation time series within each identified ADA (Navarro *et al.*, 2020). In this way, the QI is essential to understand the level of reliability and exclude the noisier moving areas (Barra *et al.*, 2022) (Figure 81). In this research only ADAs with QI = 1 have been taken into account for analysis and interpretation (Figure 81).

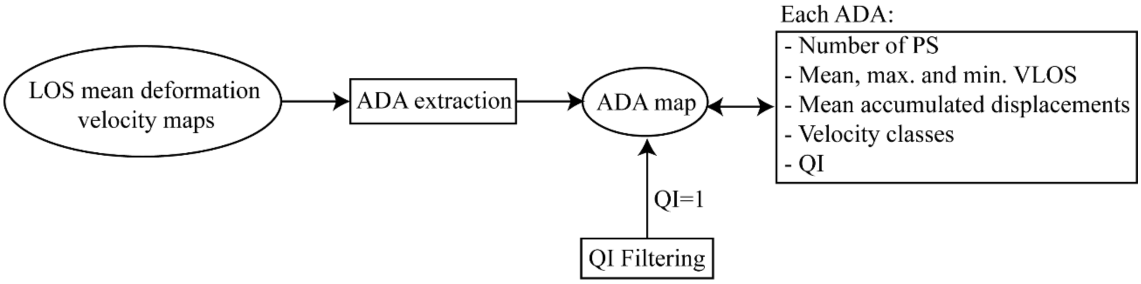

Figure 81. Simplified flowchart of ADA procedure. Taken and modified from Barra *et al.* (2022).

The processing parameters taken into account in the LMA for the identification and extraction of these ADAs are displayed in Table 13. For further and more detailed description about these processing parameters, the works of Tomás *et al.* (2019) and Navarro *et al.* (2020) can be consulted. The parameters selection of main parameters was carried out according to main characteristics of P-SBAS processing obtained (Table 13): 1) The isolation distance chosen was 180 m, because this distance must be twice the pixel resolution (Navarro *et al.*, 2020); 2) The standard deviation, the value chosen was 2. This factor is multiplied by the standard deviation obtained from the LOS mean velocity; 3) The clustering radio should be 1/3 greater than pixel resolution (Navarro *et al.*, 2020). Then, the value for this parameters was 120 m and 4) The minimum ADA size selected (minimum number of PS to draw an ADA) was 5 PS (Table 13).

Table 13. Main processing parameters of ADA tools for P-SBAS processing.

Parameters / Technique	**P-SBAS**
Pixel Resolution (m)	90.0
Isolation distance (m)	180.0
Factor for standard deviation	2
Clustering radio (m)	120.0
Minimum ADA size (Number of PS)	5

3.3 GIS integration and dataset interpretation

For the adequate interpretation of A-DInSAR results obtained, different layers and rasters are combined with geocoded PS in a GIS environment. The geo-information used for the three study areas is described below and summarized in Table 14.

3.3.1 Data collection of the study areas of Asturias

The information of both study areas in Asturias (Peñas Cape environment and Mountain region) have been downloaded and recompiled from Centro de Descargas del Instituto Geográfico Nacional and SITPA-IDEAS websites (IGN, 2020; SITPA-IDEAS, 2022) and consists of: 1) Aerial orthophotos acquired during 2017 and 2020 (PNOA Plan) for Asturias with a pixel resolution of 0.25 m (OrtoPNOA 2017-2020 CC-BY 4.0 scne.es); 2) topographic maps of Principality of Asturias and Portugal at scale 1:25,000 (BTN25 2006-2019 CC-BY 4.0 ign.es); 3) Terrain Digital Models: Elevation, Slope, and Orientation Digital Models with a cell resolution of 5 x 5 m (MDT05 2015 CC-BY 4.0 scne.es); 4) Soil, lithology, geological formation, surficial formation covers and vegetation maps at scale 1:25,000 (Cartografía Temática Ambiental del Principado de Asturias CC-BY 4.0) and 5) Land use map of 2014 by SIOSE plan (Sistema de Información de Ocupación del Suelo en España) at scale 1:25,000 (SIOSE 2014 CC-BY 4.0 scne.es) (Table 14).

In addition, with the purpose of recognising the Quaternary deposits, and specially landslides and other slope deposits in Mountain region, the surficial formations cover mapped by Domínguez-Cuesta (2003) was studied (Table 14). On the other hand, in order to know the location of underground mining workings and their potential relevance in the study area, different mining data were collected: 1) Some technical reports prepared by HUNOSA, IGME and University of Oviedo, all of them up to 2018 (HUNOSA *et al.*, 2011; HUNOSA, 2017; HUNOSA, 2018) (Table 14) and 2) Mining plans provided by Historical Archive of HUNOSA, including only those prior to 1967, due to restricted access and confidenciality of files after that year.

Lastly, hydrological dataset related to daily rainfall data from January 2018 to February 2020 at meteorological station of Oviedo (AEMET, 2020) was compiled and reviewed (Figure 58 A) (Table 14).

3.3.2 Data collection of Lisbon Metropolitan Area

For the analysis and interpretation of the ground motion detected in the LMA, the followed geo-spatial data were compiled and reviewed (Table 14): 1) orthophotos of Portugal territory acquired in 2018 (DGT, 2021) with a pixel resolution of 0.25 m; 2) topographic maps of Portugal at scale 1:25,000 provided by IGOT (Instituto de Geografía y Ordenamento do Territorio); 3) Digital Terrain Models: Elevation (with pixel resolution of 50 × 50 m and 10 × 10 m), Slope and Aspect (with pixel resolution of 50 × 50 m); 4) geological map of Portugal at 1:1,000,000 and 1:500,000 (LNEG, 1992, 2010) and 5) lithological map of LMA at scale 1:500,000 and the land use map of Portugal at scale 1:500,000 (Table 14).

On the other hand, different hydrological dataset was gathered (Table 14). Firstly, daily rainfall dataset from January 2018 to April 2020 at Meteorological Station of S. Julião do Tojal (Vialonga town; geographical location: 38,86º N, 9,13º W; Figure 66) was compiled and reviewed. Secondly, the monthly mean depth of piezometric level in Carregado town (Alenquer council; geographical location: 38,86º N, 9,13º W) between 2018 to 2020 was consulted from Sistema Nacional de Informaçao de Recursos Hídricos website (SNIRH, 2021) (Table 14).

3.3.3 A-DInSAR results validation

Different field campaigns were archieved with the purpose of validating and checking the reliability of A-DInSAR results and ADAs identified (Table 14). These field campaigns consisted of the exploration to search ground motion evidence: presence of tense cracks or scarps, damage in buildings and roads, creep phenomena, among others.

In the cases of Tazones Lighthouse landslide and the Podes Peninsula, the A-DInSAR dataset could be compared with available data of *in situ* topographical monitoring (Figure 82 A and Table 14). Different control points and feno-type markers were installed and measured (Figure 82 B) between June 2018 and February 2020 (Tazones) and September 2020 (Podes) in the framework of the COSINES project (Ref. CGL2017-83909-R). In both cases, the instrument used to observe the control points and pheno markers was a Leica TC-407 total station (precision of the angular measurement = 7"; precision of the distance measurement = 2 mm ± 2 ppm) (Figure 82 A). In addition, given the observation methodology and the level of error of the total station used, displacements of less than 2 cm are not considered significant. In order to facilitate the interpretation of the topographic measurements, an arbitrary coordinate system was adopted, so that the X-axis coincides with the greatest displacement direction (Domínguez-Cuesta *et al.*, 2022a).

Figure 82. Topographic monitoring field campaign by means of total station in **A)** Tazones Lighthouse landslide and **B)** Podes Peninsula.

In the Tazones Lighthouse landslide, 34 feno-type markers and 4 additional control points covering an area of 12,000 m^2 were installed and measured (Figure 83 A). All markers were located between 95 and 110 m a.s.l (Domínguez-Cuesta *et al.*, 2022a). Between June 2018 (when topographical monitoring started) and February 2020, a total of 20 topographic monitoring campaigns were carried out with a variable periodicity of 16 to 75 days, depending on weather conditions (Domínguez-Cuesta *et al.*, 2022a) (Figure 83 A). In the Podes Peninsula, a total of 6 feno-type markers and 15 topographic nails were installed and measured (Figure 83 B). These markers are located between 20 and 35 m a.s.l and cover an approximate area of 12,700 m^2 (Figure 83 B). Between June 2018 and September 2020, a total of 7 topographic monitoring campaigns were carried out with a six monthly monitoring periodicity.

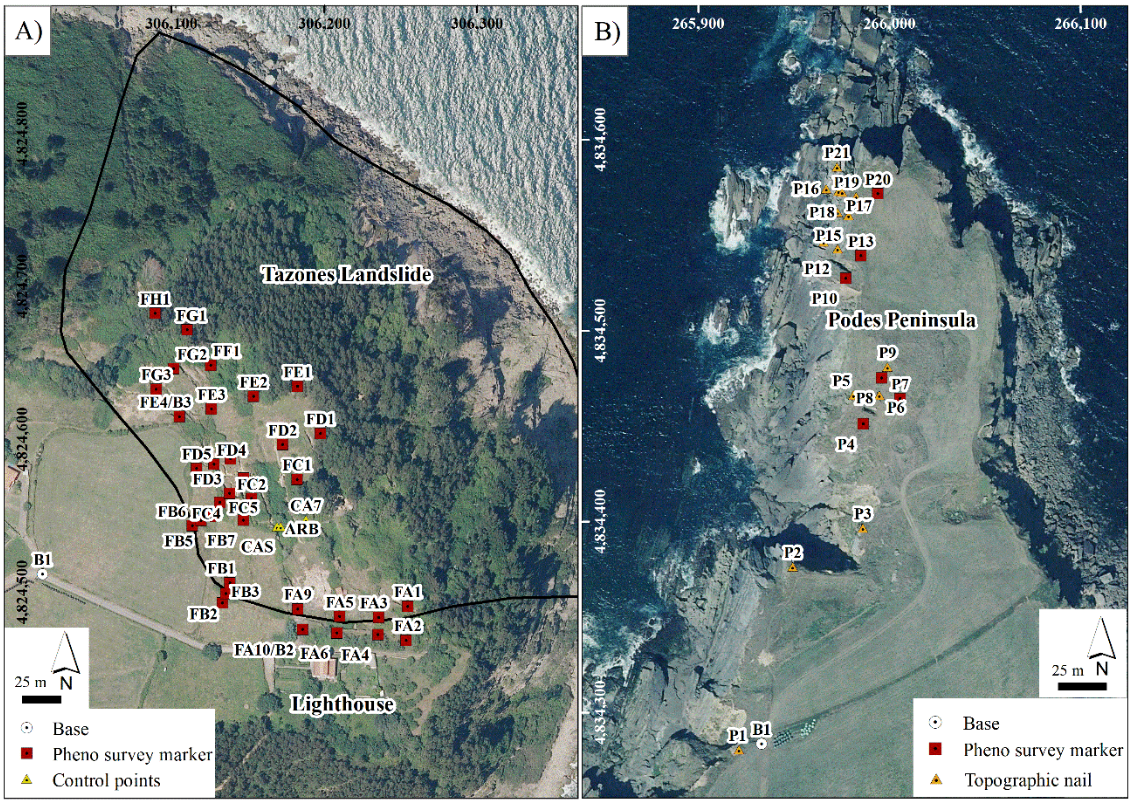

Figure 83. Topographic points installed and measured in **A)** the Tazones Lighthouse landslide and **B)** Podes Peninsula. OrtoPNOA 2020 CC-BY 4.0 scne.es.

Table 14. Dataset and geo-spatial data recompiled and reviewed for the analysis and interpretation of A-DInSAR results. Peñas Cape environment includes the Podes Peninsula.

Study Areas	**PSIG**	**P-SBAS**	**Ortophotos (Year and Resolution)**	**Topographic map (Scale)**	**DTM (Cell)**	**Land use map (Scale)**	**Rainfall dataset**	**Other data**	**ADAs**	**Vertical deformation**	**Topographic monitoring**	**Field campaign**
Peñas Cape environment	Yes	Yes	2017, 2020 (0.25 m)	1:25,000	5 x 5 m	1:25,000	-	-	No	No	Biannual 6/2018 - 9/2020	Yes
Tazones Lighthouse landslide	Yes	Yes	2020 (0.25 m)	-	-	-	-	-	No	No	Monthly 6/2018 - 2/2020	Yes
Mountain Area	Yes	No	2017, 2020 (0.25 m)	1:25,000	5 x 5 m	1:25,000	Daily 1/2018 - 2/2020	Mining technical reports (before 1967)	No	No	No	Yes
Lisbon Metropolitan Area	No	Yes	2018 (0.25 m)	1:25,000	10 x 10 m	1:500,000	Daily 1/2018 - 4/2020	Monthly piezometric level 1/2018 - 4/2020	Yes	Yes	No	Yes

4. RESULTS

The results are divided in three parts, with the following order: 1) The coastal areas of Asturias: The Peñas Cape environment, the Podes Peninsula and the Tazones Lighthouse landslide; 2) The mountain area of Asturias and 3) The Lisbon Metropolitan Area.

4.1 Coastal areas of Asturias

4.1.1 Peñas Cape environment

The LOS mean deformation velocity maps (mm year^{-1}) obtained by PSIG chain and P-SBAS processing are presented in Figure 84 and are summarized in Table 15. There were differences of total PS detected between PSIG and P-SBAS maps: 151,722 PS (811.3 PS km^{-2}) were obtained with the PSIG chain. On the contrary, with the P-SBAS processing a total of 16,654 points were measured (89.1 PS km^{-2}) (Table 15). The LOS velocity ranges estimated were similar to each other. In PSIG, the maximum LOS velocities were −17.1 and 37.4 mm year^{-1} (mean value was 0.0 ± 1.1 mm year^{-1}). In the case of the P-SBAS processing, the maximum LOS velocities were −23.0 and 38.3 mm year^{-1} (mean value was 0.0 ± 2.6 mm year^{-1}) (Figure 84 and Table 15).

In the case of PSIG, there were 146,855 PS (96.79%) with LOS mean velocity between −2.5 and 2.5 mm year^{-1} (Table 15). Instead, in P-SBAS processing the total number of PS between −2.5 and 2.5 mm year^{-1} were 12,413 (74.53%) (Table 15). Regarding the accumulated displacement, maximum displacements of PSIG were −68.5 and 78.8 mm (mean value was 0.1 ± 3.6 mm). Maximum displacements between −48.8 and 77.0 mm (mean value was 1.1 ± 5.1 mm) were measured by P-SBAS (Table 15).

The differences between both approaches can be observed in Figure 84, Figure 85 and Figure 86 and Table 15, which are presented in detail below.

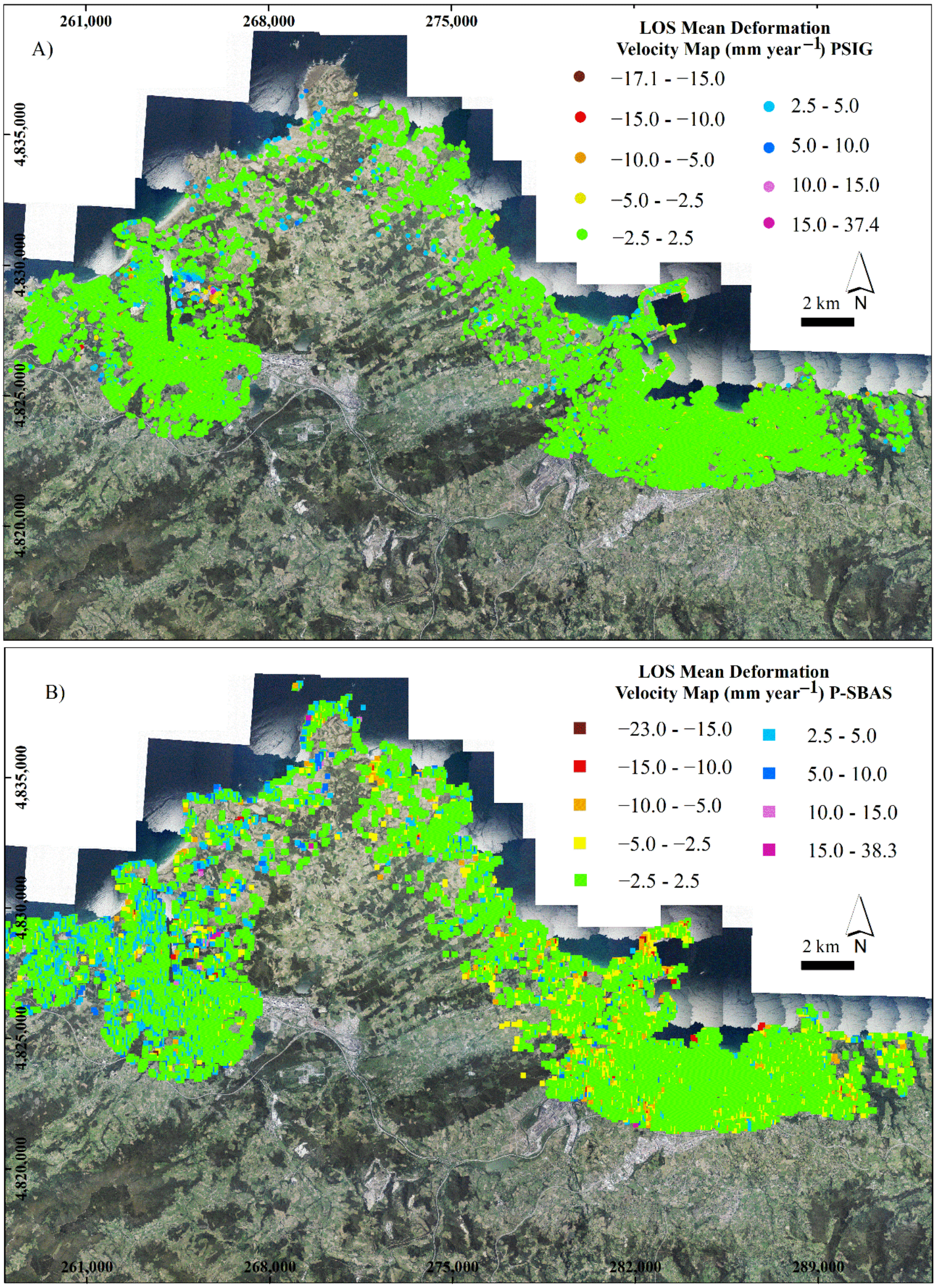

Figure 84. Peñas Cape environment. LOS mean deformation velocity map in mm year^{-1} obtained by **A)** PSIG software and **B)** P-SBAS processing. OrtoPNOA 2017 CC-BY 4.0 scne.es. Taken and modified from Cuervas-Mons *et al.* (2021d).

Figure 85 shows the LOS mean deformation velocity map (mm year^{-1}) obtained by PSIG. LOS velocity PS <−10.0 mm year^{-1} (15 PS, 0.01%) were detected, as isolated PS, over Avilés and Gijón cities and Musel Port infrastructures. They could not be considerated as good PS for the interpretation. LOS velocity rates between −10.0 - −5.0 mm year^{-1} (184 PS, 0.12%), and −5.0 to −2.5 mm year^{-1} (2,049 PS, 1.35%), appeared grouped in some areas with outstanding deformations. These deformations were associated to slope instabilities (Figure 87) and Port infrastructure affections (Figure 88). The LOS velocity rates of 2.5 - 5.0 mm year^{-1} (2,426 PS, 1.60%) were the most difficult to analyze. They could be observed along the study area as grouped and isolated PS. Moreover, they appeared over some cliffs whose orientation is predominantly to northward, that could be related to unfiltered atmospheric noise. PS with LOS rates of 5.0 - 10.0 mm year^{-1} (167 PS, 0.11%) were observed on industrial districts and open pit mining. These deformations were linked to anthropic activity (accumulation of materials). The LOS mean velocity > 10.0 mm year^{-1} were only 26 PS (0.02%). They were located over an anthropic deposit at east of Avilés. They could be related to the accumulation of material (Figure 85).

Figure 86 displays the LOS mean deformation velocity map (mm year^{-1}) obtained by P-SBAS. LOS velocity PS <−10.0 mm year^{-1} (49 PS, 0.29%) were found as isolated PS except at Musel Port, where a group of PS could be observed related to oustanding ground motions. LOS velocity rates of −10.0 - −5.0 mm year^{-1} (513 PS, 3.08%) and −5.0 to −2.5 mm year^{-1} (1,295 PS, 7.78%) appeared along the study area. These deformations presented a predominance in the east of the study area (Gijón city). These PS were equally difficult to interpret on a regional scale, as they could represent: 1) Terrain and coastal instabilities in infrastructures (Figure 88 and Figure 89) or 2) Uncorrected atmospheric component. LOS rates from 2.5 - 5.0 mm year^{-1} (1,956 PS, 11.75 %) and 5.0 - 10.0 mm year^{-1} (385 PS, 2.31 %) were observed along the study area. As in the previous case, local detailed analysis should be carried out for a correct interpretation, because at a regional scale could be related to a significant quantity of atmospheric component or artifacts. Eventually, PS with LOS mean velocity > 10.0 mm year^{-1} were 43 PS (0.26 %) and were found as isolated PS and deformation over an open pit in Avilés city; these velocities could be associated to the accumulation of anthropic materials (Figure 87 B).

Also, Figure 85 and Figure 86 allow to distinguish several differences between the results of the approaches. Firstly, P-SBAS results presented a higher distribution of dispersed active PS along the whole area, without delimiting deformation areas (Figure 86). Nonetheless, the active PS of PSIG appeared defining well-defined deformation areas (Figure 84 A and Figure 85). On the other hand, there were some sectors where PS were barely detected by PSIG. Instead, P-SBAS detected movements: the northernmost zone of the Peñas Cape and the Podes sector (Figure 84 B and Figure 86). In the first case, the LOS velocities detected were between −8.6 and 15.2 mm year^{-1}. The maximum accumulated displacements were −17.2 and 30.1 mm. In the Podes Peninsula, the PS presented LOS velocities from −6.8 to 12.9 mm year^{-1} (Figure 86).

Table 15. LOS mean deformation velocity rates (mm year^{-1}) and cumulate LOS deformation (mm) obtained. The density and total of points obtained by PSIG and P-SBAS approaches are shown. Taken and modified from Cuervas-Mons *et al.* (2021d).

Settings	**PSIG software**	**P-SBAS processing**	
Number of points (PS)	151,722	16,654	
Density of points (PS km^{-2})	811.3	89.1	
LOS mean velocity (mm year^{-1})			
Mean	0.0	0.0	
Maximum	37.4	38.3	
Minimum	−17.1	−23.0	
Standard deviation	1.1	2.6	
Accumulated LOS displacement (mm)			
Mean	0.1	1.1	
Maximum	78.8	77.0	
Minimum	−68.5	−48.8	
Standard deviation	3.6	5.1	
LOS rates PSIG (mm year^{-1})	**PSIG PS - %**	**LOS rates P-SBAS (mm year^{-1})**	**P-SBAS PS - %**
< −10.0	15 - 0.01	< −10.0	49 - 0.29
−10.0 - −5.0	184 - 0.12	−10.0 - −5.0	513 - 3.08
−5.0 - −2.5	2,049 - 1.35	−5.0 - −2.5	1,295 - 7.78
−2.5 - 2.5	146,855 - 96.79	−2.5 - 2.5	12,413 - 74.53
2.5 - 5.0	2,426 - 1.60	2.5 - 5.0	1,956 - 11.75
5.0 - 10.0	167 - 0.11	5.0 - 10.0	385 - 2.31
>10.0	26 - 0.02	>10.0	43 - 0.26

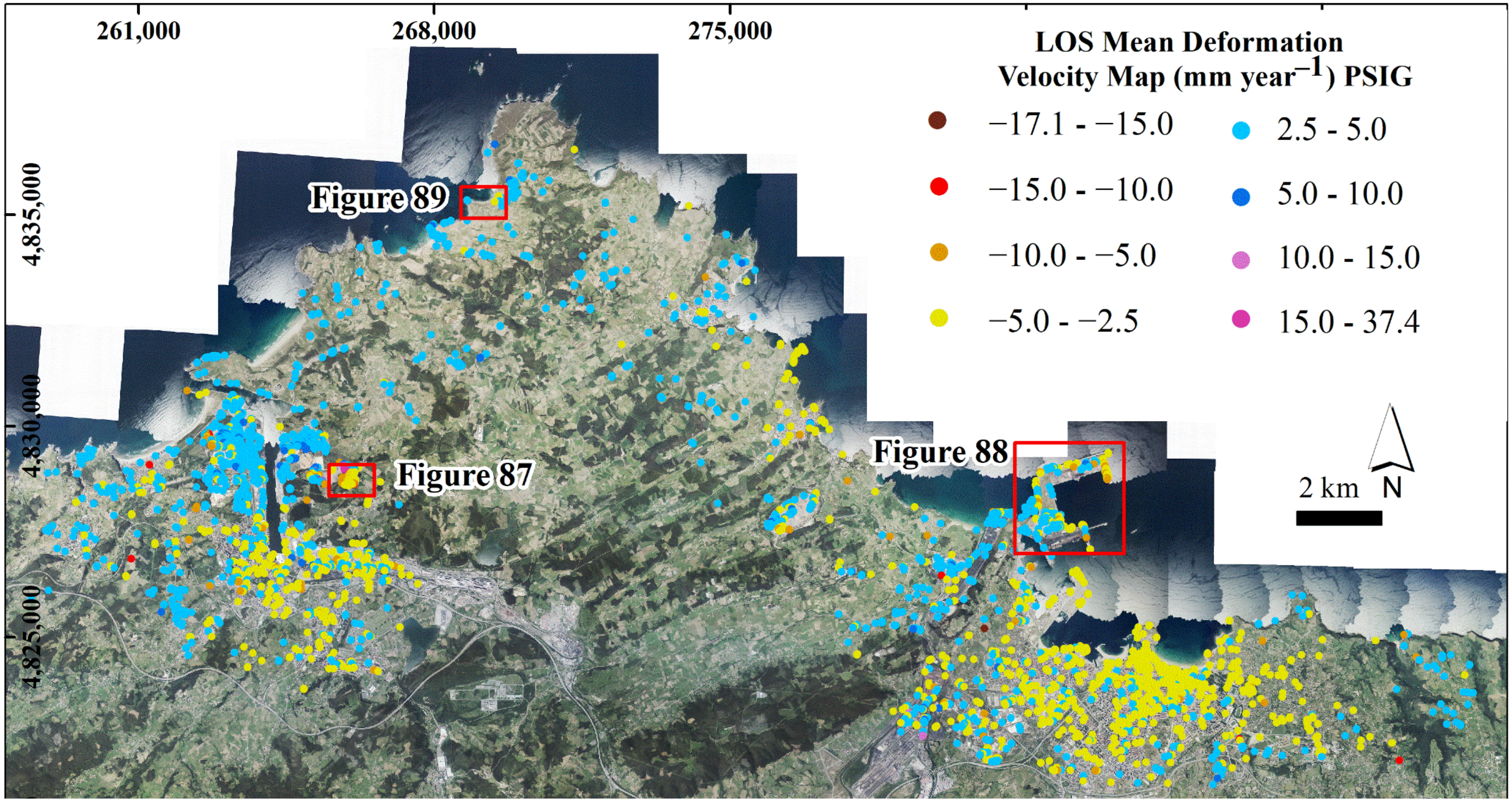

Figure 85. PSIG results obtained in the Peñas Cape environment by using PSIG approach. Non-active deformations have been removed to facilitate the visualization of active deformations. The red squares are the deformation areas explained in the text. OrtoPNOA 2017 CC-BY 4.0 scne.es. Taken and modified from Cuervas-Mons *et al.* (2021d).

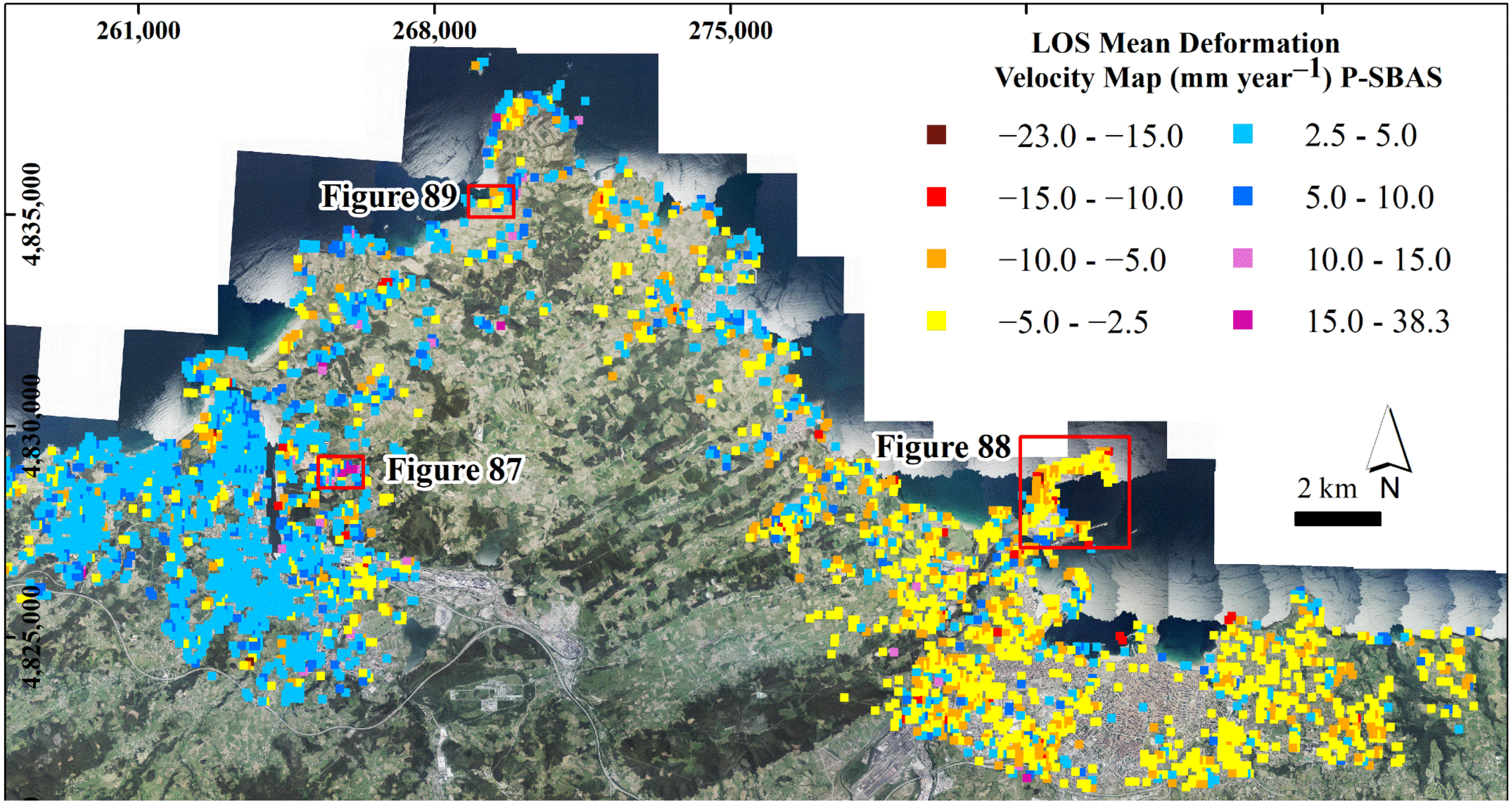

Figure 86. P-SBAS results obtained in the Peñas Cape environment by using PSIG approach. Non-active deformations have been removed to facilitate the visualization of active deformations. The red squares are the deformation areas explained in the text. OrtoPNOA 2017 CC-BY 4.0 scne.es. Taken and modified from Cuervas-Mons *et al.* (2021d).

Figure 87 shows deformations detected by PSIG and P-SBAS over an electrical station to the East of Avilés city. This area is located over anthropic materials overlying the Jurassic bedrock composed by siliceous conglomerate and sandstone. As to PSIG results, with a total of 456 PS detected, the deformations presented VLOS ranging from −12.4 to 0.6 mm year^{-1}. It could be observed a velocity increament from flat areas towards the sloped.

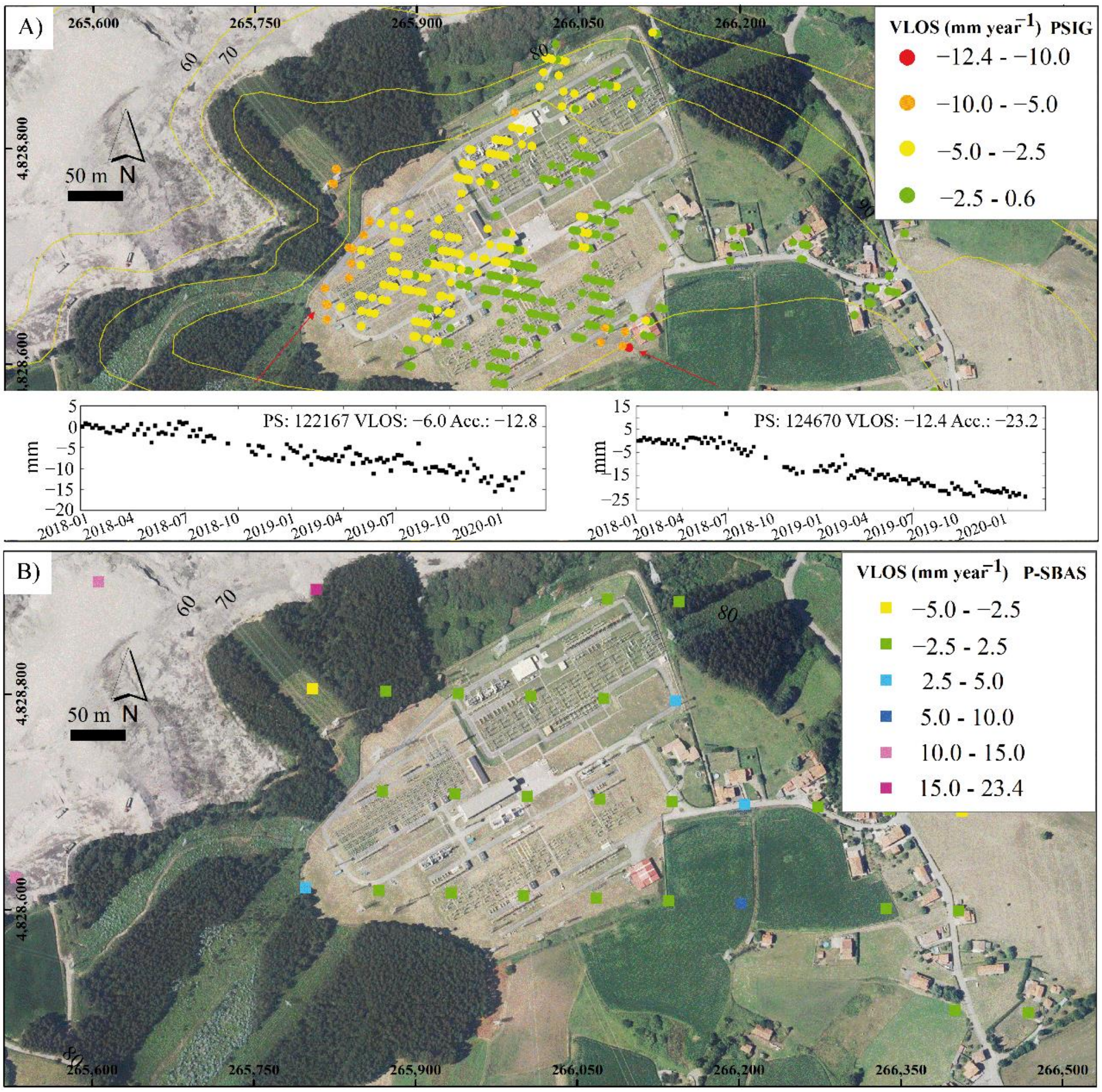

Figure 87. Ground motion detected in an electrical station to the East of Avilés city. **A)** Detected deformations and some observed time series obtained by PSIG software. **B)** Detected ground motion by P-SBAS processing. OrtoPNOA 2017 CC-BY 4.0 scne.es. Taken and modified from Cuervas-Mons *et al.* (2021d).

The deformation time series showed a maximum displacement accumulated of −23.2 mm (Figure 87 A). Their trends displayed a stable period from January to July 2018, showing a more or less constant period of ground movement until February 2020. On the other hand, P-SBAS processing (Figure 87 B) showed a total of 37 PS with VLOS rates between −5.0 and 23.4 mm year^{-1}. Contrasting the results, it could be seen that the P-SBAS processing did not detected the same deformations observed by PSIG chain (Figure 87). In addition, PS of P-SBAS results with VLOS > 5.0 mm year^{-1} were noteworthy and they could be related to atmospheric noise and anthropic activities (Figure 87 B).

Figure 88 shows deformations registered in the Musel Port breakwater wall, located close to the city of Gijón. With respect PSIG results, a total of 3,002 PS with VLOS rates ranging from −8.6 to 6.3 mm year^{-1} were detected (Figure 88 A).

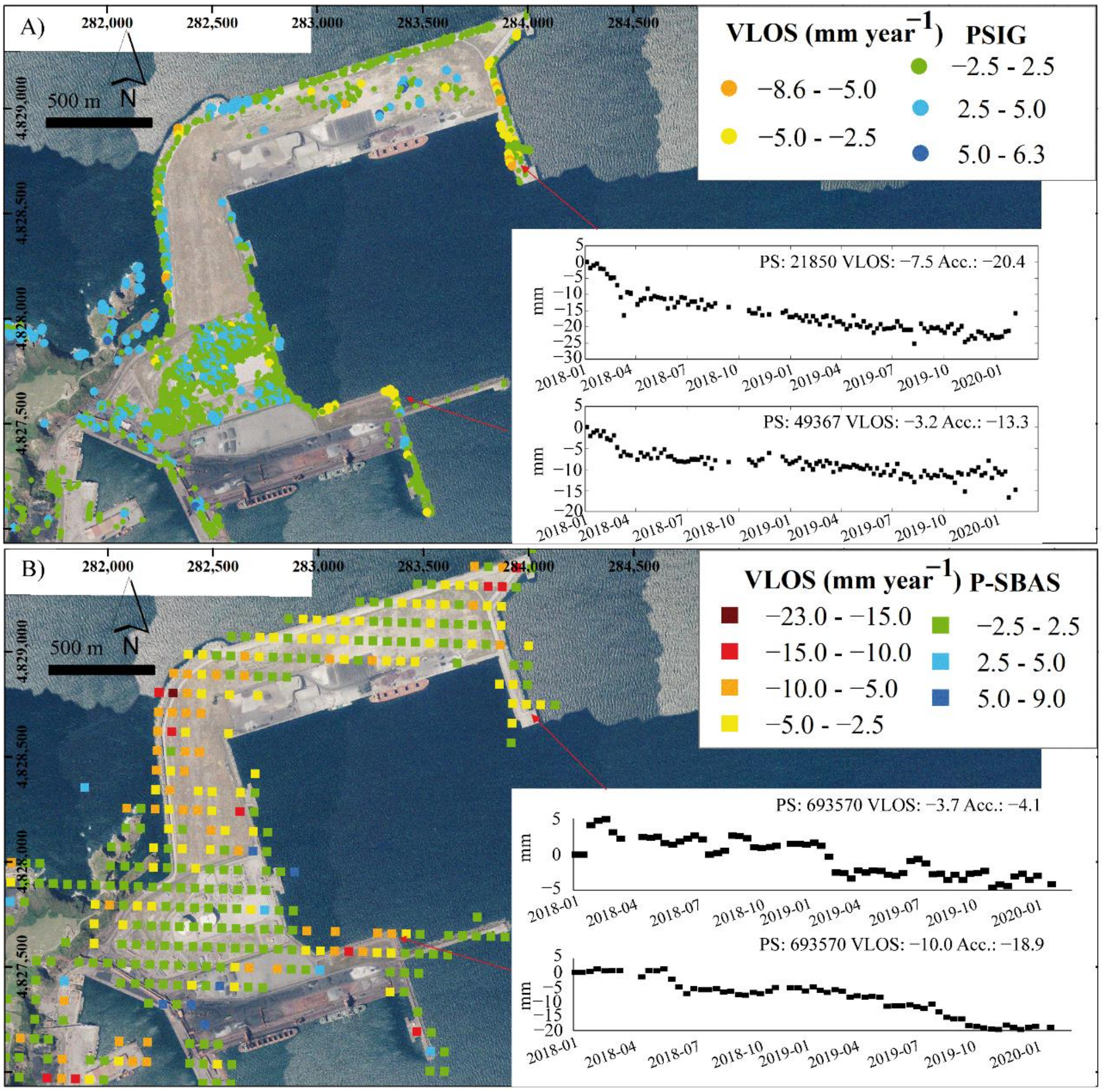

Figure 88. Detected deformations over Musel Port (Gijón city) by **A)** PSIG software and **B)** P-SBAS processing. Two representative time series are shown in both cases. OrtoPNOA 2020 CC-BY 4.0 scne.es. Taken and modified from Cuervas-Mons *et al.* (2021d).

Their deformation time series registered a maximum displacement of −35.6 mm. In general, there was an intense episode of deformation during 4 months (from January to April 2018), with accumulated displacements from −5 to −20 mm (Figure 88 A). As on April, a deformation trend was observed until February 2020, but slower, even reaching stabilization in some cases. On the other hand, the positive PS presented maximum LOS velocities of 6.3 mm year^{-1}. Their time series did not present deformation patterns. Then, these positive PS could relate to mostly noise and atmospheric contribution (Figure 88 A). On the contrary, P-SBAS processing detected 429 PS with VLOS ranges from −23.0 to 9.0 mm year^{-1} (Figure 88 B). It could see that P-SBAS results matched with the PSIG data because the areas with active PS of VLOS <−2.5 mm year^{-1} were the same, although the extent of the active zones detected with P-SBAS was larger. Also, P-SBAS removed the positive PS observed by PSIG, defining these areas as stable sectors (Figure 88). The time series observed with P-SBAS were different from each other. Figure 88 B shows two cases. The first one was very noisy, with no deformation pattern and could not be correlated with the PSIG time serie observed at the same location. The second one presented two differentiated periods: A first stabilization stage (between January and June 2018) and a second stage of deformation that reached almost 19 mm accumulated in February 2020 (Figure 88 B).

Figure 89 shows detected deformations in the coastline at West of Peñas Cape. PSIG detected 73 PS with LOS velocities ranging between −3.6 and 5.6 mm year^{-1} (Figure 89 A), while P-SBAS presented 43 PS with VLOS from −9.1 to 8.1 mm year^{-1} (Figure 89 B). In this sector, the bedrock is composed by shale, sandstone and volcanoclastic rocks, covered by rasa deposits. At the foot of the cliffs, there are beach and rockfall deposits. In both cases, and despite of the low resolution of the P-SBAS result, a coastal instability was detected (Figure 89). This deformation presented LOS velocity ranging from −9.1 to −2.5 mm year^{-1} (Figure 89). Moreover, the time series presented maximum displacements of −22.7 mm. In the case of the time series obtained by PSIG, they were some noisy, although a certain deformation pattern could be observed (Figure 89 A). Between January 2018 and February 2019 a stable period was observed. Subsequently, a continuous increase in deformation was observed until February 2020, reaching a maximum displacement of −8.3 mm (Figure 89 A). In the case of P-SBAS (Figure 89 B), the time series showed three patterns of deformation: A stable period between January and April 2018. From April onwards, there were two phases of deformation: the first between April and September 2018 and the second from October 2018 to February 2020, which was continuous and linear. The few positive PS detected with both methods can be considered as uncorrected atmospheric component or as noise (Figure 89).

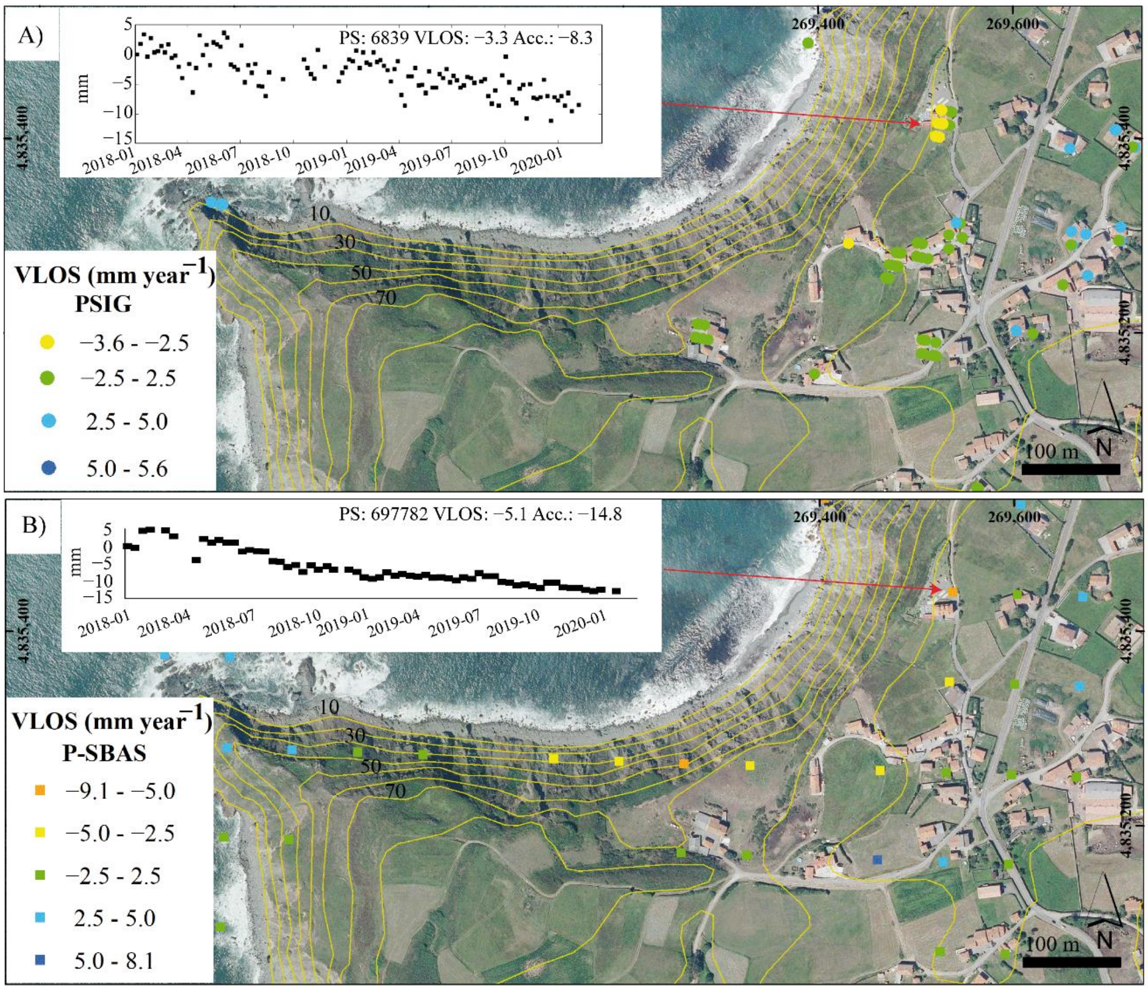

Figure 89. Deformations detected over cliffs located at West of Peñas Cape. Ground motion and time serie measured by **A)** PSIG software and **B)** P-SBAS processing. OrtoPNOA 2020 CC-BY 4.0 scne.es. Taken and modified from Cuervas-Mons *et al.* (2021d).

4.1.2 Podes Peninsula

In this sub-section, the A-DInSAR and topographic results obtained in the Podes Peninsula are presented. A LOS mean deformation velocity map with PS obtained by PSIG and P-SBAS (mm year^{-1}) is shown in Figure 90 A. In the case of PSIG, only 25 PS were measured, with VLOS rates between 1.5 and 4.5 mm year^{-1}. However, P-SBAS allowed to detect 85 PS, whose VLOS ranged from −6.8 to 12.9 mm year^{-1}. In this way, density of PS of P-SBAS processing is higher than PSIG processing (30.4 versus 8.9 PS km^{-2}) (Figure 90 A). Most of the PS detected by P-SBAS were measured at or near the cliffs and on the few buildings in the area. In the case of PSIG, only few PS were detected on these buildings.

The accumulated movements measured during topographical campaigns are shown in Figure 90 B and Table 16. All topographic points and markers presented displacements lower than 0.10 cm (Figure 90 B and Table 16). Nevertheless, these measurements could not be considered significant because they were lower than 2 cm. Also, it was observed that measurements between PS and topographic points did not match. They presented differences of more than 1 cm at all points. It is worthly that maximum displacements of topographic points (between 0.09 and 0.05 cm, Table 16) were observed in the northernmost area of the peninsula, where VLOS > 5.0 mm year^{-1} and maximum VLOS of 12.9 mm year^{-1} were detected (Figure 90 B and Figure 91 A-D, Figure 92 TS-1).

Regarding evidence of movements, different slope instabilities could be observed affecting both cliffs and surficial deposits (Figure 91). On the western side, the stratification in favour of the cliff can be appreciated, with a slip of 68º (Figure 91 A and B). This condition produces translational slides and some complex movements (Figure 91 C). In addition, at the foot of the cliff, there are rockfall deposits. In this sector, positive PS were associated to artifacts and uncorrected atmospheric component. On the other side, in the eastern sector of the peninsula, only active movements of topple and rockfall type are visible (Figure 91 E), which produce deposits at the foot of the cliff. In these locations, the positive PS detected could be showing the beginnings of the instabilities that generate these movements (Figure 90 B, Figure 91 E and Figure 92 TS-2). Moreover, there is a non-active complex movement to the southeast of the peninsula where a non-active PS was detected (Figure 90 B and Figure 91 F). Lastly, three active PS with maximum VLOS of −6.8 mm year^{-1} were detected in the southwest of the study area, which corresponds to an area with coastal instabilities (Figure 90 A and Figure 92 TS-3). The rest of the PS detected along the study area represents: 1) Coastal instabilities (Figure 92 TS-4); 2) Noise or 3) Uncorrected atmospheric component (Figure 90 A).

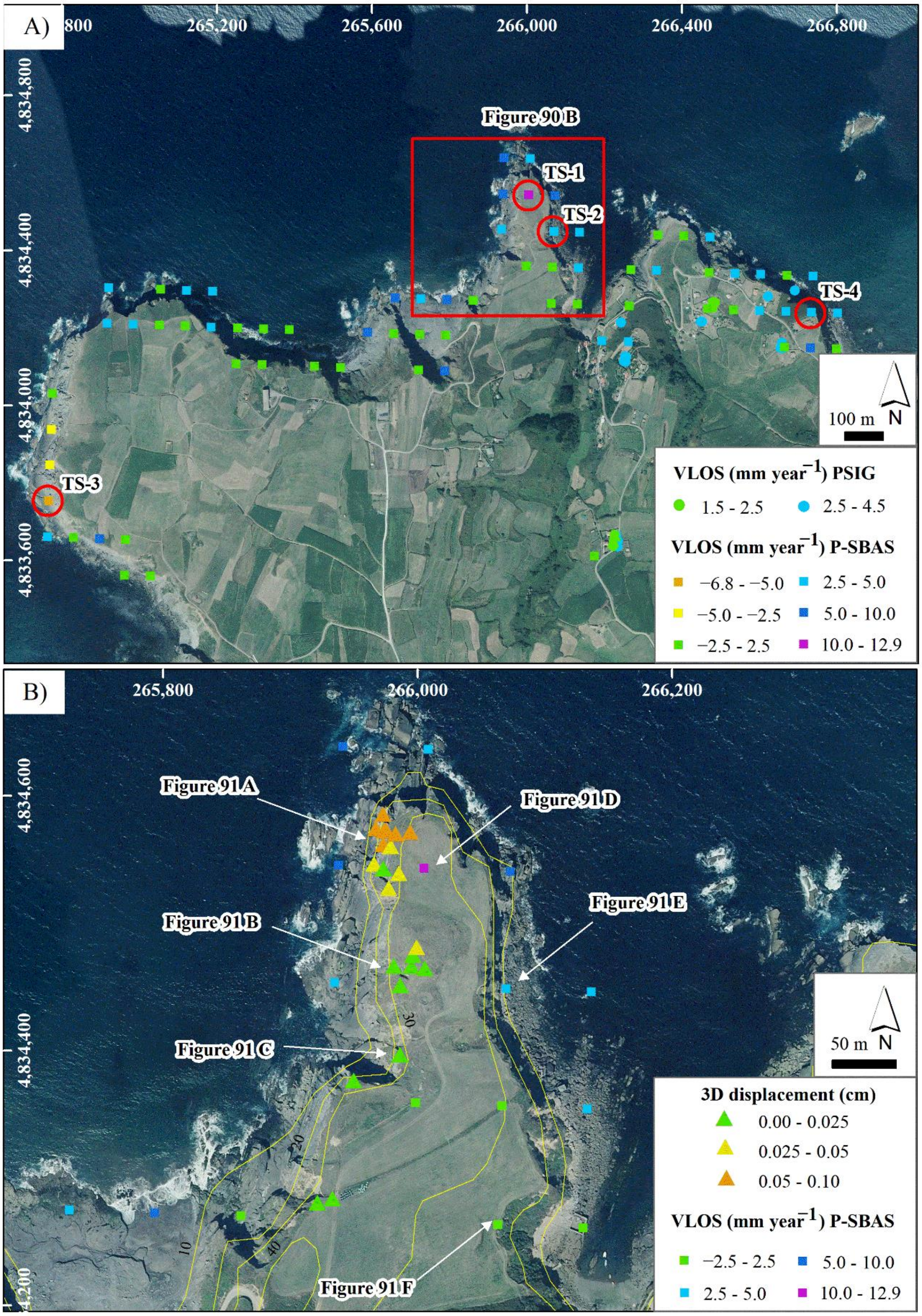

Figure 90. Movement detected in the Podes Peninsula area. **A)** LOS mean deformation velocity maps obtained by PSIG approach and P-SBAS processing. **B)** Podes Peninsula in detail: VLOS (mm year^{-1}) obtained by P-SBAS versus 3D displacement (cm) measured by means of topographic monitoring. OrtoPNOA 2020 CC-BY 4.0 scne.es. Taken and modified from Cuervas-Mons *et al.* (2021b).

Figure 91. A) and **B)** Topographic monitoring field campaign by means of total station in western side of Podes. **C)** Several complex gravity movements observed at the cliff edge. **D)** Location where PS with VLOS 12.9 mm year^{-1} were detected. **E)** and **F)** Coastal instabilities developed on the east side of Podes. Photos taken in January, 19 2021. Taken and modified from Cuervas-Mons *et al.* (2021b).

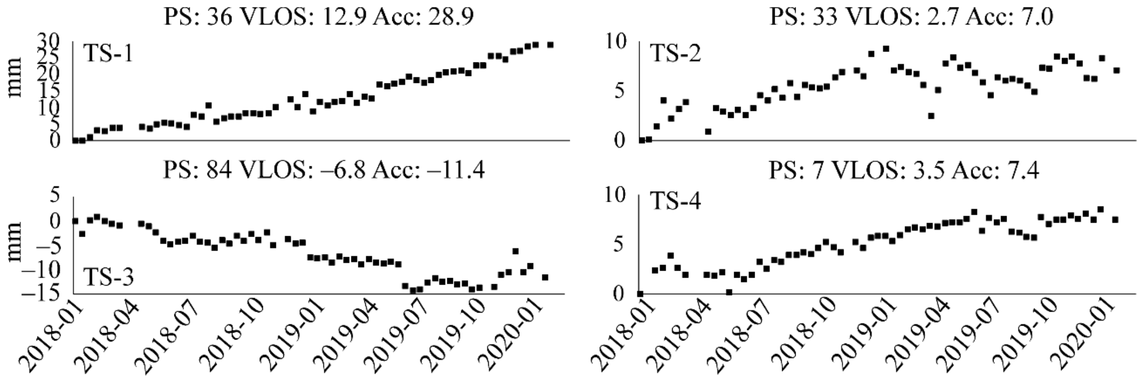

Figure 92. Time series observed in the Podes Peninsula by means of P-SBAS processing. See locations in Figure 90. Taken and modified from Cuervas-Mons *et al.* (2021b).

Table 16. Measured cumulative displacements with total station for each of the 21 markers in the 7 monitoring campaigns developed in Podes Peninsula between 2018 and 2020. Markers are ordened according to the cumulative displacements and measurements are shown in cm. See markers situation in Figure 83. Taken and modified from Cuervas-Mons *et al.* (2021b).

Marker	**25/06/2018**	**19/11/2018**	**17/01/2019**	**12/07/2019**	**05/12/2019**	**18/06/2020**	**02/09/2020**
P21	0.00	0.00	0.01	0.01	0.06	0.06	0.09
P14	0.00	0.00	0.01	0.01	0.04	0.07	0.08
P18	0.00	0.00	0.02	0.01	0.04	0.06	0.08
P20	0.00	0.02	0.03	0.02	0.06	0.03	0.07
P17	0.00	0.00	0.02	0.01	0.04	0.05	0.06
P19	0.00	0.00	0.02	0.02	0.05	0.02	0.05
P16	0.00	0.00	0.01	0.01	0.05	0.04	0.05
P11	0.00	0.00	0.01	0.02	0.05	0.05	0.04
P10	0.00	0.01	0.02	0.01	0.04	0.04	0.04
P13	0.00	0.02	0.02	0.02	0.02	0.03	0.04
P9	0.00	0.01	0.01	0.01	0.01	0.02	0.03
P15	0.00	0.00	0.02	0.03	0.06	0.01	0.03
P12	0.00	0.00	0.01	0.01	0.04	0.01	0.02
P8	0.00	0.01	0.02	0.01	0.01	0.02	0.02
P7	0.00	0.02	0.02	0.02	0.02	0.02	0.02
P2	0.00	0.03	0.02	0.01	0.01	0.01	0.02
P5	0.00	0.02	0.02	0.02	0.02	0.02	0.02
P4	0.00	0.02	0.02	0.01	0.04	0.02	0.02
P6	0.00	0.01	0.01	0.01	0.01	0.01	0.02
P1	0.00	0.01	0.01	0.01	0.01	0.01	0.01
P3	0.00	0.03	0.01	0.02	0.01	0.02	0.00

4.1.3 Tazones Lighthouse landslide

Figure 93 shows two LOS mean deformation velocity maps (mm year^{-1}) obtained by means of PSIG software and P-SBAS processing. PSIG approach allowed detecting 331 PS, with mean VLOS rangings between −5.3 and 8.5 mm year^{-1}. A total of 265 non-active PS were detected (80.06 %) (Figure 93 A). However, in the case of P-SBAS results only 20 PS were measured, whose VLOS were ranging from −3.6 to 2.9 mm year^{-1} (Figure 93 B).

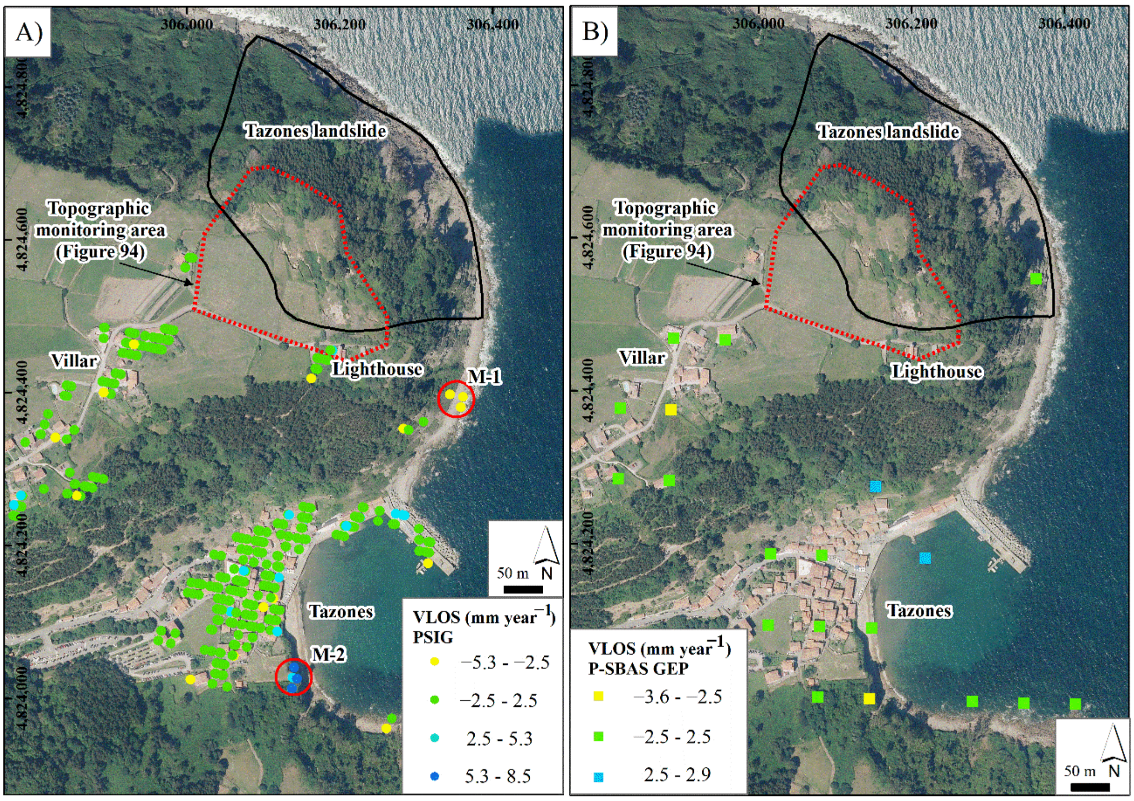

Figure 93. Tazones Lighthouse landslide and topographic monitoring area. **A)** LOS mean deformation velocity map obtained by PSIG approach. **B)** LOS mean deformation velocity map obtained by P-SBAS processing. OrtoPNOA 2020 CC-BY 4.0 scne.es. Taken and modified from Domínguez-Cuesta *et al.* (2022b).

In both approaches, all detected PS were outside the Tazones landslide area. Thus, ground motion inside of Tazones landslide could not be detected by using A-DInSAR techniques. Nevertheless, both LOS mean deformation velocity maps allowed to confirm that Villar village and Tazones Lighthouse building are on stable zones, with LOS velocities between −5.2 and 4.4 mm year^{-1}, which can be considered outside of the Tazones landslide area (Figure 93). The PS with deformations, whose LOS velocities are < −2.5 and > 2.5 mm year^{-1}, could be related to different artifacts such as uncorrected atmospheric component or topographic and orbital errors (Figure 93). On the other hand, there were two locations with active PS identified by PSIG that could be related to ground instabilities. Firstly, there were 3 PS located at East of the lighthouse and on top of cliffs with maximum VLOS of −5.3 mm year^{-1} (M-1, Figure 93 A). Secondly, at south of Tazones village, there were 4 PS with maximum VLOS of 8.5 mm year^{-1} (M-2, Figure 93 A). In both cases active PS could be related to landslide incidence.

The 3D accumulated movements measured during *in situ* topographical campaigns are shown in Figure 94 A and Table 17. The results have been grouped in nine intervals to help their analysis and interpretation. There were 10 markers which 3D displacements were less than 0.05 cm (Figure 94 A and Table 17). The remaining 28 markers showed 3D accumulated displacements between 0.06 m and 14.93 m (Figure 94 A and Table 17). This 3D largest displacement was measured by marker FG3, which recorded a distance of 14.06 m between October and November 2019 (Figure 94 A and Table 17). This displacement matched with a surficial slide developed during same time (Figure 94 B). This slide affected a sandstone, lutite and marl multilayer which bedding presents a slip of 15º - 17º towards the North. The movement occurred along the stratification plane (S0, Figure 94 B). The largest movements observed were measured in the campaingns of February 2019 and November 2019, with displacements greater than 0.3 m in 16 markers and 0.5 m in 12 markers, respectively (Figure 94 A-E and Table 17). Some remarkable movements were measured by markers FF1, FG2 and FG1 because they registered displacements higher than 1 m in a month: FF1 = 1.21 m, FG2 = 1.03 m, and FG1 = 1 m (Figure 94 A and Table 17). Markers such as FD3, CA7, FC3, FC2 and FA3 moved 0.83, 0.69, 0.56, 0.50 and 0.38 m in November 2019, respectively (Figure 94 A, C-E and Table 17). In these places, along the large and deep cracks and the most unstable areas, some small topples, rockfalls and slides have been occurring until now (Figure 94 C-E).

It is remarkable that due to the rapid progression of the Tazones Lighthouse landslide, two control points were lost between January and February 2019 (FA1) and between November and December 2019 (ARB) (Figure 94 A and Table 17). Some points can appear without data because they were either lost or damaged (CA8 and FA9). Other markers can present gaps in the movement monitoring data table because they were installed during a second installation campaign (Table 17).

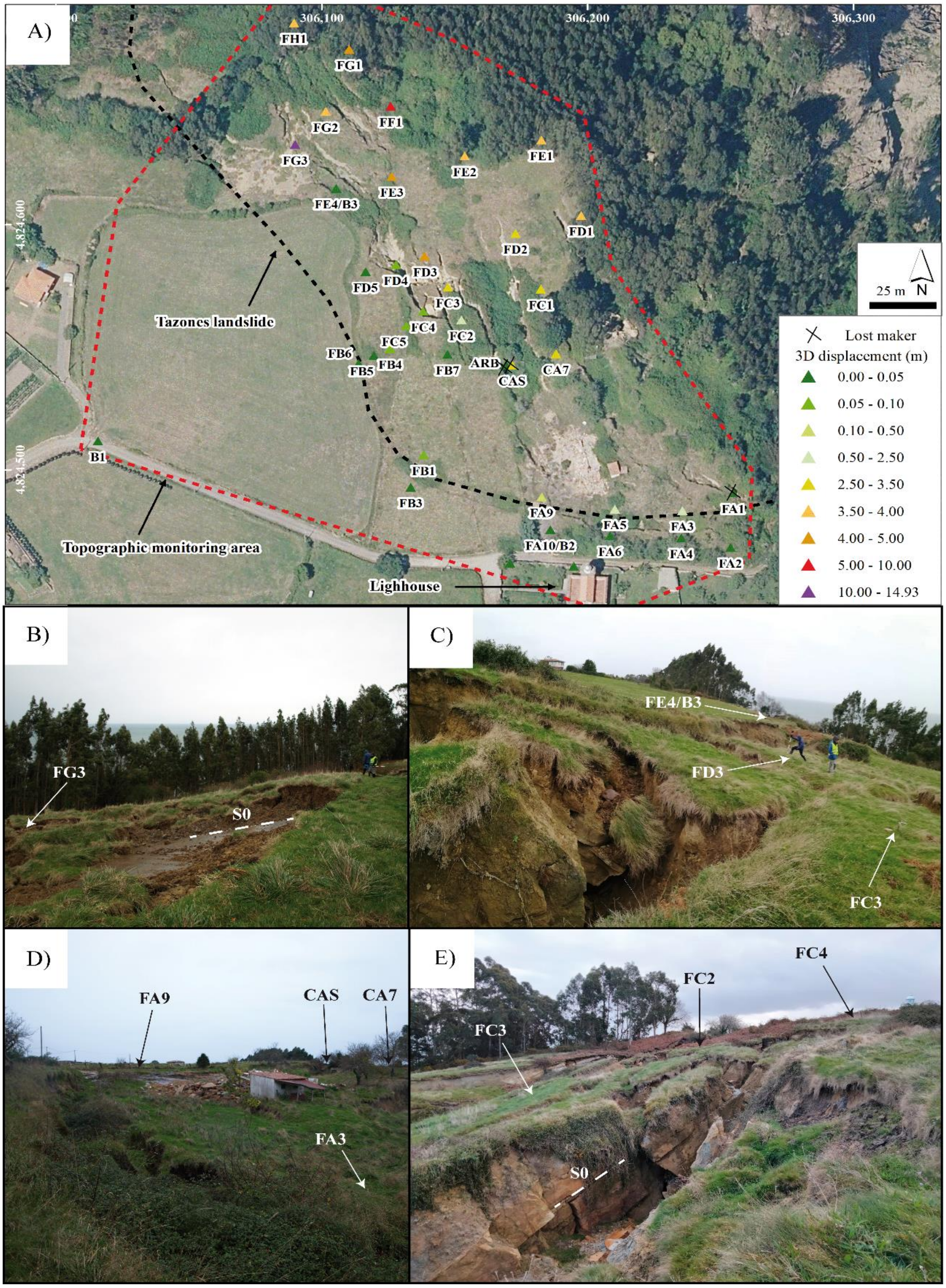

Figure 94. A) 3D displacement recorded by *in situ* monitoring in 38 markers installed at the Tazones Lighthouse landslide between June 2018 to February 2020. OrtoPNOA 2020 CC-BY 4.0 scne.es. Taken and modified from Domínguez-Cuesta *et al.* (2022a). Field evidence observed in the Tazones Lighthouse landslide: **B)** Slide developed in November 2019. **C)** Large cracks and a topple developed between November and December 2019. **D)** Area of ruins of restaurant in December 2019. **E)** State of Tazones landslide in February 2022.

Table 17. 3D cumulative displacement measured for each of the 38 markers in the 19 *in situ* monitoring campaigns developed in Tazones Lighthouse landslide between June 2018 and February 2020. Measurements are shown in m and - indicates no measurements in that campaign. Taken and modified from Domínguez-Cuesta *et al.* (2022a).

Marker	**12/06/2018**	**11/07/2018**	**27/07/2018**	**10/10/2018**	**19/11/2018**	**17/12/2018**	**17/01/2019**	**15/02/2019**	**22/03/2019**	**26/04/2019**	**24/05/2019**	**24/06/2019**	**24/07/2019**	**20/09/2019**	**18/10/2019**	**18/11/2019**	**12/12/2019**	**17/01/2020**	**14/02/2020**	**Displacement (m)**
FA1	-	0.08	0.07	0.13	0.18	0.25	0.29	-	-	-	-	-	-	-	-	-	-	-	-	Lost maker
CA8	-	-	-	-	-	-	0.06	-	-	-	-	-	-	-	-	-	-	-	-	
ARB	-	-	-	-	-	-	-	-	0.52	0.49	0.58	0.66	0.70	0.79	0.86	2.56	-	-	-	
FG3	-	0.01	0.03	0.01	0.02	0.01	0.02	0.11	0.13	0.11	0.12	0.10	0.10	0.12	0.10	14.17	14.54	14.89	14.93	10.00 - 14.93
FF1	-	-	-	-	-	-	0.13	1.07	1.45	1.67	1.76	1.85	1.88	1.96	1.99	3.20	4.34	5.91	6.60	5.00 - 10.00
FG1	-	-	-	-	-	-	0.13	0.98	1.29	1.48	1.54	1.61	1.65	1.72	1.71	2.72	3.61	4.50	4.67	4.00 - 5.00
FD3	-	0.13	0.18	0.26	0.33	0.44	0.53	1.21	1.49	1.61	1.66	1.72	1.74	1.80	1.82	2.64	3.35	4.10	4.23	
FE3	-	0.11	0.16	0.25	0.34	-	0.52	1.23	1.48	1.63	1.69	1.74	1.77	1.83	1.84	2.64	3.32	4.01	4.12	
FG2	-	0.13	0.16	0.22	0.31	0.37	0.46	1.08	1.26	1.38	1.41	1.44	1.45	1.50	1.51	2.53	3.11	3.65	3.75	3.50 - 4.00
FE2	-	-	-	-	-	-	0.10	0.81	1.08	1.22	1.27	1.33	1.35	1.41	1.43	2.23	2.92	3.62	3.75	
FH1	-	-	-	-	-	-	0.10	0.77	0.99	1.13	1.19	1.23	1.25	1.30	1.31	2.18	2.86	3.60	3.73	
FD1	-	-	-	-	-	-	0.11	0.80	1.09	1.21	1.26	1.33	1.32	1.40	1.42	2.20	2.90	3.57	3.69	
FE1	-	-	-	-	-	-	0.11	0.82	1.06	1.20	1.26	1.29	1.32	1.40	1.41	2.19	2.86	3.56	3.67	
CAS	-	-	-	-	-	-	-	-	0.35	0.43	0.53	0.59	0.63	0.69	0.73	1.63	2.46	3.29	3.45	2.50 - 3.50
FC1	-	-	-	-	-	-	0.11	0.76	1.02	1.12	1.17	1.20	1.22	1.28	1.30	2.03	2.64	3.24	3.35	
FD2	-	-	-	-	-	-	0.11	0.75	1.04	1.11	1.16	1.21	1.22	1.28	1.29	2.01	2.62	3.21	3.31	
CA7	-	-	-	-	-	-	0.09	0.68	0.95	1.02	1.07	1.11	1.15	1.19	1.20	1.89	2.47	3.05	3.17	
FC3	-	0.10	0.14	0.19	0.25	0.32	0.40	0.88	1.12	1.16	1.19	1.24	1.23	1.28	1.29	1.85	2.34	2.88	2.97	
FC2	-	-	-	-	-	-	0.06	0.51	0.66	0.76	0.78	0.82	0.82	0.86	0.87	1.37	1.74	2.15	2.21	0.50 - 2.50
FA3	-	0.09	0.09	0.16	0.20	0.26	0.31	0.69	0.77	0.87	0.91	0.93	0.95	0.98	0.97	1.35	1.63	1.89	1.94	
FA5	-	0.08	0.09	0.15	0.19	0.22	0.28	0.61	0.73	0.77	0.79	0.82	0.83	0.85	0.86	1.16	1.39	1.60	1.61	

Marker	**12/06/2018**	**11/07/2018**	**27/07/2018**	**10/10/2018**	**19/11/2018**	**17/12/2018**	**17/01/2019**	**15/02/2019**	**22/03/2019**	**26/04/2019**	**24/05/2019**	**24/06/2019**	**24/07/2019**	**20/09/2019**	**18/10/2019**	**18/11/2019**	**12/12/2019**	**17/01/2020**	**14/02/2020**	
FA9	-	0.02	0.03	0.04	0.05	0.06	0.07	0.13	0.16	0.14	0.13	0.14	0.12	0.13	0.13	0.13	0.12	0.12	0.12	0.10 - 0.50
FB2	-	0.02	0.03	0.04	0.05	0.05	0.07	0.07	0.09	0.09	0.08	0.08	0.08	0.09	0.08	0.08	0.08	0.09	0.09	0.05 - 0.10
FD4	-	0.03	0.04	0.04	0.04	0.04	0.06	0.07	0.12	0.08	0.07	0.07	0.05	0.07	0.08	0.07	0.06	0.08	0.08	
FC5	-	0.01	0.04	0.04	0.05	0.05	0.05	0.07	0.08	0.07	0.08	0.06	0.06	0.07	0.07	0.07	0.06	0.07	0.07	
FB4	-	0.02	0.05	0.04	0.04	0.05	0.06	0.07	0.10	0.07	0.08	0.07	0.05	0.06	0.06	0.06	0.06	0.07	0.07	
FC4	-	0.01	0.05	0.04	0.04	0.07	0.07	0.09	0.09	0.10	0.08	0.08	0.06	0.08	0.06	0.08	0.07	0.08	0.07	
FB1	-	0.02	0.04	0.04	0.04	0.04	0.04	0.06	0.08	0.05	0.06	0.06	0.05	0.05	0.06	0.06	0.05	0.06	0.06	
FB5	-	0.01	0.02	0.02	0.03	0.03	0.04	0.04	0.07	0.04	-	-	0.03	0.04	0.03	0.03	0.04	0.04	0.04	0.00 - 0.05
FD5	-	0.02	0.02	0.01	0.01	0.02	0.01	0.02	0.11	0.02	0.02	0.01	0.05	0.04	0.05	0.04	0.02	0.04	0.03	
FB7	-	-	-	-	-	-	0.01	0.02	0.05	0.03	0.03	0.02	0.01	0.01	0.02	0.02	0.01	0.03	0.03	
FA10	-	0.01	0.00	0.01	0.02	0.02	0.02	0.01	0.06	0.01	0.01	0.01	0.01	0.03	0.03	0.03	0.02	0.02	0.03	
FA2	-	0.03	0.01	0.03	0.02	0.03	0.03	0.02	0.02	0.02	0.03	0.04	0.02	0.01	0.03	0.03	0.01	0.01	0.02	
FB6	-	0.01	0.02	0.01	0.02	0.02	0.02	0.02	0.02	0.03	0.03	0.01	0.02	0.03	0.02	0.01	0.01	0.02	0.02	
FE4	-	0.02	0.03	0.01	0.02	0.01	0.03	0.03	0.02	0.03	0.02	0.02	0.01	0.01	0.02	0.03	0.03	0.02	0.02	
FA6	-	0.02	0.01	0.02	0.01	0.01	0.02	0.01	0.05	0.01	0.02	0.02	0.01	0.02	0.04	0.01	0.01	0.01	0.01	
FA4	-	0.02	0.02	0.02	0.01	0.02	0.02	0.03	0.02	0.02	0.02	0.02	0.01	0.01	0.02	0.02	0.01	0.01	0.01	
FB3	-	0.00	0.02	0.02	0.01	0.02	0.01	0.02	0.05	0.02	0.02	0.02	0.01	0.02	0.01	0.02	0.01	0.01	0.01	

4.2 Mountain area of Asturias

The LOS deformation velocity map obtained for the mountain area by using PSIG software (Figure 95) shows rates from −18.4 to 10.0 mm year^{-1}. A total of 40,201 PS were detected. 34,963 presented stable velocities (from −2.5 to 2.5 mm year^{-1}) and represented 86.97% of total PS (Table 18). The deformation time series showed maximum accumulated displacements of −43.4 and 36.6 mm. In addition, the PS density obtained for the study area was 58.9 PS km^{-2}. The main statistics of A-DInSAR results obtained are summarized in Table 18.

With respect to VLOS rates (Table 18), LOS velocity PS < −10.0 mm year^{-1} (11 PS, 0.03%) were detected as isolated PS along the study area, although in Langreo area they appeared as active grouped PS (Figure 96 and Figure 97 A - TS-1). These ground motion could be associated mainly to subsidence, and to a lesser extent, landslides. LOS velocity rates between −10.0 and −5.0 mm year^{-1} (75 PS, 0.19%) could be found in both isolated PS and clustered PS, defined in some cases by deformations (Figure 96). VLOS rates from −5.0 to −2.5 mm year^{-1} (1,950 PS, 4.85%) appeared grouped in some areas with deformations in the Langreo and Mieres cities. The TS observed in these PS were similar to the TS-1 (Figure 96); then, these deformations could be compatible with slope instabilities and subsidence. The LOS velocity rates of 2.5 - 5.0 mm year^{-1} (2,341 PS, 5.82%) were detected as grouped PS along the study area, showing movements in Langreo city (Figure 96). Moreover, these PS were found associated to PS with VLOS > 5 mm year^{-1}. Lastly, the PS with LOS rates of 5.0 - 10.0 mm year^{-1} (861 PS, 2.14%) were measured in Langreo city, indicating ground deformations (Figure 96 and Figure 97 B - TS-2). Deformations with VLOS > 2.5 mm year^{-1} were the most difficult ones to interpret, because they were located over flat terrains and showing an uplift. Also, positive PS with jumps in the TS could be observed at the East of the study area (Figure 96 and Figure 97 C - TS-3). These jumps were related to aliasing and phase unwrapping errors (Figure 97 C - TS-3). In addition, for the rest of the study area, PS with VLOS > 2.5 mm year^{-1} are linked to anthropic activities, such as quarries or construction sites (Figure 96).

Based on the deformations observed in Figure 95 and Figure 96 and the time series observed (Figure 97), a detailed analysis of the area corresponding to the Langreo town is carried out below.

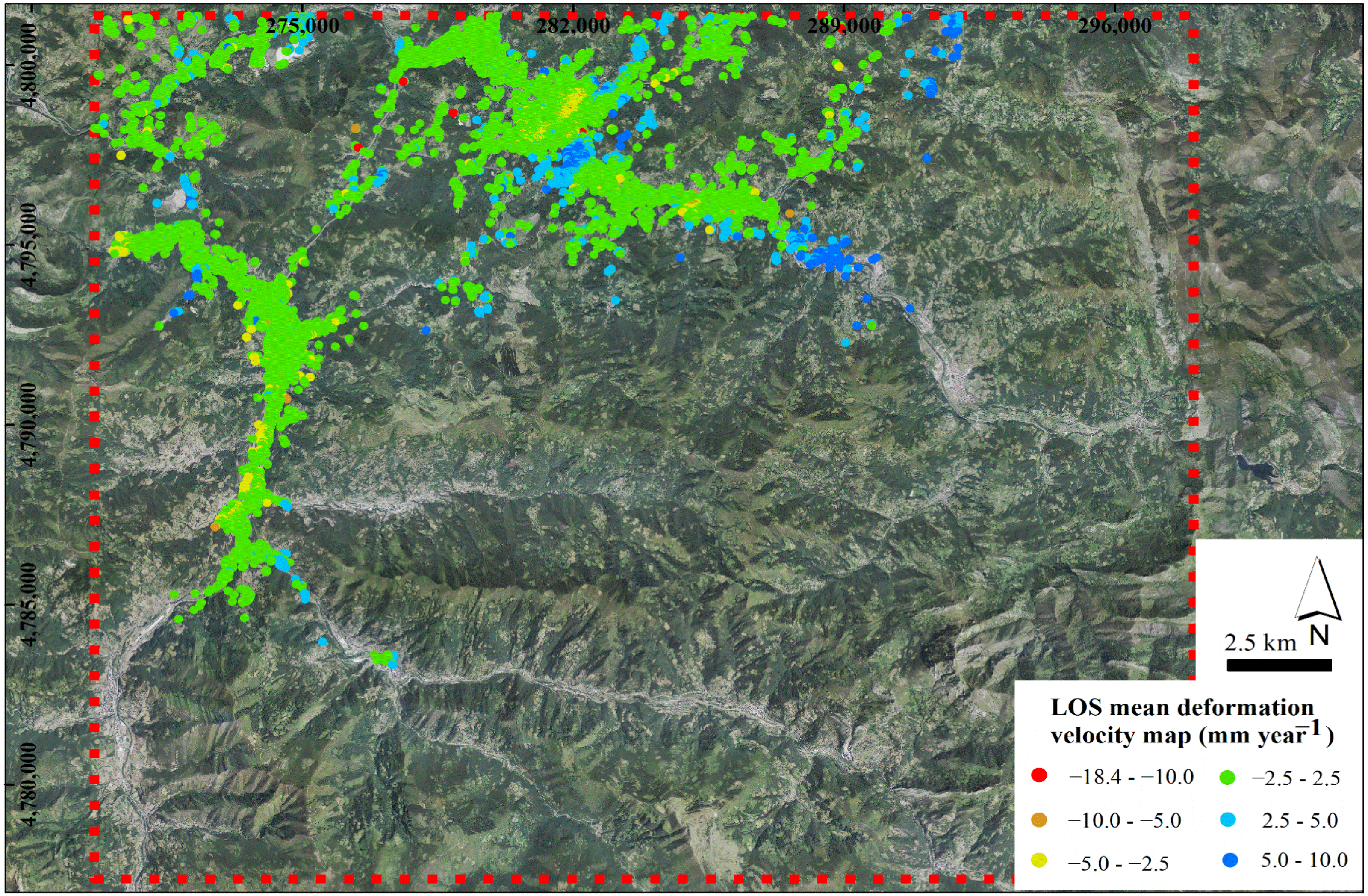

Figure 95. LOS mean deformation velocity map (mm year^{-1}) of the Asturias mountain study area between January 2018 and February 2020. OrtoPNOA 2017 CC-BY 4.0 scne.es. Taken and modified from Cuervas-Mons *et al.* (2021c, 2022a).

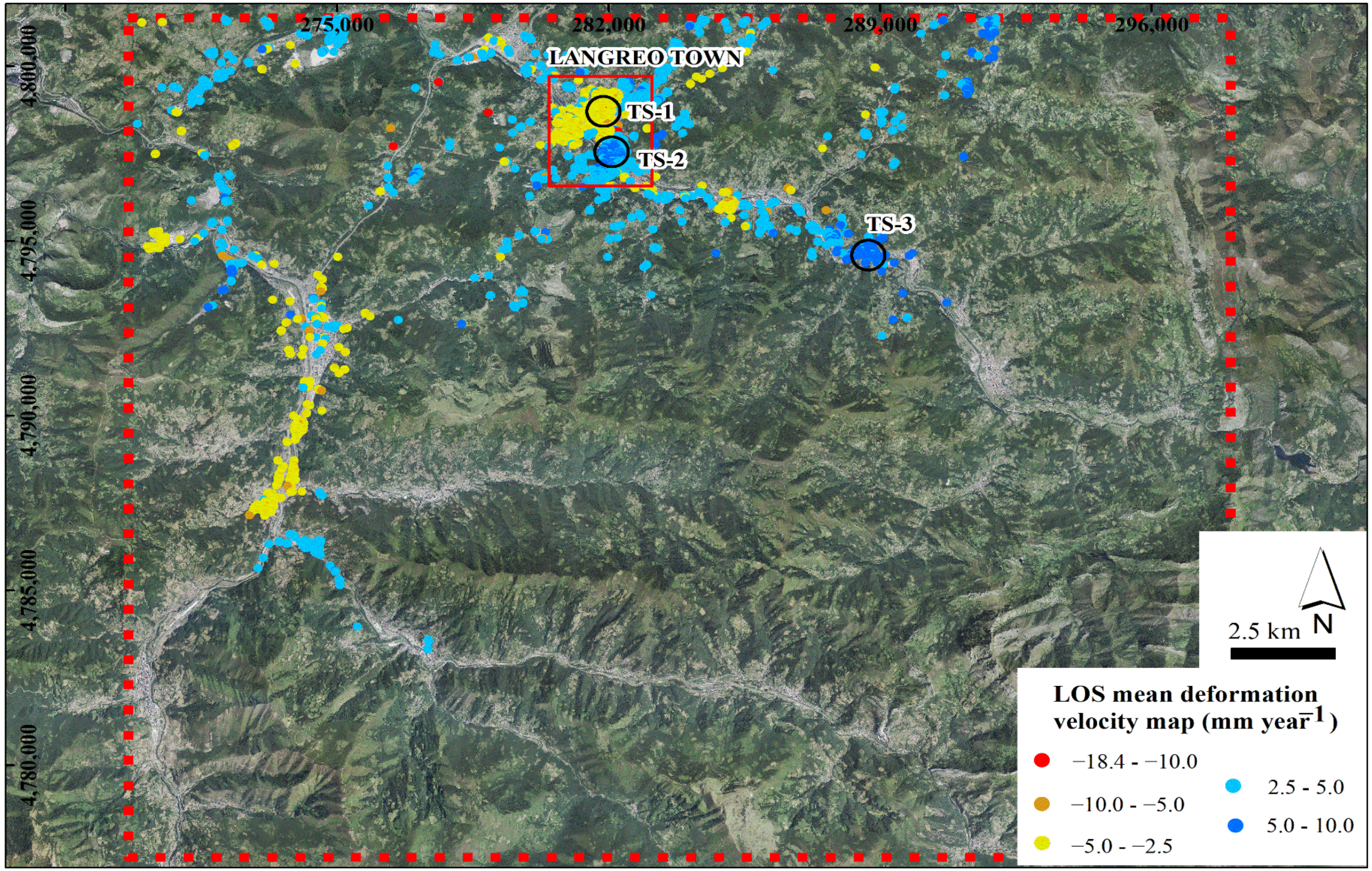

Figure 96. LOS mean deformation velocity map without stable points (mm year^{-1}) of the Asturias mountain study area between January 2018 and February 2020. Deformation time series are shown in Figure 97. The red rectangle indicates the Langreo town area where local analysis was carried out. OrtoPNOA 2017 CC-BY 4.0 scne.es. Taken and modified from Cuervas-Mons *et al.* (2021c, 2022a).

Table 18. Main statistics of the LOS mean deformation velocity map (mm year^{-1}) and the LOS velocity rates at regional scale. Taken and modified from Cuervas-Mons *et al.* (2021c, 2022a).

Main statistics	**LOS velocity Rates (mm year^{-1})**		
Mean: 0.25	**LOS Rates**	**Number of PS**	**%**
Minimum: −18.4	−18.4 - −10.0	11	0.03
Maximum: 10.0	−10.0 - −5.0	75	0.19
PS km^{-2}: 58.9	−5.0 - −2.5	1,950	4.85
	−2.5 - 2.5	34,963	86.97
Total of PS:	2.5 - 5.0	2,341	5.82
40,201	5.0 - 10.0	861	2.14

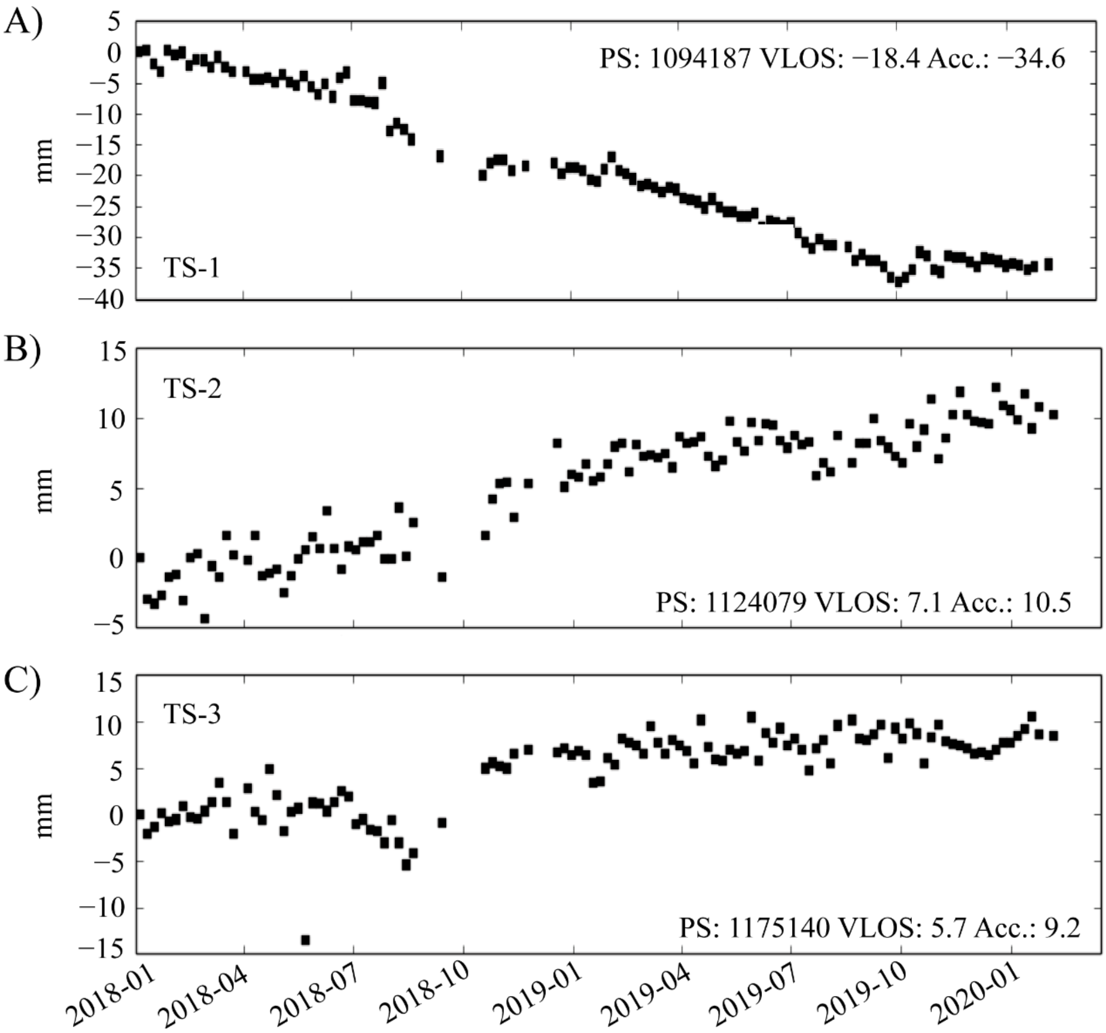

Figure 97. Obtained deformation time series. Location of TS are shown in Figure 96. **A)** TS-1 obtained over Langreo area and showing a subsidence movement. **B)** TS-2 obtained over Langreo area and showing an uplift movement. **C)** Example of an aliasing - unwrapping error error. Taken and modified from Cuervas-Mons *et al.* (2021c, 2022a).

4.2.1 Langreo town

With regard to LOS mean deformation velocities of Langreo area (Figure 98 and Table 19), VLOS showed ground deformations with rates ranging from −18.4 to 9.5 mm year^{-1}, whose average VLOS detected was −0.16 ± 2.2 mm year^{-1}. The total of PS measured was 12,946 PS, with a PS density of 1,559.8 PS km^{-2} (Table 19). As for the deformation time series, the maximum accumulated displacements were −38.9 and 36.6 mm, with an average accumulated displacement of −1.04 ± 4.9 mm (Table 19). Concerning VLOS rates, LOS velocity PS < −10.0 mm year^{-1} (6 PS, 0.05%) were detected as one group of PS in the alluvial plain, over the urban core of La Felguera (Figure 98). These PS appeared jointly with those PS with VLOS between −10.0 and −2.5 mm year^{-1}. The PS with VLOS rates among −10.0 and −5.0 mm year^{-1} (36 PS, 0.28%) were identified along the alluvial plain of La Felguera and jointly of PS with −5.0 - −2.5 mm year^{-1}. Also, these values could be found in some slope zones (Figure 98). The PS with VLOS rates between −5.0 and −2.5 mm year^{-1} (1,346 PS, 10.39%) were mainly detected over the alluvial plain and over some slopes located at the North and West of the study area. In addition, these PS could be observed over anthropic deposits located on flat and sloping terrains (Figure 98). The LOS velocity rates with 2.5 and 5.0 mm year^{-1} (880 PS, 6.80%), were observed along the urban zone of Sama, to the South of study area, covering both the alluvial plain and sloping terrains. Moreover, these PS were measured at North of Candín I pit (sector located at Northeast of the study area) (Figure 98). PS with LOS rate of 5.0 - 10.0 mm year^{-1} (537 PS, 4.15%) were located also to the South of the study area, covering the alluvial and anthropic deposits (Figure 98). In the same way, these same LOS velocities were detected in the Northeast part of the study area, both in colluvium deposits and in areas without surficial formations.

Table 19. Main statistics of the LOS mean deformation velocity map (mm year^{-1}) and the LOS velocity rates at local scale: Langreo area. Taken and modified from Cuervas-Mons *et al.* (2021c, 2022a).

Main statistics	**LOS velocity Rates (mm year^{-1})**		
Mean: −0.16	**LOS Rates**	**Number of PS**	**%**
Minimum: −18.4	−18.4 - −10.0	6	0.05
Maximum: 9.5	−10.0 - −5.0	36	0.28
σ: 2.23	−5.0 - −2.5	1,346	10.39
PS km^{-2}: 1,559.8	−2.5 - 2.5	10,141	78.33
Total of PS:	2.5 - 5.0	880	6.80
12,946	5.0 - 9.5	537	4.15

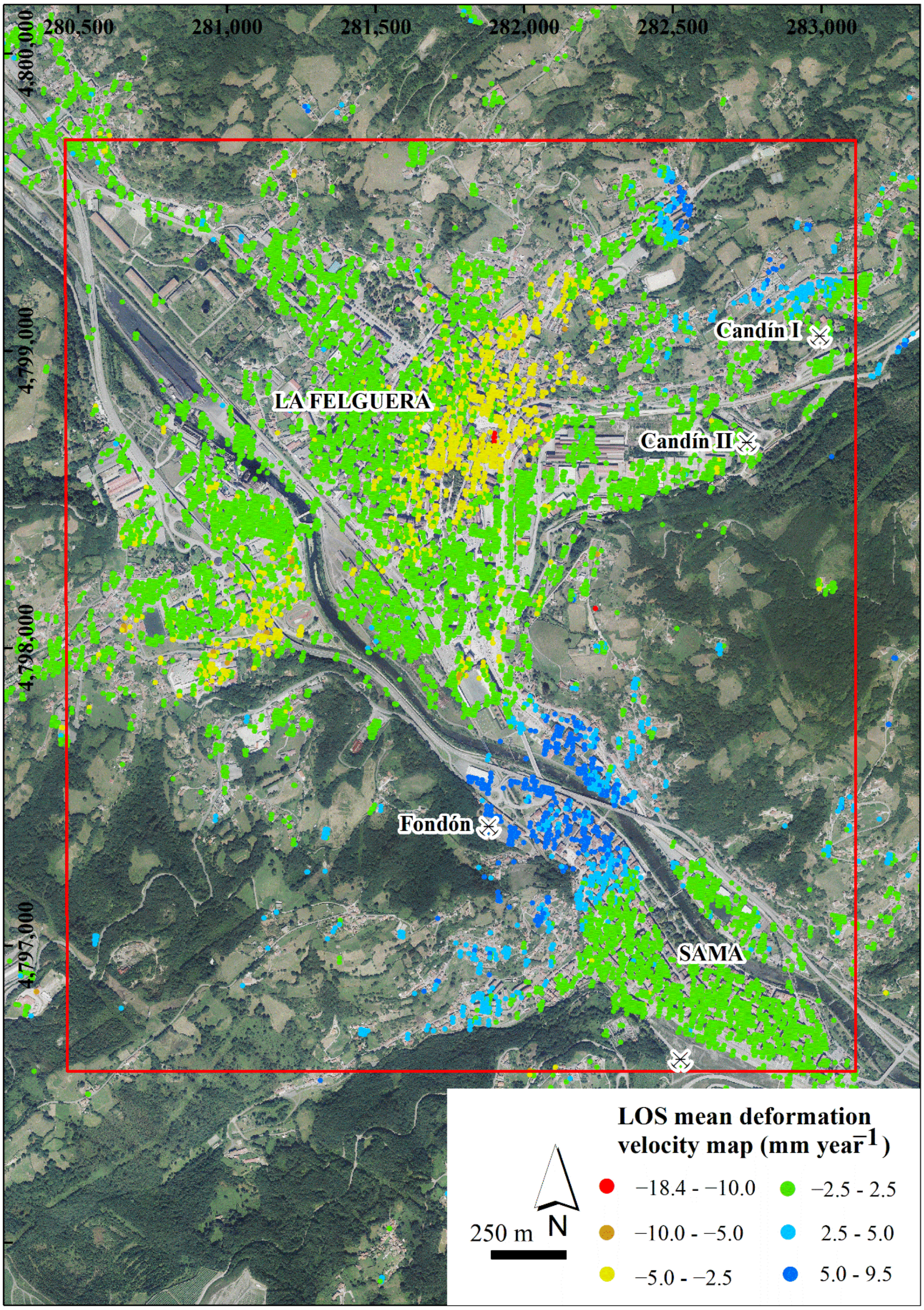

Figure 98. VLOS detected in the Langreo town. OrtoPNOA 2017 CC-BY 4.0 scne.es. Taken and modified from Cuervas-Mons *et al.* (2021c, 2022a).

A-DInSAR vs surficial formations cover

Regarding surficial formations located in the Langreo town (Figure 99), the total area of these Quaternary deposits is 4.19 km^2. A total of 10,633 VLOS PS (82.16%) were detected over these materials, with LOS velocities rates ranging from −18.4 to 9.5 mm year^{-1}. Their accumulated displacements ranged from −38.2 to 36.6 mm (Table 20). Quaternary deposits include alluvial deposits (2.64 km^2), whose mean VLOS was −0.4 mm year^{-1}; anthropic (0.71 km^2), with a VLOS average of 1.5 mm year^{-1}; colluvium (0.74 km^2), with a VLOS average of −0.5 mm year^{-1}; and flow (0.09 km^2), with a VLOS average of 1.4 mm year^{-1} (Table 20). Moreover, there was an area of 4.11 km^2 with VLOS ranging from −14.0 to 8.2 mm year^{-1}, without mapped surficial formations (Figure 99 and Table 20).

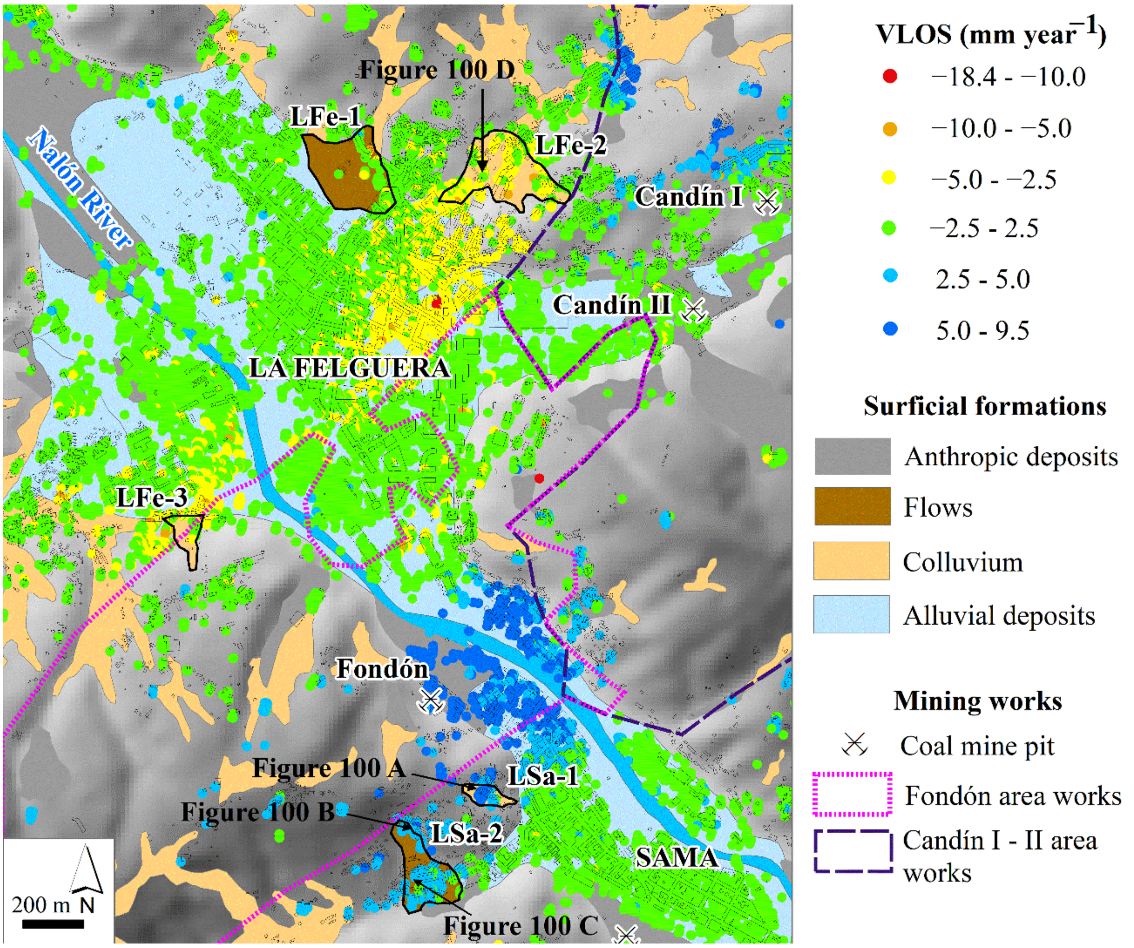

Figure 99. Surficial formations, mining works and LOS mean deformation velocity map (mm year^{-1}) of Langreo area. Taken and modified from Cuervas-Mons *et al.* (2021c, 2022a).

Table 20. Langreo study area data: Area (km^2), number of PS, % PS, VLOS (mm year^{-1}) and accumulated deformation (mm).

Surficial deposit	Area (km^2)	Number of PS	% PS	VLOS Rates (mm year^{-1})	Deformation rates (mm)
Alluvial	2.64	9,393	72.56	−18.4 - 9.5	−38.2 - 36.6
Anthropic	0.71	644	4.97	−3.0 - 9.5	−14.2 - 28.2
Colluvium	0.74	445	3.44	−6.9 - 7.4	−24.4 - 16.5
Flow	0.09	151	1.17	−6.1 - 4.9	−12.8 - 9.6
Without deposit	4.11	2,313	17.86	−14.0 - 8.2	−38.9 - 26.4

Five surficial deposits of colluvium and flow were analyzed because they presented active PS (LSa-1, LSa-2, LFe-1, LFe-2, and LFe-3; Figure 99). These identified deposits were the following:

LSa-1 is located on Sama, at the South of the study area (Figure 99). It has an extension of 8,057 m^2. This area is characterized by a maximum slope of 40º and there are some houses with meadows and county roads. Surficial formation consists of a colluvium deposit, which presented VLOS rates from 1.9 - 7.4 mm year^{-1}, and a VLOS average of 5.1 mm year^{-1}. The accumulated deformation rates ranged from 2.7 to 16.5 mm, with a displacement average of 8.9 mm. In the field it could be recognized profuse tension cracks distributed along a road. They are characterized by few of meters of length and some centimeters - millimeters wide (Figure 100 A).

LSa-2 is also located near Sama (Figure 99). It presents an area of 35,083 m^2. This sector presents different roads and abundant buildings. The slope can reach 40º. The mass movement typology is flow, whose VLOS were ranging from 0.3 - 4.9 mm year^{-1} and a mean VLOS of 3.2 mm year^{-1}. The accumulated deformation rates ranged from −4.9 to 9.6 mm, with an average of 5.1 mm of displacement. The evidence of movement include different tense cracks in the different roads (Figure 100 B), in some old buildings and houses. They present from few to tens meters of length and centimeters wide (Figure 100 C).

LFe-1 is located on La Felguera, to the North of the study area (Figure 99). This area is a neighbourhood with buildings and a forested park. The maximum slope in this sector is of 12º. As to the typology of instability, it is a flow with an area of 55,914 (m^2). 60 PS were detected, with VLOS rates ranging from −6.1 to 2.8 mm year^{-1}, being average VLOS −1.3 mm year^{-1}. The accumulated deformation presented rates from −12.8 to 6.4 mm and the mean accumulated deformation was −3.3 mm. It has not been observed movement evidence in the field.

LFe-2 is also located on La Felguera (Figure 99); in an urbanisation of villas and houses with meadow areas. This sector is characterized by present maximum slopes of 20 - 25º. The surficial formation consists of a colluvium whose extension is 57,016 m^2.

PS presented VLOS rates from −6.9 - 0.8 mm year^{-1} and a mean VLOS of −2.8 mm year^{-1}. As to accumulated deformation, PS registered between −16.7 and −0.1 mm, and a mean accumulated deformation of −7.3 mm. In addition, signs of creep movements (Figure 100 D) and abundant retaining walls to support the slopes can be found.

LFe-3 is also located on the La Felguera town, to the West of the study area (Figure 99). Unlike the previous cases, this colluvium (11,470 m^2) could not be visited because nowadays it is located in a highly anthropized area with an important industry. Here, the slope can reach 25º. Evidence of movement could not be observed because the area is an industrial sector with restricted access. The A-DInSAR results indicated VLOS rates from −4.1 - −2.0 mm year^{-1} and a mean VLOS of −2.7 mm year^{-1}. The mean accumulated deformation was −6.5 mm.

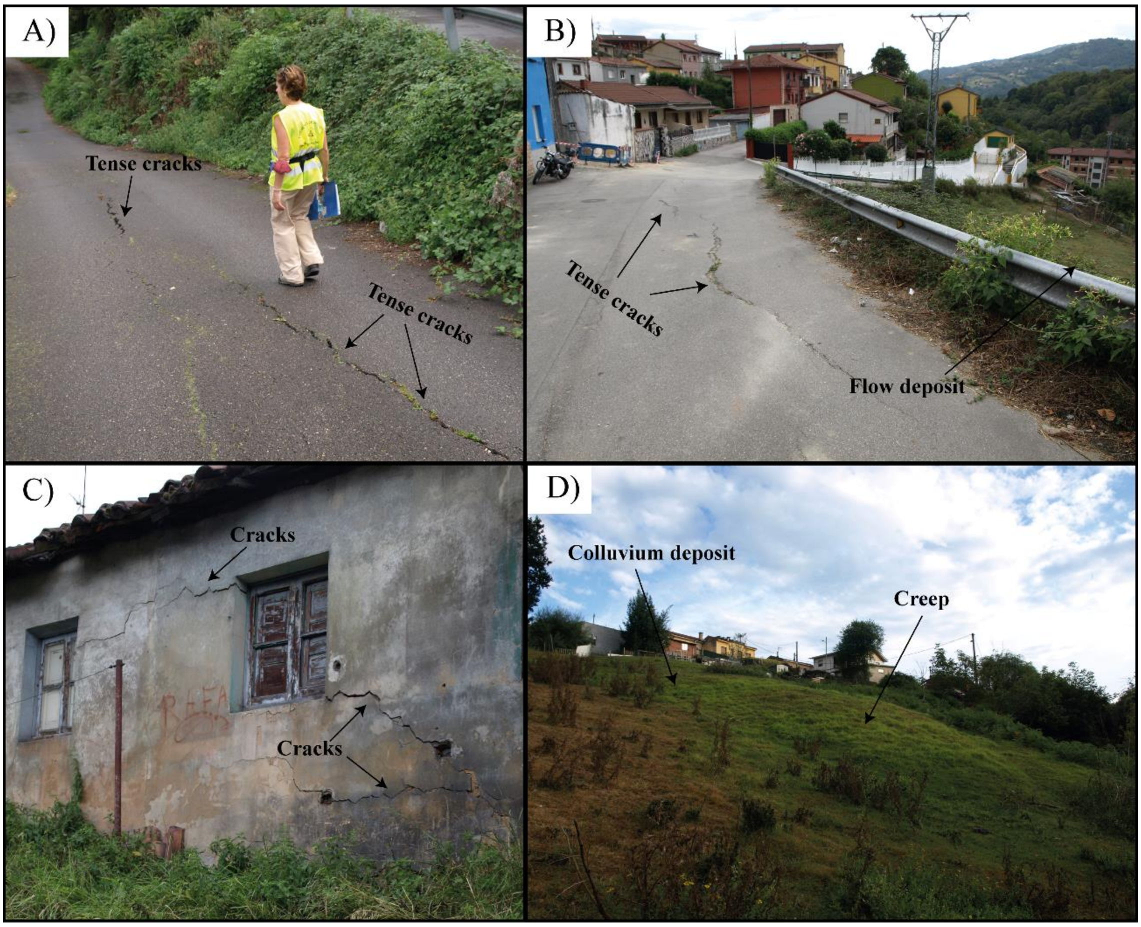

Figure 100. Field evidence observed in different surficial deposits. **A)** Cracks in a road on the top of the colluvium LSa-1. **B)** Cracks in a road on the top of the flow LSa-2. **C)** Damage in an old building located at the bottom of flow LSa-2. **D)** Creep phenomena affecting surface of colluvium LFe-2. See evidence location in Figure 99. Photos taken on September 2021.

Time series detected over studied deposits (Figure 99) were analyzed with respect to daily rainfall dataset (Figure 101). TS measured in all surficial deposits not always presented a clear tendency and were difficult to study and interpret. However, some trends and patterns could be observed.

Colluvium LFe-2 showed four deformation stages (Figure 101 A). Firstly, from January 2018 to April 2018, there was a stabilization period. Afterward, between April 2018 and March 2019, there was a rise of displacement with maximum deformation of −9 mm that coincided with rainy periods (maximum rainfall registered of 76.5 mm in February 2019). Thirdly, from March 2019 to September/October 2019, there was a stabilization of deformation that coincided with a dry season and scarce rains. Finally, there was a rise of deformation with maximum displacement of −16.7 mm from September/October 2019 to February 2020. This period matched with rainfall episodes of October 2019 (47.5 mm), November 2019 (50.5 mm) and December 2019 (54.0 mm) (Figure 101 A).

In the case of colluvium LSa-1 (Figure 101 B), TS showed a linear trend of deformation rise according to accumulated rainfall. The maximum displacement reached was 16.5 mm. On the contrary, flow LSa-2 (Figure 101 C) presented different periods of deformation corresponding with rainy periods. Firstly, from January to May 2018, there was a rise of deformation until 6 mm and monthly accumulated rainfall of 37.6 (February), 41.3 (March) and 50.3 (June) mm. Secondly, a descent and subsequent stabilization of deformation (from 6 mm to 2 mm) between June to October 2018 was developed. During this period the rainfall registered a maximum of 47.8 mm in July, although this period was characterized by being a dry season. Thirdly, from October 2018 to February/March 2019 there was an increase of displacement (from 2 to 8.6 mm) which corresponded to two important monthly rainfall episodes with 56.5 and 76.5 mm. The fourth period, between February/March 2019 and October 2019, was characterized by a stabilization of deformation, coinciding with a dry period and scarce rains. Lastly, from October 2019 to February 2020 there was a rise of displacement until a maximum of 9.6 mm. This period matched with rainfalls in October (47.5 mm), November (50.5 mm) and December (54.0 mm) (Figure 101 C).

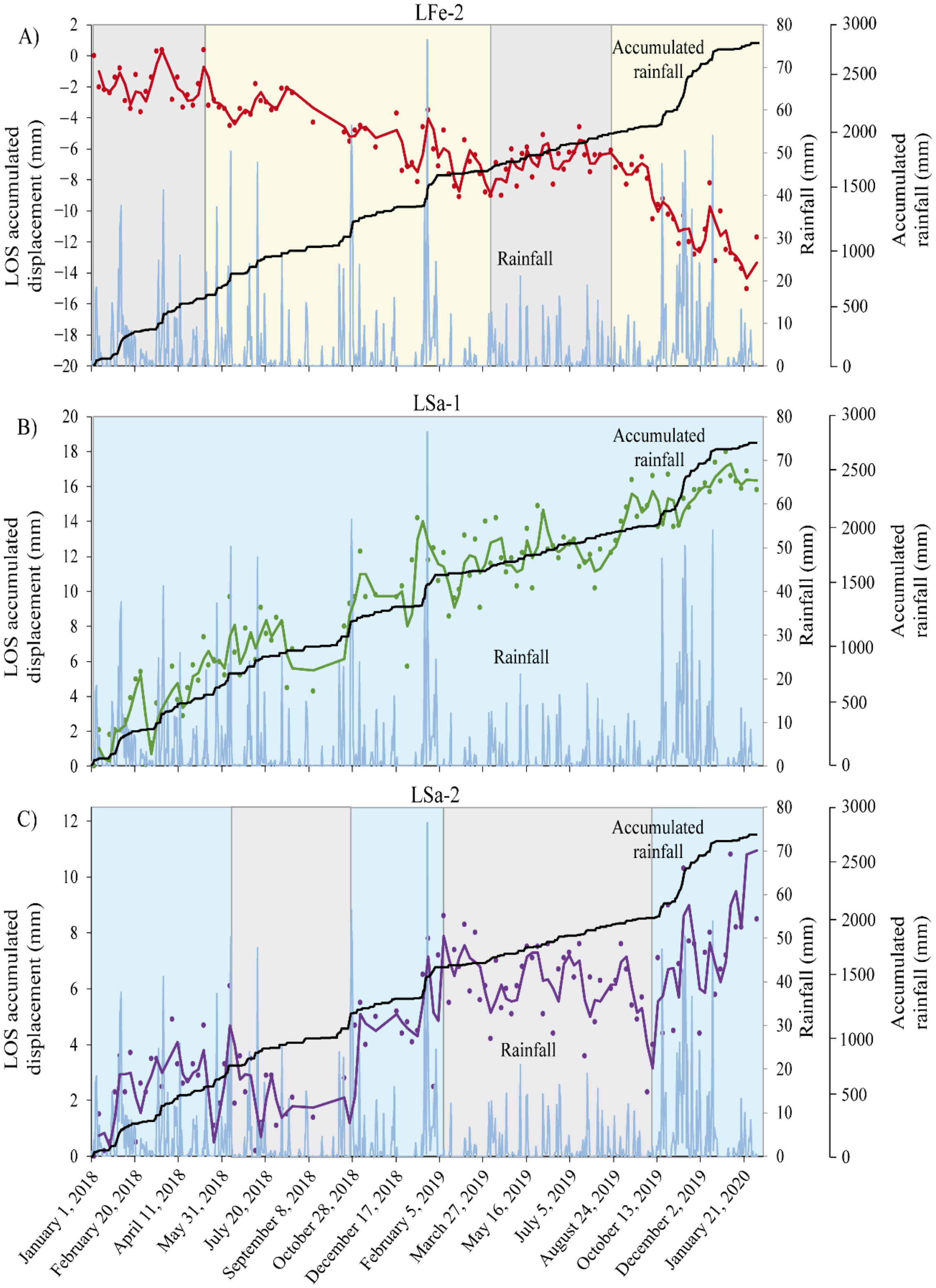

Figure 101. LOS time series of surficial deposits versus daily and accumulated rainfall data. Periods of deformation were defined according to time series with following colours: Blue, positive deformation; gray, deformation is maintained; yellow, negative deformation. **A)** Colluvium LFe-2. **B)** Colluvium LSa-1. **C)** Flow LSa-2.

A-DInSAR vs coal mined areas

As mentioned above, this area was an important coal mining sector, with the presence of: 1) Valley floor works (Figure 98), including three coal vertical pits: Fondón (1906 - 1995) (Figure 102 A), Candín I (Santa Eulalia pit, 1943 - 1996) (Figure 102 B) and Candín II (San Enrique-Lláscaras pit, 1933 - 2013) (Figure 102 C) beneficied by HUNOSA Group and 2) Mountain mining works, including La Nalona, Respinedo, Rufina and La Moral mines (from mid-19th century to early 20th century) (HUNOSA *et al.*, 2011). Fondón, Candín I and Candín II pits are located in the valley floor of Nalón river, where predominant surficial materials are anthropic and alluvial (from 1 m to greater than 10 m thickness) deposits (Figure 99). In depth, bedrock consists of 1) clay, sandstone and conglomerate mesozoic materials and 2) Carboniferous sandstone, slate and conglomerate with explotable coal layers (IGME, 1973).

With respect to these pits (HUNOSA *et al.*, 2011; HUNOSA, 2018), Fondón works involved the excavation of 327.04 km of galleries, with a total of extracted rock volume of 3,719,233 m^3, and with an extension of the underground mining network of approximately of 5.06 km^2. The maximum depth of this pit is 662 m (Figure 102 D). Candín I and Candín II works involved 271.14 km of excavated galleries, with a total extension of underground mining network of 8.28 km^2. In the case of Candín I, the maximum depth is 692 m (Figure 102 D), while Candín II pit reach 678 m of depth (Figure 102 D). Moreover, the three pits have been connecting to each other since 1973, constituting a single mining system and presenting a total extracted volume of 4,276,435 m^3 (HUNOSA, 2018) (Figure 102 D).

In the Langreo study area (Figure 98 and Table 21), the total exploited area of Fondón and Candín I-II mining works is 4.1 km^2. A total of 2,161 PS were detected in Fondón area works, with LOS velocities ranges from −14.0 to 9.5 mm year^{-1}. The average VLOS detected in this mined area was 0.9 mm year^{-1} (Table 21). In the case of Candín I-II mining works area, the total of PS detected were 1,381. The VLOS presented rates between −5.1 to 8.1 mm year^{-1}, with an average VLOS of 1.2 mm year^{-1} (Table 21).

Table 21. Significant data of vertical pits mining work areas of Langreo.

Mining works areas	Pit depth (m)	Exploited area (km^2)	Number of PS	VLOS rates (mm year^{-1})	Deformation rates (mm)
Fondón	662	2.3	2,161	−14.0 - 9.5	−38.9 - 17.5
Candín I-II	692 - 678	1.8	1,381	−5.1 - 8.2	−16.4 - 20.3

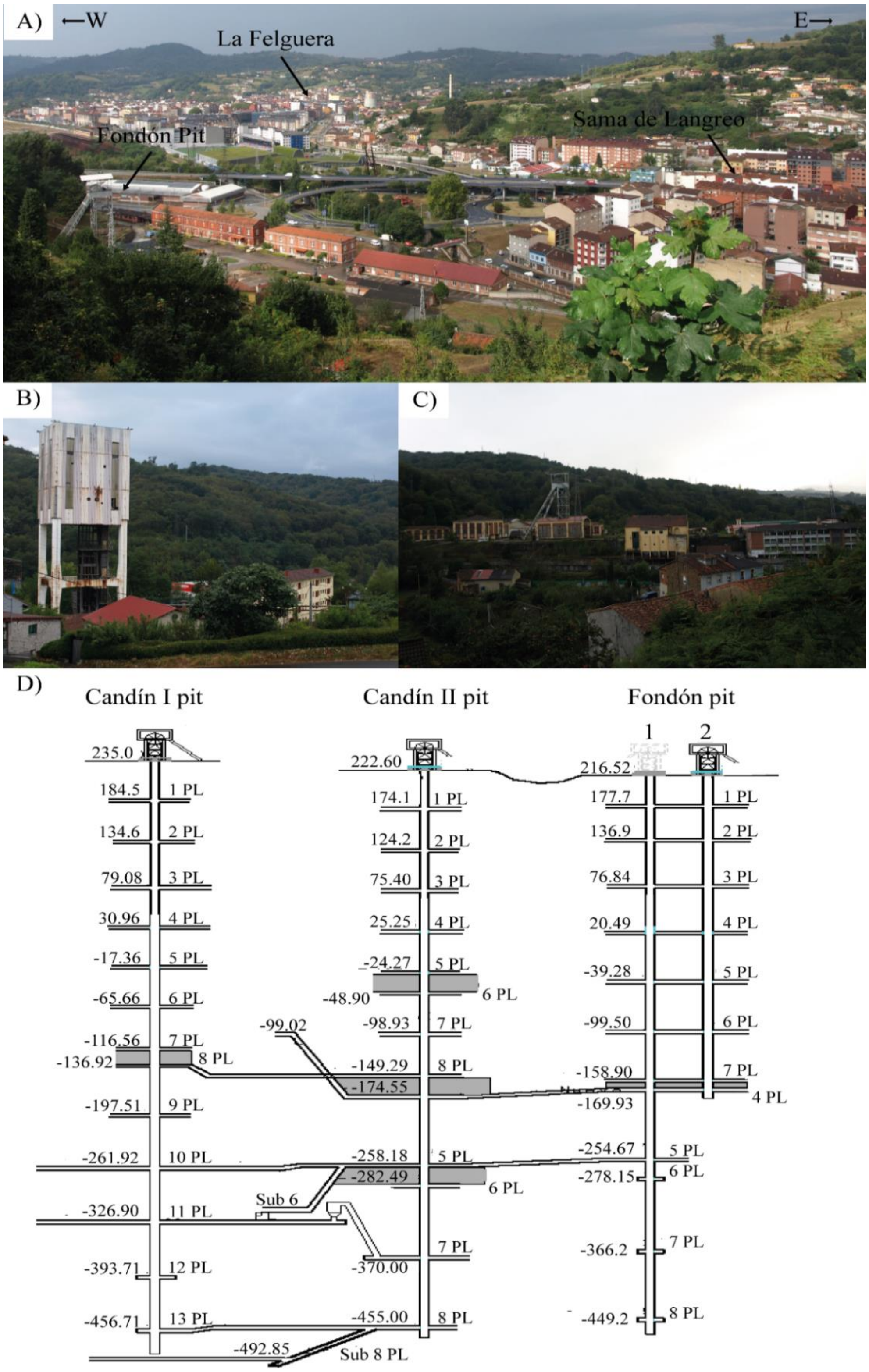

Figure 102. A) Panoramic view showing La Felguera and Sama de Langreo towns. Fondón pit can be seen in the foreground, on the left. **B)** Candín I (Santa Eulalia) pit. **C)** Candín II (Lláscaras-San Enrique) pit. **D)** General scheme of the vertical pits with main plants and connections (graphs modified from HUNOSA *et al.* (2011) and HUNOSA (2018). The geographical location of these vertical pits is displayed in Figure 98 and Figure 99. Photos taken on September 2021.

A clear relationship between the active PS detected and the location and orientation of Fondón, Candín I and Candín II mining works was observed (Figure 103 A, B and C).

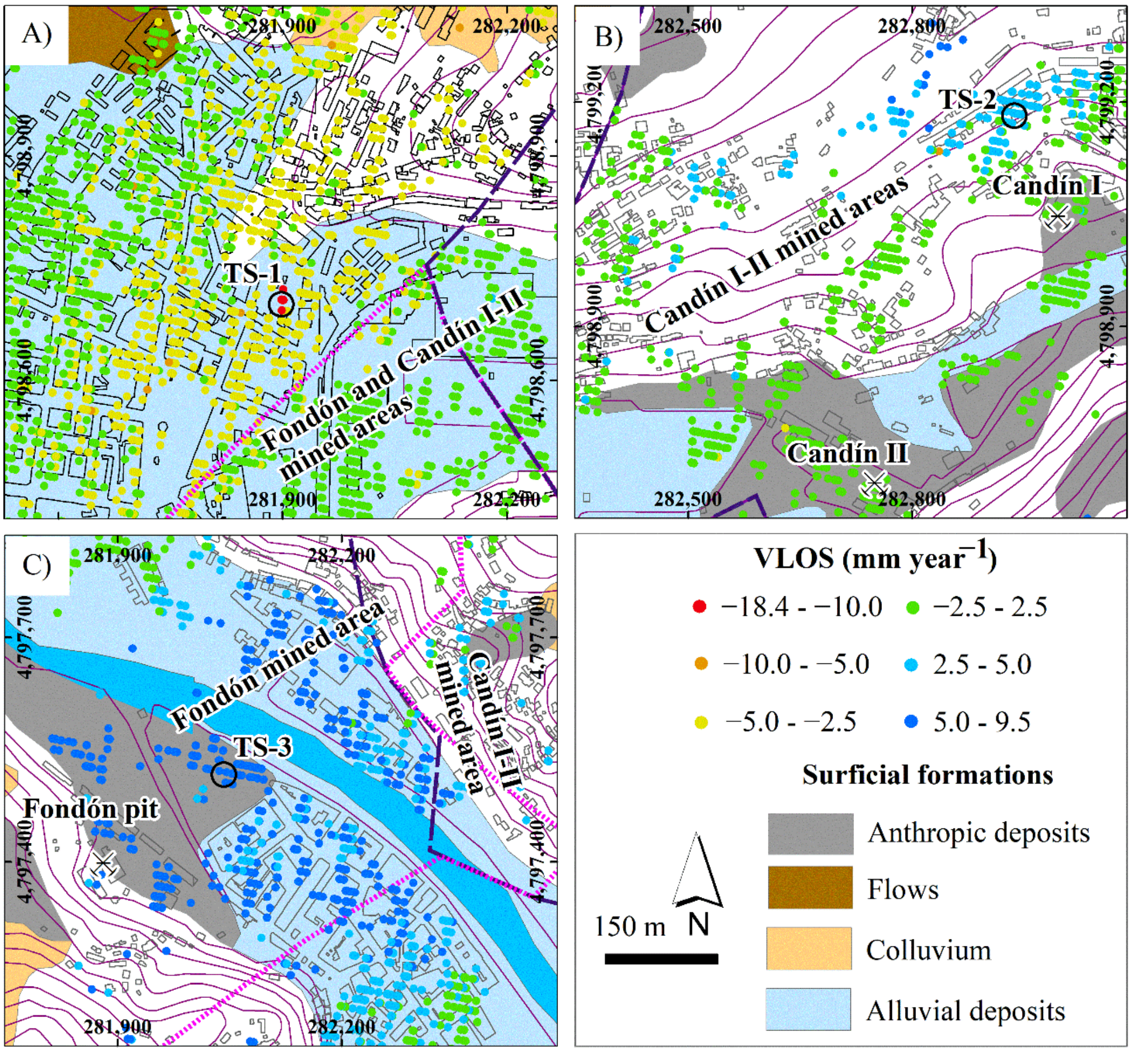

Figure 103. A) Negative deformations observed over La Felguera town. **B)** Positive deformations around the Candín I and II pits. **C)** Sector of Fondón pit, showing positive deformations. Locations of TS described below are shown. Taken and modified from Cuervas-Mons *et al.* (2021c, 2022a).

In the case of La Felguera town (Figure 103 A), the maximum VLOS detected was −18.4 mm year^{-1}. TS showed maximum accumulated displacements of −35.0 mm (Figure 103 A and Figure 104 A, TS-1). TS-1 showed a continuous and linear pattern of sinking since January 2018 to February 2020. In this location, there are alluvial deposits covering the bedrock of sandstone and conglomerate of Lower Cretaceous and below of this unit, Carboniferous lutite, sandstone and coal layers.

Regarding the Candín I-II surrounding, the VLOS ranged from −5.1 to 7.3 mm year^{-1} (Figure 103 B). TS showed accumulated displacements from −16.4 to 12.1 mm (Figure 103 B and Figure 104 B, TS-2). The surficial materials include predominantly anthropic and alluvial deposits covering the bedrock of Mesozoic sandstone, and conglomerate and Carboniferous lutite, sandstone and coal layers. In this location two ranges of PS were observed: 1) Positive deformations (>2.5 mm year^{-1}) linked to slopes, whose orientation are to Southeast (Figure 103 B) and 2) Stable PS in the proximity of the Candín I-II pits, because VLOS values were less than ± 2.5 mm year^{-1} (Figure 103 B). TS-2 showed a rise of displacement from January 2018 to July 2019 (Figure 103 B and Figure 104 B). Afterward, the pattern was stabilized with a total accumulated displacement of 6.9 mm.

In the area around of Fondón pit (Figure 103 C), the VLOS rates were ranging from −2.0 to 9.5 mm year^{-1}, being the maximum accumulated displacements of 17.5 mm. TS-3 showed a maximum displacement of 14.5 mm (Figure 103 C and Figure 104 C). In this location the predominant materials are alluvial deposits of Nalón river and anthropic deposits related to Fondón pit infrastructure (Figure 103 C). In depth, the bedrock is composed of Carboniferous lutite, sandstone and coal layers. The positive deformations (> 2.5 mm year^{-1}) formed a clear deformation halo around the vertical pit, and over the Quaternary and anthropic deposits (Figure 103 C).

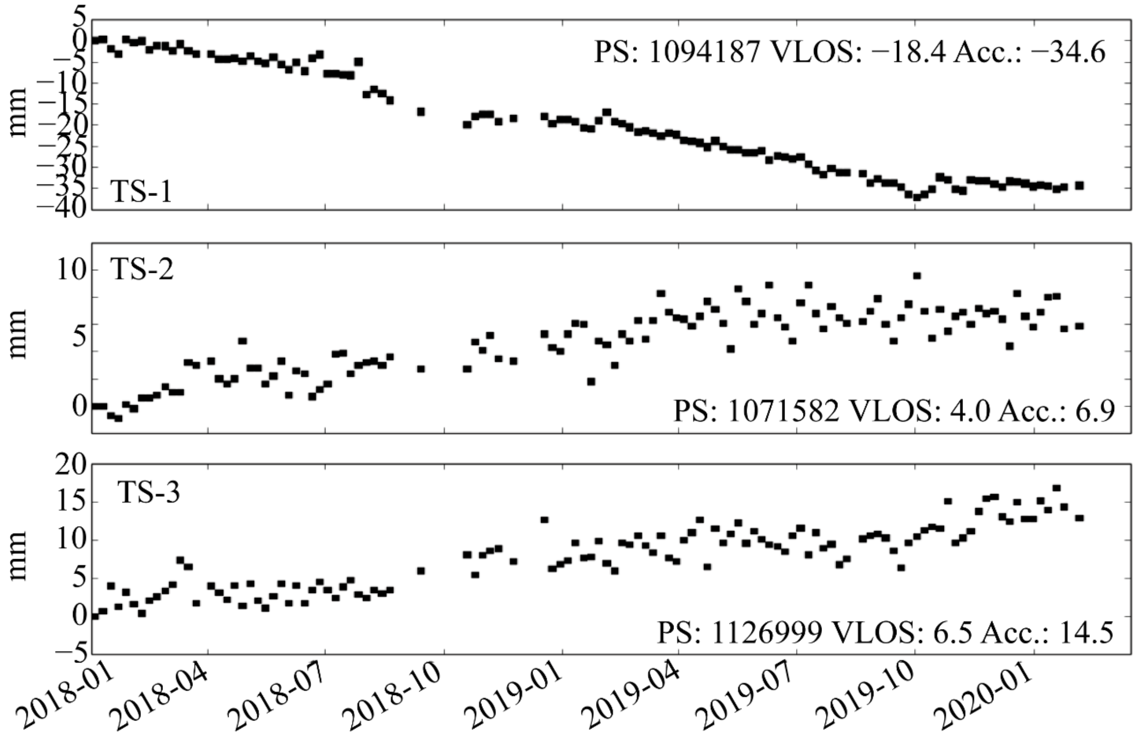

Figure 104. Deformation time series located in Langreo mining areas. See locations in Figure 103. Taken and modified from Cuervas-Mons *et al.* (2021c, 2022a).

Time series previously selected (Figure 103) were analyzed in detail with respect to the daily rainfall dataset (Figure 105). TS-1 located in the La Felguera town (Figure 105 A) and over alluvial deposits (Figure 103 A and Figure 104 A), showed a linear trend. There was not relationship between deformation and rainfall, except in October 2019, when a stabilization of the deformation (with accumulated displacement of −35 mm) can be observed coinciding with rainy periods (47.5, 50.0 and 54 mm) and with an increase in accumulated rainfall from 2,058 to 2,751.6 mm) (Figure 105 A). The TS-2 (Figure 105 B) located into the Candín I-II mined area (Figure 103 B and Figure 104 B) showed four deformation periods. First, from January to July 2018, there was an increase in displacement with a maximum deformation of 7.2 mm coinciding with rainy periods (maximum 50.3 mm in June 2019). Secondly, from July to October 2018, there was a stabilization of deformation. This period matched with scarce rainy episodes (maximum rainfall of 25.3 mm in August). Afterward, between October 2018 to April 2019 there was a new period of deformation occurred until April 2019, reaching a cumulative displacement of 9.1 mm. During this period, maximum rainfall of 76.5 mm were registered in January 2019. Finally, a stabilization period occurred between April 2019 and February 2020 (deformation remains between 9 and 6 mm) that coincided with a dry period (between May and October 2019, with maximum rainfall of 21.1 mm in May) and a rainy period between October and December 2019 (maximum rainfall of 54 mm in December) (Figure 105 B). Finally, TS-3 (Figure 105 C) located near to Fondón pit (Figure 103 C and Figure 104 C) presented four deformation periods (Figure 105 C). At first, an increase of displacement with a maximum deformation of 12.5 mm from January 2018 to March/April 2019 was registered. This period corresponded to a rainy period until February 2019 and a dry period from February to May 2019. Secondly, a stabilization (between March/April to July 2019) and a subsequent descent of deformation (until 9.7 mm) from July 2019 to October 2019 were produced. Both corresponded to a dry period (maximum rainfall of 19 mm in July). Finally, there was an increase in deformation up to 14.5 mm from October 2019 to February 2020 that matched with rainy periods and accumulated rainfall variation from 2,058 to 2,751.6 mm (Figure 105 C).

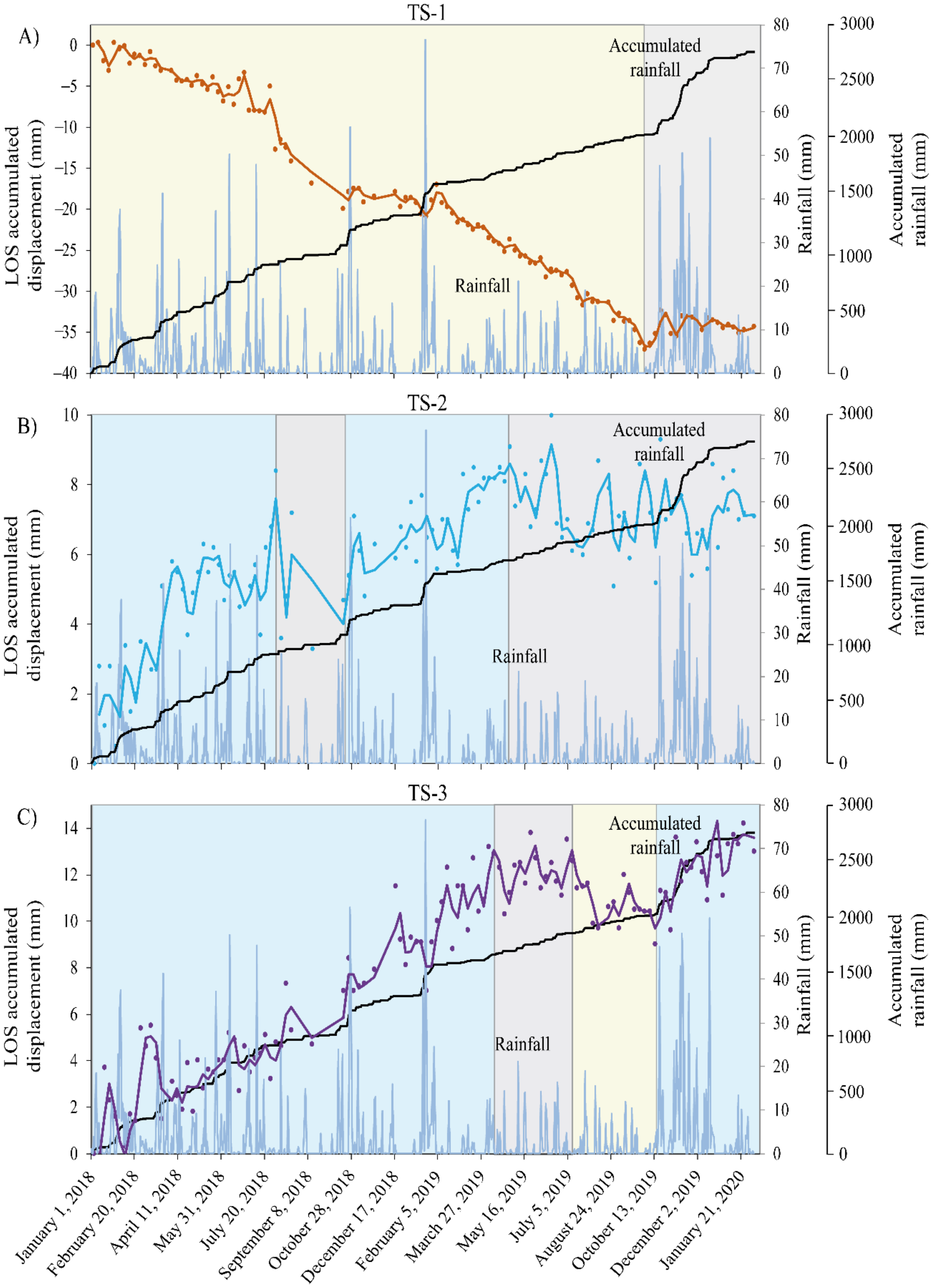

Figure 105. LOS time series of PS detected in the mined areas of Candín I-II and Fondón pits with daily and accumulated rainfall data. Periods of deformation were defined according to time series with following colours: Blue, positive deformation; gray, deformation is maintained; yellow, negative deformation. **A)** TS-1, located in La Felguera. **B)** TS-2, located in the Candín I-II mied area surrounding. **C)** TS-3, located in the Fondón mined area. See location of TS in Figure 103.

4.3 Lisbon Metropolitan Area

4.3.1 LOS mean deformation velocity maps

The LOS mean deformation velocity maps (mm year^{-1}) obtained in ascending and descending trajectories by the P-SBAS processing are presented in Figure 106 and summarized in Table 22. A total of 607,024 PS (30.3 PS km^{-2}) were obtained in ascending processing, whereas 975,215 PS were measured in descending processing (70.1 PS km^{-2}). In the LMA, the measured PS densities were 55.3 PS km^{-2} in ascending and 71.6 PS km^{-2} in descending. In order to visualize and analyze the ground movement rates in ascending dataset, only PS whose VLOS values were above ± 6.0 mm year^{-1} were considered as active PS (Figure 106 A). This threshold was selected according to the standard deviation obtained in the PS ($\sigma = \pm 2.9$) (Table 22). In the case of descending dataset, PS values higher than ±7.0 mm year^{-1} (Figure 106 A) were considered as active, because the standard deviation obtained was $\sigma = \pm 3.6$ (Table 22).

As far as the ascending dataset, the LOS velocity rates were ranging from −38.0 and 26.3 mm year^{-1}, with an average value of −2.0 ± 2.9 mm year^{-1} (Figure 106 A and Table 22). Regarding not active PS, there were 520,963 PS (85.82%). On the other hand, the maximum VLOS of −38.0 mm year^{-1} was detected in Palmela council, located in the center of the study area (Figure 106 A). In this region, the materials are Holocene alluvial deposits. Also, a maximum accumulated displacement of −74.7 mm was detected in Vila Franca de Xira over alluvial materials (clays and sands of Tagus river) over an isolated PS with VLOS of −35.0 mm year^{-1} (Figure 106 A). The mean value of accumulated displacement was −4.0 ± 6.5 mm (Table 22).

With respect to descending dataset (Figure 106 B and Table 22), the maximum LOS velocities measured were −35.4 and 23.0 mm year^{-1}. This maximum VLOS of −35.4 mm year^{-1} was measured over located alluvial deposits in Palmela council (Figure 106 B). The average value of VLOS was −1.0 ± 3.6 mm year^{-1}. On the other hand, the total of not active PS was 908,417 PS (93.15%). The maximum accumulated displacement of−74.0 mm was detected over Vila Franca de Xira region, associated to PS with VLOS of −25.2 mm year^{-1} (Figure 106 B and Table 22). The mean value of accumulated displacement was −0.6 ± 6.5 mm (Table 22).

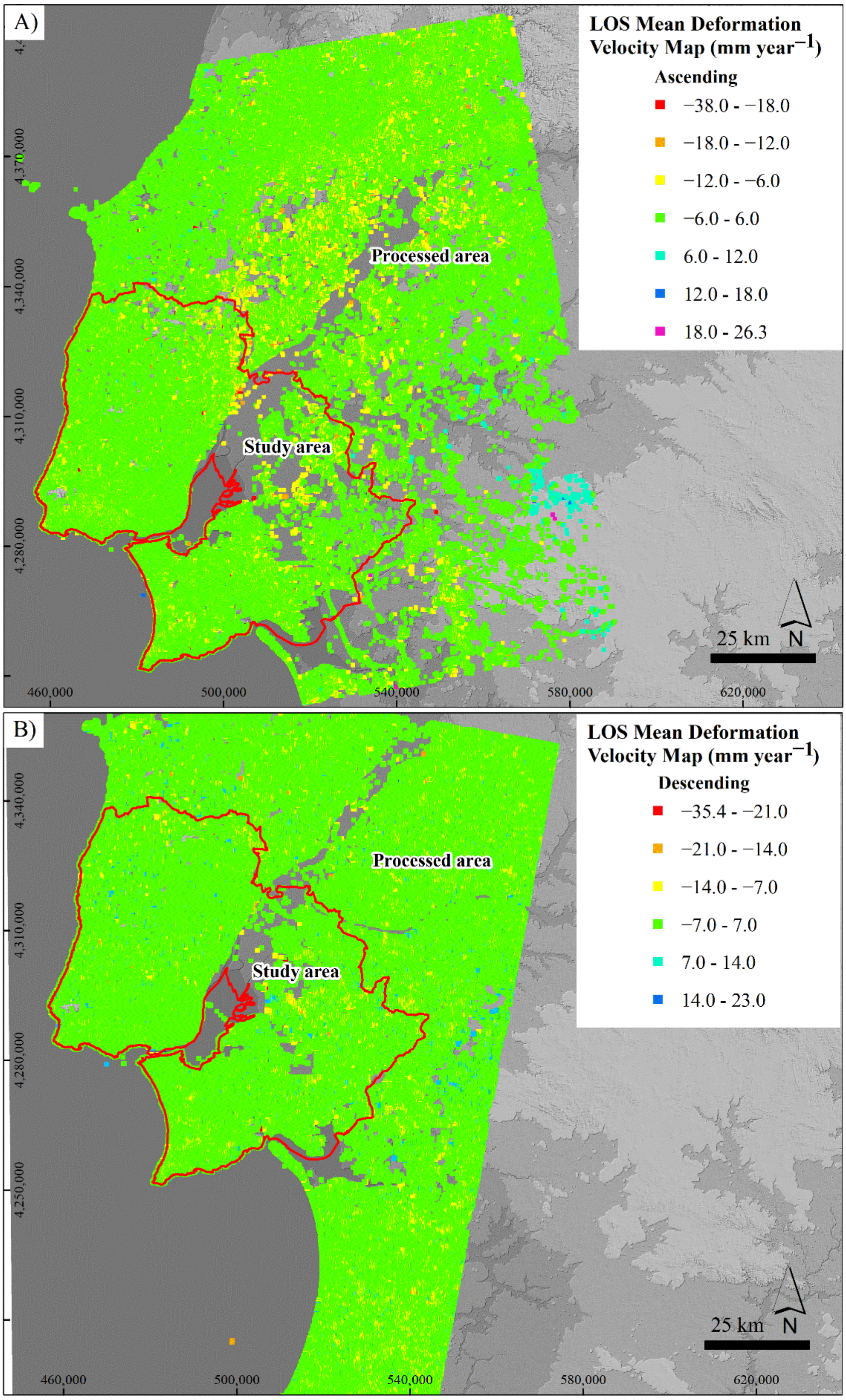

Figure 106. A) LOS mean deformation velocity map (mm year^{-1}) in ascending trajectory. **B)** LOS mean deformation velocity map in (mm year^{-1}) in descending trajectory. Taken and modified from Cuervas-Mons *et al.* (2022b).

Table 22. Main parameters of the LOS mean deformation velocity map (mm year^{-1}) of processed area in ascending and descending trajectories. Taken and modified from Cuervas-Mons *et al.* (2022b).

Parameters	**Ascending**	**Descending**
Area (km^2)	20,009	13,904
Number of points (PS)	607,024	975,215
Density of points (PS km^{-2})	30.3	70.1
	LOS velocity (mm year^{-1})	
Mean	−2.0	−1.0
Maximum	26.3	23.0
Minimum	−38.0	−35.4
Standard deviation	2.9	3.6
	Accumulated LOS displacement (mm)	
Mean	−4.0	−0.6
Maximum	53.2	46.1
Minimum	−74.7	−74.0
Standard deviation	6.5	8.2

4.3.2 ADAs at regional scale

A total number of 592 ADAs were extracted and drawn in the LMA from the PS into the LOS mean deformation velocity map in ascending trajectory (Figure 107 A and B). ADAs were composed of a minimum and maximum PS number of 5 and 795, respectively. The average number of PS per ADA was 16. The extension of ADAs ranged between 80,986 and 12,406,800 m^2, with an average of 382,398 m^2. On the other hand, Palmela was the council that registered the highest quantity of ADAs (82). It is located at Central South of study area, being Lisbon, Odivelas and Sobral de Monte Agraço the councils that registered the minimum number of ADAs (3) (Table 23). On the contrary, a total of 560 ADAs were extracted and delimited from descending dataset (Figure 107 C and D). In this case, ADAs were composed from 5 to 620 PS and presented an average of 19 PS per ADA. The extensions of ADAs were ranging between 65,389 and 11,795,965 m^2, with an average of 426,379 m^2. Conversely to ascending ADAs, Benavente was the council that registered the highest quantity of ADAs (101), while Sobral de Monte Agraço was the council with the lowest number of ADAs (0) (Table 24).

Figure 107 A and C show the distribution of ADAs along the LMA according to the maximum velocity class (mm year^{-1}). In the case of ascending ADAs, the detected velocity rates ranged from 6.6 to 38.0 mm year^{-1} (Figure 107 A). ADAs with velocities between 6.6 and 10.0 mm year^{-1} were represented throughout the whole study area and sometimes also appeared associated to ADAs with velocities between 10.0 and 20.0 mm year^{-1} (Figure 107 A). These 10.0 and 20.0 mm year^{-1} velocity rates defined areas with outstanding deformations: The Central coast, the North-central study area and the Setubal peninsula (Figure 107 A). ADAs with velocities from 20.0 to 30.0 mm year^{-1} were extracted mostly in the center and north center of the study area (Alenquer and Vila Franca de Xira) (Figure 107 A). ADAs with velocities higher than 30.0 mm year^{-1} presented extensions from 424,493 to 1,043,860 m^2 and were located in Vila Franca de Xira and Palmela councils. In the case of Vila Franca de Xira, ADAs were mostly identified on alluvial deposits of Tagus River while in Palmela they were detected in Neogene and Quaternary deposits. In the case of Alenquer, they were also extracted and drawn on Jurassic, Paleogene and Miocene rocky substrate.

On the other hand, ADAs from descending dataset ranged from 6.6 to 35.4 mm year^{-1} (Figure 107 C). Likewise, ADAs with velocities between 6.6 and 10.0 mm year^{-1} were represented throughout the study area and in association with ADAs with velocities between 10.0 and 20.0 mm year^{-1} (Figure 107 C). These 10.0 and 20.0 mm year^{-1} velocity rates defined specially deformation sectors on the south coast, in the north and east of the LMA (Figure 107 C). ADAs with velocities from 20.0 to 30.0 mm year^{-1} were drawn mostly in the center and north center of the study area (Vila Franca de Xira and Benavente) (Figure 107 C). ADAs with velocities higher than 30.0 mm year^{-1} were distributed on some sectors with extensions from 395,729 to 603,807 m^2 in south of Vila Franca de Xira and Palmela councils. In the case of ADAs located in Vila Franca de Xira, Benavente and Palmela, they were extracted over Quaternary alluvial deposits.

Figure 107 B and D display the ADAs QI. For ascending dataset, a total of 408 had QI = 1, 136 had QI = 2, 8 had QI = 3 and 40 had QI = 4 (Figure 107 B). In descending dataset a total of 93 ADAs had QI = 1, 113 had QI = 2, 100 had QI = 3 and 254 had QI = 4 (Figure 107 D). In this research, ADAs with QI = 1 only were taken into account. The ascending ADAs with QI = 1 were located predominantly in the north central and west central areas of the study area. They could also be found more widely in the eastern center and south of the study area (Figure 107 B). ADAs with QI = 2 - 4 were located both isolated or dispersed along the whole LMA(Figure 107 B).

Descending ADAs with QI = 1 were found as large and clustered zones in Central and East central of the study area. Also, they could be found as isolated and disperse deformation sectors throughout the rest of the LMA (Figure 107 D). ADAs with QI = 2 - 4, they appeared predominantly at East and South of the LMA and as isolated zones along the rest of the territory (Figure 107 D). In both cases, most of the ADAs with QI = 1 were located in cities, towns or isolated buildings. They were extracted from those PS that were located on infrastructures, such as road or railway networks.

As it has already been mentioned above, the most significant deformations were measured in the sectors of Alenquer and Vila Franca de Xira from both trajectories. Taking only into account the maximum velocity and QI = 1 of the ADAs drawn, this region was chosen to carry out the urban subsidence analysis at local scale (Table 23, Table 24 and Figure 107).

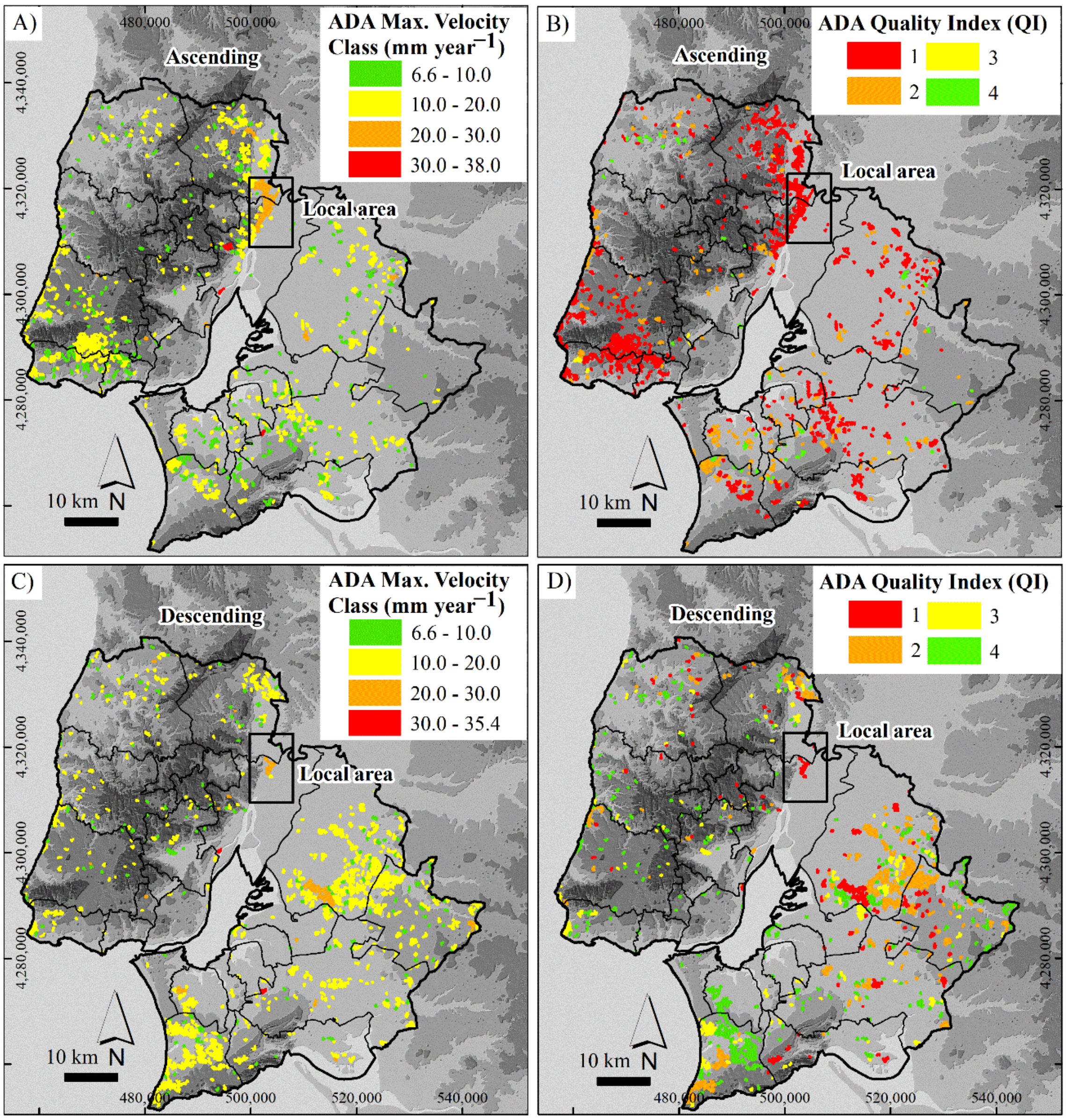

Figure 107. ADA extracted in the LMA at regional scale. **A)** Maximum Velocity Class (mm year^{-1}) of ADA from ascending dataset. **B)** ADA Quality Index (QI) in ascending trajectory. **C)** Maximum Velocity Class (mm year^{-1}) of ADA from descending dataset. **B)** ADA Quality Index (QI) in descending trajectory. Taken and modified from Cuervas-Mons *et al.* (2022b).

Table 23. Main parameters of ADA with QI = 1 for each council in ascending trajectory. Number of PS, velocity and deformation are shown according to the ADAs with QI = 1. In bold the councils corresponding to the local study area: Vila Franca de Xira - Alenquer. Taken and modified from Cuervas-Mons *et al.* (2022b).

Council	**# Total ADA (QI = 1-4)**	**# ADA (QI = 1)**	**# PS of ADA**	**Max Velocity (mm year^{-1})**	**Mean Velocity (mm year^{-1})**	**Max Deformation (mm)**	**Mean Deformation (mm)**
Alcohete	11	8	5 - 54	13.2	3.8 - 8.3	−28.2	−5.9 - −16.7
Alenquer	**67**	**63**	**5 - 795**	**25.5**	**3.2 - 13.7**	**−43.7**	**−5.0 - −32.3**
Almada	6	3	5 - 8	14.4	3.6 - 9.0	−32.3	−4.7 - −16.7
Amadora	6	4	6 - 16	29.5	3.9 - 8.2	−64.1	−8.3 - −17.3
Arruda Dos Vinhos	7	5	5 - 6	12.3	4.0 - 7.6	−45.9	−6.2 - −12.8
Barreiro	10	4	6 - 18	15.8	3.8 - 5.7	−24.2	−6.9 - −11.9
Benavente	71	58	5 - 101	20.7	3.2 - 13.1	−44.0	−5.3 - −26.3
Cascais	40	35	5 - 480	18.0	3.5 - 7.4	−38.0	−4.2 - −15.7
Lisbon	3	1	5	9.1	3.6	−46.3	−6.8
Loures	8	1	11	13.0	3.8	−31.0	−11.0
Mafra	20	9	5 - 40	13.1	3.3 - 5.7	−29.0	−7.4 - −12.3
Moita	20	17	5 - 18	15.8	3.2 - 6.2	−34.2	−5.2 - −13.3
Montijo	35	19	5 - 54	16.4	3.1 - 8.8	−35.2	−5.2 - −20.2
Odivelas	3	No data	No data	No data	No data	No data	No data
Oeiras	27	26	5 - 56	18.5	3.5 - 5.5	−31.7	−4.1 - −12.6
Palmela	82	48	5 - 68	16.8	3.6 - 11.8	−71.0	−5.2 - −21.8
Seixal	26	5	5 - 21	16.3	3.2 - 6.2	−35.1	−5.0–−12.0
Sesimbra	28	10	5 - 120	15.6	4.0 - 9.9	−33.0	−8.6 - −16.5
Setúbal	30	17	5 - 53	14.9	3.1 - 7.1	−33.8	−11.6 - −13.3
Sintra	79	68	5 - 480	25.9	2.4 - 11.1	−50.6	−5.5 - −21.3
Sobral de Monte Agraço	3	3	5	10.9	3.5 - 4.6	−20.9	−8.9 - −9.7
Torres Vedras	43	22	5 - 28	17.3	3.8 - 13.6	−36.0	−6.0 - −30.3
Vila Franca de Xira	**35**	**29**	**5 - 795**	**25.5**	**3.7 - 11.7**	**−55.6**	**−5.2 - −29.1**

Table 24. Main parameters of ADA with QI = 1 for each council in descending trajectory. Number of PS, velocity and deformation are shown according to the ADA with QI = 1. In bold the councils corresponding to the local study area: Vila Franca de Xira - Alenquer. Taken and modified from Cuervas-Mons *et al.* (2022b).

Council	**# Total ADA (QI = 1-4)**	**# ADA (QI = 1)**	**# PS of ADA**	**Max Velocity (mm year^{-1})**	**Mean Velocity (mm year^{-1})**	**Max Deformation (mm)**	**Mean Deformation (mm)**
Alcohete	12	3	6 - 18	12.2	4.0 - 6.5	−38.5	−4.9 - −6.1
Alenquer	**44**	**12**	**5 - 165**	**25.2**	**4.7 - 9.7**	**−43.5**	**17.8 - −19.1**
Almada	4	No data	No data	No data	No data	No data	No data
Amadora	2	No data	No data	No data	No data	No data	No data
Arruda Dos Vinhos	8	3	5 - 6	13.2	4.0 - 6.2	−26.0	8.8 - −9.2
Barreiro	3	No data	No data	No data	No data	No data	No data
Benavente	101	19	5 - 519	24.1	4.6 - 13.0	−43.3	15.5 - −30.0
Cascais	15	No data	No data	No data	No data	No data	No data
Lisbon	7	2	5 - 10	13.6	6.7 - 7.7	−36.2	−14.5 - −14.6
Loures	23	2	5 - 6	11.8	6.6 - 7.7	−18.6	−13.7 - −14.5
Mafra	40	2	9 - 22	17.4	10.6 - 17.4	−37.1	9.1 - −18.8
Moita	4	No data	No data	No data	No data	No data	No data
Montijo	87	18	6 - 63	18.7	3.4 - 9.1	−40.6	15.9 - −13.2
Odivelas	1	No data	No data	No data	No data	No data	No data
Oeiras	2	No data	No data	No data	No data	No data	No data
Palmela	70	8	5 - 100	18.6	4.9 - 13.4	−48.3	−4.0 - −33.3
Seixal	8	No data	No data	No data	No data	No data	No data
Sesimbra	48	1	11	9.5	5.7	−17.7	−3.1
Setúbal	25	8	5 - 87	18.4	4.4 - 8.7	−37.3	−2.9 - −16.3
Sintra	38	3	5 - 13	14.6	6.0 - 10.8	−35.8	−7.3 - −20.7
Sobral de Monte Agraço	No data	No data	No data	No data	No data	No data	No data
Torres Vedras	50	12	5 - 15	21.3	4.4 - 11.5	−49.7	10.2 - −27.1
Vila Franca de Xira	**15**	**5**	**7 - 165**	**28.6**	**6.4 - 11.4**	**−53.1**	**9.1 - −22.4**

4.3.3 Urban subsidence analysis at local scale

Vila Franca de Xira - Alenquer

This area is located on the North Center of the LMA. It includes the councils of Vila Franca de Xira and Alenquer (Figure 107). This sector is characterized by the presence of significant industry, factories and urban areas (Figure 108). Also, there are critical infrastructure networks that connect Lisbon with the center and North of Portugal. The most important infrastructure is the Thermoelectrical Station and industrial area of Carregado (Figure 109.

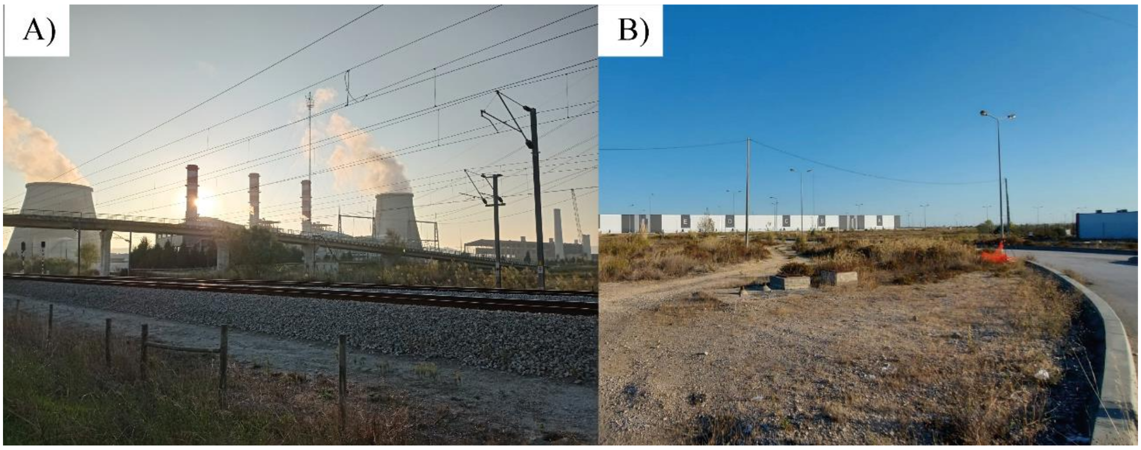

Figure 108. Main infrastructures located in Vila Franca de Xira - Alenquer (Carregado area). **A)** Thermoelectrical Station. **B)** Industrial area. Taken and modified from Cuervas-Mons *et al.* (2022b).

From a lithological point of view, the bedrock is constituted by dolostone, limestone, slate, marl, sandstone and conglomerate of Jurassic, Paleogene and Miocene ages (Figure 109). The towns of Vila Franca de Xira, Carregado and Alenquer are located over Jurassic and Miocene calcareous and siliciclastic materials and Quaternary deposits (Figure 109). The quaternary materials include Pleistocene terraces (made by sands, clays and pebbles) and Holocene alluvial deposits of Tagus River (made by clays and sands). Moreover, there are gravity and eluvial deposits covering the Jurassic bedrock. Anthropic deposits are also very common in the area (Figure 109).

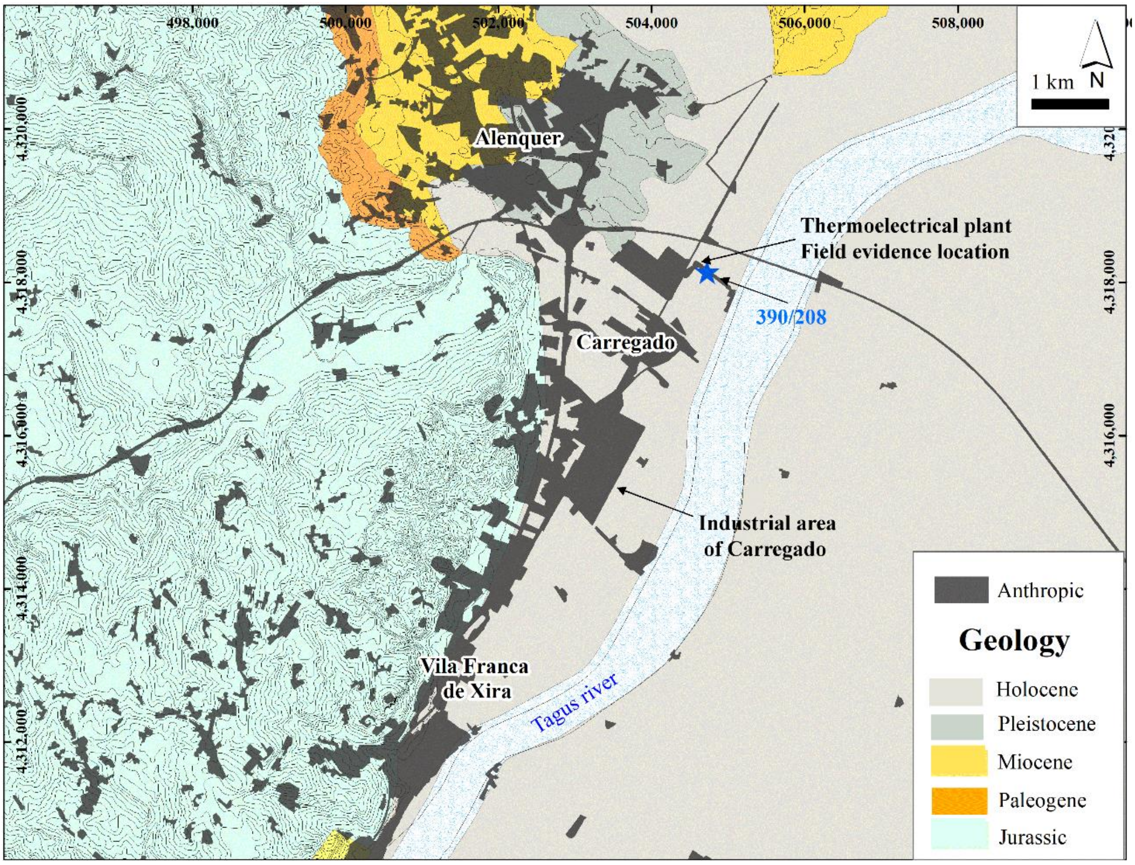

Figure 109. Geological settings of Vila Franca de Xira - Alenquer and location of evidence observed in field campaigns in October and November 2021. Blue star represents location of water well (code 390/208). Taken and modified from Cuervas-Mons *et al.* (2022b).

As to validate the ground motion by field campaigns, evidence of movement could not be observed in the majority of the deformation locations because the area has got wide restricted access sectors (Figure 108). However, near the Carregado thermoelectric plant, a group of open tense cracks could be observed affecting a road. They were characterized by tens of meters of length and some centimetres wide (Figure 110 A-C). The road runs parallel to a water channel, which connects the thermoelectric plant with the Tagus River.

Figure 110. Movement evidence observed during field campaigns. Photos taken in October and November 2021. **A)** and **B)** Tension cracks in a road in Vila Franca de Xira surrounding and near the Carregado thermoelectric plant. **C)** Opened tense cracks. See location in Figure 109. Taken and modified from Cuervas-Mons *et al.* (2022b).

Figure 111 A shows the ADAs defined and their detected PS from ascending processing. A total of 24 ADAs were extracted with 2,717 PS measured into the ADAs. 2,616 isolated PS had been rejected during ADA processing from a total of 4,878 PS detected (53.6 % of total). Regarding the type of terrain where the PS were located (Figure 109 and Figure 111 A), all of them were detected above artificial reflectors such as: 1) Urban, industry and factory areas located over alluvial deposits; 2) Buildings located in the mountain and slope zones, on Jurassic, Paleogene and Miocene materials and 3) Infrastructures such as roads, highways and railways. The extensions of ADAs ranged from 104,928 to 12,406,800 m^2. All ADAs presented a QI = 1. The main ADA identified presented the maximum extension (12,406,800 m^2) and it was constituted by 795 PS. It was located over the towns of Vila Franca de Xira, Carregado and Alenquer (Figure 111 A). In this sector, there are are mainly Quaternary alluvial and anthropic deposits and Miocene and Paleogene sedimentary rocks (Figure 109 and Figure 111 A). It presented an average VLOS of −6 mm year^{-1} and maximum VLOS of −25.5 mm year^{-1} (Figure 111 A). A maximum displacement of −55.6 mm was detected, associated to a VLOS of −25.5 mm year^{-1} (Figure 111 A). This maximum VLOS was detected over the industrial area of Vila Franca de Xira and Carregado. On the other hand, other 3 ADAs presented maximum VLOS between −7.4 and −18.5 mm year^{-1} and were located over buildings, industry, roads and railway situated over alluvial and anthropic deposits (Figure 111 A). These ADAs were characterized by maximum accumulated displacement of −33.3 mm.

Figure 111 B shows the ADAs drawn and their PS detected from descending dataset. A total of 6,048 PS were measured, with VLOS rates from −25.2 to 17.4 mm year^{-1}, from which 5,699 were rejected (94.2 % of total) subsequently. Thus, there were 349 PS into the ADAs. The main ADA, with an extension of 2,216,415 m^2 presented a maximum velocity of −25.2 mm year^{-1}. On the other hand, the active deformations (<−7.0 mm year^{-1}) were mainly restricted to the industrial area of Vila Franca de Xira - Carregado (Figure 111 B) and small zones that coincided with the active PS and ADAs of ascending dataset (locations of TS-1 and TS-3) (Figure 111 B). For the rest of area, only an area with QI = 4 was extracted (Figure 111 B).

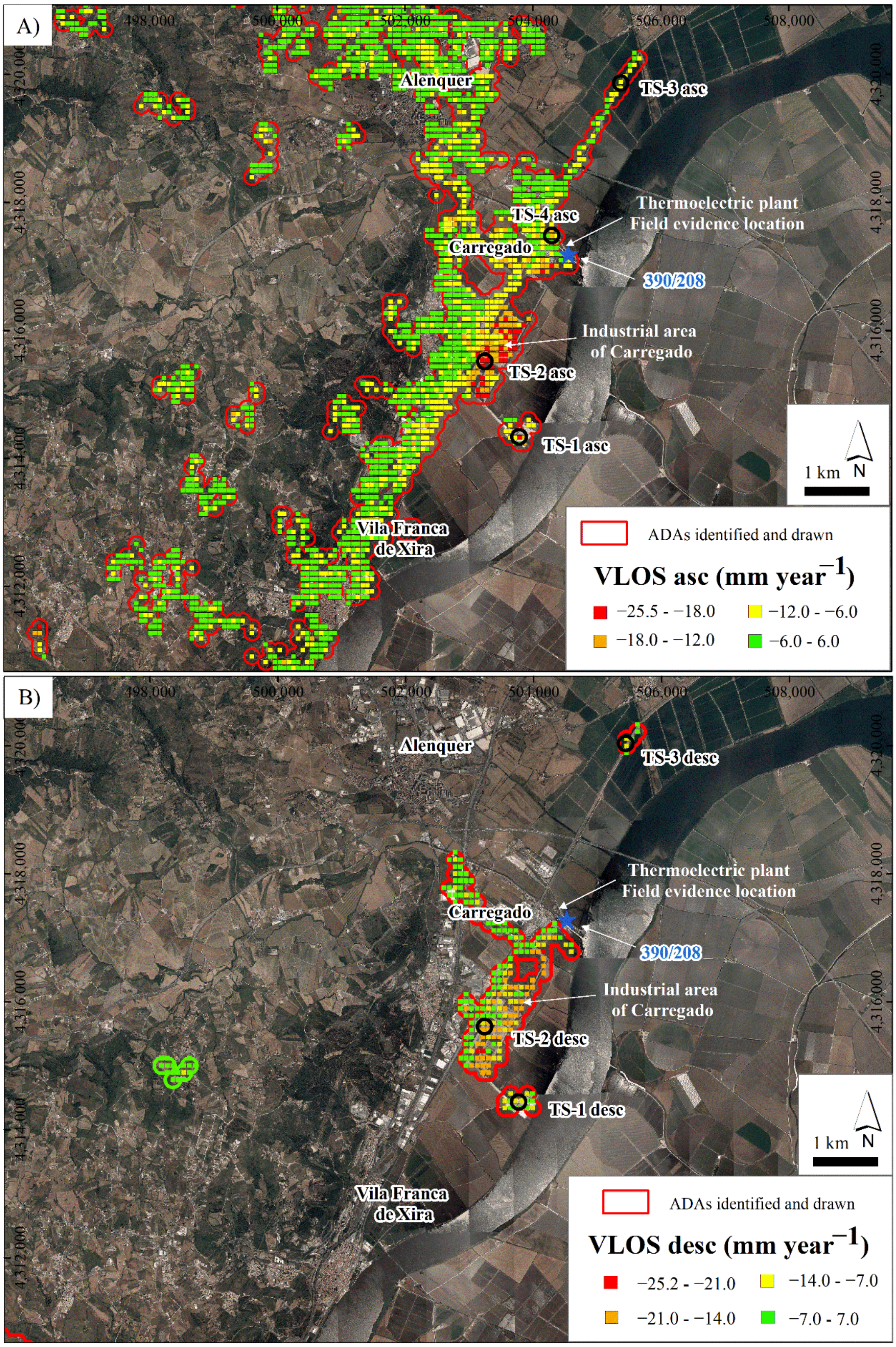

Figure 111. **A)** Identified ADAs and detected ascending PS (only PS into the ADA). **B)** Identified ADAs and detected descending PS (only PS into the ADA). Blue star represents the location of water well (code 390/208). See photos in Figure 108 and Figure 110. Taken and modified from Cuervas-Mons *et al.* (2022b).

A-DInSAR dataset vs hydrological data

Different TS were selected to be compared to rainfall and piezometric data (Figure 111). Below TS were described below with respect to daily rainfall dataset and monthly piezometric level (PL 390/208) (Figure 111 and Figure 112). TS were selected according to: 1) Ground motion detected and ADAs drawn (Figure 111) and 2) Evidence of movement found in the field campaigns (Figure 110).

Three periods of rise (between January to February 2018, between September 2018 to March 2019 and from September 2019 to April 2020) and 2 periods of drop (from February to September 2018 and between April to September 2019) of the piezometric level could be identified (Figure 112). These periods of rise matched with rainfall episodes, while periods of drop matched with dry or scarce rainfall episodes (Figure 112). Average annual precipitation for the analyzed time was 412.0 mm, with a total accumulated precipitation of 970.2 mm between January 2018 and April 2020 (Figure 112). On the other hand, analyzed TS showed different patterns and different noise levels. Descending TS (Figure 112 B) are noisier than ascending TS (Figure 112 A). TS-1, located in an industrial area near the Tagus river (Figure 111), presented different trends. Ascending TS-1 (Figure 112 A) displayed a linear trend until September 2019, when presented a stabilization of displacement until April 2020. This period of stabilization coincided with rainfall episodes and piezometric level recuperation. Descending TS-1 (Figure 112 B) presented periods of increase and stabilization of displacement that were independent of rainfall and piezometric records. Both TS-2, located in the industrial sector of Vila Franca de Xira - Carregado (Figure 112), showed linear trends independent of rainfall record and piezometric level during the lapse analyzed (Figure 112). On the other hand, both TS-3 located at North of study area (Figure 111), showed different patterns of rising and descending of displacement without relation with rainfall data and piezometric level (Figure 112). Finally, TS-4 was located where evidence of movements were observed and it was only displayed in ascending processing(Figure 111 A). This TS showed increases of displacement that did not seen to be related to rainfall or piezometric level records. Nevertheless, from September 2019, it showed a stabilization in the deformation coinciding with a rainfall episode and a rise in the piezometric level (Figure 112 A).

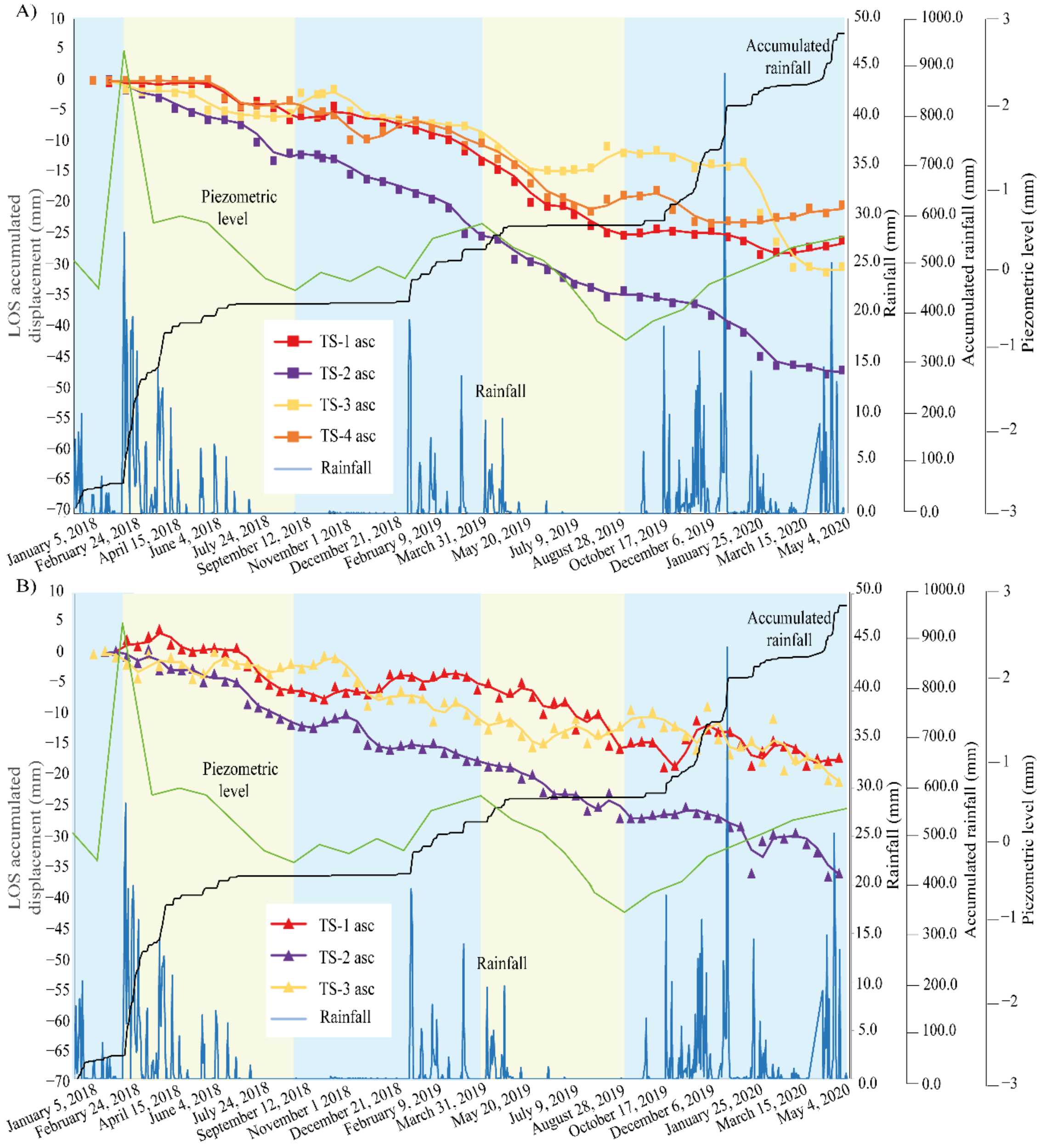

Figure 112. Deformation time series (mm), daily rainfall dataset (mm), accumulated precipitation (mm) and piezometric level (m) between January 2018 and April 2020. Distinghised periods were defined according to piezometric level fluctuations: Blue indicates going up or holding and yellow indicates going down. **A)** Time Series from ascending dataset. **B)** Time Series from descending dataset. See location of TS in Figure 111. Taken and modified from Cuervas-Mons *et al.* (2022b).

Vertical velocity

Figure 113 shows the Vertical velocity estimated from VLOS in both trajectories. The output format of Vertical velocity map (mm year^{-1}) was a raster with a pixel resolution of 90 x 90 m. Two sectors, A and B, were identified with high Vertical velocities. The Sector A corresponded to the industrial polygon of Vila Franca de Xira - Carregado towns. This sector presented mainly Vertical velocity from −20 to −25 mm year^{-1} and a maximum Vertical velocity estimated of −32.4 mm year^{-1} (Figure 113 B, Profiles A - A`and B - B`). This sector is located on anthropic materials and alluvial deposits of Tagus River (clays and sands). It presents an extension of 2,601,950 m^2. In Sector B, it was identified a maximum Vertical velocity of −19.0 mm year^{-1} (Figure 113 B, profile C - C`) although the average Vertical velocity was −15.0 mm year^{-1}. This sector corresponds to an industry located over alluvial and anthropic materials next to the Tagus River, with an area of 222,846 m^2.

Comparing ADAs obtained from ascending and descending trajectories with Vertical velocity, it could be observed that deformation zones (Sectors A and B) matched better with descending ADAs than ascending ADAs (Figure 111 and Figure 113). On the other hand, ADAs where time series TS-3 and TS-4 were located (Figure 111), presented maximum Vertical velocities of −5.0 mm year^{-1} (Figure 113). However, in these locations, maximum ascending and descending VLOS detected were −18.0 (Figure 111 A) and −14.0 mm year^{-1} (Figure 111 B), respectively.

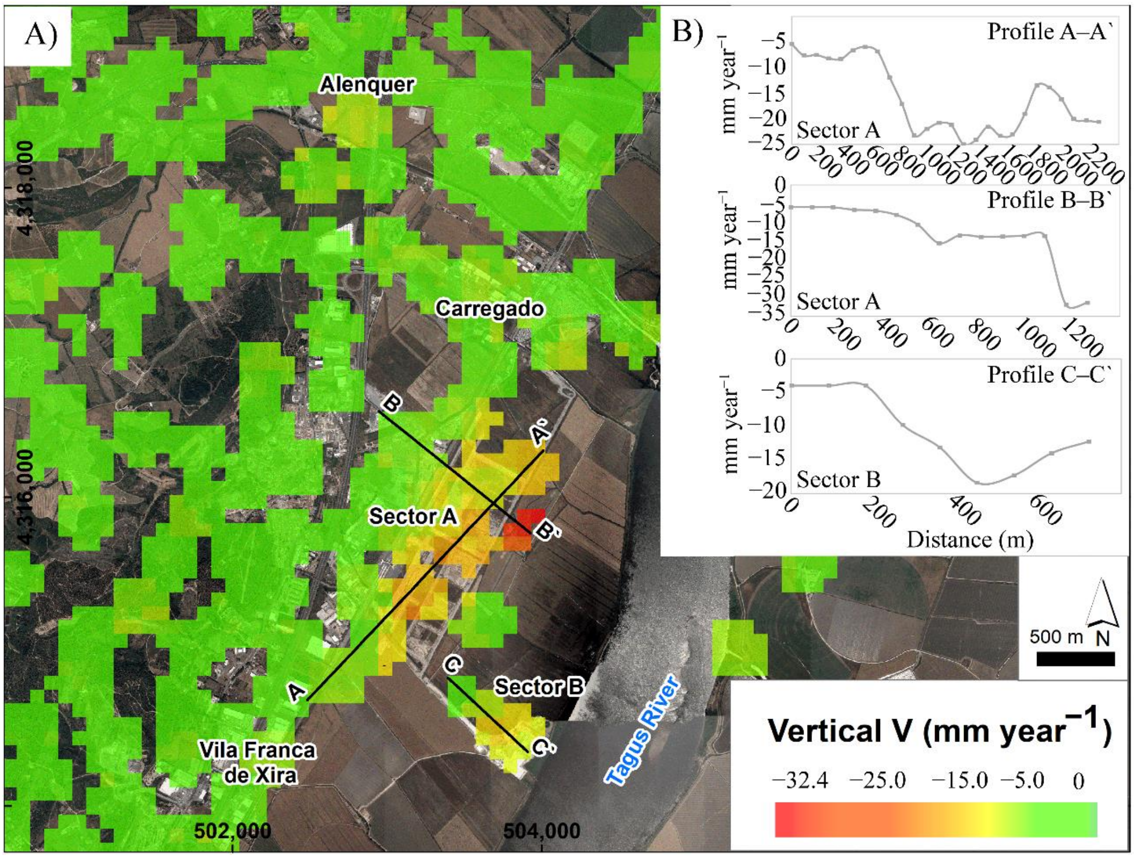

Figure 113. Vila Franca de Xira - Alenquer area. Vertical velocity (mm year^{-1}) raster (pixel 90 x 90 m) and location of Vertical velocity profiles. **B)** Profiles of Vertical velocity (mm year^{-1}). Taken and modified from Cuervas-Mons *et al.* (2022b).

5. DISCUSSION

In this section, the interpretation and discussion of the results analyzed and described are carried out. The discussion is divided in the following sub-chapters: 1) Coastal areas: Peñas Cape environment, Podes Peninsula and Tazones Lighthouse landslide; 2) Mountain area: Langreo town; 3) Lisbon Metropolitan Area and 4) Future research lines.

5.1 Coastal areas of Asturias

The results are discussed below in the following order: 1) PSIG and P-SBAS results at regional scale to detect and monitor coastal instabilities; 2) A-DInSAR results and topographic measurements carried out in the Podes Peninsula; 3) Topographic monitoring measurements and A-DInSAR results carried out in the Tazones Lighthouse landslide; 4) Observed relationships between coastal instabilities identified with respect to coastal retreat and landslide activity at regional and local scale. Moreover, observed limitations in the application of the A-DInSAR techniques are shown and 5) Suggestions to improve the interpretations carried out in this research.

5.1.1 Peñas Cape environment

In all coastal areas studied two different A-DInSAR approaches were tested (section 4.1). One of them is a robust and controlled software (PSIG), and the other one is an unsupervised and automatic service (P-SBAS, implemented in the GEP service). The main purposes of implementing both approaches were to (Cuervas-Mons *et al.*, 2021d): 1) Increase the amount of PS in the study area, avoiding unmonitored areas and 2) Facilitate the analysis and interpretation of the detected deformation areas.

The LOS mean deformation velocity maps obtained (Figure 84, Figure 85 and Figure 86) have allowed to observe similar VLOS rates at regional scale. Nevertheless, they present important differences in the interpretation of the obtained datasets at regional and local scales. There are several factors that could explaine those differences (Cuervas-Mons *et al.*, 2021d): 1) Pixel resolution (14 x 4 m of PSIG product versus 90 x 90 m of P-SBAS map); 2) Degree of selection and manipulation of the input parameters during the A-DInSAR processing and 3) Implemented technique in each approach. Thus, PSIG software is based on the PSI technique (Ferreti *et al.*, 2000; 2001; Biescas *et al.*, 2007), while the other approach runs with P-SBAS technique (Casu *et al.*, 2014, De Luca *et al.*, 2015; Manunta *et al.*, 2019).

Both used software have allowed to detect different coastal instabilities at regional scale (Figure 87, Figure 88 and Figure 89). Firstly, in Figure 87, the deformations were located over an electrical station, in which ground movements have been related with slope instabilities developed on 1) a destabilized slope and 2) anthropic fill settlements. Secondly, different ground motions were detected in the Musel Port (Figure 88). These movements could be linked to wave processes and tides. Additionally, being an area gained to the sea, the deformations could be due to ground settlements developed on the filler materials (Almazán-Gárate and Palomino-Monzón, 2000). Moreover, the observed trends of positive accumulated ground motion could be related to: 1) Accumulation of materials (anthropic activities) and 2) Noise and artifacts. In both cases, VLOS are greater than 5 mm year^{-1} (Cuervas-Mons *et al.*, 2021d). Finally, both PSIG and P-SBAS processing allowed to identify a coastal instability to the West of Peñas Cape (Figure 89), involving a coastal landslide developed in the cliff. It affects the bedrock overlying rasa deposits. On the other hand, Domínguez-Cuesta *et al.* (2020) indicates that the West of Peñas Cape is showing the greatest coastal retreat in the region. In this way, a coastal retreat of 13.38 m, between 2006 and 2017 has been measured in this area (Domínguez-Cuesta *et al.*, 2020). According to Cuervas-Mons *et al.* (2021d), this slope instability can be directly related to erosion of the cliff foot by undercutting sea action.

5.1.2 Podes Peninsula

Concerning the local analysis carried out in the Podes Peninsula (sub-section 4.1.2), both A-DInSAR processing have allowed to distinguish some local ground motions related to coastal instabilities developed on top of the cliffs (Cuervas-Mons *et al.*, 2021b). Maximum VLOS detected related to these instabilities were −6.8 mm year^{-1} and higher than 5 mm year^{-1} (Figure 90 and Figure 92). These instabilites are supposed to be directly related to coastal activity and retreat. According to Domínguez-Cuesta *et al.* (2020), the maximum retreat rate registered in the Podes Peninsula was 0.71 m per year between 2006 and 2017.

On the other hand, this area shows the high complexity of analyzing coastal instabilities by means of *in situ* instrumentation and A-DInSAR techniques (Cuervas-Mons *et al.*, 2021b). This is due to the typology of slope movements that occur along the Asturian coast and the morphology of the coastline (Figure 91). The obtained data by topographic monitoring could not be considered reliable as they are all below the precision level of the total station used (Cuervas-Mons *et al.*, 2021b) (Figure 90 B and Table 16). In the case of A-DInSAR results, the majority of PS detected were related to uncorrected atmospheric components and noise (Cuervas-Mons *et al.*, 2021b). However, it could be observed the P-SBAS processing is a useful tool and support service for more robust software such as the PSIG approach. This is reflected in the difference of obtained density of PS: 30.4 PS km^{-2} in the case of P-SBAS versus 8.9 PS km^{-2} of PSIG.

5.1.3 Tazones Lighthouse landslide

Regarding LOS mean deformation velocity maps obtained by PSIG and P-SBAS approaches (Figure 93), results were unsatisfactory and did not allow analysis of ground deformation in the Tazones landslide area. However, PS detected by both approaches have allowed: 1) To recognize the Tazones lighthouse and the Villar village as stable areas (Figure 93), and 2) To verify the western and southern limits of the Tazones landslide (Dominguez-Cuesta *et al.*, 2022b). On the other hand, topographic points measured showed significant displacements of the landslide, which moved more than 1 m at some points and reached a maximum displacement of 14.93 m between November 2019 and February 2020 (Figure 94 A and Table 17). In addition, field evidence such as open and deep cracks has shown the existence of different surficial movements (rockfall, slide and topple events) in the Tazones landslide area (Figure 94 B-E). According to Dominguez-Cuesta *et al.* (2022a), the Tazones landslide can be summarized like a complex mass movement with a primary planar landslide type and secondary flow, topple and rockfall movements. The first two years of monitoring of the 38 installed marker points (Figure 94) showed that, spatially, the movement is strongly influenced by lithology/rock structure (S0 and joints system) and, temporally, by rainfall, soil moisture and sea waves (Dominguez-Cuesta *et al.*, 2022a).

According to Dominguez-Cuesta *et al.* (2022b), ground motion could not be monitor by means of A-DInSAR techniques due to the following factors: 1) High complexity of the area, predominantly forested, and the absence of adequate natural reflectors and 2) Too fast velocity of the mass movement for be detected by means of A-DInSAR techniques. One way to solve the problem of the lack of PS could be installation of artificial reflectors PCR (Passsive Corner Reflectors) or AR (Active Reflectors), which would allow obtaining a good response from the SAR signal and identifying adequate PS (Crosetto *et al.*, 2020; Luzi *et al.*, 2021). There are previous experiences where these artificial reflectors systems have been successfully applied in forested landslides (see, for example, the works by Crosetto *et al.* (2013) and Darvishi *et al.* (2018)).

5.1.4 Limitations of A-DInSAR techniques

According to Domínguez-Cuesta *et al.* (2020), asturian coast retreat data measured between 2006 and 2017, presents rates from 0.25 and 2.19 m year^{-1}. Also, between 2006 and 2017 there were several important meteorological events. For example, on June 2010 and February 2014 there were storms and intense rainfall episodes that resulted in numerous instabilities and damages along the Asturian coast (Flor-Blanco *et al.*, 2013; Valenzuela *et al.*, 2017; Domínguez-Cuesta *et al.*, 2019; 2020). The majority of mass movements registered were rockfalls, flows and undetermined events (Valenzuela *et al.*, 2017). However, these typologies of slope instabilities cannot be measured by using A-DInSAR methods due to their high velocity and their sudden development. In spite of this fact, and although this work has not studied the entire Asturian coast, different coastal instabilities have been detected by means of A-DInSAR techniques at regional and local scale (Figure 84, Figure 85, Figure 86, Figure 87, Figure 88, Figure 89, Figure 90 and Figure 93). The most intense deformations detected by A-DInSAR were obtained in the Musel port, located close to Gijón city (Figure 85, Figure 86 and Figure 88). This particular case has been directly related to differential settlements produced by coastal processess and retreat (Cuervas-Mons *et al.*, 2021d). According to Zhao *et al.* (2011) and Zhao *et al.* (2015) this type of zones gained to the sea present high coastal incidence and relevant damages in the civil and port infrastructures. These authors estimated maximum velocities of −10 and −50 mm year^{-1}, in coastal airport of Hong Kong and the coastal urban area of Shangai city, respectively. In the case of the Musel port, deformations have showed maximum VLOS values of −8.6 and −23.0 mm year^{-1} (Figure 88).

The main limitation factors to apply A-DInSAR techniques in the Peñas Cape environment, including the Podes Peninsula, and in the Tazones Lighthouse landslide were (Cuervas-Mons *et al.*, 2021d): 1) The scarcity of natural PS due to the fact that the Asturian coast is a predominantly non-urban territory; 2) The orientation of the terrain; in particular, terrains with NE orientations cause slope movements to be parallel to the direction of the satellite sensor. Consequently, these movements are practically impossible to detect by means of A-DInSAR; 3) The high inclination of the slopes in some sectors, resulting in shadow and foreshortening effects (Colesanti and Wasowski, 2006) and therefore, no signal areas and a drastic reduction of the spatial resolution and 4) The instability velocity; the main typologies are rockfalls and flows, with velocities ranging from slow to extremely fast (> 13 m month^{-1} - > 5 m s^{-1}). Thus, these slope instability typologies are undetectable through A-DInSAR techniques (Canuti *et al.*, 2004).

5.2 Mountain area of Asturias: Langreo Town

The results of the mountain area allowed to focus on the analysis and interpretation of ground motion detected in the Langreo town. Results are discussed below in the following order: 1) Ground motion detected in surficial deposits and 2) Deformations detected over mined areas of Fondón and Candín I-II vertical pits.

5.2.1 Ground motion related to mass movements affecting surficial deposits

In the Langreo town area, 5 surficial deposits (LSa-1, LSa-2, LFe-1, LFe-2, and LFe-3) could be studied (Figure 99). Their main characteristics are listed in Table 25. Considering the activity status threshold of state of activity of ± 2.5 mm year^{-1} and the evidence observed in the field campaign (Figure 100), LSa-1, LSa-2 and LFe-2 (Figure 99 and Figure 100) can be classified as active mass movements. As movement evidence, they present present tension cracks, building damage or creep phenomena (Figure 100). On the other hand, landslide LFe-1 is defined (Figure 99) as not active landslide, because mean VLOS is lower than ± 2.5 mm year^{-1} and no evidence of ground movement has been observed (Table 25). Finally, the state of activity of landslide LFe-3 (Figure 99) could not be defined because it could not be accesed, although average VLOS is −2.7 mm year^{-1} (Table 25).

The analysis of TS of each surficial deposit with respect to daily rainfall (Figure 101) shows that LSa-2 and LFe-2 present a clear relation with respect to rainfall episodes, observing an increase of displacement in those periods with important rainy seasons. On the contrary, TS of LSa-1 do not show relationship with daily rainfall records (Figure 101). In this line, Valenzuela *et al.* (2017) pointed out the majority of landslide activity (1,232 events of a total of 1,455 records between 1980 and 2015) compiled in Asturias was registered during high monthly rainfall. Works from Dominguez-Cuesta *et al.* (1999) and Valenzuela *et al.* (2019) established meteorological patterns and rainfall episodes as main landslide triggering factors in Asturias. In Langreo area there is no evidence that coal mining activity has produced slope movements. However, the concurrence of both phenomena is known in other areas of the Central Coal Basin (Riesgo-Fernández *et al.*, 2020) and in other coal mining regions of World (Arca *et al.*, 2018; Yang *et al.*, 2022). In the case of the LSa-2 and LFe-2 mass movements, the main trigger for the movement seems to be the rainfall episodes.

On the other hand, there are 0.51 km^2 of colluvium and 0.23 km^2 of anthropic deposits without monitoring by means of A-DInSAR dataset. This could be because their PS density was either very low or were not PS detected. These cases are due to the lack of adequate and good reflectors, because these mapped surficial formations are predominatly located on non-urban or on heavily vegetated areas. It must be taken into account that the colluvium and anthropic deposits such us mining dumps are very susceptible to mass movements (López-Fernández *et al.*, 2002; Domínguez-Cuesta *et al.*, 2007).

5.2.2 Ground motion related to mining impact

Ground motion detected in La Felguera (maximum VLOS of −18.4 mm year^{-1}) and over the Fondón mining area (maximum VLOS of 9.5 mm year^{-1}) (Figure 99 and Figure 103) could be linked to coal mining activity since there is presence and proximity of exploited mining areas. However, there is little information to corroborate this hypothesis. The scarce mining data regarding the exact location of underground mining works and other geological and mining data at depth do not allow to confirm if these deformations are produced by mining incidence. Mined areas of Candín I and Candín II pits (Figure 99 and Figure 103 A-B) with non-active PS (VLOS ± 2.5 mm year^{-1}) would show that there is no coal mining incidence in these zones.

The analysis of TS-1 and 2 (Figure 103, Figure 104 and Figure 105 A and B) with respect to daily rainfall records shows that there is not strong relationship between deformation and rainfall events. On the contrary, relationships are observed between the displacements of TS-3 (located in the Fondón mined area, Figure 103 C, Figure 104 and Figure 105 C) and rainfall episodes. It presents displacements of 12.5 and 14.5 mm with accumulated rainfalls of 1662.7 and 2751.6 mm, respectively. As pumping and piezometric level data of Fondón pit are not available, it cannot be affirmed or ruled out that these movements are influenced by fluctuation of groundwater in these abandoned mine workings. It is well-known the geohazards related to flooding events (e.g. Zhao and Konietzky, 2021) and alteration of aquifer regime (e.g. Chen *et al.*, 2022) in other coal underground mining areas of the World. In this line, in the Central Coal Basin there are 16 vertical pits, including the pits of Fondón and Candín I and II, where water level is periodically measured (Álvarez-Álvarez and Fernández-Álvarez, 2021). However, as mentioned above, during the course of this work it was not possible to access this dataset due to its confidential nature and restricted access.

Table 25. Main characteristics, LOS mean and rates velocity (mm year^{-1}) and LOS displacement accumulated (mm) by each mass movement detected in the study area.

Mass movement	**Sector**	**Area (m^2)**	**PS**	**VLOS rates (mm year^{-1})**	**Mean VLOS**	**Acc. Defo rates (mm)**	**Mean Acc. Defo (mm)**	**Typology**	**Activity state**	**Movement evidence**
LSa-1	Sama	8,057	24	1.9 - 7.4	5.1	2.7 - 16.5	8.9	Colluvium	Active	Tense cracks in a road
LSa-2	Sama	35,083	91	0.3 - 4.9	3.2	−4.9 - 9.6	5.1	Flow	Active	Tense cracks in roads and building damages
LFe-1	La Felguera	55,914	60	−6.1 - 2.8	−1.3	−12.8 - 6.4	−3.3	Flow	Not active	Not observed
LFe-2	La Felguera	57,016	156	−6.9 - 0.8	−2.8	−16.7 - −0.1	−7.3	Colluvium	Active	Creep Slope walls
LFe-3	La Felguera	11,470	19	−4.1 - −2.0	−2.7	−9.8 - −3.3	−6.5	Colluvium	No data	No data

5.3 Lisbon Metropolitan Area

5.3.1 Reliability of ADAs for targeting urban subsidence

The extraction and draw of ADAs at regional scale from both LOS mean deformation velocity maps has allowed to: 1) Remove isolated PS that can be due to uncorrected atmospheric component or noise and, therefore, to avoid misinterpretation; 2) Reduce considerably the analysis time of the LOS mean deformation velocity maps obtained (Figure 106) and 3) Focus the study of urban subsidence at local scale (Figure 111). The differences observed between ascending and descending ADAs (velocities, location of ADAs and number of ADAs with QI = 1: 409 ascending and 93 descending ADAs) (Figure 107, Table 23 and Table 24) are due to level of noise in the PS detected and number of isolated PS presented in the LOS mean deformation velocity maps (Figure 106). This variance observed between ascending and descending level of noise could be due to the locations of the reference points. In the case of ascending processing, the reference point was located over the city of Lisbon (Figure 106 A). However, the descending reference point was located over a rural area with very low density of measurement points (Figure 106 B). The inadequate location of the reference point of the descending processing could have substantially affected the results obtained. This is shown by the low number of ADAs with QI = 1. Another reason could be the higher number of SAR images used in the descending (61) versus ascending (48) processing.

5.3.2 Urban subsidence assessment

Urban subsidence was evaluated in the Vila Franca de Xira - Alenquer region (Sub-section 4.3.3) with a maximum Vertical velocity of −32.5 mm year^{-1} and maximum LOS velocity of −25.5 mm year^{-1} (in ascending) and −25.2 mm year^{-1} (in descending). A total of 4 ascending ADAs and 3 descending ADAs have been associated to urban and industrial subsidence (Figure 111). In this sense, ADAs from descending processing have proven to be more adequate that ascending ADAs because they focus better the subsidence area. In this case, 2,616 PS in ascending and 5,699 PS in descending were rejected (53.6 and 94.2 % of total PS detected) during ADA procedure. Two sectors (A and B) have been identified, with extensions of 2,601,950 and 222,846 m^2 approximately (Figure 111 and Table 26). Descending ADAs match better the estimated Vertical velocities in Sectors A and B (Figure 113 and Table 26). According to Heleno *et al.* (2011), the maximum rates of subsidence measured in this region between 1992 and 2006 (more specifically in Vialonga town, 10 km Southward from Vila Franca de Xira), were from 14 to 15 mm year^{-1}, with an average of 6 and 11 mm year^{-1}. This last rate was obtained over industrial and factory areas. These authors have proposed that subsidence phenomena are due to groundwater over-exploitation and subsequent compaction of the detrital layers of these aquifers. Moreover, they mentioned that piezometric levels in Vialonga descended 65 m in 27 years (from 1966 to 1993) (Heleno *et al.*, 2011). However, in this research the observed and analyzed time series show that there is not a clear relation between the measured rates of subsidence, with respect to rainfall dataset and piezometric level (Figure 112). The main hydrological systems identified in this region are (Heleno *et al.*, 2011): A deep Cretaceous porous aquifer with a thick of 180 m; An intermediate clay aquitard of 150 m of thickness and a sand-clay-limestone Miocene aquifer of 150 m thick. Nevertheless, in our local study area, the main aquifer systems are the Holocene alluvial materials (clays and sands) and the Pleistocene fluvial deposits (sands, clays and pebbles) (SNIRH, 2021). They are porous, free and semi-confined aquifers (SNIRH, 2021).

Regarding the nature and origin of subsidence phenomena observed in this research, it can be mainly due to the compaction of the alluvial materials, whose thicknesses are from 5 to 20 m (Carvalho *et al.*, 2018), and anthropic deposits. This process can be particularly observed in the industrial polygon of Vila Franca de Xira-Carregado, where the TS-2 is located (Figure 111). This industrial area has been identified as Sector A (Figure 113). Additionally, this process is almost continuous throughout the studied period. On the other hand, TS do not show correlation with respect to piezometric level. Therefore, it cannot justify the attribution of the deformation detected are due to ground water exploitation. However, with the exposed results and available hydrological data, this process proposed by Heleno *et al.* (2011) cannot be excluded. In any case, with respect to this previous study, this research represents an important advancement in the assessment of urban subsidence in the LMA, because Sentinel-1A-DInSAR has been applied for the first time, using the P-SBAS technique of the GEP service and ADA tools. Additionally, the P-SBAS technique has been demonstrated to be a useful approach for detecting ground motion at the regional and local scales (Galve *et al.*, 2017; Cigna and Tapete, 2021; Cuervas-Mons *et al.*, 2021d; Reyes-Carmona *et al.*, 2021). The software of ADA tools (Barra *et al.*, 2017; Tomás *et al.*, 2019; Navarro *et al.*, 2020), is very reliable for reducing the regional analysis of the ground motion detected and, therefore, allows to analyze and interpret, in more detail, specific areas with active deformations (Solari *et al.*, 2018; Qiu *et al.*, 2021; Barra *et al.*, 2022).

Regarding the maximum VLOS and Vertical velocity detected and described in this research, these values can be compared with other published works on the subsidence issue (Meisina *et al.*, 2008; Polcari *et al.*, 2014; Solari *et al.*, 2016; Delgado-Blasco *et al.*, 2019). These authors have measured maximum VLOS from −6 to higher than −20 mm year^{-1} and they have proposed as main origin of subsidence phenomena the urban development and consolidation of recent and soft sediments. On the other hand, the ADAs obtained from both trajectories represent an opportunity to analyze, in the future, other areas of the LMA that are well-known, regarding the existing geohazards (Zêzere, 2001; Heleno *et al.*, 2011; Oliveira *et al.*, 2015; Marques, 2018).

Table 26. Comparative of main subsidence sectors identified by ascending and descending ADAs and Vertical deformation. See location of sectors in Figure Figure 111 and Figure 113.

	Ascending		**Descending**		**Vertical deformation**	
Sector	Max. VLOS (mm year^{-1})	Area of ADA (m^2)	Max. VLOS (mm year^{-1})	Area of ADA (m^2)	Max. Velocity (mm year^{-1})	Area (m^2)
A	−25.5	12,406,800	−25.2	2,216,415	−32.4	2,601,950
B	−18.5	251,940	−20.8	233,685	−19.0	222,846

5.4 Improvements and future lines of research

5.4.1 Proposals for the coastal areas of Asturias

Based on the above, different ways can be considered to improve the results and interpretations obtained in the coastal areas of Asturias: 1) To conduct a post-processing by means of ADA tools (Barra *et al.*, 2017; Navarro *et al.*, 2020) with the main purpose of defining, delimiting and analyzing ADAs at both regional and local scales; 2) To conversion of VLOS measurements into VSLOPE values (Bianchini *et al.*, 2013; Béjar-Pizarro *et al.*, 2017). This is a procedure that consists of the projection of the VLOS along the line of maximum slope. It allows correcting the geometric distortions produced by the satellite orbit type with respect to the topography of the terrain; 3) To compare the obtained A-DInSAR results with daily rainfall dataset; 4) To carry out ascending reprocessing of the coastal areas for the same period of time studied in this research and 5) In the particular cases of the Podes Peninsula and the Tazones Lighhouse landslide, to implement the PCR and AR approaches and to carry out A-DInSAR reprocessing.

5.4.2 Proposals for the Langreo town area

For the detection of active ground motion not analyzed in this research, it would be necessary to apply other auscultation techniques, such as inclinometers, topographic monitoring, UAV photogrametry, LIDAR and GNSS techniques, and geophysical methods (Mansour *et al.*, 2011; Jaboyedoff *et al.*, 2012; Colomina and Molina, 2014; Domínguez-Cuesta *et al.*, 2021; Domínguez-Cuesta *et al.*, 2022b). Another possibility is the implementation of corner reflectors to enhance the SAR signal (Crosetto *et al.*, 2013; Luzi *et al.* 2021) and then, perform subsequent reprocessing.

On the other hand, several ways to improve interpretations of the ground motion detected over Fondón and Candín I and II pits can be to: 1) Know the exact location of all the mining works of the Fondón, Candín I and II pits; 2) Study and assess the daily or monthly pumping data and piezometric levels of the three pits and 3) Reprocess of the study area by means of ascending Sentinel-1 SAR images during the same period of time; subsequently, to estimate the Vertical component of the deformation. This approach would help to interpret the negative deformations detected over the town of La Felguera and to relate them to land subsidence.

5.4.3 Proposals for the Lisbon Metropolitan Area

Regarding ground subsidence control in this area, Sentinel-1A-DInSAR techniques have provided satisfactory results, so it is suggested to continue monitoring using these techniques. In addition, the installation of *in situ* instruments, such as levellers, inclinometers, or borehole extensometers (Galloway *et al.*, 1999; Fernández-Oliveras, 2009; Shirzaei *et al.*, 2021), would facilitate the monitoring and tracking of detected ground subsidence. These *in situ* measurements can substantially support the A-DInSAR and ADAs results obtained. On the other hand, a larger set of piezometric dataset is required to improve knowledge about the groundwater exploitation process.

Lastly, some limitations of this research can be highlighted, such as the low precision of the results from P-SBAS processing (90 × 90 m) and short study time (2 years and 4 months). Therefore, the options for improvement of this research in the future could be to: 1) Perform a reprocessing with both trajectories using commercial PSIG software (Biescas *et al.*, 2007; Devanthéry *et al.*, 2014, 2019); 2) Increase the survey period. This approach would substantially improve the resolution and accuracy of the obtained A-DInSAR results (pixel resolution of 14 × 4 m). More years of ground motion analysis would help to better understand the nature of the detected subsidence in the LMA and, more specifically, in Vila Franca de Xira and Alenquer. In addition, this research provides the opportunity and potential to analyze new areas that have not been studied in this work. Another future approach could be the application of ADA tools to extract and draw ADAs from Vertical velocity. Thus, this new approach would better define the identified A and B sectors (Figure 113).

5.4.4 Future lines of research

Although the carried out research has presented coherent and satisfactory results and interpretations with respect to the goals set, some different future lines of work are proposed in order to continue advancing in this line of research:

To install and use PCR and AR (Crosetto *et al.*, 2013; Luzi *et al.*, 2021) in some of the studied areas with the main objective of reprocessing the area with Sentinel-1 dataset.

This approach will provide a suitable PS to detect and monitor ground motion related to landslide activity in those areas where other detailed monitoring data are available, such as the Tazones Lighthouse landslide or the Podes Peninsula.

To continue with the topographic monitoring campaigns in the study areas of the Tazones Lighthouse landslide and the Podes Peninsula. Also, it would be necessary to continue the analysis of studied areas of Asturias from new A-DInSAR reprocessing by means of ascending Sentinel-1 SAR images. Subsequently, to apply the post-processing methodologies of ADA tools (Barra *et al.*, 2017; Tomás *et al.*, 2019; Navarro *et al.*, 2020) and Vertical and Horizontal components estimation (Notti *et al.*, 2014; Béjar-Pizarro *et al.*, 2017).

To survey other areas within the Asturias region and the LMA that have not been analyzed in this research and that have presented active ground motion related to mass movements or land subsidence.

6. CONCLUSIONS

6.1 Global highlights

This work has shown the usefulness of remote sensing methods, such as A-DInSAR techniques, for processing and interpreting LOS mean deformation velocity maps linked to terrain movements. In particular, the PSI and P-SBAS techniques have proved useful for the study of slope instabilities and subsidence phenomena in Asturias (Spain) and in the Lisbon Metropolitan Area (Portugal). This research has allowed to improve the knowledge of mass movement activity, coastal instabilities and the incidence of coal mining in Asturias. Significant advancement has also been carried out in the assessment of urban subsidence in the Lisbon Metropolitan Area. The proposed future lines of research will allow improving the results, interpretations and conclusions reached in this research.

Below, the main contributions achieved for each study area are shown.

6.2 Coastal areas of Asturias

A-DInSAR techniques have been applied in different coastal areas of Asturias using a dataset of 113 descending IW SLC SAR images of Sentinel-1A/B from January 2018 to February 2020. Both professional software (PSIG chain) and unsupervised approach (P-SBAS from GEP service) were applied.

In the Peñas Cape environment, including the Podes Peninsula, ground settlements and slope instabilities have been detected, with maximum VLOS of −12.4 and −23.0 mm year^{-1}, affecting essential infrastructures such as an electrical station located in Avilés and the Musel Port in Gijón. In addition, a coastal instability developed in a cliff located at West of Peñas Cape was detected with a maximum VLOS of −9.1 mm year^{-1}. These results allow to highlight that A-DInSAR techniques can be succesfully used to detect, model and monitor ground instabilities in cliff coasts at regional and local scales. Furthermore, from a methodological point of view, the combined use of both techniques in the Peñas Cape environment has allowed to define the geometry and characteristics of the cliffs (in relation to the satellite descending trajectories), together with the nature of the slope instabilities as the main factors limiting the application of A-DInSAR. It has been demonstrated as the P-SBAS processing can be a useful support tool for those A-DInSAR processing performed with other commercial - robust software.

The main contributions achieved with respect to the Tazones Lighthouse landslide have been: To corroborate the limits of the destabilized area and, therefore, to confirm Villar village and the Lighthouse of Tazones are outside the unstable sector. Nevertheless, the A-DInSAR techniques were unable to detect ground motion recorded by the total station in the destabilized area. These topographic auscultation techniques allowed to characterize the movement of the Tazones Lighthouse landslide with a maximum displacement of 14.93 m between November 2019 and February 2020. Main limited factors have been the high complexity of the predominantly forested area, the absence of adequate natural reflectors and the mass movement velocity, which is too fast to be detected by means of A-DInSAR methods.

6.3 Mountain area of Asturias

A-DInSAR techniques have been applied in the mountain area of Asturias using the dataset of 113 descending IW SLC SAR images of Sentinel-1A/B from January 2018 to February 2020. The professional software PSIG chain has been applied.

It has been possible to detect and monitor 5 surficial deposits, 3 of them with active motion. The maximum VLOS detected were −6.9 and 7.4 mm year^{-1}. The comparison between TS and daily rainfall records has allowed relating the detected movements with rainfall episodes. Maximum accumulated deformations of −17 mm were recorded coinciding with 152 mm of rainfall between October and December 2019.

Maximum VLOS of −18.4 mm year^{-1} and 9.5 mm year^{-1} were measured over La Felguera and Sama de Langreo, where Fondón, Candín I and II coal mining pits are located. However, due to the confidenciality and the lack of in-depth data of these exploited areas, it cannot be asserted that deformations detected are due to coal mining. A plausible hypothesis is that the Fondón pit operates as an artificial aquifer which would be currently recovering from rising groundwater level, which would justify the uplift detected around the pit.

In this study area, it has been demonstrated the applicability and usefulness of A-DInSAR techniques and Sentinel-1 SAR data when study area is characterized by presenting confidential and restricted information about geological, hydrological and mining settings.

6.4 Lisbon Metropolitan Area

A-DInSAR processing and the ADA tools have been applied to the Lisbon Metropolitan Area using two datasets of 48 ascending and 61 descending IW SLC SAR images of Sentinel-1A from January 2018 to April 2020. For A-DInSAR processing, the P-SBAS processing from GEP service was applied.

Four ascending and three descending ADAs related to urban and industrial subsidence have been detected and assessed. The maximum detected VLOS has been −25.5 mm year^{-1}, while the maximum Vertical velocity has been −32.4 mm year^{-1}. The comparison of VLOS, ADAs, and Vertical velocity has helped to interpret the results and properly draw the subsidence sectors of 2,601,950 and 222,846 m^2, respectively. The origin of the detected urban/industrial subsidence has been related, according to geological and hydrological data, to the compaction of alluvial deposits and anthropic materials. However, the fact that the subsidence may also be due to groundwater over-exploitation should not be disregarded, although more hydrological data would be needed to support this hypothesis.

6. CONCLUSIONES

6.1 Aspectos globales destacados

Este trabajo ha puesto de manifiesto la utilidad de métodos remotos de auscultación, como las técnicas A-DInSAR, para procesar e interpretar mapas de velocidades medias de deformación LOS relacionadas con movimientos del terreno. En particular, las técnicas PSI y P-SBAS, se han mostrado útiles para el estudio de inestabilidades de ladera y fenómenos de subsidencia en Asturias (España) y en el Área Metropolitana de Lisboa (Portugal). Esta investigación ha permitido progresar en el conocimiento de la actividad de los movimientos en masa, de las inestabilidades costeras y de la incidencia de la minería del carbón en Asturias. Asimismo, se ha logrado un avance significativo en la evaluación de la subsidencia urbana del Área Metropolitana de Lisboa. Las diferentes líneas de investigación futura propuestas permitirán mejorar los resultados, interpretaciones y conclusiones logradas en esta investigación.

A continuación, se indican las principales contribuciones alcanzadas para cada área de estudio.

6.2 Áreas costeras de Asturias

Se han aplicado las técnicas A-DInSAR en diferentes zonas costeras de Asturias utilizando un conjunto de datos de 113 imágenes SAR descendentes IW SLC de Sentinel-1A/B, desde enero de 2018 hasta febrero de 2020, aplicándose tanto un software profesional (PSIG chain), como un software no supervisado (P-SBAS del servicio GEP).

En el entorno del Cabo de Peñas, incluyendo la Península de Podes, se han detectado asentamientos del terreno e inestabilidades de ladera con VLOS máximas de −12,4 y −23,0 mm año^{-1}, afectando a infraestructuras esenciales, como una central eléctrica en Avilés y el Puerto del Musel, en Gijón. Además, se detectó una inestabilidad costera desarrollada al oeste del Cabo de Peñas con VLOS máxima de −9,1 mm año^{-1}. Estos resultados permiten destacar que las técnicas A-DInSAR pueden ser utilizadas con éxito para detectar, modelar y monitorizar inestabilidades del terreno en costas acantiladas a escala regional y local. Además, desde el punto de vista metodológico, el uso combinado de ambas técnicas en el entorno del Cabo de Peñas ha permitido definir la geometría y las características de los acantilados en relación con las trayectorias descendentes de los satélites, junto con la naturaleza de las inestabilidades de ladera, como los factores principales que limitan la aplicación de A-DInSAR. Se ha demostrado como el procesado P-SBAS puede ser una herramienta útil de apoyo para aquellos procesados A-DInSAR realizados con otro software comercial - robusto.

Las principales aportaciones alcanzadas respecto al deslizamiento del Faro de Tazones, han sido: corroborar los límites de la zona desestabilizada y, por tanto, que el pueblo de Villar y el Faro de Tazones se encuentran fuera del sector inestable. Sin embargo, las técnicas A-DInSAR no han permitido detectar los movimientos del terreno dentro de la zona desestabilizada registrados mediante estación total. Estas técnicas topográficas de auscultación permitieron caracterizar el movimiento del deslizamiento del Faro de Tazones, con un desplazamiento máximo de 14,93 m medido entre noviembre de 2019 y febrero de 2020. Los principales factores limitantes han sido la alta complejidad de la zona, predominantemente boscosa, la ausencia de reflectores naturales adecuados y la velocidad del movimiento en masa, demasiado rápida para ser detectada mediante los métodos A-DInSAR.

6.3 Área montañosa de Asturias

Se han aplicado las técnicas A-DInSAR en la zona montañosa de Asturias utilizando el conjunto de datos de 113 imágenes descendentes IW SLC SAR de Sentinel-1A/B, de enero de 2018 a febrero de 2020 y aplicando el software profesional PSIG.

Se han podido detectar y monitorizar 5 recubrimientos superficiales, 3 de ellos con movimiento activo. Las VLOS máximas medidas en estos depósitos han sido −6,9 y 7,4 mm/año. La comparativa entre los registros de las TS y de precipitación diaria ha permitido relacionar los movimientos detectados con episodios de precipitación. Se registraron deformaciones acumuladas máximas de −17 mm coincidiendo con 152 mm de precipitaciones entre octubre y diciembre de 2019.

Se midieron VLOS máximas de −18,4 mm/año y 9,5 mm/año sobre La Felguera y Sama de Langreo, donde se ubican las explotaciones mineras de carbón de Fondón, Candín I y II. Aunque, debido a la confidencialidad y a la falta de datos en profundidad de las zonas explotadas, no se puede afirmar que las deformaciones detectadas se deban a la minería del carbón, una hipótesis plausible es que el pozo Fondón funcione como acuífero artificial que, actualmente, se estaría recuperando debido a la subida del nivel del agua subterránea, lo que justificaría el levantamiento detectado alrededor del pozo.

En esta área de estudio, se ha demostrado la aplicabilidad y utilidad de las técnicas A-DInSAR y de los datos SAR del Sentinel-1 cuando el área de estudio se caracteriza por presentar información confidencial y restringida sobre los entornos geológicos, hidrológicos y mineros.

6.4 Área Metropolitana de Lisboa

En el Área Metropolitana de Lisboa se han aplicado el procesamiento A-DInSAR y el ADA tools utilizando dos conjuntos de datos de 48 imágenes ascendentes y 61 descendentes IW SLC SAR de Sentinel-1A, de enero de 2018 a abril de 2020. Para el procesado A-DInSAR se ha aplicado la técnica P-SBAS del servicio GEP.

Se han detectado y evaluado 4 ADAs ascendentes y 3 descendentes relacionadas con hundimientos urbanos e industriales. La VLOS máxima detectada ha sido de −25,5 mm año^{-1}, mientras que la velocidad Vertical máxima ha sido de −32,4 mm año^{-1}. La comparación de VLOS, ADAs y la velocidad Vertical ha ayudado a interpretar los resultados y a zonificar adecuadamente los sectores de subsidencia de 2.601.950 y 222.846 m^2, respectivamente. El origen de la subsidencia urbana/industrial detectada se ha relacionado, según los datos geológicos e hidrológicos, con la compactación de depósitos aluviales y materiales antrópicos. Sin embargo, no debe descartarse el hecho de que la subsidencia pueda deberse también a la sobreexplotación de las aguas subterráneas, aunque serían necesarios más datos hidrológicos para apoyar esta hipótesis.

7. REFERENCES

Agencia Estatal de Meteorología (AEMET). (2020). *AEMET OpenData*. Retrieved from https://www.aemet.es/es/datos_abiertos/AEMET_OpenData

Alaska Satellite Facility (ASF). (2022). *ASF Data Search Vertex.* Retrieved from https://search.asf.alaska.edu/#/

Almazán-Gárate, J. L., and Palomino-Monzón, M. C. (2000). *Introducción a la ingeniería Portuaria: Sistema Portuario Español. Obras Exteriores.* Madrid, Spain: Universidad Politécnica de Madrid. 74 pp.

Álvarez-Álvarez, L., and Fernández-Álvarez, J. P. (2021). Regional Groundwater Flow Modelling of the Asturian Central Coal Basin (Spain). *Mine Water and the Environment 40*, 919-930.

Anderson, N., Martinez, A., Hopkins, J. F., and Carr, T. R. (1998). Salt dissolution and surface subsidence in central Kansas: A seismic investigation of the anthropogenic and natural origin models. *Geophysics 63*, 366-378.

Antonello, G., Casagli, N., Farina, P., Leva, D., Nico, G., Sieber, A. J., and Tarchi, D. (2004). Ground-based SAR interferometry for monitoring mass movements. *Landslides 1*, 21-28.

Arbizu, M., Aller, J., and Méndez-Bedia, I. (1995). Rasgos geológicos de la región del Cabo Peñas. In C. Aramburu, and F. Bastida, *Geología de Asturias* (pp. 231-246). Gijón, Spain: 1st ed. TREA S.L.

Arca, D., Kutoğlu, H. Ş., and Beek, K. (2018). Landslide susceptibility mapping in an area of underground mining using the multicriteria decision analysis method. *Environmental Monitoring and Assessment 190*, 725.

Arnaud, A., Adam, N., Hanssen, R., Inglada, J., Duro, J., Closa, J., and Eineder, M. (2003). ASAR ERS Interferometric Phase Continuity. *Proceedings International Geoscience and Remote Sensing Symposium*, (pp. 1133-1135). 21-25 July 2003. Toulouse, France.

Ayala, F. J., Olcina, J., and Vilaplana, J. M. (2004). Impacto social de los riesgos naturales en España en el periodo 1990-2000. *Gerencia de riesgos XXI*, 17-29.

Azañón, J. M., Mateos, R., Notti, D., Galve, J. P., Fernández, F., Roldán, F. J., Monserrat, O., Lamas, F. and Pérez, V. (2016). Reactivación de deslizamientos costeros por el desarrollo urbanístico en el litoral granadino. Monitorización DInSAR e inventario de daños. *Geogaceta 59*, 83-86.

Bahamonde, J., Cossio, J., Muñoz de la Nava, P., and Cembranos, V. (1986). *Posibilidades de Azabaches en Asturias.* Madrid, España: IGME. 104 pp.

Baldi, P., Casula, G., Cenni, N., Loddo, F., and Pesci, A. (2009). GPS-based monitoring of land subsidence in the Po Plain (Northern Italy). *Earth and Planetary Science Letters 288*, 204-212.

Bandini, A., Berry, P., and Boldini, D. (2015). Tunnelling-induced landslides: The Val di Sambro tunnel case study. *Engineering Geology 196*, 71-87.

Barra, A., Monserrat, O., Mazzanti, P., Esposito, C., Crosetto, M., and Scarascia-Mugnozza, G. (2016). First insights on the potential of Sentinel-1 for landslides detection. *Geomatics, Natural Hazards and Risk 7* , 1874-1883.

Barra, A., Monserrat, O., Navarro, J., Angelats, E., and Crosetto, M. (2019). *Deliverable D.2.6: Software tools to produce the 6-day ADA map and User manual.* CTTC/CERCA: U-Geohaz - "Geohazard impact assessment for urban areas" Grant Agreement No. 783169, 79 pp.

Barra, A., Reyes-Carmona, C., Herrera, G., Galve, J. P., Solari, L., Mateos, R. M., Azañón, J. M., Béjar-Pizarro, M., López-Vinielles, J., Palamà, R., Crosetto, M., Sarro, R., Cuervas-Mons, J., and Monserrat, O. (2022). From satellite interferometry displacements to potential damage maps: A tool for risk reduction and urban planning. *Remote Sensing of Environment 282,* 113294.

Barra, A., Solari, L., Béjar-Pizarro, M., Monserrat, O., Bianchini, S., Herrera, G., Crosetto, M., Sarro, R., González-Alonso, E., Mateos, R. M., Ligüerzana, S., and Moretti, S. (2017). A Methodology to Detect and Update Active Deformation Areas Based on Sentinel-1 SAR Images. *Remote Sensing 9*, 1002.

Bayer, B., Simoni, A., Schmidt, D., and Bertello, L. (2017). Using advanced InSAR techniques to monitor landslide deformations induced by tunneling in the Northern Apennines, Italy. *Engineering Geology 226*, 20-32.

Béjar-Pizarro, M., Álvarez Gómez, J. A., Staller, A., Luna, M. P., Pérez-López, R., Monserrat, O., Chunga, K., Lima, A., Galve, J. P., Martínez Díaz, J. J., Mateos, R. M., and Herrera, G. (2018). InSAR-Based Mapping to Support Decision-Making after an Earthquake. *Remote Sensing 10*, 899.

Béjar-Pizarro, M., Notti, D., Mateos, R. M., Ezquerro, P., Centolanza, G., Herrera, G., Bru, G., Sanabria, M., Solari, L., Duro, J., and Fernández, J. (2017). Mapping Vulnerable Urban Areas Affected by Slow-Moving Landslides Using Sentinel-1 InSAR Data. *Remote Sensing, 9*, 876.

Berardino, P., Costantini, M., Franceschetti, G., Iodice, A., Pietranera, L., and Rizzo, V. (2003). Use of differential SAR interferometry inmonitoring and modelling large slope instability at Maratea (Basilicata, Italy). *Engineering Geology 68*, 31-51.

Berardino, P., Fornaro, G., Lanari, R., and Sansosti, E. (2002). A New Algorithm for Surface Deformation Monitoring Based on Small Baseline Differential SAR Interferograms. *IEEE Transactions on Geoscience and Remote Sensing 40*, 2375-2383.

Bianchini, S., Herrera, G., Mateos, R. M., Notti, D., Garcia, I., Mora, O., and Moretti, S. (2013). Landslide Activity Maps Generation by Means of Persistent Scatterer Interferometry. *Remote Sensing 5*, 6198-6222.

Biescas, E., Crosetto, M., Agudo, M., Monserrat, O., and Crippa, B. (2007). Two Radar Interferometric Approaches to Monitor Slow and Fast Land Deformation. *Journal of Surveying Engineering 133*, 66-71.

Bonachea, J., Bruschi, V. M., Fernández-Maroto, G., Remondo, J., González-Díez, A., Diáz de Terán, J. R., and Cendrero, A. (2014). Geomorphic Hazards in Spain. In F. Gutiérrez, and

M. Gutiérrez, *Landscapes and Landforms of Spain* (pp. 319-345). Dordrecht: Springer Science+Business Media.

Borecka, A., and Herzig, J. (2015). Ground Penetrating Radar Investigations of Landslides: A Case Study in a Landslide in Radziszów. *Studia Geotechnica et Mechanica 37*, 11-18.

Boumans, R. M., and Day, J. W. (1993). High precision measurements of sediment elevation in shallow coastal areas using a sedimentation-erosion table. *Estuaries 16*, 375-380.

Bovenga, F., Nutricato, R., Refice, A., Guerriero, L., and Chiaradia, M. T. (2004). SPINUA: A Flexible Processing Chain for ERS/ENVISAT Long Term Interferometry. *Proceedings of the 2004 Envisat and ERS Symposium.* 6-10 September. Salzburg, Austria.

Bovenga, F., Pasquariello, G., Pellicani, R., Refice, A., and Spilotro, G. (2017). Landslide monitoring for risk mitigation by using corner reflector and satellite SAR interferometry: The large landslide of Carlantino (Italy). *Catena 151*, 49-62.

Bozzano, F., Cipriani, I., Mazzanti, P., and Prestininzi, A. (2011). Displacement patterns of a landslide affected by human activities: insights from ground-based InSAR monitoring. *Natural Hazards 59*, 1377-1396.

Bru, G., Escayo, J., Fernández, J., Mallorquí, J. J., Iglesias, R., Sansosti, E., Abajo, T., and Morales, A. (2018). Suitability Assessment of X-Band Satellite SAR Data for Geotechnical Monitoring of Site Scale Slow Moving Landslides. *Remote Sensing 10*, 936.

Bruckl, E., Brunner, F. K., Lang, E., Mertl, S., Muller, M., and Stary, U. (2013). The Gradenbach observatory - monitoring deep-seated gravitational slope deformation by geodetic, hydrological , and seismological methods. *Landslides 10*, 815-829.

Bruschi, V. M., Coratza, P., Piacentini, D., and Soldati, M. (2012). Geomorphological features of the Rio della Rocca valley (northern Apennines, Italy). *Journal of Maps 8*, 445-452.

Bucx, T. M., van Ruiten, J. M., Erkens, G., and de Lange, G. (2015). An integrated assessment framework for land subsidence in delta cities. *Proceedings of the International Association of Hydrological Sciences 372*, (pp. 485-491).

Cabral, J., Moniz, C., Ribeiro, P., Terrinha, P., and Matias, L. (2003). Analysis of seismic reflection data as a tool for the seismotectonic assessment of a low activity intraplate basin - the Lower Tagus Valley (Portugal). *Journal of Seismology 7*, 431-447.

Callaway, J. C., Cahoon, D. R., and Lynch, J. C. (2013). The Surface Elevation Table-Marker Horizon Method for measuring Wetland Accretion and Elevation Dynamics. In R. D. DeLaune, K. R. Reddy, C. J. Richardson, and J. P. Megonigal, *Methods in Biogeochemistry of Wetlands* (pp. 901-917). Madison, USA: Soil Science Society of America.

Camino Mayor, J. (1995). *Los Castros marítimos en Asturias.* Oviedo: Real Instituto de Estudios Asturianos, 252 pp.

Campos Costa, A., Sousa, M. L., Carvalho, A., and Coelho, E. (2010). Evaluation of seismic risk and mitigation strategies for the existing building stock: application of LNECloss to the metropolitan area of Lisbon. *Bulletin of Earthquake Engineering 8*, 119-134.

Cando Jácome, M., Martínez-Graña, A. M., and Valdés, V. (2020). Detection of Terrain Deformations Using InSAR Techniques in Relation to Results on Terrain Subsidence (Ciudad de Zaruma, Ecuador). *Remote Sensing 12*, 1598.

Canuti, P., Casagli, N., Ermini, L., Fanti, R., and Farina, P. (2004). Landslide activity as a geoindicator in Italy: significance and new perspectives from remote sensing. *Environmental Geology 45*, 907-919.

Carboni, F., Porreca, M., Valerio, E., Mariarosaria, M., De Luca, C., Azzaro, S., Ercoli, M., and Barchi, M. R. (2022). Surface ruptures and off-fault deformation of the October 2016 central Italy earthquakes from DInSAR data. *Scientific reports 12*, 3172.

Carnec, C., and Delacourt, C. (2000). Three years of mining subsidence monitored by SAR interferometry. *Journal of Applied Geophysics 43*, 43-54.

Carnec, C., Massonnet, D., and King, C. (1996). Two examples of the application of SAR interferometry to sites of small extent. *Geophysical Research Letters 23*, 3579-3582.

Carvalho, J., Dias, R., Ghose, R., Teves-Costa, P., Borges, J., Narciso, J., Pinto, C., and Leote, J. (2018). Near-surface Characterization of the Lisbon and Lower Tagus Valley Area, Portugal, for Seismic Hazard Assessment: VS30 and Soil Classification Maps. *Bulletin of the Seismological Society of America 108*, 2854-2876.

Carvalho, J., Matias, H., Torres, L., Manupella, G., Pereira, R., and Mendes-Victor, L. (2005). The structural and sedimentary evolution of the Arruda and Lower Tagus sub-basins, Portugal. *Marine and Petroleum Geology 22*, 427-453.

Cascini, L., Fornaro, G., and Peduto, D. (2010). Advanced low- and full-resolution DInSAR map generation for slow-moving landslide analysis at different scales. *Engineering Geology 112*, 29-42.

Casu, F., Elefante, S., Imperatore, P., Zinno, I., Manunta, M., De Luca, C., and Lanari, R. (2014). SBAS-DInSAR parallel processing for deformation time-series computation. *IEEE Journal of Selected Topics in Applied Earth Observations and Remote Sensing 7*, 3285-3296.

Catalão, J., Nico, G., Lollino, P., Conde, V., and Lorusso, G. (2016). Integration of InSAR Analysis and Numerical Modeling for the Assessment of Ground Subsidence in the City of Lisbon, Portugal. *IEEE Journal of Selected Topics in Applied Earth Observations and Remote Sensing 9*, 1663-1673.

Catani, F., Farina, P., Moretti, S., Nico, G., and Strozzi, T. (2005). On the application of SAR interferometry to geomorphological studies: estimation of landform attributes and mass movements. *Geomorphology 66*, 119-131.

Chae, B. G., Park, H. J., Catani, F., Simoni, A., and Berti, M. (2017). Landslide prediction, monitoring and early warning: a concise review of state-of-the-art. *Geosciences Journal 21*, 1033-1070.

Chan, Z., Yu, W., Wang, W., Zhang, J., Liu, X., and Zhu, J. (2017). An approach for accurately retrieving the vertical deformation component from two-track InSAR measurements. *International Journal of Remote Sensing 38*, 1702-1719.

Chang, L., Dollevoet, R. P., and Hanssen, R. F. (2016). Nationwide Railway Monitoring Using Satellite SAR Interferometry. *IEEE Journal of Selected Topics in Applied Earth Observations and Remote Sensing 10*, 596-604.

Chen, W., Li, W., He, J., Qiao, W., and Yang, Y. (2022). Impact of mining-induced bed separation spaces on a cretaceous aquifer: a case study of the Yingpanhao coal mine, Ordos Basin, China. *Hydrogeology Journal 30*, 691-706.

Chen, Z., Montpetit, B., Bank, S., White, L., Behnamian, A., Duffe, J., and Pasher, J. (2021). InSAR Monitoring of Arctic Landfast Sea Ice Deformation Using L-Band ALOS-2, C-Band Radarsat-2 and Sentinel-1. *Remote Sensing 13*, 4570.

Chrzanowski, A., and Chen, Y. Q. (1991). Use of the Global Positioning System (GPS) for Ground Subsidence Measurements in Western Venezuela Oil Fields. *Fourth International Symposium on Land Subsidence*, (pp. 419-431). 12-17 May. Houston, USA.

Cian, F., Delgado Blasco, J. M., and Carrera, L. (2019). Sentinel-1 for Monitoring Land Subsidence of Coastal Cities in Africa Using PSInSAR: A Methodology Based on the Integration of SNAP and StaMPS. *Geosciences 9*, 124.

Cigna, F., and Tapete, D. (2021). Present-day land subsidence rates, surface faulting hazard and risk in Mexico City with 2014-2020 Sentinel-1 IW InSAR. *Remote Sensing of Environment 253*, 112161.

Cigna, F., and Tapete, D. (2021). Sentinel-1 Big Data Processing with P-SBAS InSAR in the Geohazards Exploitation Platform: An Experiment on Coastal Land Subsidence and Landslides in Italy. *Remote Sensing 13*, 885.

Cigna, F., Banks, V. J., Donald, A. W., Donohue, S., Graham, C., Hughes, D., McKinley, J. M., and Parker, K. (2017). Mapping Ground Instability in Areas of Geotechnical Infrastructure Using Satellite InSAR and Small UAV Surveying: A Case Study in Northern Ireland. *Geosciences 7*, 51.

Cignetti, M., Manconi, A., Manunta, M., Giordan, D., De Luca, C., Allasia, P., and Ardizzone, F. (2016). Taking Advantage of the ESA G-POD Service to Study Ground Deformation Processes in High Mountain Areas: A Valle dÀosta Case Study, Northern Italy. *Remote Sensing 8*, 852.

Cloething, S., and Burov, E. B. (2011). Lithospheric folding and sedimentary basin evolution: a eview and analysis of formation mechanisms. *Basin Research 23*, 257-290.

Colesanti, C., and Wasowski, J. (2006). Investigating landslides with space-borne Synthetic Aperture Radar (SAR) interferometry. *Engineering Geology 88*, 173-199.

Colomina, I., and Molina, P. (2014). Unmanned aerial systems for photogrammetry and remote sensing: A review. *ISPRS Journal of Photogrammetry and Remote Sensing 92*, 79-97.

Comissão Exècutiva Metropolitana de Lisboa. (2019). *Área Metropolitana de Lisboa. Plano metropolitano de adaptaçao às alterações climáticas.* Área Metropolitana de Lisboa. 143 pp.

Consoritum of International Agricultural Research Centers (CGIAR). (2020). *SRTM 90 m DEM DIgital Elevation Database. SRTM Data Dowload Manager*. Retrieved from https://srtm.csi.cgiar.org/srtmdata/

Corsa, B., Barba-Sevilla, M., Tiampo, K., and Meertens, C. (2022). Integration of DInSAR Time Series and GNSS Data for Continuous Volcanic Deformation Monitoring and Eruption Early Warning Applications. *Remote Sensing 14*, 784.

Corsini, A., Farina, P., Antonello, G., Barbieri, M., Casagli, N., Coren, F., Guerri, L., Ronchetti, F., Sterzai, P., and Tarchi, D. (2006). Spaceborne and ground-based SAR interferometry as tools for landslide hazard management in civil protection. *International Journal of Remote Sensing 27*, 2351-2369.

Costantini, M. (1998). A novel phase unwrapping method based on network programming. *IEEE Transactions on Geoscience and Remote Sensing 36*, 813-821.

Costantini, M., Farina, A., and Zirilli, F. (1999). A fast phase unwrapping algorithm for SAR interferometry. *IEEE Transactions on Geoscience and Remote Sensing 37*, 452-460.

Crans, W., Mandl, G., and Haremboure, J. (1980). On the theory of growth faulting: a geomechanical delta model based on ravity sliding. *Journal of Petroleum Geology 2*, 265-307.

Crippa, C., and Agliardi, F. (2021). Practical Estimation of Landslide Kinematics Using PSI Data. *Geoscience 11*, 214.

Crosetto, M., Crippa, B., Biescas, E., Monserrat, O., and Agudo, M. (2005). State-of-the-Art of Land Deformation Monitoring Using Differential SAR Interferometry. *ISPRS Workshop 2005.* 17-20 May 2005. Hannover, Germany.

Crosetto, M., Gili, J. A., Monserrat, O., Cuevas-González, M., Corominas, J., and Serral, D. (2013). Interferometric SAR monitoring of the Vallcebre landslide (Spain) using corner reflectors. *Natural Hazards and Earth System Sciences 13*, 923-933.

Crosetto, M., Luzi, G., Monserrat, O., Barra, A., Cuevas-González, M., Palamà, R., Krishnakumar, V., Wassie, Y., Mirmazloumi, S. M., Espín-López, P., and Crippa, B. (2020). Deformation Monitoring using SAR Interferometry and Active and Passive Reflectors. *XXIV ISPRS Congress 2020* (pp. 287-292). Volume XLIII-B3-2020.

Crosetto, M., Monserrat, O., Cuevas, M., and Crippa, B. (2011). Spaceborne Differential SAR Interferometry: Data Analysis Tools for Deformation Measurement. *Remote Sensing 3*, 305-318.

Crosetto, M., Monserrat, O., Cuevas-González, M., Devanthéry, N., and Crippa, B. (2016). Persistent Scatterer Interferometry: A review. *ISPRS Journal of Photogrammetry and Remote Sensing 115*, 78-89.

Crosta, G. B., and Frattini, P. (2008). Rainfall-induced landslides and debris flows. *Hydrological Processes 22*, 237-260.

Cruden, D. M. (1991). A Simple Definition of a Landslide. *Bulletin of the International Association of Engineering Geology 43*, 27-29.

Cruden, D. M., and Varnes, D. J. (1996). Landslide types and processes. In *Landslides: Investigation and Mitigation* (pp. 36-75). Transportation Research Board, National Academy of Sciences.

Cuervas-Mons, J., Domínguez-Cuesta, M. J., and Carrillo, J. A. (2021a). Análisis de movimientos del terreno en Guayaquil (Ecuador) mediante G-POD (A-DInSAR). *Geogaceta 69*, 47-50.

Cuervas-Mons, J., Domínguez-Cuesta, M. J., González-Pumariega, P., López-Fernández, C., Valenzuela, P., Mateos-Redondo, F., Monserrat, O., Barra, A., and Jiménez-Sánchez, M. (2021b). Monitorización del retroceso costero en la costa acantilada de Podes (Cabo Peñas, N de España) mediante técnicas topográficas y DInSAR. *Geo-Temas 18. X Congreso Geológico de España* (pp. 246). Vitoria-Gasteiz, España: Sociedad Geológica de España.

Cuervas-Mons, J., Domínguez-Cuesta, M. J., Mateos-Redondo, F., Monserrat, O., and Barra, A. (2021c). Ground motion detected in Central South Asturias (N Spain) by using Sentinel-1 SAR data. *EGU General Assembly 2021*, EGU21-28. Online.

Cuervas-Mons, J., Domínguez-Cuesta, M. J., Mateos-Redondo, F., Monserrat, O., and Barra, A. (2022a). Mining impact in a coal exploitation under an urban area: detection by Sentinel-1 SAR data. *EGU General Assembly 2022*, EGU22-8095. Online.

Cuervas-Mons, J., Domínguez-Cuesta, M. J., Redondo, F., Barra, A., Monserrat, O., Valenzuela, P., and Jiménez-Sánchez, M. (2021d). Sentinel-1 Data Processing for Detecting and Monitoring of Ground Instabilities in the Rocky Coast of Central Asturias (N Spain). *Remote Sensing 13*, 3076.

Cuervas-Mons, J., Zêzere, J. L., Domínguez-Cuesta, M. J., Barra, A., Reyes-Carmona, C., Monserrat, O., Oliveira, S. C., and Melo, R. (2022b). Assessment of Urban Subsidence in the Lisbon Metropolitan Area (Central-West of Portugal) Applying Sentinel-1 SAR Dataset and Active Deformation Areas Procedure. *Remote Sensing 14*, 4084.

Darvishi, M., Schlögel, R., Bruzzone, L., and Cuozzo, G. (2018). Integration of PSI, MAI, and Intensity-Based Sub-Pixel Offset Tracking Results for Landslide Monitoring with X-Band Corner Reflectors—Italian Alps (Corvara). *Remote Sensing 10*, 409.

De Luca, C., Cuccu, R., Elefante, S., Zinno, I., Manunta, M., Casola, V., Rivolta, G., Lanari, R., and Casu, F. (2015). An On-Demand Web Tool for the Unsupervised Retrieval of Earth`s Surface Deformation from SAR Data: The P-SBAS Service within the ESA G-POD Environment. *Remote Sensing 7*, 15630-15650.

De Novellis, V., Castaldo, R., De Luca, C., Pepe, S., Zinno, I., Casu, F., Lanari, R., and Solaro, G. (2017). Source modelling of the 2015Wolf volcano (Galápagos) eruption inferred from Sentinel 1-A DInSAR deformation maps and pre-eruptive ENVISAT time series. *Journal of Volcanology and Geothermal Research 334*, 246-256.

Del Soldato, M., Tomás, R., Pont, J., Herrera, G., García López-Davalillos, J. C., and Mora, O. (2016). A multi-sensor approach for monitoring a road bridge in the Valencia harbor (SE Spain) by SAR Interferometry (InSAR). *Rendiconti Della Società Geologica Italiana 41*, 235-238.

Delgado-Blasco, J. M., Foumelis, M., Stewart, C., and Hooper, A. (2019). Measuring Urban Subsidence in the Rome Metropolitan Area (Italy) with Sentinel-1 SNAP-StaMPS Persistent Scatterer Interferometry. *Remote Sensing 11*, 129.

Deparis, J., Garambois, S., and Hantz, D. (2007). On the potential of Ground Penetrating Radar to help rock fall hazard assessment: A case study of a limestone slab, Gorges de la Bourne (French Alps). *Engineering Geology 94*, 89-102.

Devanthéry, N., Crosetto, M., Monserrat, O., Crippa, B., and Mróz, M. (2019). Data analysis tools for persistent scatterer interferometry based on Sentinel-1 data. *European Journal of Remote Sensing 52 (1)*, 15-25.

Devanthéry, N., Crosetto, M., Monserrat, O., Cuevas-González, M., and Crippa, B. (2014). An Approach to Persistent Scatterer Interferometry. *Remote Sensing 6*, 6662-6679.

Di Traglia, F., De Luca, C., Manzo, M., Nolesini, T., Casagli, N., Lanari, R., and Casu, F. (2021). Joint exploitation of space-borne and ground-based multitemporal InSAR measurements for volcano monitoring: The Stromboli volcano case study. *Remote Sensing of Environment 260*, 112441.

Dindi, E. (2015). An assessment of the performance of the geophysical methods as a tool for the detection of zones of potential subsidence in the area southwest of Nakuru town, Kenya. *Environmental Earth Sciences 73*, 3643-3653.

Direçao-Geral do Território (DGT). (2021). *Cartografia Topográfica. Ortofotos Digitais*. Retrieved from https://www.dgterritorio.gov.pt/cartografia/cartografia-topografica/ortofotos/ortofotos-digitais

Dirección General de Protección Civil y Emergencias (DGPCE). (2020). *Fallecidos por Riesgos Naturales en España en 2019.* Subdirección General de Prevención, Planificación y Emergencias. Ministerio del Interior. 12 pp.

Domínguez-Cuesta, M. J. (2003). *Geomorfología e inestabilidad de laderas en la Cuenca Carbonífera Central (Valle del Nalón, Asturias). Análisis de la susceptibilidad ligada a los movimientos superficiales del terreno.* Tesis Doctoral. Universidad de Oviedo. 223 pp.

Domínguez-Cuesta, M. J., Ferrer-Serrano, A., Rodríguez-Rodríguez, L., López-Fernández, C., and Jiménez-Sánchez, M. (2020). Análisis del retroceso de la costa cantábrica en el entorno del Cabo Peñas (Asturias, N España). *Geogaceta 68*, 63-66.

Domínguez-Cuesta, M. J., González-Pumariega, P., Valenzuela, P., López-Fernández, C., Rodríguez-Rodríguez, L., Ballesteros, D., Mora, M., Meléndez, M., Herrera, F., Marigil, M. A., Pando, L., Cuervas-Mons, J., and Jiménez-Sánchez, M. (2022a). Understanding the retreat of the Jurassic Cntabrian coast (N. Spain): Comprehensive monitoring and 4D evolution model of the Tazones Lighthouse landslide. *Marine Geology 449*, 106836.

Domínguez-Cuesta, M. J., Jiménez-Sánchez, M., and Berrezueta, E. (2007). Landslides in the Central Coalfield (Cantabrian Mountains, NW Spain): Geomorphological features, conditioning factors and methodological implications in susceptibility assessment. *Geomorphology 89*, 358-369.

Domínguez-Cuesta, M. J., Jiménez-Sánchez, M., and Rodríguez García, A. (1999). Press archives as temporal records of landslides in the North of Spain: relationships between rainfall and instability slope events. *Geomorphology 30*, 125-132.

Domínguez-Cuesta, M. J., Jiménez-Sánchez, M., González-Fernández, J. A., Quintana, L., Flor, G., and Flor-Blanco, G. (2015). GIS as a tool to detect flat erosion al surfaces in coastal areas: a case study in North Spain. *Geologica Acta 13(2)*, 97-106.

Domínguez-Cuesta, M. J., Quintana, L., Valenzuela, P., Cuervas-Mons, J., Alonso, J. L., and García Cortés, S. (2021). Evolution of a human-induced mass movement under the influence of rainfall and soil moisture. *Landslides 18*, 3685-3693 .

Domínguez-Cuesta, M. J., Rodríguez-Rodríguez, L., López-Fernández, C., Pando, L., Cuervas-Mons, J., Olona, J., González-Pumariega, P., Serrano, J., Valenzuela, P., and Jiménez-Sánchez, M. (2022b). Using Remote Sensing Methods to Study Active Geomorphologic Processes on Cantabrian Coastal. *Remote Sensing 14*, 5139.

Domínguez-Cuesta, M. J., Valenzuela, P., Rodríguez-Rodríguez, L., Ballesteros, D., Jiménez-Sánchez, M., Piñuela, L., and García-Ramos, J. C. (2019). Cliff Coast of Asturias. In J. A. Morales, *The Spanish Coastal System. Dynamic Processes, Sediments and Management* (pp. 49-77). Cham, Switzerland: Springer Nature Switzerland AG.

Duque, S., Mallorqui, J. J., Blanco, P., and Monells, D. (2007). Application of the Coherent Pixels Technique (CPT) to urban monitoring. *2007 Urban Remote Sensing Joint Event* (pp. 1-7). 11-13 April 2007. Paris, France.

Duro, J., Inglada, J., Closa, J., Adam, N., and Arnaud, A. (2003). High Resolution Differential Interferometry using time series of ERS and ENVISAT ASAR data. *Proceedings of FRINGE 2003 Workshop.* 1-5 December 2003. Frascaty, Italy.

Dzurisin, D. (2007). *Volcano Deformation: New Geodetic Monitoring Techniques.* Springer Berlin, Heidelberg, 442 pp.

Epifânio, B., Zêzere, J. L., and Neves, M. (2014). Susceptibility assessment to different types of landslides in the coastal cliffs of Lourinhã (Central Portugal). *Journal of Sea Research, 93*, 150-159.

Euillades, L. D., Euillades, P. A., Riveros, N. C., Masiokas, M. H., Ruiz, L., Pitte, P., Elefante, S., Casu, F., and Balbarani, S. (2016). Detection of glaciers displacement time-series using SAR. *Remote Sensing of Environment 184*, 188-198.

European Space Agency (ESA). (2019). *ESA Sentinel 1 Missions*. Retrieved from https://sentinel.esa.int/web/sentinel/missions/sentinel-1

European Space Agency (ESA). (2022a). *Copernicus Open Access Hub*. Retrieved from https://scihub.copernicus.eu/

European Space Agency (ESA). (2022b). *European Space Agency, eoPortal Directory, Missions - S*. Retrieved from https://www.eoportal.org/satellite-missions

European Space Agency (ESA). (2022c). *Sentinel Online. The Sentinel-1 Toolbox*. Retrieved from https://sentinels.copernicus.eu/web/sentinel/toolboxes/sentinel-1

Ezquerro, P., Herrera, G., Marchamalo, M., Tomás, R., Béjar-Pizarro, M., and Martínez, R. (2014). A quasi-elastic aquifer deformational behavior: Madrid aquifer case study. *Journal of Hydrology 519*, 1192-1204.

Fernández-Oliveras, M. P. (2009). *Determinación de movimientos verticales del terreno mediante técnicas de interferometría radar DInSAR.* Tesis Doctoral. E.T.S. de Caminos, Canales y Puertos. Universidad de Granada. 206 pp.

Fernández-Viejo, G., Llana-Fúnez, S., Acevedo, J., and López-Fernández, C. (2021). The Cantabrian Fault at Sea. Low Magnitude Seismicity and Its Significance Within a Stable Setting. *Frontiers in Earth Science 9*, 645061.

Ferrer, M. (1995). Los movimientos de ladera en España. In I. T. (ITGE), *Reducción de Riesgos Geológicos en España* (pp. 69-82). Madrid, Spain.

Ferreti, A., Fumagalli, A., Novali, F., Patri, C., Rocca, F., and Rucci, A. (2011). A New Algorithm for Processing Interferometric Data-Stacks: SqueeSAR. *IEEE Transactions on Geoscience and Remote Sensing 49*, 3460-3470.

Ferreti, A., Prati, C., and Rocca, F. (2000). Nonlinear subsidence rate estimation using permanent scatterers in differenital SAR interferometry. *IEEE Transactions on Geoscience and Remote Sensing 38*, 2202-2212.

Ferretti, A., Monti-Guarnieri, A., Prati, C., and Rocca, F. (2007). *InSAR Principles: Guidelines for SAR Interferometry Processing and Interpretation.* ESA Publications. 250 pp.

Ferretti, A., Prati, C., and Rocca, F. (2001). Permanent Scatterers in SAR interferometry. *IEEE Transactions on Geoscience and Remote Sensing 39*, 8-20.

Fialko, Y., Sandwell, D., Simons, M., and Rosen, P. (2005). Three-dimensional deformation caused by the Bam, Iran, earthqueake and the origin of shallow slip deficit. *Nature 435*, 295-299.

Flor, G. (1983). Las Rasas Asturianas: Ensayos de Correlación y Emplazamiento. *Trabajos de Geología 13*, 65-81.

Flor, G., and Flor-Blanco, G. (2014). Raised beaches in the Cantabrian Coast. In F. Gutiérrez, and M. Gutiérrez, *Landscapes and Landsforms of Spain* (pp. 1-10). Cham, Switzerland: Springer Nature Switzerland AG.

Flor, G., del Busto, J. A., and Flor-Blanco, G. (2006). Morphological and Sedimentary Patterns of Ports ofthe Asturian Region (NW Spain). *Journal of Coastal Research 48*, 35-40.

Flor-Blanco, G., Flor, G., and Pando, L. (2013). Evolution of the Salinas-El Espartal and Xagó beach/dune systems in north-western Spain over recent decades: evidence for responses to natural processes and anthropogenic interventions. *Geo-Marine Letters 33*, 143-157.

Fuente Alonso, P., and Sáenz de Santa María Benedet, J. A. (1999). La tectónica y microtectónica de la Cuenca Carbonífera Central de Asturias. *Trabajos de Geología 21*, 121-141.

Gabriel, A. K., Goldstein, R. M., and Zebker, H. A. (1989). Mapping Small Elevation Changes Over Large Areas: Differential Radar Interferometry. *Journal of Geophysical Research 94*, 9183-9191.

Galloway, D. L., Erkens, G., Kuniansky, E. L., and Rowland, J. C. (2016). Preface: Land subsidence processes. *Hydrogeology Journal 24*, 547-550.

Galloway, D. L., Jones, D. R., and Ingebritsen, S. E. (1999). *Land subsidence in the United States.* U.S. Geological Survey, 177 pp.

Galve, J. P., Pérez-Peña, J. V., Azañón, J. M., Closson, D., Caló, F., Reyes-Carmona, C., Jabaloy, A., Ruano, P., Mateos, R. M., Notti, D., Herreram G., Béjar-Pizarro, M., Monserrat, O., and Bally, P. (2017). Evaluation of SBAS InSAR Service of the European Space Agency`s Geohazard Exploitation Platform (GEP). *Remote Sensing 9*, 1291.

Gambolati, G., and Teatini, P. (2021). *Land Subsidence and its Mitigation.* Ontario, Canada: Groundwater Project. 92 pp.

García, R. A., Cruz Oliveira, S., and Zêzere, J. L. (2016). Assessing population exposure for landslide risk analysis using dasymetric cartography. *Natural Hazards and Earth System Sciences 16*, 2769-2782.

García-Loygorri, A. (1971). El Carbonífero de la Cuenca Central Asturiana. *Trabajos de Geología 3*, 101-150.

García-Ramos, J. C., and Aramburu, C. (2010). Las sucesiones litorales y marinas del Jurásico Superior. Acantilados de Tereñes (Ribadesella) y de la playa de la Griega (Colunga), Guía de Campo (excursión B). *V Congreso del Jurásico de España.* Colunga, España.

Garg, S., Motagh, M., Indu, J., and Karanam, V. (2022). Tracking hidden crisis in India’s capital from space: implications of unsustainable groundwater use. *Scientific Reports 12*, 651.

Gili, J. A. (1989). Control de movimientos. Auscultación de taludes y laderas inestables. In J. Corominas, *Estabilidad de Taludes y Laderas Naturales* (pp. 167-214). Barcelona: Monografía Nº 3, Sociedad Española de Geomorfología.

Gili, J. A. (2003). Instrumentación para control de movimientos de ladera: Sistema GPS y otros. *Operatividad de la instrumentación en aguas subterráneas, suelos contaminados y riesgos geológicos* (pp. 235-246). Madrid: IGME.

Gili, J. A., Corominas, J., and Rius, J. (2000). Using Global Positioning System techniques in landslide monitoring. *Engineering Geology 55*, 167-192.

González de Vallejo, L. (2002). *Ingeniería Geológica.* Pearson Education. 744 pp.

González Moradas, M. R., and Lima de Montes, Y. (2001). Cartografía del riesgo a los deslizamientos en la zona central del Principado de Asturias. *Mapping 73*, 6-15.

Graniczny, M., Colombo, D., Kowalski, Z., Przyiucka, M., and Zdanowski, A. (2015). New results on ground deformation in the Upper Silesian Coal Basin (southern Poland) obtained during the DORIS Project (EU-FP-7). *Pure and Applied Geophysics 172*, 3029–3042.

Gray, L., Joughin, I., Tulaczyk, S., Spikes, V. B., Bindschadler, R., and Jezek, K. (2005). Evidence for subglaciar water transport in the West Antarctic Ice Sheet through three-dimensional satellite radar interferometry. *Geophysical Research Letters 32*, L03501.

Grit, M., and Kanli, A. I. (2016). Integrated Seismic Survey for Detecting Landslide Effects on High Speed Rail Line at Istanbul–Turkey. *Open Geosciences 8*, 161-173.

Gu, K., Shi, B., Liu, C., Jiang, H., Li, T., and Wu, J. (2018). Investigation of land subsidence with the combination of distributed fiber optic sensing techniques and microstructure analysis of soils. *Engineering Geology 240*, 34-47.

Guéguen, Y., Deffontaines, B., Fruneau, B., Al Heib, M., de Michele, M., Raucoules, D., Guise, Y., and Planchenault, J. (2009). Monitoring residual mining subsidence of Nord/Pas-de-Calais coal basin from differential and Persistent Scatterer Interferometry (Northern France). *Journal of Applied Geophyscis 69*, 24-34.

Gulati, S., Nutricato, R., Nitti, D. O., and Samarelli, S. (2021). Spaceborne SAR Interferometry Exploitation for Longitudinal Ground Deformation Monitoring. *IEEE Aerospace Conference (50100)*, (pp. 1-10). 6-13 March 2021. Big Sky, Montana (EEUU).

Gutiérrez-Claverol, M., and García-Ramos, J. C. (2016). La geología de Asturias a través de las Topografías Médicas. *Trabajos de Geología 36*, 203-236.

Gutierrez-Claverol, M., and Luque-Cabal, C. (1994). *Recursos del Subsuelo de Asturias*. 2º Edición, Universidad de Oviedo. 392 pp.

Gutiérrez-Santolalla, F., Gutiérrez-Elorza, M., Marín, C., Maldonado, C., and Younger, P. L. (2005). Subsidence hazard avoidance based on geomorphological mapping in the Ebro River valley mantled evaporite karst terrain (NE Spain). *Environmental Geology 48*, 370–383.

Guzzetti, F., Mondini, A. C., Cardinali, M., Fiorucci, F., Santangelo, M., and Chang, K. T. (2012). Landslide inventory maps: New tools for an old problem. *Earth-Science Reviews 112*, 42-66.

Guzzetti, F., Peruccacci, S., Rossi, M., and Stark, C. P. (2007). Rainfall thresholds for the initiation of landslides in central and southern Europe. *Meteorology Atmospheric Physics 98*, 239-267.

Hache, U., Blum, P., da Silva, P. F., Andersen, P., Pilz, J., Chalov, S. R., Malet, P., Auflic, M. J., Andres, N., Poyiadji, E., Lamas, P. C., Zhang, W., Peshevski, I., Pétursson, H. G., Kurt, T., Dobrev, N., García-Davalillo, J. C., Halkia, M., Ferri, S., Gaprindashvili, G., Engström, J., and Keellings, D. (2016). Fatal landslides in Europe. *Landslides 13*, 1545–1554.

Haghighi, M. H., and Motagh, M. (2019). Ground surface response to continuous compaction of aquifer system in Tehran, Iran: Results from a long-term multi-sensor InSAR analysis. *Remote Sensing of Environment 221*, 534-550.

Hammad, M., Mucsi, L., and Leeuwen, B. V. (2019). Landslide Investigation using Differentiañ Synthetic Aperture Radar Interferometry: A Case Study of Balloran Dam Area in Syria. *The International Archives of the Photogrammetry, Remote Sensing and Spatial Information Sciences - Geoinformation for Disaster Management.* 3-6 September 2019 (pp. 133-138). Prague, Czech Republic.

Heleno, S. I., Oliveira, L. G., Henriques, M. J., Falcão, A. P., Lima, J. N., Cooksley, G., Ferreti, A., Fonseca, A. M., Lobo-Ferreira, J. P., and Fonseca, J. F. (2011). Persistent Scatterers Interferometry detects and measures ground subsidence in Lisbon. *Remote Sensing of Environment 115*, 2152-2167.

Herrera, G., Ezquerro, P., Tomás, R., Béjar-Pizarro, M., López-Vinielles, J., Rossi, M., Mateos, R. M., Carreón-Freyre, D., Lambert, J., Teatini, P., Cabral-Cano, E., Erkens, G., Galloway, D., Hung, W. C., Kakar, N., Sneed, M., Tosi, L., Wang, H., and Ye, S. (2021). Mapping the global threat of land subsidence. *Science 371*, 34-36.

Herrera, G., Fernández-Merodo, J. A., Mulas, J., Pastor, M., Luzi, G., and Monserrat, O. (2009). A landslide forecasting model using ground based SAR data: The Portalet case study. *Engineering Geology 105*, 220-230.

Herrera, G., Gutiérrez, F., García-Davalillo, J., Guerrero, J., Notti, D., Galve, J. P., Fernández-Merodo, J. A., and Cooksley, G. (2013). Multi-sensor advanced DInSAR monitoring of very slow landslides: The Tena Valley case study (Central Spanish Pyrenees). *Remote Sensing of Environment 128*, 31-43.

Herrera, G., Notti, D., García López-Davalillo, J. C., Mora, O., Cooksley, G., Sánchez, M., Arnaud, A., and Crosetto, M. (2011). Analysis with C- and X-band satellite SAR data of the Portalet landslide area. *Landslides 8*, 195-206.

Herrera, G., Tomás, R., López-Sánchez, J. M., Delgado, J., Vicente, F., Mulas, J., Cooksley, G., Sanchez, M., Duro, J., Arnaud, A., Blanco, P., Duque, S., Mallorquí, J. J., De la Vega-Panizo, R., and Monserrat, O. (2009). Validation and comparison of Advanced Differential Interferometry Techniques: Murcia metropolitan area case study. *ISPRS Journal of Photogrammetry and Remote Sensing 64*, 501-512.

Hooper, A. (2008). A multi-temporal InSAR method incorporating both persistent scatterer and small baseline approaches. *Geophysical Research Letters 35*, L16302.

Hooper, A., Segall, P., and Zebker, H. A. (2007). Persistent scatterer interferometric synthetic aperture radar for crustal deformation analysis, with application to Volcán Alcedo, Galápagos. *Journal of Geophysical Research 112*, B07407.

Hooper, A., Zebker, H. A., Segall, P., and Kampes, B. (2004). A new method for measuring deformation on volcanoes and other natural terrains using InSAR persistent scatterers. *Geophysical Research Letters 31*, L23611.

Hu, L., Navarro-Hernández, M. I., Liu, X., Tomás, R., Tang, X., Bru, G., Ezquerro, P., and Zhang, Q. (2022). Analysis of regional large-gradient land subsidence in the Alto Guadalentín Basin (Spain) using open-access aerial LiDAR datasets. *Remote Sensing of Environment 280*, 113218.

HUNOSA. (2017). *Ejecución y Limpieza de Colector Pozo Fondón.* Tomo I: Memoria, Reporte Técnico. 52 pp.

HUNOSA. (2018). *Informe técnico para la solicitud de concesión para el aprovechamiento geotérmico a denominar Fondón.* Reporte Técnico. 76 pp.

HUNOSA, IGME and UNIOVI. (2011). *Estudio sobre la inundación de los pozos mineros en la Zona Candín (Valle del Nalón).* Tomo I: Memoria, Reporte Técnico. 180 pp.

Hussain, Y., Schlögel, R., Innocenti, A., Hamza, O., Iannucci, R., Martino, S., and Havenith, H. B. (2022). Review on the Geophysical and UAV-Based Methods Applied to Landslides. *Remote Sensing 14*, 4564.

Instituto Geográfico Nacional (IGN). (2020). *Centro de Descargas. Organismo Autónomo Centro Nacional de Información Geográfica*. Retrieved from https://centrodedescargas.cnig.es/CentroDescargas/index.jsp

Instituto Geológico y Minero de España (IGME). (1972a). *Mapa Geológico de España 1:50000 Gijón. Hoja 14 (13-3).* Segunda serie - Primera Edición. Ministerio de Industria.

Instituto Geológico y Minero de España (IGME). (1972b). *Mapa Geológico de España 1:50000 Avilés. Hoja 13 (12-3).* Segunda serie - Primera Edición. Ministerio de Industria.

Instituto Geológico y Minero de España (IGME). (1973). *Mapa Geológico de España 1:50000 Mieres. Hoja 53 (13-05).* Segunda serie - Primera Edición. Ministerio de Industria.

Instituto Nacional de Estadística (INE). (2021). *Demografía y Población*. Retrieved from https://www.ine.es/dyngs/INEbase/es/categoria.htm?c=Estadistica_Pandcid=1254734710984

Jaboyedoff, M., Oppikofer, T., Abellán, A., Derron, M. H., Loye, A., Metzger, R., and Pedrazzini, A. (2012). Use of LIDAR in landslide investigations: a review. *Natural Hazards 61*, 5-28.

Jackson, J. A., and Bates, R. L. (1997). *Glossary of geology.* American Geological Institute. 769 pp.

Jarvis, A., Reuter, H. I., Nelson, A., and Guevara, E. (2008). *Hole-filled seamless SRTM data V4, International Centre for Tropical Agriculture (CIAT).* Retrieved from CGIAR-CSI SRTM 90m DEM Digital Elevation Database: https://srtm.csi.cgiar.org/

Jeannin, M., Garambois, S., Grégoire, C., and Jongmans, D. (2006). Multiconfiguration GPR measurements for geometricfracture characterization in limestone cliffs (Alps). *Geophysics 71*, B85.

Jiang, N., Li, H. B., Li, C. J., Xiao, H. X., and Zhou, J. W. (2022). A Fusion Method Using Terrestrial Laser Scanning and Unmanned Aerial Vehicle Photogrammetry for Landslide Deformation Monitoring Under Complex Terrain Conditions. *IEEE Transactions on Geosciences and Remote Sensing 60*, 4707214.

Jiménez-Sánchez, M., and Ballesteros, D. (2017). Metodología de evaluación del riesgo geoarquelógico en castros marítimos: El Castiellu (Asturias, España). *Geogaceta 62*, 59-62.

Jiménez-Sánchez, M., Domínguez-Cuesta, M. J., Ballesteros, D., López-Fernández, C., González-Pumariega, P., and Valenzuela, P. (2019). Implicaciones del retroceso costero de acantilados en la conservación del patrimonio cultural: el ejemplo del Castro de El Castiellu de Podes (Asturias, Norte de España). *XV Reunión Nacional del Cuaternario.* 1-5 Julio 2019. Bilbao, España.

Jongmans, D., and Garambois, S. (2007). Geophysical investigation of landslides: A review. *Nulletin Société Géologique de France 178*, 101-112.

Jordá-Bordehore, L., Riquelme, A., Cano , M., and Tomás, R. (2017). Comparing manual and remote sensing field discontinuity collection used in kinematic stability assessment of failed rock slopes. *International Journal of Rock Mechanics and Mining Sciences 97*, 24-32.

Joughin, I., Smith, B. E., and Abdalati, W. (2010). Glaciological advances made with interferometric synthetic aperture radar. *Journal of Glaciology 56*, 1026-1042.

Joughin, I., Winebrenner, D., Fahnestock, M., Kwok, R., and Krabill, W. (1996). Measurement of ice sheet topography using satellite-radar interferometry. *Journal of Glaciology 42*, 12-22.

Julivert, M. (1976). La estructura de la región de Cabo Peñas. *Trabajos de Geología 8*, 203-309.

Karantanellis, E., Marinos, V., Vassilakis, E., and Hölbling, D. (2021). Evaluation of Machine Learning Algorithms for Object-Based Mapping of Landslides Zones Using UAV Data. *Geosciences 11*, 305.

Karpytchev, M., Ballu, V., Krien, Y., Becker, M., Goodbred, S., Spada, G., Calmant, S., Shum, C. K., and Khan, Z. (2018). Contributions of a Strengthened Early Holocene Monsoon and Sediment Loading to Present-Day Subsidence of the Ganges-Brahmaputra Delta. *Geophysical Research Letters 45*, 1433-1442.

Kearns, T. J., Wang, G., Bao, Y., Jiang, J., and Lee, D. (2015). Current Land Subsidence and Groundwater Level Changes in the Houston Metropolitan Area (2005-2012). *Journal of Surveying Engineering 141*, 05015002.

Keaton, J. R., and DeGraff, J. V. (1996). Surface Observation and Geologic Mapping. In *Landslides: Investigation and Mitigation* (pp. 178-230). Transportation Research Board, National Academy of Sciences.

Kim, J. H., Yi, M. J., Hwang, S. H., Song, Y., Cho, S. J., and Lee, S. K. (2003). Application of Integrated Geophysical Methods to Investigate the Cause of Ground Subsidence of a Highly Civilized Area. *Geosystem Engineering 6*, 74-80.

Klees, R., and Massonet, D. (1998). Deformation Measurements Using SAR Interferometry: Potential and Limitations. *Geologie en Mijnbouw 77*, 161-176.

Klemas, V. V. (2015). Coastal and Environmental Remote Sensing from Unmanned Aerial Vehicles: An Overview. *Journal of Coastal Research 31*, 1260-1267.

Kooi, H., and de Vries, J. J. (1998). Land subsidence and hydrodynamic compaction of sedimentary basins. *Hydrology and Earth System Sciences 2*, 159-171.

Kuang, J., Ge, L., Metternicht, G. I., Hay-Man Ng, A., Wang, H., Zare, M., and Kamranzad, F. (2019). Coseismic deformation and source model of the 12 November 2017 Mw 7.3 Kermanshah Earthquake (Iran-Iraq border) investigated through DInSAR measurements. *International Journal of Remote Sensing 40*, 532-554.

Kuras, P., Ortyl, L., Owerko, T., Salamak, M., and Lazinski, P. (2020). GB-SAR in the Diagnosis of Critical City Infrastructure - A Case Study of a Load Test on the Long Tram Extradosed Bridge. *Remote Sensing 12*, 3361.

Kwok, R., Siegert, M. J., and Carsey, F. D. (2000). Ice motion over Lake Vostok, Antarctica: constraints on inferences regarding the accreted ice. *Journal of Glaciology 46*, 689-694.

Laboratório Nacional de Energia e Geologia (LNEG). (1992). *Geological Map of Portugal 1992, Scale 1:1,000,000.*

Laboratório Nacional de Energia e Geologia (LNEG). (2010). *Geological Map of Portugal 2010, Scale 1:500,000.*

Lanari, R., Berardino, P., Bonano, M., Casu, F., Manconi, A., Manunta, M., Manzo, M., Pepe, A., Sansosti, E., Solaro, G., Tizzani, P., and Zeni, G. (2010). Surface displacements associated with the L'Aquila 2009 Mw 6.3 earthquake (central Italy): New evidence from SBAS-DInSAR time series analysis. *Geophysical Research Letters 37*, L20309.

Lanari, R., Casu, F., Manzo, M., Zeni, G., Berardino, P., Manunta, M., and Pepe, A. (2007). An Overview of the Small BAseline Subset Algorithm: A DInSAR Technique for Surface Deformation Analysis. *Pure and Applied Geophysics 164*, 637-661.

Leal, M., Boavida-Portugal, I., Fragoso, M., and Ramos, C. (2019). How much does an extreme rainfall event cost? Material damage and relationships between insurance, rainfall, land cover and urban flooding. *Hydrological Sciences Journal 64*, 673-689.

Leal, M., Fragoso, M., Lopes, S., and Reis, E. (2020). Material damage caused by high-magnitude rainfall based on insurance data: Comparing two flooding events in the Lisbon Metropolitan Area and Madeira Island, Portugal. *International Journal of Disaster Risk Reduction 51*, 101806.

Lobo Ferreira, J. P., and Oliveira, M. M. (2004). Groundwater vulnerability assessment in Portugal. *Geofisica Internacional 43*, 541-550.

López-Fernández, C., Arias-Prieto, D., Fernández-Viejo, G., Pando, L., and Castells-Fernández, E. (2013). Surface Subsidence Induced by Groundwater Drainage Tunneling in Granite Residual Soils (Burata Railway Tunnel, Spain). *Journal of Geotechnical and Geoenvironmental Engineering 139*, 821-824.

López-Fernández, C., Llana-Fúnez, S., Fernández-Viejo, G., Domínguez-Cuesta, M. J., and Díaz-Díaz, L. M. (2020). Comprehensive characterization of elevated coastal platforms in the north Iberian margin: A new template to quantify uplift rates and tectonic patterns. *Geomorphology 364*, 107242.

López-Fernández, C., Torres Alonso, M., and Gutiérrez Claverol, M. (2002). Los movimientos del terreno en las laderas del valle del río Caudal y la incidencia de las escombreras del carbón en los mismos. *Trabajos de Geología 23*, 35-52.

Lu, Z., Masterlark, T., and Dzurisin, D. (2005). Interferometric synthetic aperture radar study of Okmok volcano, Alaska, 1992–2003: Magma supply dynamics and postemplacement lava flow deformation. *Journal of Gephysical Research 110*, B02403.

Lundgren, P., Berardino, P., Coltelli, M., Fornaro, G., Lanari, R., Puglisi, G., Sansosti, E., and Tesauro, M. (2003). Coupled magma chamber inflation and sector collapse slip observed with SAR interferometry on Mt. Etna volcano. *Journal of Geophysical Research - Solid Earth 108*, 2247-2261.

Luzi, G., Espín-López, P. F., Pérez Mira, F., Monserrat, O., and Crosetto, M. (2021). A Low-Cost Active Reflector for Interferometric Monitoring Based on Sentinel-1 SAR Images. *Sensors 21*, 2008.

Mansour, M. F., Morgenstern, N. R., and Martin, C. D. (2011). Expected damage from displacement of slow-moving slides. *Landslides 8*, 117-131.

Manunta, M., De Luca, C., Zinno, I., Casu, F., Manzo, M., Bonano, M., Fusco, A., Pepe, A., Onorato, G., Berardino, P., De Martino, P., and Lanari, R. (2019). The Parallel SBAS Approach for Sentinel-1 Interferometric Wide Swath Deformation Time-Series Generation: Algorithm Description and Products Quality Assessment. *IEEE Transactions On Geoscience and Remote Sensing 57*, 6259-6281.

Margottini, C., Canuti, P., and Sassa, K. (2013). *Landslide Science and Practice: Volume 1: Landslide Inventory and Susceptibility and Hazard Zoning.* Springer; 2013th edition. 625 pp.

Marques, F. (2018). Regional Scale Sea Cliff Hazard Assessment at Sintra and Cascais Counties, Western Coast of Portugal. *Geosciences 8*, 80.

Martos de la Torre, E. M. (2014). *Caracterización hidrogeológica de la Cuenca del Río Turón (Asturias) en relación con la clausura de explotaciones mineras de carbón.* Tesis Doctoral. Universidad de Oviedo. 348 pp.

Massonet, D., and Feigl, K. L. (1998). Radar interferometry and its application to changes in the Earth's surface. *Review of Geophysics 36*, 441-500.

Mateos, R. M., Ezquerro, P., Azañón, J. M., Gelabert, B., Herrera, G., Fernández-Merodo, J. A., Spizzichino, D., Sarro, R., García-Moreno, I., and Béjar-Pizarro, M. (2018). Coastal lateral spreading in the world heritage site of the Tramuntana Range (Majorca, Spain). The use of PSInSAR monitoring to identify vulnerability. *Landslides 15*, 797–809.

Mateos-Redondo, F., Pascual-Lombardía, P., and Monserrat, O. (2016). Aplicación de la Interferometría Basada en Radar (InSAR) en la Monitorización de la Deformación del Patrimonio Arquitectónico. *Congreso Euro-Americano REHABEND 2016*, (pp. 1-9). 24-27 Mayo, Burgos, España.

Mc Cann, D. M., and Forster, A. (1990). Reconnaissance geophysical methods in landslide investigations. *Engineering Geology 29*, 59-78.

Medeiros, E., Brandão, A., Tormenta Pinto, P., and Silva Lopes, S. (2021). Urban Planning Policies to the Renewal of Riverfront Areas: The Lisbon Metropolis Case. *Suistanibility 13*, 5665.

Meisina, C., Zucca, F., Notti, D., Colombo, A., Cucchi, A., Savio, G., Giannico, C., and Bianchi, M. (2008). Geological Interpretation of PSInSAR Data at Regional Scale. *Sensors 8*, 7469-7492.

Melo, R., van Asch, T., and Zêzere, J. L. (2018). Debris flow run-out simulation and analysis using a dynamic model. *Natural Hazards and Earth System Sciences 18*, 555–570.

Menéndez-Duarte, R., Marquínez, J., and Devoli, G. (2003). Slope instability in Nicaraguatriggered by Hurricane Mitch:distribution of shallowmass movements. *Environmental Geology 44*, 290-300.

Meyer, F. (2019). Chapter 2. Spaceborne Synthetic Aperture Radar: Principles, Data Access, and Basic Processing Techniques. In *The SAR Handbook. Comprehensive Methodologies for Forest Monitroing and Biomass Estimation* (pp. 21-64). SERVIR GLOBAL.

Mikkelsen, P. E. (1996). Field Instrumentation. In *Landslides: Investigation and Mitigation* (pp. 278-316). Transportation Research Board, National Academy of Sciences.

Mondini, A. C., Guzzetti, F., Chang, K. T., Monserrat, O., Martha, T. R., and Manconi, A. (2021). Landslide failures detection and mapping using Synthetic Aperture Radar: Past, present and future. *Earth-Science Reviews 216*, 103574.

Monserrat, O., and Barra, A. (2020). *E.4.1.2: Tutorial para la correcta interpretación de los mapas generados con el SAR satelital.* Interreg Sudoe RISKCOAST. 18 pp.

Monserrat, O., Crosetto, M., and Luzi, G. (2014). A review of ground-based SAR interferometry for deformation measurement. *ISPRS Journal of Photogrammetry and Remote Sensing 93*, 40-48.

Monserrat, O., Crosetto, M., Iglesias, R., Rossi, G., Calcagni, L., and Crippa, B. (2009). A Tool for 2+1D Phase Unwrapping: Application examples. *Proceedings of Fringe 2009 Workshop* (6 pp.). 30 November-4 December 2009. Frascati, Italy.

Monte Carreño, V. (2004). *El azabache: piedra mágica, joya, emblema jacobeo.* . Gijón, España: Editorial Picu Urriellu. 190 pp.

Mora, M., Domínguez-Cuesta, M. J., Jiménez-Sánchez, M., López-Fernández, C., Pando, L., Meléndez, M., Flor, G., Marigil, M. A., Valenzuela, P., Ballesteros, D., and Rodríguez-Rodríguez, L. (2018). Proyecto COSINES: Abordando el reto de relacionar fenómenos meteorológicos costeros y retroceso de acantilados en Asturias. *XXXV Jornadas Científicas de la AME - 19º Encuentro hispano-luso de Meteorología.* León, España: Asociación Meteorológica Española.

Mora, O., Mallorquí, J. J., and Broquetas, A. (2003). Linear and Nonlinear Terrain Deformation Maps From a Reduced Set of Interferometric SAR Images. *IEEE Transactions on Geoscience and Remote Sensing 41*, 2243-2253.

Mulas, J., Aragón, R., Martínez, M., Lambán, J., García-Aróstegui, J. L., Fernández-Grillo, A. I., Hornero Díaz, J., Rodríguez, J. M., and Rodríguez, J. M. (2003). Geotechnical and hydrogeological analysis of land subsidence in Murcia (Spain). *Materials and Geoenvironment 50*, 249-252.

Navarro, J. A., Tomás, R., Barra, A., Pagán, J. I., Reyes-Carmona, C., Solari, L., Vinielles, J. L., Falco, S., and Crosetto, M. (2020). ADAtools: Automatic Detection and Classification of Active Deformation Areas from PSI Displacement Maps. *ISPRS International Journal of Geo-Information 9*, 584.

Navarro-Freixas, C. (2013). *Auscultación de laderas inestables en minería y obra civil.* Al-top Topografía. 28 pp.

Noferini, L., Pieraccini, M., Mecatti, D., Macaluso, G., Atzeni, C., Mantovani, M., Marcato, G., Pasuto, A., Silvano, S., and Tagliavini, F. (2007). Using GB-SAR technique to monitor slow moving landslide. *Engineering Geology 95*, 88-98.

Notti, D., Galve, J. P., Mateos, R. M., Monserrat, O., Lamas-Fernández, F., Fernández-Chacón, F., Roldán-García, F. J., Pérez-peña, J. V., Crosetto, M., and Azañón, J. M. (2015). Human-induced coastal landslide reactivation. Monitoring by PSInSAR techniques and urban damage survey (SE Spain). *Landslides 12*, 1007-1014.

Notti, D., Herrera, G., Bianchini, S., Meisina, C., García-Davalillo, J. C., and Zucca, F. (2014). A methodology for improving landslide PSI data analysis. *International Journal of Remote Sensing 12*, 703-719.

Nutricato, R., Nitti, D. O., Bovenga, F., Rana, F., D´Aprile, C., Frattini, P., Crosta, G., Venuti, G., Chiaradia, M. T., Ober, G., and Candela, L. (2009). MORFEO Project: C- and X-

Band SAR Interferometric Analysis over Alpine Regions (Italy). *Proceedings of Fringe 2009 Workshop.* 30 November-4 December 2009. Frascati, Italy.

Oliveira, L., Teves-Costa, P., Pinto, C., Carrilho Gomes, R., Almeida, I. M., Ferreira, C., Pereira, T., and Sotto-Mayor, M. (2020). Seismic microzonation based on large geotechnical database: Application to Lisbon. *Engineering Geology 265*, 105417.

Oliveira, S. C., Zêzere, J. L., Catalão, J., and Nico, G. (2015). The contribution of PSInSAR interferometry to landslide hazard in weak rock-dominated areas. *Landslides 12*, 703-719.

Orellana, F., Delgado-Blasco, J. M., Foumelis, M., D´Aranno, P. J., Marsella, M. A., and Di Mascio, P. (2020). DInSAR for Road Infrastructure Monitoring: Case Study Highway Network of Rome Metropolitan (Italy). *Remote Sensing 12*, 3697.

Ortiz-Zamora, D., and Ortega-Guerrero, A. (2010). Evolution of long-term land subsidence near Mexico City: Review, field investigations, and predictive simulations. *Water Resources Research 46*, W01513.

Osmanoglu, B., Sunar, F., Wdowinski, S., and Cabral-Cano, E. (2016). Time series analysis of InSAR data: Methods and trends. *ISPRS Journal of Photogrammetry and Remote Sensing 115*, 90-102.

Oteo, C. (1978). Técnicas de instrumentación en Mecánica de Rocas. *Boletín de la Sociedad Española de Mecánica de Suelos y Cimentaciones 34*, 3-38.

Palamà, R., Crosetto, M., Rapinski, J., Barra, A., Cuevas-González, M., Monserrat, O., Crippa, B., Kotulak, N., Mróz, M., and Mleczko, M. (2022). A Multi-Temporal Small Baseline Interferometry Procedure Applied to Mining-Induced Deformation Monitoring. *Remote Sensing 14*, 2182.

Pando, L., Pulgar, J. A., and Gutiérrez-Claverol, M. (2013). A case of man-induced ground subsidence and building settlement related to karstified gypsum (Oviedo, NW Spain). *Environmental Earth Sciences 68*, 507-519.

Parmar, H., Bafghi, A. Y., and Najafi, M. (2019). Impact of ground surface subsidence due to underground mining on surface infrastructure: the case of the Anomaly No. 12 Sechahun, Iran. *Environmental Earth Sciences 78*, 409.

Pepe, S., D´Auria, L., Castaldo, R., Casu, F., De Luca, C., De Novellis, V., Sansosti, E., Solaro, G., and Tizzani, P. (2018). The Use of Massive Deformation Datasets for the Analysis of Spatial and Temporal Evolution of Mauna Loa Volcano (Hawai'i). *Remote Sensing 10*, 968.

Pereira, S., Santos, P. P., Zêzere, J. L., Tvares, A. O., Garcia, R. A., and Cruz Oliveira, S. (2020). A Landslide risk index for municipal land use planning in Portugal. *Science of the Total Environment 735*, 139463.

Pérez-Estaún, A., Bastida, F., Alonso, J. L., Marquínez, J., Aller, J., Álvarez-Marrón, J., Marcos, A., and Pulgar, J. A. (1988). A Thin-Skinned Tectonics Model for an Arcuate Fold and Thrust Belt: The Cantabrian Zone (Variscan Ibero-Armorican Arc). *Tectonics 7*, 517-537.

Perissin, D., Wang, Z., and Lin, H. (2012). Shanghai subway tunnels and highways monitoring through Cosmo-SkyMed Persistent Scatterers. *Journal of Photogrammetry and Remote Sensing 73*, 58-67.

Peternel, T., Janža, M., Šegina, E., Bezak, N., and Macek, M. (2022). Recognition of Landslide Triggering Mechanisms and Dynamics Using GNSS, UAV Photogrammetry and In Situ Monitoring Data. *Remote Sensing 14*, 3277.

Pieraccini, M., and Miccinesi, L. (2019). Ground-Based Radar Interferometry: A Bibliographic Review. *Remote Sensing 11*, 1029.

Polcari, M., Albano, M., Saroli, M., Tolomei, C., Lancia, M., Moro, M., and Stramondo, S. (2014). Subsidence detected by multi-pass differential SAR interferometry in the Cassino Plain (Central Italy): Join effect of the geological and anthropogenic factors? *Remote Sensing 6*, 9676-9690.

Porzucek, S., and Loj, M. (2021). Microgravity Survey to Detect Voids and Loosening Zones in the Vicinity of the Mine Shaft. *Energies 14*, 3021.

Prokopovich, N. P. (1979). Genetic classification on land subsidence. In S. K. Saxena, *Evaluation and prediction of subsidence* (pp. 389-399). Pensacola Beach: American Society of Civil Engineering.

Qiu, Z., Monserrat, O., Crosetto, M., Krishnakumar, V., and Zhou, L. (2021). An innovative extraction methodology of active deformation areas based on Sentinel-1 SAR dataset: The catalonia case study. *International Journal of Remote Sensing 42*, 6228-6244.

Raucoules, D., Colesanti, C., and Carnec, C. (2007). Use of SAR interferometry for detecting and assenssing ground subsidence. *Geoscience 339*, 289-302.

Raucoules, D., Le Cozannet, G., Wöppelmann, G., de Michele, M., Gravelle, M., Daag, A., and Marcos, M. (2013). High nonlinear urban ground motion in Manila (Philippines) from 1993 to 2010 observed by DInSAR: Implications for sea-level measurement. *Remote Sensing of Environment 139*, 386-397.

Raucoules, D., Maisons, C., Carnec, C., Le Mouelic, S., King, C., and Hosford, S. (2003). Monitoring of slow ground deformation by ERS radar interferometry on the Vauvert salt mine (France). Comparison with ground-based measurement. *Remote Sensing of Environment 88*, 468-478.

Reyes-Carmona, C., Barra, A., Galve, J. P., Monserrat, O., Pérez-Peña, J. V., Mateos, R. M., Notti, D., Ruano, P., Millares, A., López-Vinielles, J., and Azañón, J. M. (2020). Sentinel-1 DInSAR for Monitoring Active Landslides in Critical Infrastuctures: The case of the Rules Reservoir (Southern Spain). *Remote Sensing 12*, 809.

Reyes-Carmona, C., Galve, J. P., Moreno-Sánchez, M., Riquelme, A., Ruano, P., Millares, A., Teixidó, T., Sarro, R., Pérez-Peña, J. V., Barra, A., Ezquerro, P., López-Vinielles, J., Béjar-Pizarro, M., Azañón, J. M., Monserrat, O., and Mateos, R. M. (2021). Rapid characterisation of the extremely large landslide threatening the Rules Reservoir (Southern Spain). *Landslides 18*, 3781-3798.

Riesgo-Fernández, P., Rodríguez-Granda, G., Krzemién, A., García Cortés, S., and Fidalgo-Valverde, G. (2020). Subsidence versus natural landslides when dealing with property damage liabilities in underground coal mines. *International Journal of Rock Mechanics and Mining Sciences 126*, 104175.

Rignot, E., Vaughan, D. G., Schmeltz, M., Dupont, T., and MacAyeal, D. (2002). Acceleration of Pine Island and Thwaites Glaciers, West Antarctica. *Annals of Glaciology 34*, 189-194.

Rodrigues, M. L., Machado, C. R., and Freire, E. (2011). Geotourism Routes in Urban Areas: A Preliminary Approach to the Lisbon Geoheritage Survey. *Geojournal of Tourism and Geosites 8*, 281-294.

Rodríguez-Rodríguez, L., González-Lemos, S., Ballesteros, D., Valenzuela, P., Domínguez-Cuesta, M. J., Llana-Fúnez, S., and Jiménez-Sánchez, M. (2018). Timing of paraglacial rock-slope failures and denudation signatures in the Cantabrian Mountains (North Iberian Peninsula). *Land Degradation and Development 29*, 3159-3173.

Rogers, C. D., Dijikstra, T. A., and Smalley, I. J. (1994). Hydroconsolidation and subsidence of loess: Studies from China, Russia, North America and Europe. *Engineering Geology 37*, 83-113.

Rosen, P., Hensley, S., Joughin, I. R., Li, F. K., Madsen, S. N., Rodríguez, E., and Goldstein, R. M. (2000). Synthetic Aperture Radar Interferometry. *Proceedings of the IEEE 88*, 333-382.

Rossi, G., Tanteri, L., Tofani, V., Vannoci, P., Moretti, S., and Casagli, N. (2018). Multitemporal UAV surveys for landslide mapping and characterization. *Landslides 15*, 1045-1052.

Rott, H. (2009). Advances in interferometric synthetic aperture radar (InSAR) in earth system science. *Progress in Physical Geography 33*, 769-791.

Salvador, C. I. (1993). La sedimentación durante el Westfaliense en una cuenca de antepaís (Cuenca Carbonífera Central de Asturias, N de España). *Trabajos de Geología 19*, 195-254.

Sanabria, M. P., Guardiola-Albert, C., Tomás, R., Herrera, G., Prieto, A., Sánchez, H., and Tessitore, S. (2014). Subsidence activity maps derived from DInSAR data: Orihuela case study. *Natural Hazards and Earth System Sciences 14*, 1341-1360.

Sarychikhina, O., Gómez-Palacios, D., Delgado-Argote, L. A., and González-Ortega, A. (2021). Application of satellite SAR interferometry for the detection and monitoring of landslides along the Tijuana - Ensenada Scenic Highway, Baja California, Mexico. *Journal of South American Earth Sciences 107*, 103030.

Satirapod, C., Trisirisatayawong, I., Fleitout, L., Garaud, J., and Simons, W. (2013). Vertical motions in Thailand after the 2004 Sumatra - Andaman Earthquake from GPS observations and its geophysical modelling. *Advances in Space Research 51*, 1565-1571.

Sato, M., and Kuwano, R. (2015). Influence of location of subsurface structures on development of underground cavities induced by internal erosion. *Soils and Foundations 55*, 829-840.

Schenato, L. (2017). A Review of Distributed Fibre Optic Sensors for Geo-Hydrological Applications. *Applied Sciences 7*, 896.

Shiklomanov, N. I., Streletskiy, D. A., Little, J. D., and Nelson, F. E. (2013). Isotropic thaw subsidence in undisturbed permafrost landscapes. *Geophysical Research Letters 40*, 6356–6361.

Shirzaei, M., Freymueller, J., Törnqvist, T. E., Galloway, D. L., Dura, T., and Minderhoud, P. S. (2021). Measuring, modelling and projecting coastal land subsidence. *Nature Reviews Earth and Environment 2*, 40-58.

Sistema Nacional de Informaçao de Recursos Hídricos (SNIRH). (2021). *Águas Subterráneas. Pontos de Água Subterrânea*. Retrieved from https://snirh.apambiente.pt

SITPA-IDEAS. (2022). *Sistema de Información Territorial e Infrasestructuras de Datos Espaciales de Asturias*. Retrieved from Centro de Descargas: https://ideas.asturias.es/centro-de-descargas

Sneed, M., Ikehara, M., Balloway, D., and Amelung, F. (2001). *Detection and measurement of land subsidence using global positioning system and interferometric synthetic aperture radar, Coachella Valley, California, 1996-1998.* Sacramento, California, EEUU: Water-Resources Investigations. Report 01-4193, US Geological Survey. 34 pp.

Solari, L., Barra, A., Herrera, G., Bianchini, S., Monserrat, O., Béjar-Pizarro, M., Crosetto, M., Sarro, R., and Moretti, S. (2018). Fast detection of ground motions on vulnerable elements using Sentinel-1 InSAR data. *Geomatics, Natural Hazards and Risk 9*, 152-174.

Solari, L., Ciampalini, A., Raspini, F., Bianchini, S., and Moretti, S. (2016). PSInSAR Analysis in the Pisa Urban Area (Italy): A Case Study of Subsidence Related to Stratigraphical Factors and Urbanization. *Remote Sensing 8* , 120.

Solari, L., Del Soldato, M., Montalti, R., Bianchini, S., Raspini, F., Thuegaz, P., Bertolo, D., Tofani, V., and Casagli, N. (2019). A Sentinel-1 based hot-spot analysis: landslide mapping in north-western Italy. *International Journal of Remote Sensing 40*, 7898-7921.

Solaro, G., De Novellis, V., Castaldo, R., De Luca, C., Lanari, R., Manunta, M., and Casu, F. (2016). Coseismic Fault Model of Mw 8.3 2015 Illapel Earthquake (Chile) Retrieved from Multi-Orbit Sentinel 1-A DInSAR Measurements. *Remote Sensing 8*, 323.

Sousa, J. J., and Bastos, L. (2013). Multi-temporal SAR interferometry reveals acceleration of bridge sinking before collapse. *Natural Hazards and Earth System Sciences 13*, 659-667.

Spizzichino, D., Margottini, C., Trigila, A., Iadanza, C., and Linser, S. (2010). *Mapping the impacts of natural hazards and technological accidents in Europe—an overview of the last decade.* EEA Technical report No 13/2010. 144 pp.

Strozzi, T., Farina, P., Corsini, A., Ambrosi, C., Thüring, M., Zilger, J., Wiesmann, A., Wegmüller, U., and Werner, C. (2005). Survey and monitoring of landslide displacements by means of L-band satellite SAR interferometry. *Landslides 2*, 193-201.

Strozzi, T., Wegmüller, U., Werner, C. L., Wiesmann, A., and Spreckels, V. (2003). JERS SAR Interferometry for Land Subsidence Monitoring. *IEEE Transactions on Geoscience and Remote Sensing 41*, 1702-1708.

Suo, W., Lu, Y., Shi, B., Zhu, H., Wei, G., and Jiang, H. (2016). Development and application of a fixed-point fiber-optic sensing cable for ground fissure monitoring. *Journal of Civil Structural Health Monitoring 6*, 715-724.

Tarchi, D., Ohlmer, E., and Sieber, A. (1997). Monitoring of Structural Changes by Radar Interferometry. *Research in Nondetructive Evaluation 9*, 213-225.

Teixeira, P., Almeida, L., Brandão, J., Costa, S., Pereira, S., and Valério, E. (2018). Non-potable use of Lisbon underground water: microbiological and hydrochemical data from a 4-year case study. *Environmental Monitoring and Assessment 190*, 455.

Tessitore, S., Fernández-Merodo, J. A., Herrera, G., Tomás, R., Ramondini, M., Sanabria, M., Duro, J., Mulas, J., and Calcaterra, D. (2015). Regional subsidence modelling in Murcia city (SE Spain) using 1-D vertical finite element analysis and 2-D interpolation of ground surface displacements. *Proceedings of the International Association of Hydrological Sciences 372*, (pp. 425-429).

Tofani, V., Raspini, F., Catani, F., and Casagli, N. (2013). Persistent Scatterer Interferometry (PSI) Techique for Landslide Characterization and Monitoring. *Remote Sensing 5*, 1045-1065.

Tomás, R., Márquez, Y., López-Sánchez, J. M., Delgado, J., Blanco, P., Mallorquí, J. J., Martínez, M., Herrera, G., and Mulas, J. (2005). Mapping ground subsidence induced by aquifer overexploitation using advanced Differential SAR Interferometry: Vega Media of the Segura River (SE Spain) case study. *Remote Sensing of Environment 98*, 269-283.

Tomás, R., Pagán, J. I., Navarro, J. A., Cano, M., Pastor, J. L., Riquelme, A., Cuevas-González, M., Crosetto, M., Barra, A., Monserrat, O., López-Sánchez, J. M., Ramón, A., Ivorra, S., Del Soldato, M., Solari, L., Bianchini, S., Raspini, F., Novali, F., Ferreti, A., Costantini, M., Trillo, F., Herrera, G., and Casagli, N. (2019). Semi-Automatic Identification and Pre-Screening of Geological-Geotechnical Deformational Processes Using Persistent Scatterer Interferometry Datasets. *Remote Sensing 11*, 1675.

Tomás, R., Romero, R., Mulas, J., Marturià, J. J., Mallorquí, J. J., López-Sánchez, J. M., Herrera, G., Gutiérrez, F., González, P. J., Fernández, J., Duque, S., Concha-Dimas, A., Cocksley, G., Castañeda, C., Carrasco, D., and Blanco, P. (2014). Radar interferometry techniques for the study of ground subsidence phenomena: a review of practical issues through cases in Spain. *Environmental Earth Sciences 71*, 163-181.

Truyols, J., and Julivert, M. (1976). La sucesión paleozoica entre Cabo Peñas y Antromero (Cordillera Cantábrica). *Trabajos de Geología 8*, 5-30.

U.S. government. (2021). *GPS: The Global Positioning System*. Retrieved from https://www.gps.gov/

United States Geological Survey (USGS). (2016). *USGS Fact Sheet 2004-3072: Landslide Types and Processes*. Retrieved from https://pubs.usgs.gov/fs/2004/3072/

United States Geological Survey (USGS). (2022). *Land Change Science Program*. Retrieved from https://www.usgs.gov/programs/land-change-science-program

Valenzuela, M., García-Ramos, J. C., and Suárez de Centi, C. (1986). The Jurassic sedimentacion in Asturias (N Spain). *Trabajos de Geología 16*, 121-132.

Valenzuela, P. (2017). *Landslide triggering in Asturias (NW Spain). Rainfall and soil moisture conditions modelling.* Tesis Doctoral. Universidad de Oviedo. 193 pp.

Valenzuela, P., Domínguez-Cuesta, M. J., López-Fernández, C., González-Pumariega, P., Jiménez-Sánchez, M., Mora, M., and Marigil, M. A. (2019). Monitoring an active mass movement in the Asturias cliff coast (North of Spain): preliminary data. *EGU General Assembly 2019*, EGU2019-10052. 7-12 April 2019, Vienna, Austria.

Valenzuela, P., Domínguez-Cuesta, M. J., Meléndez-Asensio, M., Jiménez-Sánchez, M., and Saénz de Santa María, J. A. (2015). Active sinkholes: A geomorphological impact of the Pajares Tunnels (Cantabrian Range, NW Spain). *Engineering Geology 196*, 158-170.

Valenzuela, P., Domínguez-Cuesta, M. J., Mora García, M. A., and Jiménez-Sánchez, M. (2017). A spatio-temporal landslide inventory for the NW of Spain: BAPA database. *Geomorphology 293*, 11-23.

Valenzuela, P., Zêzere, J. L., Domínguez-Cuesta, M. J., and Mora , M. A. (2019). Empirical rainfall thresholds for the triggering of landslides in Asturias (NW Spain). *Landslides 16*, 1285-1300.

Van Den Eeckhaut, M., Poesen, J., Verstraeten, G., Vanacker, V., Nyssen, J., Moeyersons, J., van Beek, L. P. H., and Vandekerckhove, L. (2007). Use of LIDAR-derived images for mapping old landslides under forest. *Earth Surface Processes and Landforms 32*, 754-769.

Vanicek, P., Castle, R. O., and Balazs, E. I. (1980). Geodetic leveling and its applications. *Review of Geophysics 18*, 505-524.

Varnes, D. J. (1978). Slope Movement Types and Processes. In *Landslides: Analysis and Control* (pp. 11-33). Transportation Research Board, National Research Council.

Vaz, N., Mateus, M., Pinto, L., Neves, R., and Dias, J. M. (2019). The Tagus Estuary as a Numerical Modeling Test bed: A review. *Geosciences 10*, 4.

Vaz, T., Zêzere, J. L., Pereira, S., Cruz Oliveira, S., García, R. A., and Quaresma, I. (2018). Regional rainfall thresholds for landslide occurrence using a centenary database. *Natural Hazards and Earth System Sciences 18*, 1037–1054.

Veci, L., Lu, J., Prats-Iraola, P., Scheiber, R., Collard, F., Fomferra, N., and Engdahl, M. (2014). The Sentinel-1 Toolbox. *Proceedings of the IEEE International Geoscience and Remote Sensing Symposium (IGARSS)*, (pp. 1-3). 13-18 July 2014. Quebec city, Canada.

Wallemacq, P., Below, R., and McClean, D. (2018). *Economic losses, poverty and disasters: 1998-2017*. United Nations Office for Disaster Risk Reduction. 31 pp.

Wang, G., Joyce, J., Phillips, D., Shrestha, R., and Carter, W. (2013). Delineating and defining the boundaries of an active landslide in the rainforest of Puerto Rico using a combination of airborne and terrestrial LIDAR data. *Landslides 10*, 503-513.

Wang, H., Xu, C., and Ge, L. (2007). Coseismic deformation and slip distribution of the 1997 Mw 7.5 Manyi, Tibet, earthqueake from InSAR measurements. *Journal of Geodynamics 44*, 200-212.

Wasowski, J., Nutricato, R., Nitti, D. O., and Chiaradia, M. T. (2018). Adavanced satellite radar interferometry for deformation monitoring and infrastructure control in open-cast mines and oil/gas fields. *Innovative Infrastructure Solutions 3*, 68.

Webb, E. L., Friess, D. A., Krauss, K. W., Cahoon, D. R., Guntenspergen, G. R., and Phelps, J. (2013). A global standard for monitoring coastal wetland vulnerability to accelerated sea-level rise. *Nature Climate Change 3,* 458-465.

Wegmüller, U., Werner, C., Strozzi, T., and Wiesmann, A. (2004). Multi-Temporal Interferometric Point Target Analysis. In *Series in Remote Sensing: Volume 3, Analysis of Multi-Temporal Remote Sensing Images. Proceedings of the Second International Workshop on the Multitemp 2003.* (pp. 136-144). Ispra: Edited by: Paul Smits and Lorenzo Bruzzone.

Werner, C., Wegmüller, U., Strozzi, T., and Wiesmann, A. (2003). Interferometric point target analysis for deformation mapping. *Proceedings of IGARSS*, 21-25.

Wicks, C. W., Thatcher, W., and Dzurisin, D. (2006). Uplift, thermal unrest and magma intrusion at Yellowstone caldera. *Nature 440*, 1033-1036.

Wieczorek, G. F. (1996). Landslide triggering mechanisms. In *Landslides: Investigation and Mitigation* (pp. 76-90). Transportation Research Board, National Academy of Sciences.

Wolstencroft, M., Shen, Z., Törnqvist, T. E., Milne, G. A., and Kulp, M. (2014). Understanding subsidence in the Mississippi Delta region due to sediment, ice, and ocean loading: insights from geophysical modelling. *Journal of Geophysical Research: Solid Earth 119*, 3838-3856.

Wu, J. H., Shi, B., Cao, D. F., Jiang, H. T., Wang, X. F., and Gu, K. (2017). Model test of soil deformation response to draining-recharging conditions based on DFOS. *Engineering Geology 226*, 107-121.

Wu, P. C., Wei, M., and D´Hondt, S. (2022). Subsidence in Coastal Cities Throughout the World Observed by InSAR. *Geophysical Research Letters 49,* e2022GL098477.

Yalcinkaya, E., Alp, H., Ozel, O., Gorgun, E., Martino, S., Lenti, L., Bourdeau, C., Bigarre, P., and Coccia, S. (2016). Near-surface geophysical methods for investigating the Buyukcekmece landslide in Istanbul, Turkey. *Journal of Applied Geophysics 134*, 23-35.

Yang, D., Qiu, H., Ma, S., Liu, Z., Du, C., Zhu, Y., and Cao, M. (2022). Slow surface subsidence and its impact on shallow loess landslides in a coal mining area. *Catena 209*, 105830.

Yu, L., Yang, T., Zhao, Q., Liu, M., and Pepe, A. (2017). The 2015-2016 Ground Displacements of the Shangai Coastal Area Inferred from a Combined Cosmo-SkyMed/Sentinel-1 DInSAR Analysis. *Remote Sensing 9,* 1194.

Yun, S., Segall, P., and Zebker, H. (2006). Constraints on magma chamber geometry at Sierra Negra Volcano, Galapagos Islands, based on InSAR observations. *Journal of Volcanology and Geothermal Research 150*, 232-243.

Zêzere, J. L. (2001). *Distribuçao e Ritmo dos Movimientos de Vertente na Região a Norte de Lisboa.* Ph.D. Thesis, Universidade de Lisboa. 167 pp.

Zhang, C. C., Shi, B., Gu, K., Liu, S. P., Wu, J. H., Zhang, S., Zhang, L., Jiang, H. T., and Wei, G. Q. (2018). Vertically Distributed Sensing of Deformation Using Fiber Optic Sensing. *Geophysical Research Letters 45*, 11732-11741.

Zhang, X., Feng, M., Zhang, H., Wang, C., Tang, Y., Xu, J., Yan, D., and Wang, C. (2021). Detecting Rock Glacier Displacement in the Central Himalayas Using Multi-Temporal InSAR. *Remote Sensing 13*, 4738.

Zhang, Y., Lian, X., Ge, L., Liu, X., Du, Z., Yang, W., Wu, Y., Hu, H., and Cai, Y. (2022). Surface Subsidence Monitoring Induced by Underground Coal Mining by Combining DInSAR and UAV Photogrammetry. *Remote Sensing 14*, 4711.

Zhao, J., and Konietzky, H. (2021). An overview on flooding induced uplift for abandoned coal mines. *International Journal of Rock Mechanics and Mining Sciences 148*, 104955.

Zhao, Q., Lin, H., Gao, W., Zebker, H. A., Chen, A., and Yeung, K. (2011). InSAR detection of residual settlement of an ocean reclamation engineering project: a case study of Hong Kong International Airport. *Journal of Oceanography 67*, 415-426.

Zhao, Q., Pepe, A., Gao, W., Lu, Z., Bonano, M., He, M. L., Wang, J., and Tang, X. (2015). A DInSAR Investigation of the Ground Settlement Time Evolution of Ocean-Reclaimed Lands in Shanghai. *IEEE Journal of Selected Topics in Applied Earth Observations and Remote Sensing 8*, 1763-1781.

Zhong, W., Chu, T., Tissot, P., Wu, Z., Chen, J., and Zhang, H. (2022). Integrated coastal subsidence analysis using InSAR, LiDAR, and land cover data. *Remote Sensing of Environment 282*, 113297.

Zhu, L., Gong, H., Li, X., Wang, R., Chen, B., Dai, Z., and Teatini, P. (2015). Land subsidence due to groundwater withdrawal in the northern Beijing plain, China. *Engineering Geology 193*, 243-255.

Appendix I

113 SAR IW SLC Sentinel-1A/B images in descending orbit (Central Asturias)

Image	Date	Orbit	Image	Date	Orbit	Image	Date	Orbit	Image	Date	Orbit
1	20180104	20001	**30**	20180703	22626	**59**	20190306	15230	**88**	20190902	17855
2	20180110	9105	**31**	20180709	11730	**60**	20190312	26301	**89**	20190908	28926
3	20180116	20176	**32**	20180715	22801	**61**	20190318	15405	**90**	20190914	18030
4	20180122	9280	**33**	20180721	11905	**62**	20190324	26476	**91**	20190920	29101
5	20180128	20351	**34**	20180727	22976	**63**	20190330	15580	**92**	20190926	18205
6	20180203	9455	**35**	20180802	12080	**64**	20190405	26651	**93**	20191002	29276
7	20180209	20526	**36**	20180808	23151	**65**	20190411	15755	**94**	20191008	18380
8	20180215	9630	**37**	20180814	12255	**66**	20190417	26826	**95**	20191014	29451
9	20180221	20701	**38**	20180820	23326	**67**	20190423	15930	**96**	20191020	18555
10	20180227	9805	**39**	20180913	23676	**68**	20190429	27001	**97**	20191026	29626
11	20180305	20876	**40**	20181019	24201	**69**	20190505	16105	**98**	20191101	18730
12	20180311	9980	**41**	20181025	13305	**70**	20190511	27176	**99**	20191107	29801
13	20180317	21051	**42**	20181031	24376	**71**	20190517	16280	**100**	20191113	18905
14	20180323	0155	**43**	20181106	13480	**72**	20190523	27351	**101**	20191119	29976
15	20180404	10330	**44**	20181112	24551	**73**	20190529	16455	**102**	20191125	19080
16	20180410	21401	**45**	20181124	24726	**74**	20190604	27526	**103**	20191201	30151
17	20180416	10505	**46**	20181218	25076	**75**	20190610	16630	**104**	20191207	19255
18	20180422	21576	**47**	20181224	14180	**76**	20190616	27701	**105**	20191213	30326
19	20180428	10680	**48**	20181230	25251	**77**	20190622	16805	**106**	20191219	19430
20	20180504	21751	**49**	20190105	14355	**78**	20190628	27876	**107**	20191225	30501
21	20180510	10855	**50**	20190111	25426	**79**	20190704	16980	**108**	20191231	19605
22	20180516	21926	**51**	20190117	14530	**80**	20190710	28051	**109**	20200106	30676
23	20180522	11030	**52**	20190123	25601	**81**	20190716	17155	**110**	20200112	19780
24	20180528	22101	**53**	20190129	14705	**82**	20190722	28226	**111**	20200118	30851
25	20180603	11205	**54**	20190204	25776	**83**	20190728	17330	**112**	20200124	19955
26	20180609	22276	**55**	20190210	14880	**84**	20190803	28401	**113**	20200205	20130
27	20180615	11380	**56**	20190216	25951	**85**	20190809	17505			
28	20180621	22451	**57**	20190222	15055	**86**	20190821	17680			
29	20180627	11555	**58**	20190228	26126	**87**	20190827	28751			

Appendix II

48 SAR IW SLC Sentinel-1A images in ascending orbit (Study area of Lisbon Metropolitan Area)

Image	Date	Orbit	Image	Date	Orbit
1	20180126	9346	**30**	20190608	27592
2	20180213	20592	**31**	20190626	16871
3	20180303	9871	**32**	20190708	17046
4	20180321	21117	**33**	20190726	28292
5	20180408	10396	**34**	20190813	17571
6	20180426	21642	**35**	20190831	28817
7	20180514	10921	**36**	20190918	18096
8	20180601	22167	**37**	20191006	29342
9	20180619	11446	**38**	20191024	18621
10	20180707	22692	**30**	20191117	18971
11	20180725	11971	**40**	20191205	30217
12	20180812	23217	**41**	20191223	19496
13	20180830	12496	**42**	20200110	30742
14	20180911	12671	**43**	20200128	20021
15	20180929	23917	**44**	20200215	31267
16	20181005	13021	**45**	20200304	20546
17	20181017	13196	**46**	20200322	31792
18	20181104	24442	**47**	20200409	21071
19	20181122	13721	**48**	20200427	32317
20	20181210	24967			
21	20181228	14246			
22	20190115	25492			
23	20190202	14771			
24	20190220	26017			
25	20190310	15296			
26	20190328	26542			
27	20190415	15821			
28	20190503	27067			
29	20190521	16346			

Appendix III

69 SAR IW SLC Sentinel-1A images in descending orbit (Study area of Lisbon Metropolitan Area)

Image	Date	Orbit	Image	Date	Orbit	Image	Date	Orbit
1	20180126	20322	**30**	20190109	25397	**59**	20191223	30472
2	20180207	20497	**31**	20190121	25572	**60**	20200104	30647
3	20180219	20672	**32**	20190202	25747	**61**	20200116	30822
4	20180303	20847	**33**	20190214	25922	**62**	20200128	30997
5	20180315	21022	**34**	20190226	26097	**63**	20200209	31172
6	20180327	21197	**35**	20190310	26272	**64**	20200221	31347
7	20180408	21372	**36**	20190322	26447	**65**	20200304	31522
8	20180420	21547	**37**	20190403	26622	**66**	20200316	31697
9	20180502	21722	**38**	20190415	26797	**67**	20200328	31872
10	20180514	21897	**39**	20190427	26972	**68**	20200409	32047
11	20180526	22072	**40**	20190509	27147	**69**	20200421	32222
12	20180607	22247	**41**	20190521	27322			
13	20180619	22422	**42**	20190602	27497			
14	20180701	22597	**43**	20190614	27672			
15	20180713	22772	**44**	20190626	27847			
16	20180725	22947	**45**	20190708	28022			
17	20180806	23122	**46**	20190720	28197			
18	20180818	23297	**47**	20190801	28372			
19	20180830	23472	**48**	20190813	28547			
20	20180911	23647	**49**	20190825	28722			
21	20180923	23822	**50**	20190906	28897			
22	20181005	23997	**51**	20190918	29072			
23	20181017	24172	**52**	20190930	29247			
24	20181029	24347	**53**	20191012	29422			
25	20181110	24522	**54**	20191024	29597			
26	20181122	24697	**55**	20191105	29772			
27	20181204	24872	**56**	20191117	29947			
28	20181216	25047	**57**	20191129	30122			
29	20181228	25222	**58**	20191211	30297			

RESUMEN

INTRODUCCIÓN

En esta tesis doctoral se han aplicado varias técnicas A-DInSAR (Interferometría SAR Diferencial Avanzada) con el objetivo principal de detectar, modelizar y monitorear movimientos del terreno desde enero de 2018 a febrero de 2020, en tres áreas de la zona central de Asturias (N de España) y en el Área Metropolitana de Lisboa (SO de Portugal). Concretamente, en Asturias las zonas de estudio corresponden al entorno del Cabo Peñas (incluyendo la Península de Podes), el deslizamiento del Faro de Tazones y a un área montañosa situada en la Cuenca Carbonífera Central.

Motivación y justificación

En Asturias (N de España) y en el Área Metropolitana de Lisboa (AML, SO de Portugal), al igual que en otras partes del mundo, existe un importante problema relacionado con las inestabilidades de ladera y los fenómenos de subsidencia. Estos procesos generan enormes pérdidas económicas cada año e, incluso, causan pérdidas humanas.

Debido a la alta incidencia de estos fenómenos, desde 1995, el Departamento de Geología de la Universidad de Oviedo lleva recopilando datos sobre inestabilidades del terreno, creando más tarde la base de datos BAPA (Base de datos de Argayos del Principado de Asturias), con el fin de registrar y clasificar los movimientos del terreno que se producen en el territorio asturiano (Domínguez-Cuesta et al., 1999; Valenzuela, 2017). De esta forma, se registran aproximadamente 62 eventos de inestabilidades de ladera y hundimientos al año, con un número máximo anual de eventos registrados de 262 (en 2013). Un informe estimó el coste directo total de los deslizamientos en Asturias en 66 millones de euros anuales (González Moradas y Lima de Montes, 2001). Por otro lado, Asturias ha sido una importante región de minería de carbón subterránea y a cielo abierto, desde el siglo XIX hasta el siglo XXI. Esta actividad minera del carbón viene asociada a múltiples problemas ligados a inestabilidades de laderas y fenómenos de subsidencia (López-Fernández et al., 2002; Riesgo-Fernández et al., 2020), lo que tradicionalmente ha dado lugar a un carácter confidencial y de acceso restringido de la mayor parte de los datos geológico-mineros disponibles de las diferentes explotaciones. Concretamente, el acceso es muy limitado a cualquier tipo de información relativa a geología en profundidad, localización de labores mineras subterráneas, datos de sondeos, bombeos y niveles de agua y/o información de índole geotécnica de zonas minadas o próximas a éstas. En el caso concreto de la Cuenca Carbonífera Central, tan solo es posible acceder a algunos datos geológico-mineros o de carácter hidrogeológico contenidos en planes mineros anteriores a 1967, año en el que se crea HUNOSA y en algunos documentos técnicos publicados posteriormente por HUNOSA.

Por otro lado, la AML se caracteriza por un alto y rápido desarrollo urbanístico e industrial en los últimos 40 años. Este hecho ha provocado un aumento de los riesgos geológicos y la necesidad de una adecuada planificación urbanística, lo que ha llevado a autores como Campos Costa et al. (2010) y Carvalho et al. (2018) a abordar estudios de la peligrosidad sísmica o de licuefacción de suelos, mientras que otros investigadores se han centrado en el riesgo de inundaciones y daños en edificios producidos por episodios de lluvias extremas (Leal et al., 2019; Leal et al., 2020). En cuanto a los procesos de inestabilidad de laderas, Melo et al. (2018) y Vaz et al. (2018) estudiaron los umbrales de precipitación regionales y locales que determina la ocurrencia de movimientos en masa en la región de Lisboa. Por su parte, Pereira et al. (2020) realizaron un índice de riesgo de deslizamientos en Portugal, reconociendo la AML como una importante zona de riesgo de deslizamientos. En esta línea, se ha estimado una extensión de 18.000 ha con incidencia de deslizamientos (Comissão Exècutiva Metropolitana de Lisboa, 2019), lo que corresponde al 5,9% del territorio del AML. Además, otros estudios se centraron en la planificación y las políticas urbanas (Medeiros et al., 2021), la hidrodinámica y la geoquímica del río Tajo (Vaz et al, 2019), entre otros.

Durante las dos últimas décadas, las técnicas basadas en el Radar de Apertura Sintética (SAR) se han utilizado con éxito en la detección, modelización y seguimiento de las deformaciones del terreno (Ferreti et al., 2001; Berardino et al., 2002). Estas técnicas calculan con precisión milimétrica el desplazamiento de la superficie del suelo que se produce entre dos imágenes de radar diferentes, recogidas por sensores a bordo de un satélite. Una comparación progresiva de las imágenes durante un cierto periodo de tiempo (normalmente años) permite un análisis multitemporal del desplazamiento, mediante el cual se pueden obtener series temporales de desplazamiento de la superficie y velocidades medias anuales (Massonet y Feigl, 1998). Además, estas técnicas permiten el seguimiento de grandes extensiones de terreno (~ 10.000 km^2). Por tanto, la aplicación de técnicas A-DInSAR puede ser adecuada para la detección, modelización y seguimiento de movimientos del terreno asociados a inestabilidades y subsidencia de laderas en Asturias y en la AML.

Considerando que las técnicas A-DInSAR sólo son capaces de detectar movimientos muy lentos (< 1.6 m/año) (Canuti et al., 2004), en esta investigación se plantea evaluar el potencial y las limitaciones de las técnicas A-DInSAR para la cartografía y monitorización de movimientos rápidos del terreno. Para ello, se han utilizado los datos de Sentinel-1 mediante diferentes softwares: uno robusto y supervisado (técnica PSI del software PSIG), uno no supervisado y automático (técnica P-SBAS del servicio GEP) y métodos de post-procesado A-DInSAR, seguimiento topográfico y campañas de campo.

Objetivos

El objetivo principal de este trabajo es aplicar las técnicas A-DInSAR a la detección, modelización y seguimiento de los movimientos del terreno asociados a fenómenos de inestabilidad y subsidencia de laderas en tres áreas de la región de Asturias (España) y en el Área Metropolitana de Lisboa (Portugal). Los objetivos específicos son los siguientes:

- ✓ Procesar, presentar e interpretar los mapas de velocidad media LOS (mm/año) y las series temporales de deformación (mm) vinculadas a procesos de inestabilidad y subsidencia de laderas en Asturias y en el Área Metropolitana de Lisboa.
- ✓ Comparar los resultados de los movimientos del terreno obtenidos con las técnicas PSIG y P-SBAS entre sí y con las técnicas tradicionales de auscultación.
- ✓ Establecer el origen de las inestabilidades de ladera y procesos de subsidencia detectados en Asturias y en el Área Metropolitana de Lisboa.
- ✓ Analizar el potencial de las técnicas A-DInSAR para evaluar las inestabilidades de ladera y la subsidencia en Asturias y en el Área Metropolitana de Lisboa.

METODOLOGÍA

La investigación ha supuesto las siguientes etapas metodológicas:

1) Procesamientos A-DInSAR a partir de los softwares PSIG y P-SBAS utilizando tres grupos de imágenes SAR diferentes: i) 113 imágenes SAR de los satélites Sentinel-1A/B en órbita descendente, desde enero de 2018 a febrero de 2020; ii) 48 imágenes SAR en órbita ascendente y iii) 61 en órbita descendente del satélite Sentinel-1A desde enero de 2018 a abril de 2020.

2) Obtención de mapas de velocidades medias de deformación en la dirección suelo-satélite (LOS) (mm/año) y de las series temporales de deformación (mm).

3) Aplicación de las metodologías de post-procesado A-DInSAR de Active Deformation Areas (ADA tools) y estimación de las componentes Vertical y Horizontal de la deformación.

4) Integración en un Sistema de Información Geográfica de toda la información con datos geoespaciales y medidas topográficas tomadas mediante estación total y validación de las deformaciones obtenidas mediante salidas de campo.

5) Interpretación desde el punto de vista geológico-geotécnico de los resultados obtenidos.

RESULTADOS Y DISCUSIÓN

Los resultados fueron analizados en el siguiente orden: 1) resultados PSIG y P-SBAS a escala regional para la detección y seguimiento de inestabilidades costeras; 2) resultados A-DInSAR y medidas topográficas realizadas en la Península de Podes; 3) medidas de seguimiento topográfico y resultados A-DInSAR realizados en el deslizamiento del Faro de Tazones; 4) relaciones observadas entre las inestabilidades costeras identificadas con respecto al retroceso de la costa y la actividad de los deslizamientos a escala regional y local; discusión de limitaciones observadas y 5) sugerencias para mejorar las interpretaciones llevadas a cabo en esta investigación.

Áreas costeras

En el entorno del Cabo Peñas se han detectado velocidades máximas LOS de −17,1 a 37,4 y −23,0 a 38,3 mm/año, relacionadas con asentamientos del terreno e inestabilidades de ladera. Las deformaciones más intensas detectadas por A-DInSAR se observaron en el puerto del Musel, situado cerca de la ciudad de Gijón. Este caso particular se ha relacionado directamente con los asentamientos diferenciales.

Los principales factores limitantes para aplicar las técnicas A-DInSAR en el entorno del Cabo de Peñas, incluyendo la Península de Podes, y en el deslizamiento del Faro de Tazones fueron: 1) la escasez de *permanent scatterers* (PS) naturales debido a que la costa asturiana es un territorio predominantemente no urbano; 2) la orientación del terreno; en particular, los terrenos con orientaciones NE provocan que los movimientos de ladera sean paralelos a la dirección del sensor del satélite. En consecuencia, estos movimientos son prácticamente imposibles de detectar mediante A-DInSAR; 3) la elevada inclinación de las laderas en algunos sectores, lo que provoca efectos de sombra y escorzo (Colesanti y Wasowski, 2006) y, por tanto, zonas sin señal y una drástica reducción de la resolución espacial y 4) la velocidad de inestabilidad; las principales tipologías son desprendimientos de rocas y flujos, con velocidades que van de lentas a extremadamente rápidas (> 13 m/mes - > 5 m/s). Así, estas tipologías de inestabilidad de ladera son indetectables mediante técnicas A-DInSAR (Canuti et al., 2004).

En el deslizamiento del faro de Tazones, los mapas de velocidades media de deformación LOS obtenidos no han permitido visualizar la deformación ocurrida para el periodo de observación, dada la ausencia de PS ligada a la predominancia de zonas de pastos. Sin embargo, los PS detectados en el entorno próximo a la masa de terreno deslizada ha permitido conocer que el faro de Tazones y el pueblo de Villar son actualmente zonas estables y verificar los límites oeste y sur del deslizamiento de Tazones. Por otro lado, las medidas topográficas han mostrado desplazamientos mensuales máximos de algunos puntos desde 1 m, hasta más de 14 m. Sin embargo, las características del movimiento y la naturaleza del terreno no han permitido obtener buenos resultados con las técnicas A-DInSAR.

Área montañosa

En el sector de la Cuenca Carbonífera Central, las deformaciones medidas presentaron velocidades máximas LOS de −18,4 y 9,5 mm/año. Estas velocidades son compatibles con fenómenos de subsidencia y de recuperación del nivel freático en un entorno de minería subterránea de carbón. Sin embargo, debido a la confidencialidad de los datos geológico-mineros, estas hipótesis no pudieron ser corroboradas. También se detectaron deformaciones relacionadas con inestabilidades de ladera superficiales. En este sentido, , se pudieron estudiar 5 depósitos superficiales. Considerando el umbral de estado de actividad de ± 2,5 mm/año y las evidencias observadas en la campaña de campo tres de ellos pueden clasificarse como movimientos en masa activos. Como evidencias de movimiento, presentan grietas de tensión, daños en edificios o fenómenos de *creep*.

Área Metropolitana de Lisboa

En el Área Metropolitana de Lisboa se han obtenido 4 ADAs en órbita ascendente y 3 ADAs en órbita descendente, relacionadas con subsidencia industrial y urbana con una velocidad máxima LOS estimada de −25,5 mm/año. La máxima velocidad Vertical medida fue −32,4 mm/año. Se han identificado dos sectores con subsidencia (A y B), con extensiones de 2.601.950 y 222.846 m^2.

En cuanto a la naturaleza y origen de los fenómenos de subsidencia observados en esta investigación, se relacionan con depósitos antrópicos y con la compactación de los materiales aluviales, cuyos espesores son de 5 a 20 m (Carvalho et al., 2018). Este proceso puede observarse particularmente en el polígono industrial de Vila Franca de Xira-Carregado (identificado como sector A).

CONCLUSIONES

Aspectos globales destacados

Este trabajo ha puesto de manifiesto la utilidad de métodos remotos de monitorización , como las técnicas A-DInSAR, para procesar e interpretar mapas de velocidades medias de deformación LOS relacionadas con movimientos del terreno. En particular, las técnicas PSI y P-SBAS, se han mostrado útiles para el estudio de inestabilidades de ladera y fenómenos de subsidencia en Asturias (España) y en el Área Metropolitana de Lisboa (Portugal). Esta investigación ha permitido progresar en el conocimiento de la actividad de los movimientos en masa, las inestabilidades costeras y la incidencia de la minería del carbón en Asturias. Asimismo, se ha logrado un avance significativo en la evaluación de la subsidencia urbana del Área Metropolitana de Lisboa. Las diferentes líneas de investigación futura propuestas permitirán mejorar los resultados, interpretaciones y conclusiones logradas en esta investigación.

A continuación, se indican las principales contribuciones alcanzadas para cada área de estudio.

Áreas costeras de Asturias

Se han aplicado las técnicas A-DInSAR en diferentes zonas partiendo de 113 imágenes SAR descendentes IW SLC de Sentinel-1A/B, desde enero de 2018 hasta febrero de 2020, aplicándose tanto un software comercial (PSIG *chain*), como un software no supervisado (P-SBAS del servicio GEP).

En el entorno del Cabo de Peñas, incluyendo la Península de Podes, se han detectado asentamientos del terreno e inestabilidades de ladera con VLOS máximas de −12,4 y −23,0 mm año^{-1}, afectando a infraestructuras esenciales, como una central eléctrica en Avilés y el Puerto del Musel, en Gijón. Además, se detectó una inestabilidad costera desarrollada al oeste del Cabo de Peñas con VLOS máxima de −9,1 mm año^{-1}. Estos resultados permiten destacar que las técnicas A-DInSAR pueden ser utilizadas con éxito para detectar, modelar y monitorizar inestabilidades del terreno en costas acantiladas a escala regional y local. Además, desde el punto de vista metodológico, el uso combinado de ambas técnicas en el entorno del Cabo de Peñas, ha permitido definir la geometría y las características de los acantilados en relación con las trayectorias descendentes de los satélites, junto con la naturaleza de las inestabilidades de ladera, como los factores principales que limitan la aplicación de A-DInSAR. Se ha demostrado que el procesado P-SBAS puede ser una herramienta útil de apoyo para aquellos procesados A-DInSAR realizados con otro software comercial/robusto.

Las principales aportaciones alcanzadas respecto al deslizamiento del Faro de Tazones, han sido: corroborar los límites de la zona desestabilizada y, por tanto, que el pueblo de Villar y el Faro de Tazones se encuentran fuera del sector actualmente inestable. Sin embargo, las técnicas A-DInSAR no han permitido detectar los movimientos del terreno registrados mediante estación total. Estas técnicas topográficas de auscultación permitieron caracterizar el movimiento del deslizamiento del Faro de Tazones, con un desplazamiento máximo de 14,93 m medido entre noviembre de 2019 y febrero de 2020. Los principales factores limitantes han sido la alta complejidad de la zona, predominantemente boscosa, la ausencia de reflectores naturales adecuados y la velocidad del movimiento en masa, demasiado rápida para ser detectada mediante los métodos A-DInSAR.

Área montañosa de Asturias

Se han aplicado las técnicas A-DInSAR utilizando 113 imágenes descendentes IW SLC SAR de Sentinel-1A/B, de enero de 2018 a febrero de 2020 y aplicando el software comercial PSIG.

Se han podido detectar y monitorizar 5 recubrimientos superficiales, 3 de ellos con movimiento activo. Las VLOS máximas medidas en estos depósitos han sido −6,9 y 7,4 mm/año. La comparativa entre los registros de las TS y de precipitación diaria ha permitido relacionar los movimientos detectados con episodios de precipitación. Se registraron deformaciones acumuladas máximas de −17 mm coincidiendo con 152 mm de precipitaciones entre octubre y diciembre de 2019.

Se midieron VLOS máximas de −18,4 mm/año y 9,5 mm/año sobre La Felguera y Sama de Langreo, donde se ubican las explotaciones mineras de carbón de Fondón, Candín I y II. Aunque, debido a la confidencialidad y a la falta de datos en profundidad de las zonas explotadas, no se puede afirmar que las deformaciones detectadas se deban a la minería del carbón, una hipótesis plausible es que el pozo Fondón funcione como acuífero artificial que, actualmente, se estaría recuperando debido a la subida del nivel del agua subterránea, lo que justificaría el levantamiento detectado alrededor del pozo.

En esta área de estudio, se ha demostrado la aplicabilidad y utilidad de las técnicas A-DInSAR y de los datos SAR del Sentinel-1 cuando el área de estudio se caracteriza por presentar información confidencial y restringida sobre los entornos geológicos, hidrológicos y mineros.

Área Metropolitana de Lisboa

En esta zona urbana se han aplicado el procesamiento A-DInSAR y el ADA *tools* utilizando dos conjuntos de 48 imágenes ascendentes y 61 descendentes IW-SLC SAR de Sentinel-1A, de enero de 2018 a abril de 2020. Para el procesado A-DInSAR se ha aplicado la técnica P-SBAS del servicio GEP.

Se han detectado y evaluado 4 ADAs ascendentes y 3 descendentes relacionadas con hundimientos urbanos e industriales. La VLOS máxima detectada ha sido de −25,5 mm año^{-1}, mientras que la velocidad Vertical máxima ha sido de −32,4 mm año^{-1}. La comparación de VLOS, ADAs y la velocidad Vertical ha ayudado a interpretar los resultados y a zonificar adecuadamente los sectores de subsidencia de 2.601.950 y 222.846 m^2, respectivamente. El origen de la subsidencia urbana/industrial detectada se ha relacionado, según los datos geológicos e hidrológicos, con la compactación de depósitos aluviales y materiales antrópicos. Sin embargo, no debe descartarse el hecho de que la subsidencia pueda deberse también a la sobreexplotación de las aguas subterráneas, aunque serían necesarios más datos hidrológicos para apoyar esta hipótesis.